

NSK Technical Journal

Motion & Control

No. 29 June 2018

Special Issue of Automotive Products

*To Make a Contribution
to Next-Generation
Automobile Society*

**Autonomous
driving
technology**

**Wheel Hub
Motor!**

**Electric Power
Steering**



ISSN1342-3630

NSK

MOTION & CONTROL No. 29

NSK Technical Journal

Printed and Published: June 2018

ISSN1342-3630

Publisher: NSK Ltd., Ohsaki, Shinagawa, Tokyo, JAPAN

Public Relations Department

TEL +81-3-3779-7050

FAX +81-3-3779-7431

Editor: Hirotoshi ARAMAKI

Managing Editor: Hitoshi EBISAWA

Design, Typesetting & Printing: Kuge Printing Co., Ltd.

© NSK Ltd.

The contents of this journal are the copyright of NSK Ltd.

Contents

Preface

Automotive Products and Technologies	<i>N. Goto</i>	1
--	----------------	----------

Technical Articles

Transmission-Equipped Wheel Hub Motor Consisting of Two Electric Motors and the Performance Evaluation	<i>R. Morita, S. Yamamoto, M. Oike</i>	2
Estimation of Traction Curves under Practical Operating Conditions	<i>H. Itagaki</i>	10
Improving the Efficiency of Derivative Development through Systematic Restructuring.....	<i>M. Oba</i>	23
Weight Reduction of Column-Type EPS through Gearbox Thinning	<i>T. Kichikawa, T. Koike, T. Ishii</i>	35
Recent Technical Trends in Hub Unit Bearings.....	<i>T. Sakaguchi</i>	43
Low-Friction Technology for Tapered Roller Bearings.....	<i>Y. Saikawa</i>	51
CFD Analysis of Tapered Roller Bearings and Ball Bearings for Reducing Agitation Torque	<i>Y. Wen, S. Miyata</i>	60
Enhanced Performance of Rolling Bearings by Improving the Resistance of Rolling Elements to Surface Degradation.....	<i>H. Komata, Y. Iwanaga, T. Ueda, K. Ueda</i>	70
Relationship between Supplied Oil Flow Rates and Oil Film Thicknesses under Starved Elastohydrodynamic Lubrication	<i>T. Maruyama, T. Saitoh</i>	83

New Products

BELTOP8 High-Reliability and Low-Friction Ball Bearings for CVTs		96
Super-Long-Life Needle Rollers for Automobile Transmissions		98
Plastic Pin Internal Contractile Steering Column		100

Automotive Products and Technologies

Nobuo Goto
Senior Vice President,
Head of Automotive Technology Development Center

Dear reader:

We very much appreciate your interest in NSK's Technical Journal Motion & Control No. 29.

In this issue, entitled "Automotive Products and Technologies," we feature NSK's latest technologies and products related to automobiles, and we hope that you will read it through.

As you are well aware, due to remarkable progress and innovation in the automotive sector in recent years, new terms are now enjoying widespread use, such as "autonomous driving," "car sharing," "continuous Internet connection," and "motorization." Therefore, unprecedented future visions, in which the term "mobility" is more appropriate than "automotive," are presently in the making. This is not just a part of the process toward an ideal form that the automotive society has been pursuing since its inception but also a movement aligned with global environmental conservation and the securing of traffic safety.

NSK is responding to this trend in the area of Motion & Control, and this includes not only the long-awaited weight and loss reduction of machine elements but also responses to new driving sources that are electrically motorized, delicate, have swift control by computer, and more. With the four core technologies of tribology, materials, numerical simulation, and mechatronics, we have strived to enhance the functions and performance of machine elements, particularly bearings and linear motion products, and systems such as electric power steering. In this particular issue, we will introduce the latest technologies in our product lineup as well as those that fall under the above-mentioned new terms.

Looking ahead, we will continue to highly value your guidance and encouragement.



Nobuo Goto

Transmission-Equipped Wheel Hub Motor Consisting of Two Electric Motors and the Performance Evaluation

Ryuhō Morita, Shin Yamamoto and Mitsuru Oike
Automotive Technology Development Center

Abstract

Electrification of cars is rapidly proceeding in recent years. Wheel hub motors are known as one of the most promising electrical drive units, because they are applicable to various types of vehicle, such as hybrid electric vehicles (HEVs), electric vehicles (EVs), and fuel cell vehicles (FCVs). However, commercialization has yet to be achieved due to the difficulty in motor miniaturization while delivering both large drive torque and sufficient maximum speed. NSK has focused on the problem and developed a downsizing technology of the wheel hub motor by using two small electric motors and a unique transmission. The wheel hub motor has two speeds (Low/High) for forward and achieves shockless and smooth gear shifting by controlling the rotational directions and speeds of the two electric motors. We have built a test vehicle in order to conduct driving tests and confirmed fundamental functions and performance of the wheel hub motor.

1. Introduction

Wheel hub motors, also known as in-wheel motors, have garnered significant attention recently as a drive unit suitable for the diversification of cars. This is due to their being applicable to various drive types, such as HEVs, EVs, and FCVs, without depending on their body structure.

Wheel hub motors can benefit the environment by reducing the energy consumption of cars due to their reduced weight, so they can reduce drivetrain parts including engines and transmissions. Safety is also enhanced because the drive torque from each wheel can be controlled at will. Furthermore, comfort is improved since indoor space can be enlarged.

Yet despite these advantages, designing and manufacturing lighter, smaller wheel hub motors that fully meet both the required driving capability and the mountability near the wheels are extremely difficult, which is why they have not been put into wide use.

To address these problems, we the authors developed a wheel hub motor consisting of two motors. In this article, we introduce our proposal for the structure of the wheel hub motor, transmission mechanism, and control methods as well as test vehicle results.

2. Transmission Mechanism Requirements for Electric Vehicles (EVs)

Most of the electric drive units currently equipped with EVs have fixed stage reducers rather than transmissions.

Generally, the ideal driving performance diagram for vehicles and torque-speed performance diagram of an e-motor are not similar in shape. Therefore, when using a fixed-stage reducer and gaining the necessary driving performance, excess motor power generators and motor size are also enlarged.

This is described in Figure 1 (a). Striving to gain this necessary level of driving performance requires larger motors, and this is not favorable for drive units that must be compact and light-weight in relation to wheel hub motors.

On the other hand, Figure 1 (b) shows the desired driving performance and torque-speed performance of a motor for vehicles with a two-speed transmission. Wheel hub motors can be downsized since the maximum output of vehicles and output performance with which the motor and transmission are combined often correspond, and excess power can be reduced as shown in Figure 1 (a). Also, as the areas with high motor efficiency are expanded, and those that are constantly used for driving performance diagrams draw near, not only the efficiency of EVs can be improved; their cruising distance will inevitably be extended as well.

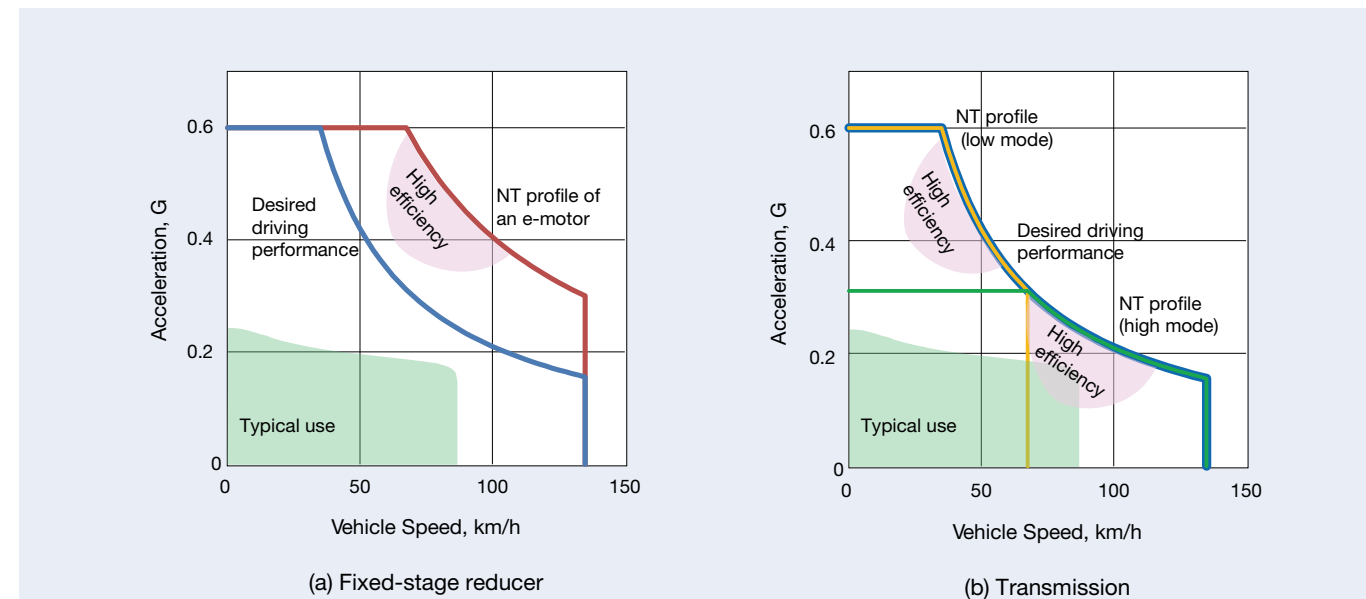


Fig. 1 Driving performance and NT profiles of an electric motor

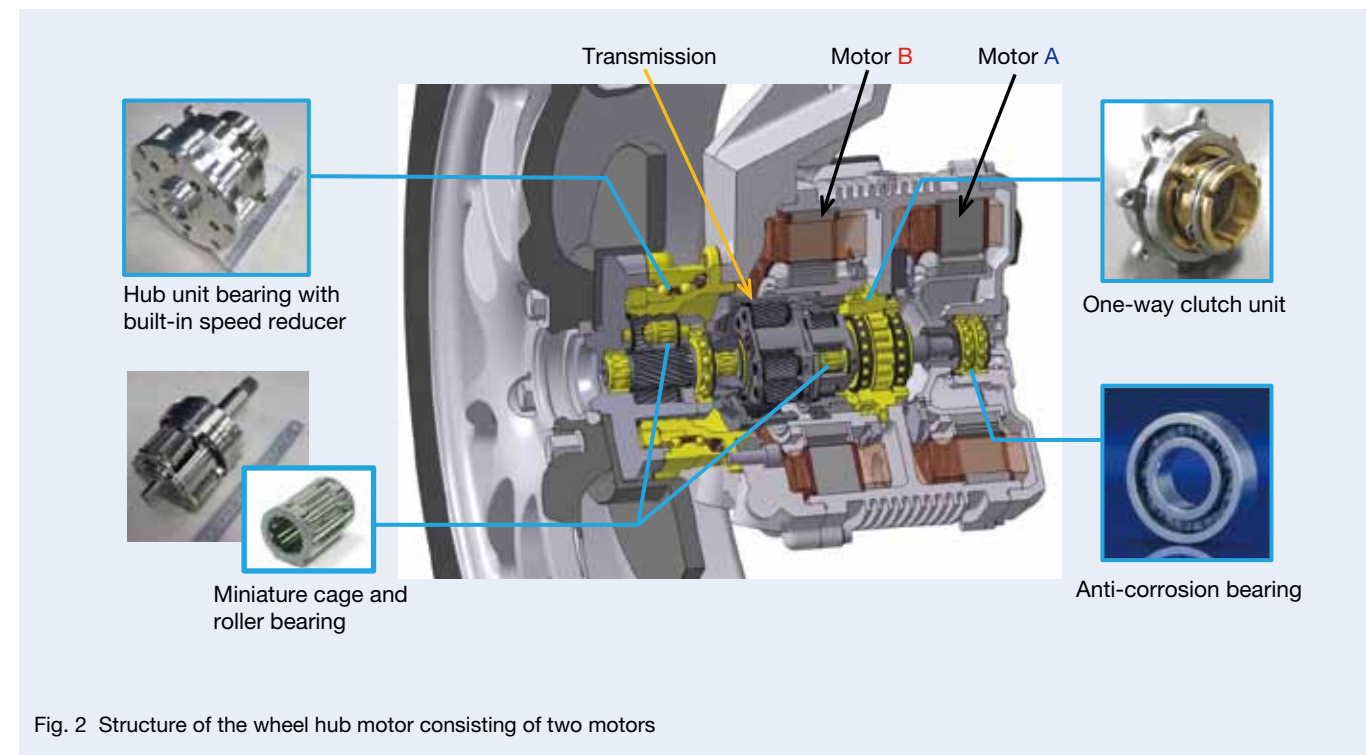


Fig. 2 Structure of the wheel hub motor consisting of two motors

3. Structure and Features of the Wheel Hub Motor Consisting of Two Motors

As shown in Figure 2, the wheel hub motor consisting of two motors is comprised of two inner type rotors, transmission consisting of two planetary gear sets, and a one-way clutch unit as well as a hub unit bearing with a

built-in final speed reducer. The transmission is placed at the bore of the two motors. The one-way clutch unit is used to shift operation and regulates the rotational direction of a single pinion planetary gear carrier. While the output of the transmission is reduced by approximately one-fourth by the hub bearing with a built-in final speed reducer mounted to the suspension upright, it amplifies the torque

and is transmitted to the wheel. Figure 3 shows the construction of the wheel hub motor. Gear construction of the wheel hub motor is shown in Figure 3 as well as major specifications for each wheel in Table 1.

The weight of the wheel hub motor consisting of two motors can be reduced by 30% if it achieves the same level of performance as one motor and fixed-stage reducer combined. Moreover, the wheel hub motor consisting of two motors achieves gear shifting by controlling the rotational direction and speed of these motors.

More specifically, three options are selectable as follows:

- (1) Low speed and low mode of large torque
- (2) High speed and high mode of small torque
- (3) Reverse

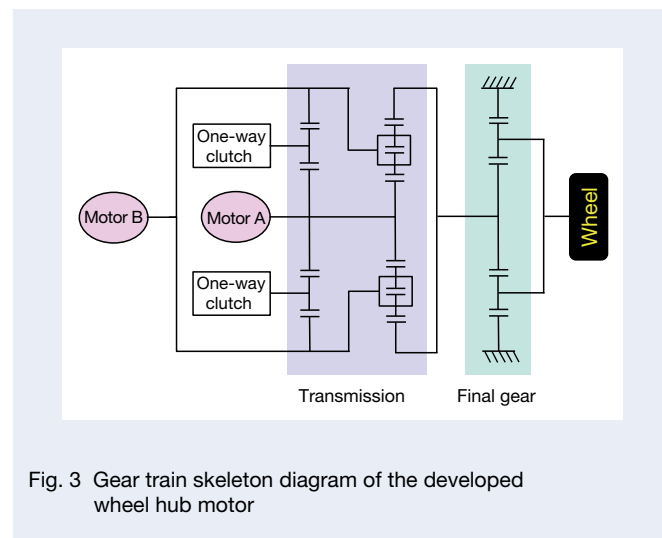


Fig. 3 Gear train skeleton diagram of the developed wheel hub motor

Table 1 Major specifications of the developed wheel hub motor

Item	Value
Max. power	25 kW
Max. torque (Low mode)	850 Nm
Max. torque (High mode)	400 Nm
Max. vehicle speed	135 km/h

4. Shift Mechanism of the Wheel Hub Motor

4.1 Low mode operation

Figure 4 is a lever diagram for low mode that describes the rotational direction and torque direction of each point.

Motor A and motor B have to rotate in opposite directions in order to engage the one-way clutch unit and move the support point of the double pinion planetary ring gear (R2) to the forward side. Also, slightly shifting the supporting point (R2) of the double pinion planetary gear against the supporting point (C1) of the one-way clutch unit (making a slight difference between the gear ratio of the single pinion planetary gear and the gear ratio of the double pinion planetary gear) achieves the ideal speed reduction ratio. At low mode, when transmitting the power of motor A into the ring gear (R2) of the double pinion planetary gear, some power flows from the double pinion planetary gear's carrier (C2) into the single pinion planetary unit's ring gear (R1) and once again forms a power circulation passage that drives the single pinion planetary unit's sun gear (S1). In low mode to engage the one-way clutch unit, the rotating speed ratio of motor A and motor B is constant. Also in this mode, moving forward is possible as long as either motor A or motor B is functioning properly, which makes it advantageous in terms of fail-safe.

4.2 High mode operation

In high mode, since the torque direction of motor B is the same as that of motor A and the one-way clutch unit is separated, the carrier of the single pinion planetary gear can be freely rotated. This is when the power circulating passage from the ring gear of the single pinion planetary gear to the sun gear disappears. As a result of its disappearance, the lever diagram for high mode has become Figure 5.

As the power of motor A is transmitted to the sun gear (S2) of the double pinion planetary gear, while that of power B is being transmitted to the carrier (C2) of the double pinion planetary gear, it is outputted from the double pinion planetary gear to the final speed reducer. If at this time the torque direction of the two motors is the same, the motor is designed to turn to high mode regardless of the rotational direction of motor B.

4.3 Reverse mode operation

Figure 6 shows a lever diagram for reverse mode. The condition in reverse mode is essentially the same as that in high mode, apart from the wheel's rotational direction, since the one-way clutch is separated. Turning the sun gear (S3) of the final speed reducer and ring gear (R2) of the double pinion planetary gear for the reverse side is necessary in order to reverse the vehicle; however, setting the two motors at the same rotating speed makes

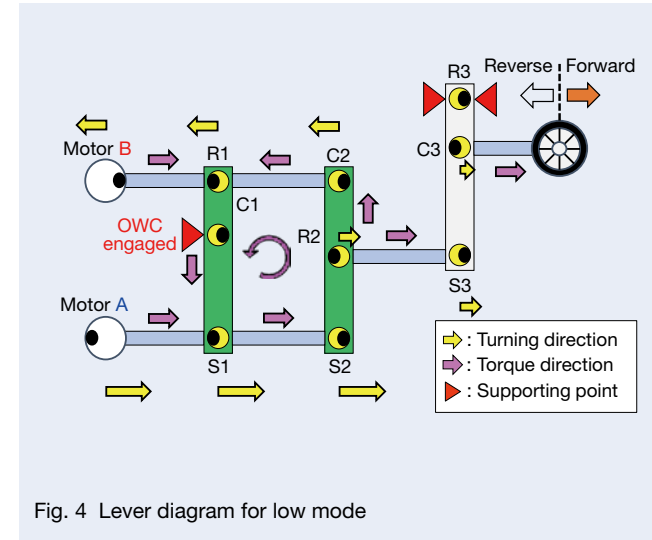


Fig. 4 Lever diagram for low mode

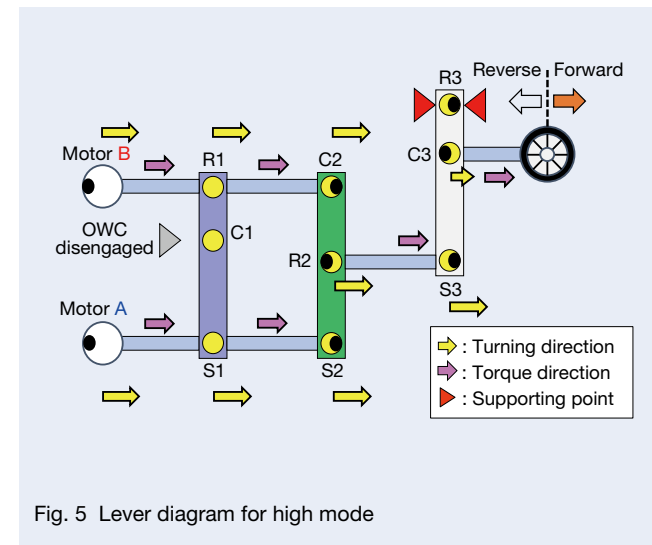


Fig. 5 Lever diagram for high mode

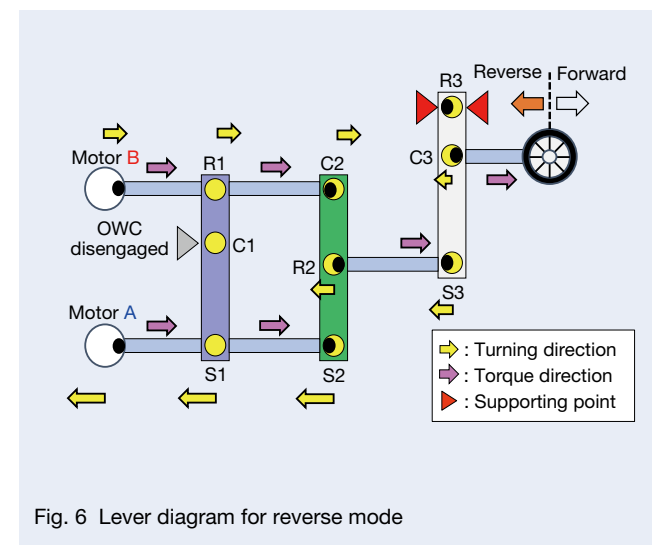


Fig. 6 Lever diagram for reverse mode

reversing impossible. The reason for this is the one-way clutch unit regulates the rotational direction of the single pinion planetary gear's carrier (C1) in one direction. Therefore, if the rotational direction of the wheel for forward is defined as CW and that of the wheel for reverse is defined as CCW, the reverse operation requires that the rotational speed ratio of the two motors is maintained within a certain range in a way that avoids engaging the one-way clutch by turning motor A and motor B in the direction of CCW and CW, respectively.

When the rotational speed of motor A and motor B remains within the area (a) of Figure 7, a wheel rotates in the reverse direction. On the other hand, if the rotational speed of motor A and motor B remains within the area (b), a wheel rotates in the forward direction. However, in the case of the area (c) in which the one-way clutch is engaged, the rotational speed of motor A and motor B will never become area (c). The boundary of each area is uniquely determined by the gear ratio that constitutes the transmission.

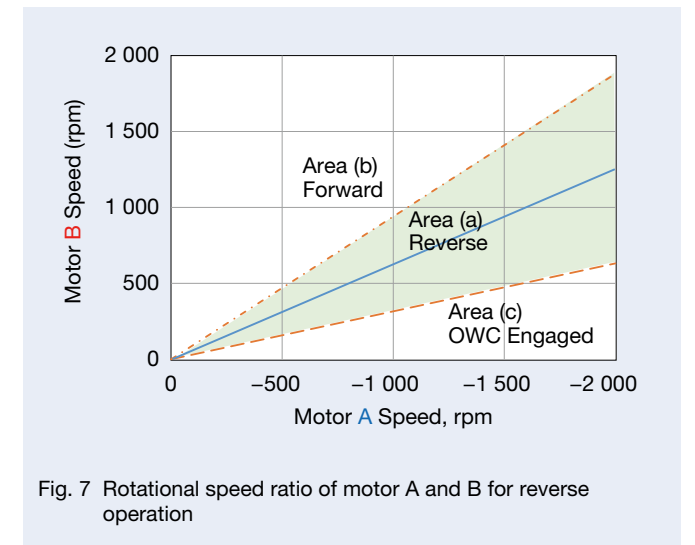


Fig. 7 Rotational speed ratio of motor A and B for reverse operation

5. Mounting to a Test Vehicle and Control Method

5.1 Test vehicle and system configuration

A test vehicle was manufactured for the purpose of evaluating various functions of the wheel hub motor (Figure 8). As the test vehicle can separate its mainframe from its front and rear sub-frames, the vehicle can also handle experiments for electric drive units except for those with a wheel hub motor or electric power steering. While the inverter for the wheel hub motor is positioned inside the front removable frame, the power control box is positioned at the rear removable frame. Currently, the wheel hub motor is mounted at the front two wheels.

Figure 9 shows a system diagram of the test vehicle, which is controlled using a dSPACE Tandem-AutoBox. As the Autobox calculates torque/speed demand from the accelerator pedal angle, condition of the forward/reverse changeover switch, and condition of the low/high changeover switch, it transmits the torque/speed demand

to the two inverters. One of the inverters controls one wheel while the inverter separately controls motor A and motor B inside the wheel hub motor. The rated value of 400V DC power is supplied from the power source control box to the inverter. The control box is separated from the Autobox to ensure safety. The rotating angle and speed of the two motors inside the wheel hub motor are detected by an eddy current angle sensor.

5.2 Low mode control method

In low mode, both motor A and motor B are torque controlled. The controller sends the torque demand value to the inverters that are in proportion to the accelerator pedal angle. The torque command for motor A is given for the CW direction and that for motor B is given for the CCW one, respectively. At this time, the one-way clutch is engaged and the carrier rotation of the single pinion planetary unit is regulated. Not only power is circulated between the single and double pinion planetary gears; a great deal of speed reduction ratio can also be achieved as well.

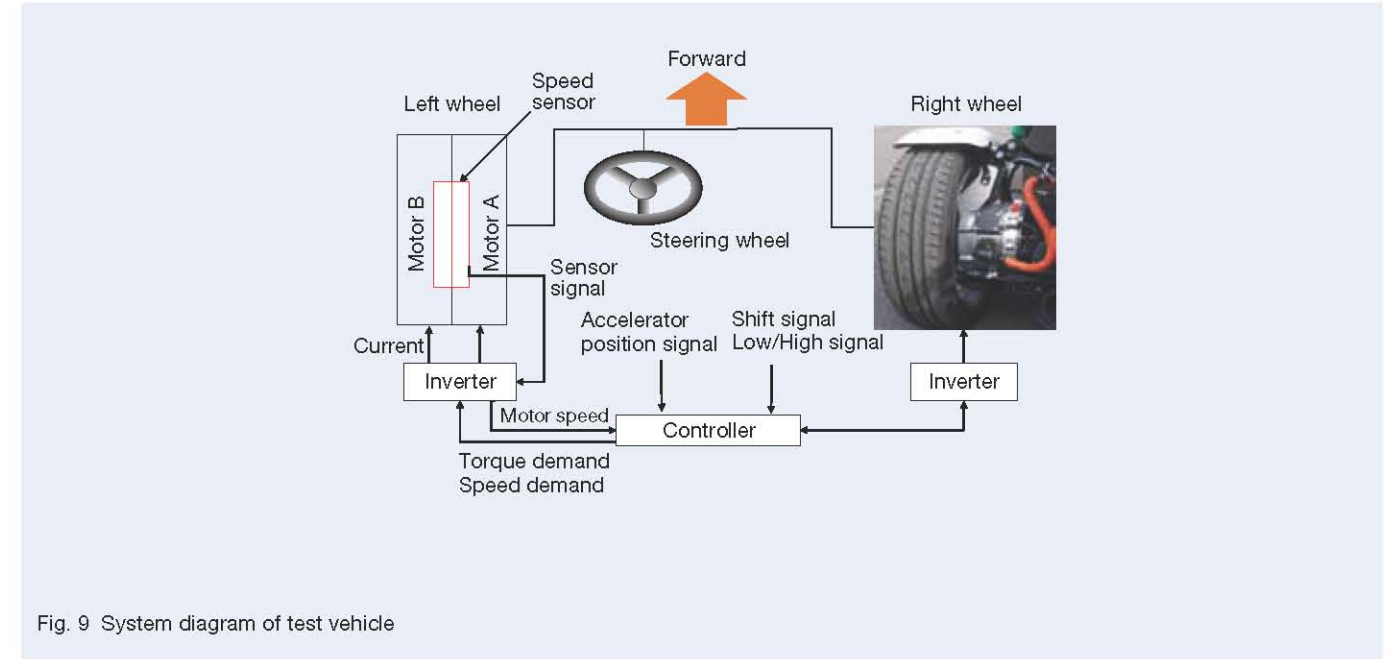


Fig. 9 System diagram of test vehicle

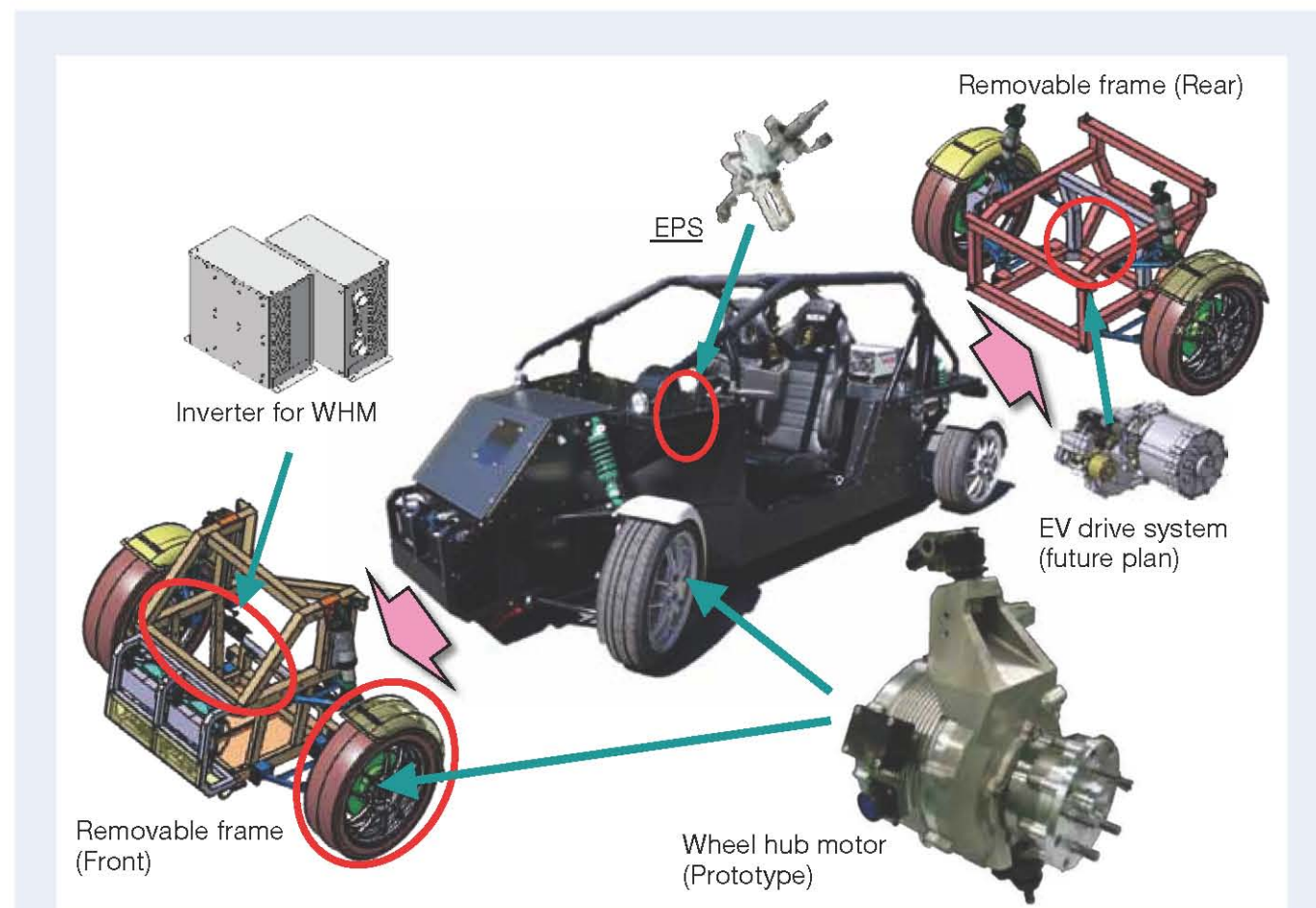


Fig. 8 Test vehicle for wheel hub motor

5.3 High mode control method

In high mode, motor A is torque-controlled while motor B is speed-controlled. Motor A receives torque demand in the CW direction that is proportionate to the accelerator pedal angle. Meanwhile, the speed of motor B is controlled to follow motor A as a target value of rotating speed. When referring to the rotating speed of motor A as a target speed value of motor B, smoothing the speed detected by the sensor is required through a low pass filter, which is effective for restraining the motor rotation so that it does not become vibratory under certain conditions.

5.4 Shift control method

The wheel hub motor consisting of two motors is mutually switchable between low mode and high mode without shift shock. There is no shift shock even if a mode is switched in arbitrary timing, since shifting from low mode to high mode is a movement from which the one-way clutch is detached.

On the contrary, controlling to suppress shift shock is needed since shifting from high mode to low mode brings about a sudden change by engaging the one-way clutch. More specifically, the control is required in order to ensure not only that wheel torque right before the shifting and the one right after engaging the one-way clutch correspond but also that the output torque of motor B is at the minimum. Immediately after the shifting starts, the motor torque is maintained (approximately 200 ms) until the one-way clutch is engaged, and torque demand is subsequently made to gradually increase so that it corresponds to the low mode demand. By doing this, engaging the one-way

clutch by high acceleration can be prevented and the sudden change of wheel torque, after engaging the one-way clutch, i.e., shift shock, can be suppressed.

5.5 Reverse mode control method

To realize the reverse operation of the wheel hub motor consisting of two motors, the motor must be driven with the one-way clutch detached, and the wheels must be rotated in the reverse direction. At this point, the speed of motor A and motor B is controlled since the rotational direction and torque direction of motor B do not correspond.

When reversing, the AutoBox sends the inverter a speed demand so that the rotating speed of motor A and motor B can remain within the area (a) of Figure 7. Since speed control is implemented in the course of reversing, operability and riding quality worsen when the sensitivity of speed demand for the accelerator pedal angle becomes too high. As a countermeasure for this problem, when the accelerator position is drastically reduced, smooth reversing can be achieved by imposing restrictions on the time change rate of speed demand by the two motors.

6. Driving Test Results

6.1 High/Low shifting test results

Figure 10 shows the test results for upshift from low mode to high mode. Upshifting starts at 0 sec, low mode at 0 sec, and high mode after 0 sec. Until 0 sec, both motor A and motor B rotate in reverse by torque control. Immediately after the shifting starts from low mode to high mode at 0 sec, the rotating speed of motor A and motor B continues to change until they finally correspond. There is no discontinuity in wheel speed before or after the shifting. Furthermore, no shift shock can be confirmed since there is no major change in the front-back direction accelerations of the vehicle.

Figure 11 shows the test results for downshift from high mode to low mode. The downshifting starts at 0 sec. Before 0 sec, or high mode, the transition mode starts at 0 sec, and then low mode after 0 sec. At 0 sec, motor B switches from speed control to torque control. Then, torque demand of motor A and motor B adjusts the output so that wheel torque becomes the same as the one in high mode before shifting starts. More specifically, 0.7 times more torque demand set from the accelerator pedal angle in low mode is sent to motor A as well as 0.1 times more the one that is sent to motor B, which is maintained until the one-way clutch is engaged. During this process, motor A rotates in reverse from motor B. When the one-way clutch is engaged, the rotational speed ratio of motor A and motor B becomes that of low mode. At and after 200 ms, at which point a sufficient amount of time has passed to engage the one-way clutch, torque demand for these two motors must be gradually increased in order to correspond to that set by the accelerator pedal angle. During the series of control, there is no discontinuity in wheel speed between the start and completion of the shifting. Also, no shift shock can be confirmed since there is no large spike-shaped waveform, although a slight fluctuation in the front-rear direction is detected immediately after the shifting starts.

6.2 Driving test results in reverse mode

Figure 12 shows the test results for operation in reverse. The target value for rotating the speed of motor A and motor B is set on the straight line that passes through the center of the area (a) in Figure 7. This is to secure a margin by avoiding infiltration outside of the area (a) where reversing is possible, since the motor speed breaks the speed relationship between the two motors by disturbance at times of extremely low speed. It was verified that the wheel can be rotated in the reverse direction if motor A and motor B are driven through targeting on the straight line. It was also confirmed that although the accelerator pedal is reversed at 5 sec, vehicle speed can be smoothly reduced by restricting the change ratio of demand without sensitively following the accelerator pedal angle.

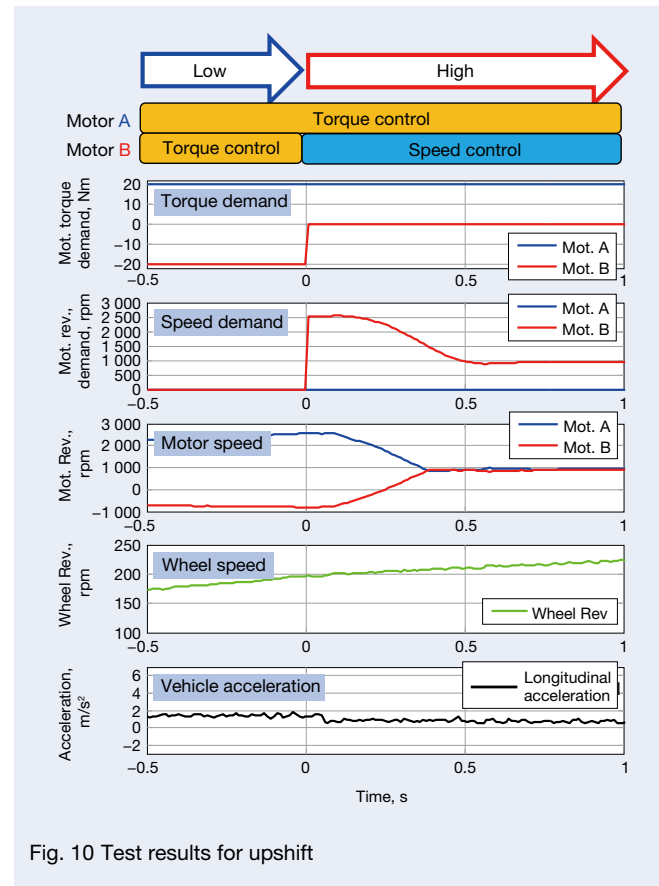


Fig. 10 Test results for upshift

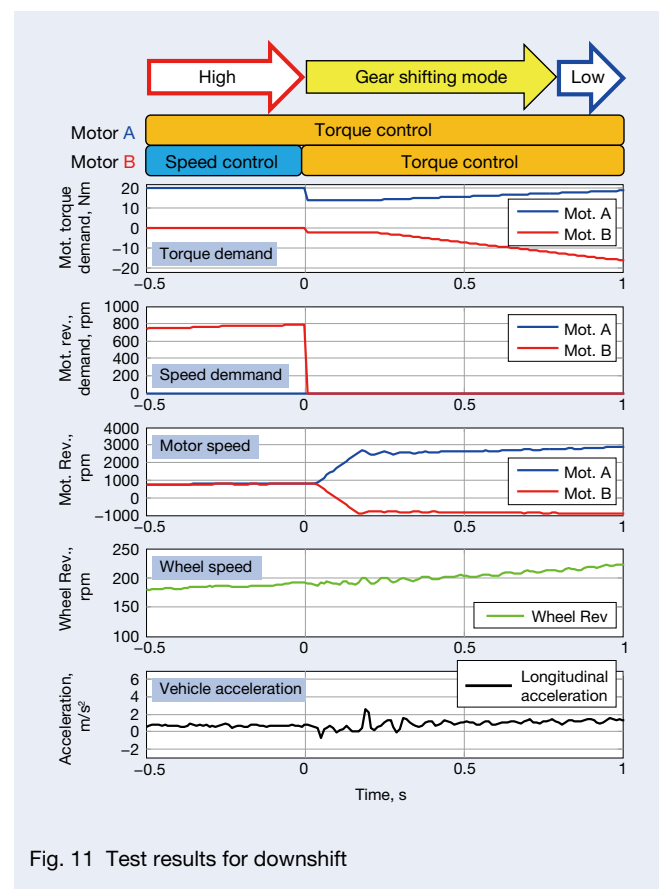


Fig. 11 Test results for downshift

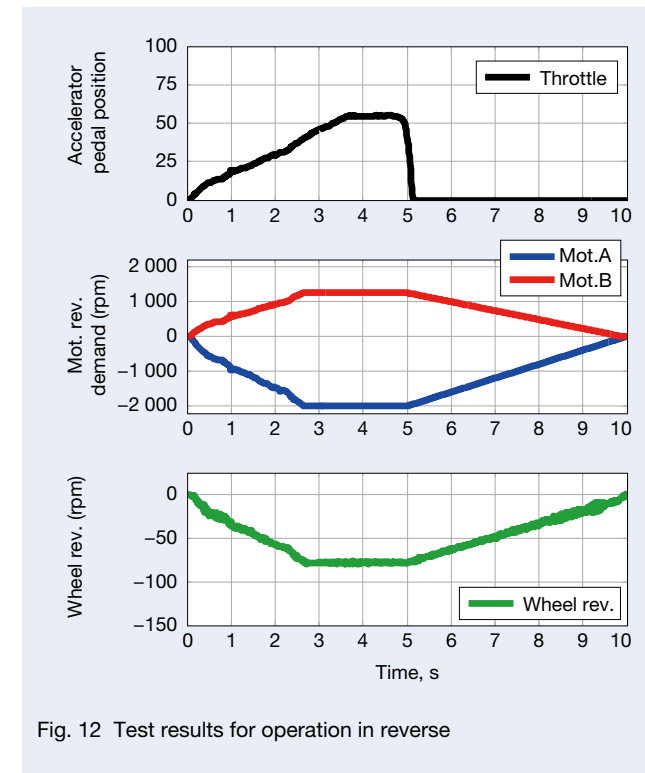


Fig. 12 Test results for operation in reverse

7. Conclusion

With the development of the wheel hub motor consisting of two motors, basic performance was verified using a prototype-equipped test vehicle. Through this test, we confirmed not only basic functions, such as low mode, high mode, and reversing, but also shifting without shock while driving.

This development was undertaken with the aim of commercializing machine elements used for the wheel hub motor unit, and they include:

1. Hub unit bearings with a built-in speed reducer
2. Miniature cage and roller for planetary gears
3. One-way clutch unit
4. Corrosion resistant insulation bearings

Throughout our development of wheel hub motors, we shall continue to endeavor to reach the most current levels of performance required for next-generation machine elements and be fully prepared for the practical application of these motors.

References

- 1) S. Murata, "Vehicle Dynamics Innovation with In-Wheel Motor," Proc. EVTeC'11, (2011)1-6.
- 2) H. Fujimoto, "Motion Control of Electric Vehicle with In-wheel Motor and Tire Lateral Force Sensor," Journal of Society of Automotive Engineers of Japan, Vol. 65, No. 3 (2011) 91-97.
- 3) H. Fukudome, "Reduction of Vehicle Longitudinal Vibration by In-Wheel Motors," Proc. 2015 JSAE Congress(Autumn), 19-15A (2015) 448-453.



Ryuhō Morita



Shin Yamamoto



Mitsuru Oike

Estimation of Traction Curves under Practical Operating Conditions

Hirofumi Itagaki
Automotive Technology Development Center

Abstract

To make the traction drive device compact, lightweight, and highly efficient, it is important to accurately estimate traction curves that express the rheological behavior of the oil film formed at the contact area of the rolling elements. A method for estimating traction curves based on creep theory has been proposed. Compared with other methods, this method features few free parameters in the mathematical model, allowing for simple calculations.

The method requires curve fitting using measured traction curves to identify a parameter (limiting shear stress) depending on temperature. However, it is more practical to obtain this temperature-dependent limit shear stress without curve fitting; therefore, this paper proposes a method for estimating traction curves that can simultaneously estimate the limiting shear stress by applying conventional methods based on creep theory.

1. Introduction

The traction drive device transmits power through an oil film generated at the contact portion formed when the smooth surfaces of a pair of rolling elements are pressed against each other. It has features such as low noise and low vibration, and it is capable of continuously variable transmission. Taking advantage of these features, the traction drive device is used as an increase/reduction gearbox and as the transmission of automobiles, aircraft, and various other industrial machines.

One of the traction drive devices is the toroidal continuously variable transmission shown in Figure 1. As shown in the drawing, the toroidal continuously variable transmission can change the gear ratio ($i_v = R_2/R_1$) in a stepless manner by changing the tilt angles of the rollers, that is, by changing the distances (rotation radii R_1 and R_2) from the disc rotation shaft to the contact point.

An elastic fluid lubricating film is formed at the contact portion of the paired rolling elements (discs, rollers) rotating while receiving a clamping force, F_c , and a tangential force (traction force F_t) generated as the shear resistance of the oil film is transmitted between the rotating bodies. This traction force F_t is proportional to the clamping force F_c , and its proportionality constant is called a traction coefficient ($\mu = F_t / F_c$). In addition, the peripheral velocity U_2 of the driven side rolling element slightly lags behind the peripheral velocity U_1 of the driving side rolling element. In this article, the ratio of the peripheral velocity difference ($\Delta U = U_1 - U_2$) to the driving side rolling element peripheral velocity is defined as the creep rate ($C_r = \Delta U / U_1$).

It is known that the traction coefficient μ shows a change, as shown in Figure 2, depending on the creep rate C_r , and this μ - C_r curve is called a traction curve. As shown in the drawing, the traction coefficient linearly increases (linear region) as the creep rate increases and gradually tends to decrease after indicating the maximum value (μ_{max}) while gradually decreasing the gradient. A decrease

in the traction coefficient with respect to an increase in the creep rate means that excessive slipping will occur in the rolling elements and disable the power transmission, a condition that must be avoided. More specifically, the traction coefficient ($\mu_d = T_r / (R \cdot F_c)$) of the operating point in the drive conditions (transmission torque; T_r , clamping force; F_c , and contact point turning radius; R) must fall, as shown in Figure 2, within the linear region.

It is known that the shape of the traction curve varies depending on operating conditions (oil temperature, peripheral velocity, contact pressure, spin, etc.) other than the creep rate¹⁻¹¹. Therefore, in determining the clamping force F_c to be given to the traction drive device, it is necessary for μ_d , in consideration of the change in the shape of the curve depending on the operating conditions, to have a sufficient margin with respect to μ_{max} under any operating conditions. In order to set this margin to the safe side, that is, to reduce μ_d , it is only necessary to increase F_c as apparent from the above related equation ($\mu_d = T_r / (R \cdot F_c)$). However, if F_c is increased unreasonably, the size and weight of the device must be increased to accept the increased F_c , which leads to a reduction in transmission efficiency and lifespan. Therefore, in order to guarantee the function and improve the performance (compactness/lightweight and high efficiency) of the traction drive device, it is necessary to determine the optimal specifications by accurately grasping shapes of the traction curves, which are anticipated for an actual machine.

Many methods of estimating traction curves have been proposed¹¹⁻¹⁸, one of which is the method based on creep theory¹⁸. This method, which is an applied version of the theory¹⁹ used for evaluating driving and braking forces between the rail and railway in railroad facilities, is said to be simple because it has few free parameters of the mathematical model (rheology model of oil film) used in the calculation when compared to the other methods. Although there is only one free parameter requiring identification using experimental

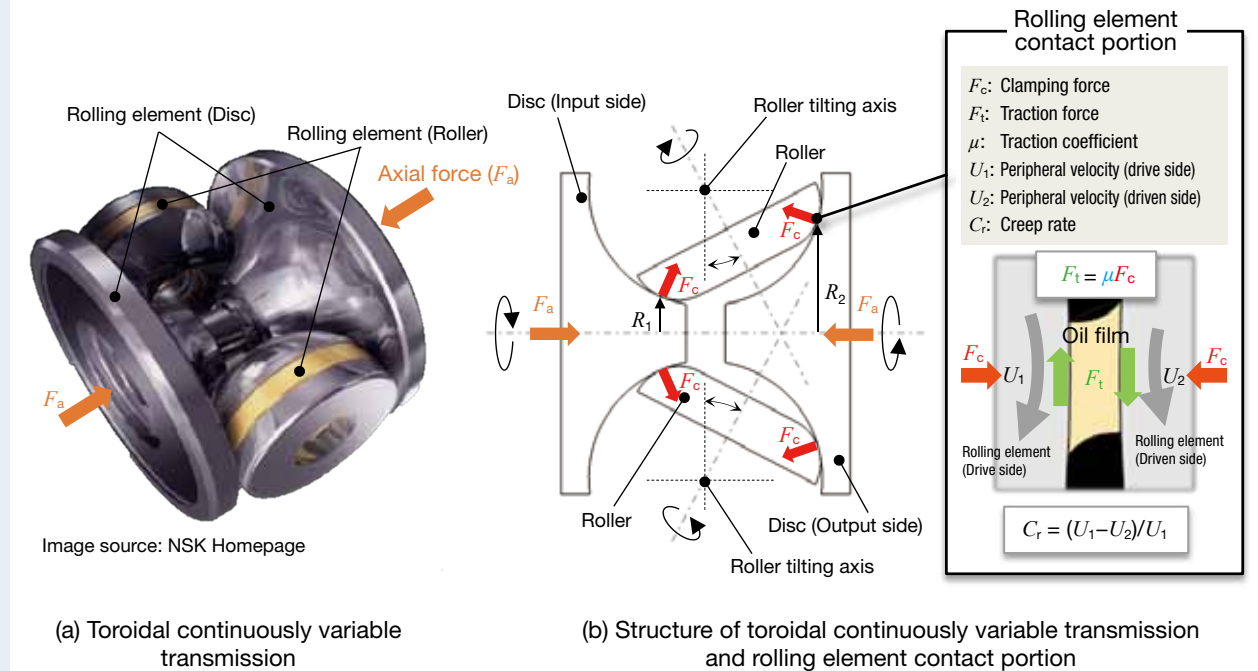


Fig. 1 Outline of a toroidal continuously variable transmission

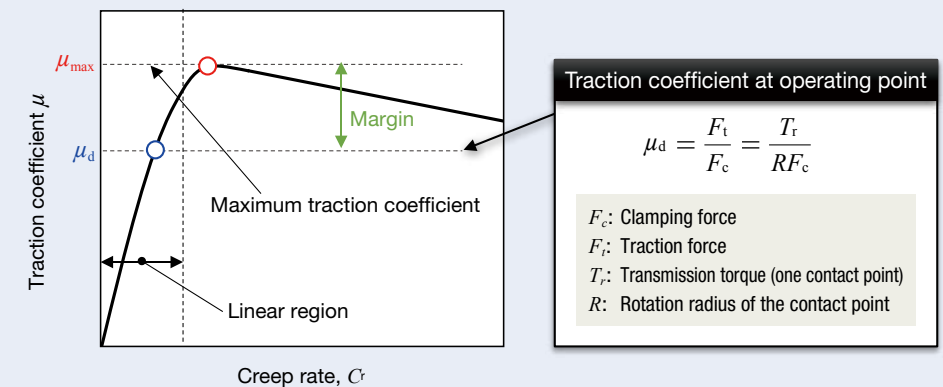


Fig. 2 Relationship between creep rate and traction coefficient (Traction curve)

results (limiting shear stress), this has a temperature dependency. The relationship between limiting shear stress and temperature is expressed as a function of the creep rate obtained from the actual measurement result of the traction curve (regression curve of the traction curve negative gradient part), and this is considered in the rheology model. (For more details, see Section 3.)

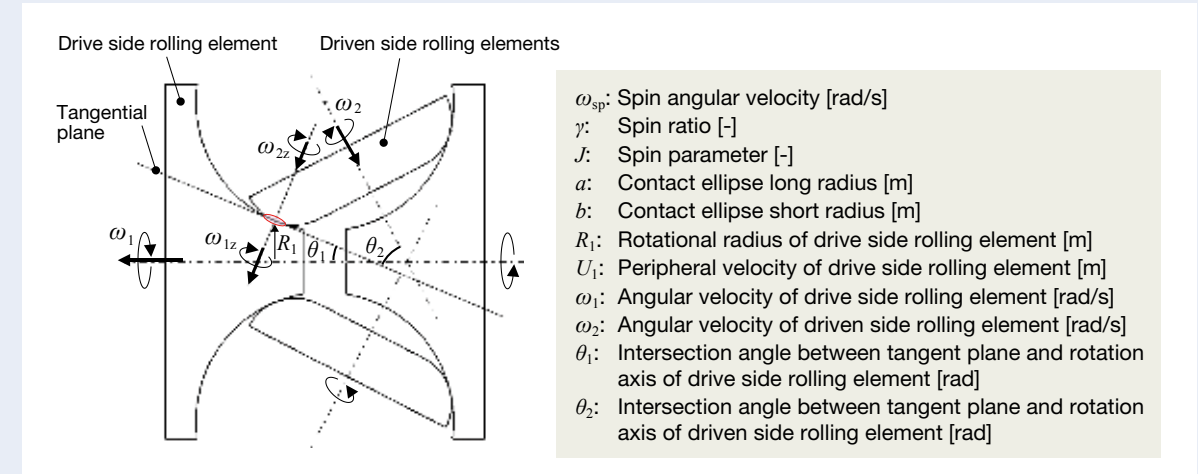
Incidentally, when identifying the free parameters of the rheology model, it is convenient to use the traction curve acquired from element testing machines (for example, four-cylinder testing machine⁷⁻⁸⁾ and two-cylinder testing machines⁹⁻¹¹⁾, which are simpler in rolling element shape than the actual machine). The reason is that eliminating the deformation and other effects of rolling elements as much as possible and obtaining free parameters as values specific to the oil film by eliminating the deformation of and other effects on the rolling elements as much as possible can be applied to various actual machines with different rolling element shapes. From such a practical point of view, there is room for improvement in the above conventional method in which the limiting shear stress of oil is taken into consideration as a function of the creep rate. Because if the rolling elements have different shapes and sizes (different heat capacities), there is a difference in temperature rise with respect to the creep rate, and therefore it is considered that a difference also occurs in the relationship between the limiting shear stress and the creep rate. More specifically, according to the conventional method, it is necessary to measure the traction curve for each target model and to previously obtain the regression curve of the negative gradient part.

Therefore, this paper makes a proposal of a traction curve estimation method as an applied version of the conventional method based on creep theory. In the proposed method, a traction curve is estimated while obtaining the oil film temperature rise with the creep rate change and the limiting shear stress changing depending on the oil film temperature.

2. Influence of Spin on Traction Curves

Many of the rolling elements of a traction drive device are accompanied by spin at their contact portions. Spin will be explained by taking a toroidal continuously variable transmission as an example. As shown in Figure 3, spin is a rotational motion that occurs when a rotating shaft of the two contacting rolling elements and the tangent plane do not intersect at one point, and its relative angular velocity is called a spin angular velocity (ω_{sp}). The spin angular velocity ω_{sp} is expressed as a difference ($\omega_{sp} = \omega_{1z} \sin \theta_1 - \omega_{2z} \sin \theta_2$) in the tangential plane normal direction component of the angular velocity of the rolling element, and the degree of influence is evaluated by a spin ratio (γ), a spin parameter (J), or the like. These defining equations are as shown in Figure 3, and as can be seen from the same equations, in the case of the toroidal continuously variable transmission, the spin amount changes frequently due to shift operation.

Next, the influence of spin on the traction curve will be explained. The authors are developing a high-power two-roller traction tester designed to measure the traction curves under the conditions of high power and spin, which are anticipated for an actual traction drive device¹⁰⁻¹¹⁾. The schematic of this test machine is illustrated in Figure 4. The tester provides a creep by rotating two rollers at different peripheral velocities to measure a traction coefficient. In addition to the supply oil temperature, peripheral velocity, and contact pressure (clamping force), it is possible to adjust the spin ratio by tilting the rotating shaft of one of the rollers. An example of the traction curves measured with the tester is shown in Figure 5. In the drawing, traction curves are depicted in the case where there is no spin (referred to as a pure rolling condition) and in the case where there is a spin (referred to as a spin condition). Operating conditions (peripheral velocity, contact pressure, and oil temperature) other than the spin ratio are the same. The rheological properties of the oil



Definition	Formula
Spin angular velocity	$\omega_{sp} = \omega_{1z} \sin \theta_1 - \omega_{2z} \sin \theta_2$
Spin ratio	$\gamma = \frac{\omega_{sp}}{\omega_1}$
Spin parameter	$J = \frac{\omega_{sp} \sqrt{ab}}{U_1} = \frac{\gamma \omega_1 \sqrt{ab}}{R_1 \omega_1} = \frac{\gamma \sqrt{ab}}{R_1}$

Fig. 3 Spin in the rolling element contact area

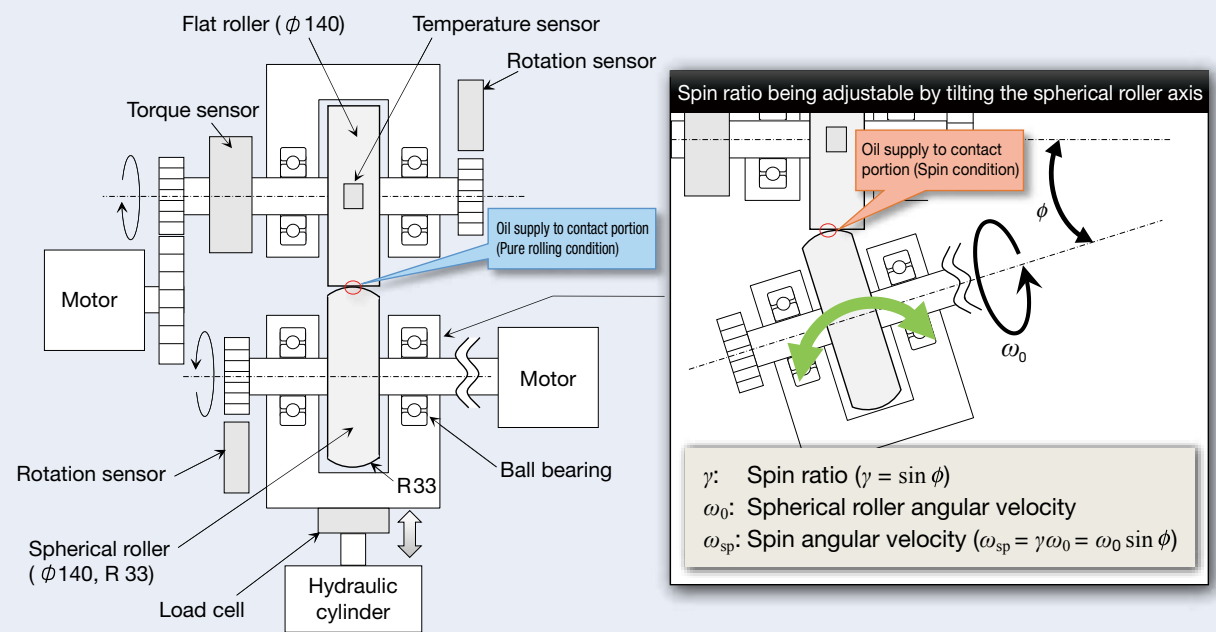


Fig. 4 Schematic of a high-power two-roller traction tester^{10), 11)}

(traction oil) used in the tests are as shown in Table 1. From Figure 5, it is possible to understand that even at the same contact pressure, peripheral velocity, and oil temperature, the rise of the curve is dulled and the maximum traction coefficient is lowered due to the influence of spin as compared with the case of the pure rolling condition. In addition, when comparing the results of Figure 5 (a) and 5 (b), it can be seen that the degree of decrease in traction coefficient due to spin is more conspicuous in the result of Figure 5 (b) where the spin parameter J is larger.

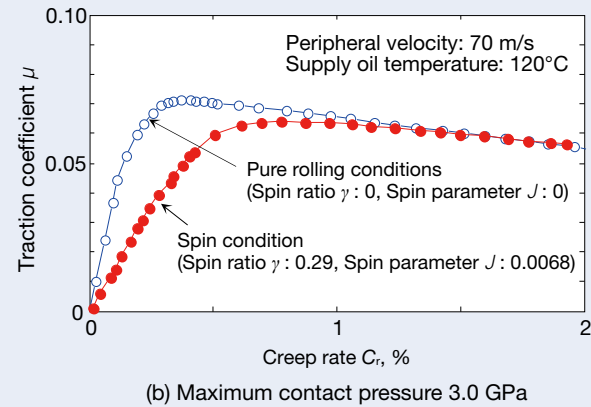
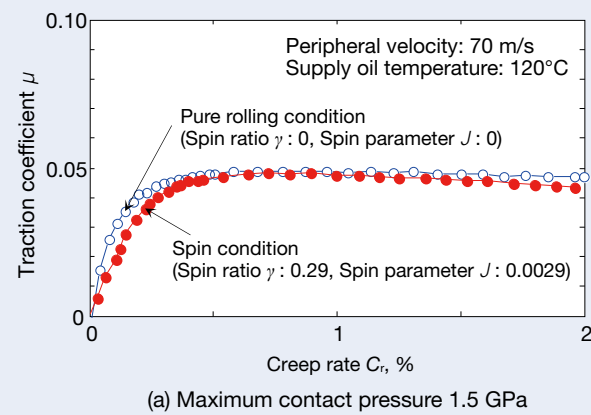


Fig. 5 Traction curves measured with a high-power two-roller traction tester

Table 1 Rheological properties of traction oil

Property value	Value	
Density (Atmospheric pressure, 15°C)	0.934 g/cm ³	
Kinematic viscosity	40°C	19.74 mm ² /s
	100°C	4.45 mm ² /s
Pressure-viscosity coefficient	40°C	21.2 GPa ⁻¹
	100°C	14.4 GPa ⁻¹

The method for estimating traction curves based on creep theory is to calculate, from the traction curve shape under pure rolling conditions, a traction shape under the same peripheral velocity, contact pressure and oil temperature conditions, and the spin condition. Therefore, it is possible to conclude that this method is particularly effective for a device such as a toroidal continuously variable transmission, in which the amount of spin fluctuates frequently during operation.

Therefore, this paper proposes the traction curve estimation method as an applied version of the conventional method based on creep theory and makes an evaluation of validity by comparing the estimated result of the traction curve with the actually measured result of the traction curve. It is to be noted that the actual results of traction curves shown below are all obtained with the above high-power two-roller traction tester, and the rheological properties of the traction oil used in the test are as shown in Table 1.

3. Traction Curve Estimation Based on Creep Theory

In this section, a conventional traction curve estimation method based on creep theory will be explained.

3.1 Calculation procedure

An outline of the calculation procedure is shown in Figure 6 and below.

- (1) Element division of contact area**
The contact area obtained by Hertzian contact theory is divided into elements and a coordinate system with the ellipse center set as the origin. In addition, distributions of contact pressure $P(x, y)$ and slip velocity $u(x, y)$ are obtained.
- (2) Calculation of shear stress distribution**
At each coordinate point, an elastic shear stress vector τ_e and limiting shear stress τ_L are obtained for the comparison. Then, let the smaller one be the shear stress $\tau(x, y)$ at that coordinate point.
- (3) Calculation of traction coefficient**
The component area is multiplied by the x direction (rolling direction) component $\tau_x(x, y)$ of the shear stress at each coordinate point, and the total sum of them is taken as traction force F_t to calculate the traction coefficient ($\mu = F_t / F_c$).
- (4) Generation of traction curve**
For each creep rate of the calculation range, a traction coefficient is obtained according to the above-described procedures (1)–(4).

The shear stress obtained in Procedure (2) will be detailed.

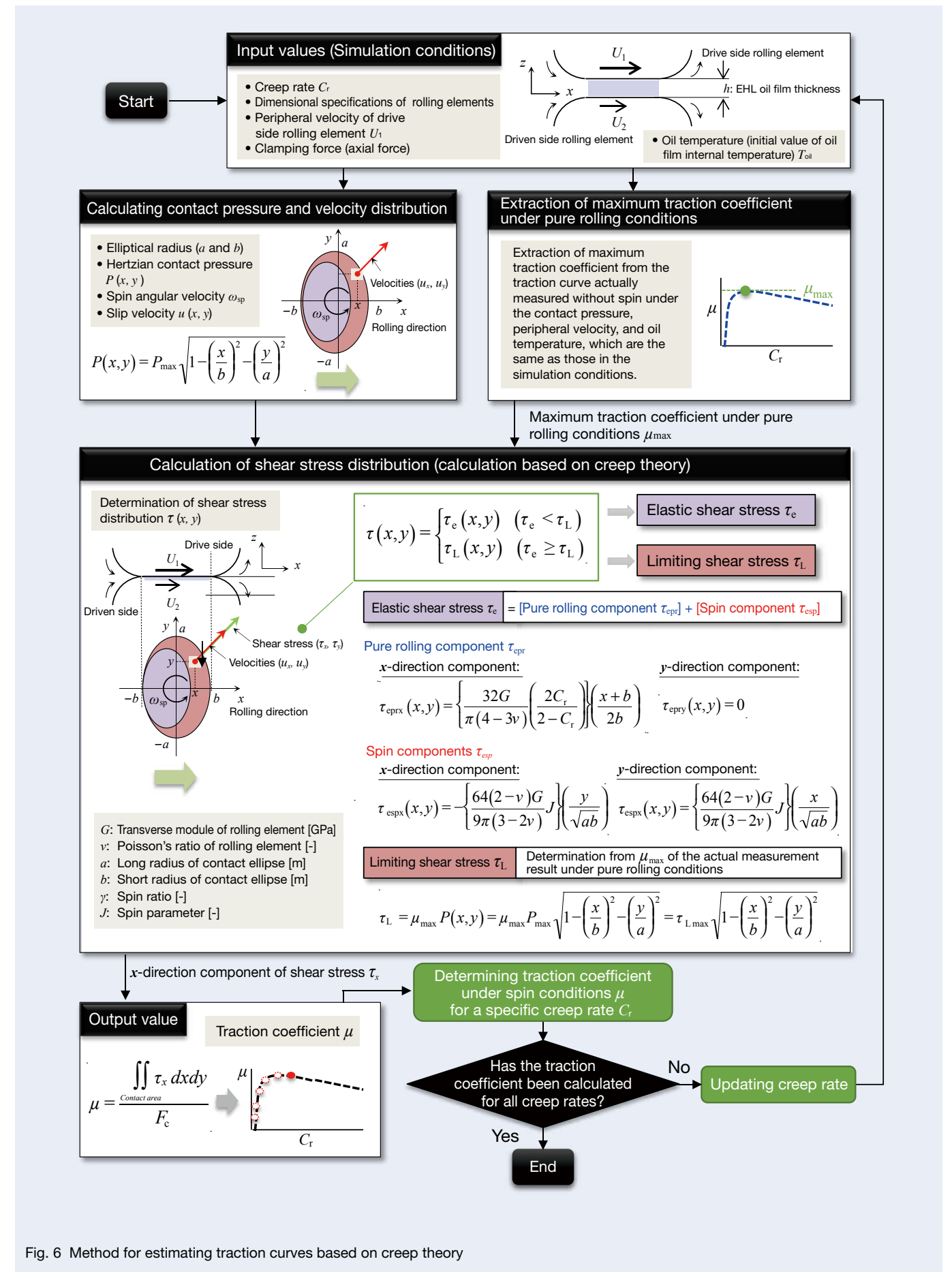


Fig. 6 Method for estimating traction curves based on creep theory

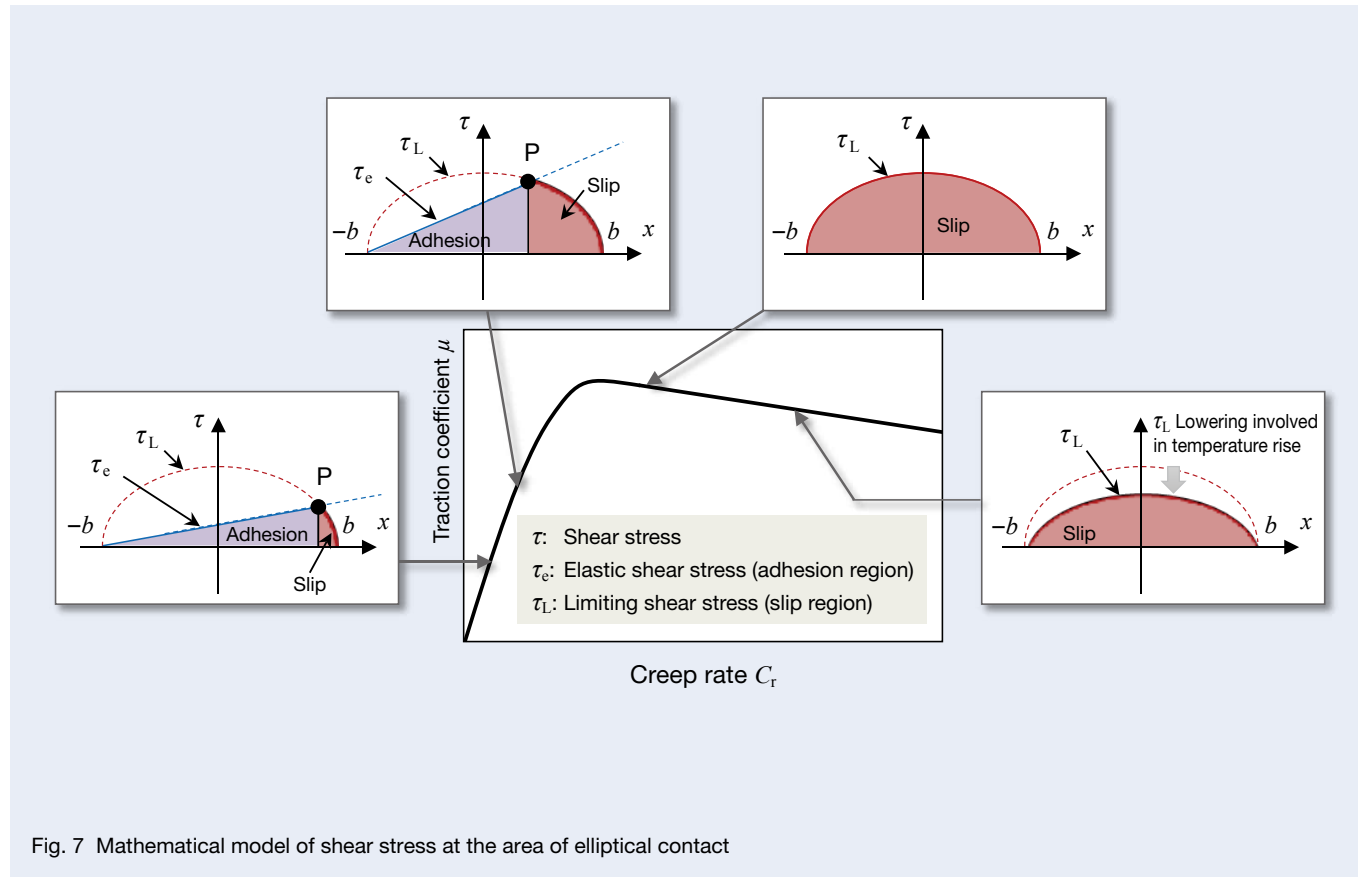


Fig. 7 Mathematical model of shear stress at the area of elliptical contact

According to this calculation, the shear stress distribution inside the contact ellipse becomes as shown in Figure 7. As the creep rate increases, the elastic shear stress increases. Therefore, the intersection P with the limiting shear stress moves to the left, and the slip region (the region reaching the limiting shear stress) expands. This corresponds to the process in which the change in the traction coefficient dulls as the creep rate increases in the traction curve and finally reaches the maximum value. In addition, the traction coefficient turns to decrease after reaching the maximum value, which results from the limiting shear stress decreasing due to temperature rise accompanying heat generation by shearing.

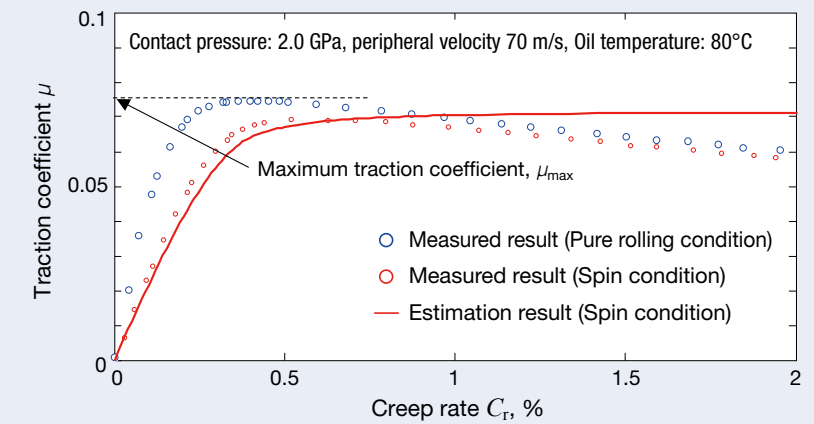
It is to be noted that as indicated by the equation in Figure 6, the distribution of limiting shear stress is assumed to follow the contact pressure distribution. Here, as for the maximum traction coefficient μ_{\max} , its value is treated as being known at the same contact pressure, peripheral velocity, and oil temperature as those in the calculation conditions and under the pure rolling conditions.

3.2. Traction curve estimation results

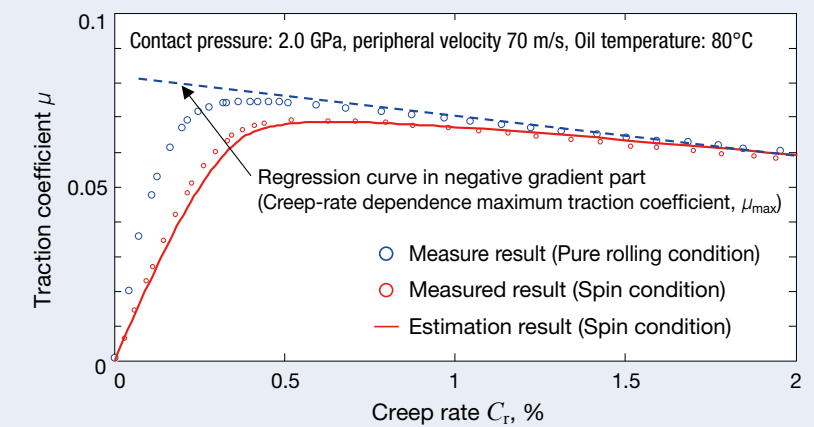
Traction curve estimation results obtained by the process described in the preceding section (Maximum contact pressure P_{\max} : 2.0 GPa, peripheral velocity U : 70 m/s, oil temperature T_{oil} : 80°C, spin ratio γ : 0.29) are shown in Figure 8 together with the experimental results under the same conditions.

When obtaining the results shown in Figure 8 (a), the limiting shear stress was calculated using the value of μ_{\max} obtained from the actual traction curve measurement under the pure rolling conditions that are also shown in Figure 8 (a). In the region from the rise of the traction curve to the maximum traction coefficient, the estimation result and the measurement result are mainly in agreement. However, they do not match in the region after reaching the maximum traction coefficient. This is due to the fact that the reduction of the limiting shear stress accompanying the temperature rise cannot be taken into account in the calculation.

In view of the above, a regression curve (indicated by the blue line in Figure 8 (b)) was obtained from the negative gradient portion of the traction curve under



(a) In case of not considering the temperature dependence of limiting shear stress



(b) In case of considering the temperature dependence of limiting shear stress

Fig. 8 Traction curves calculated with conventional methods

the pure rolling conditions. Then, this was used as the creep rate dependent μ_{\max} and also used to calculate the limiting shear stress. The result is shown in Figure 8 (b). According to Figure 8 (b), it is understood that, under the spin condition, the estimation result and the actual measurement result also coincide with the negative gradient part, and the temperature dependency of the limiting shear stress can be taken into consideration.

4. Traction Curve Estimation Using Limiting Shear Stress Map

In the conventional method described in the preceding section, the temperature dependence of the limiting

shear stress is indirectly taken into consideration as the reduction amount of the traction coefficient with respect to the creep rate. However, the amount of temperature rise with respect to the creep rate varies depending on the heat capacity, which is formulated by the shapes and dimensions of the rolling elements of the target device. Therefore, in order to enhance the versatility of the conventional method, it is better to express the limiting shear stress as a function of the oil film temperature.

Therefore, in consideration of the above points, this section will improve the conventional method and verify the validity of the proposed method.

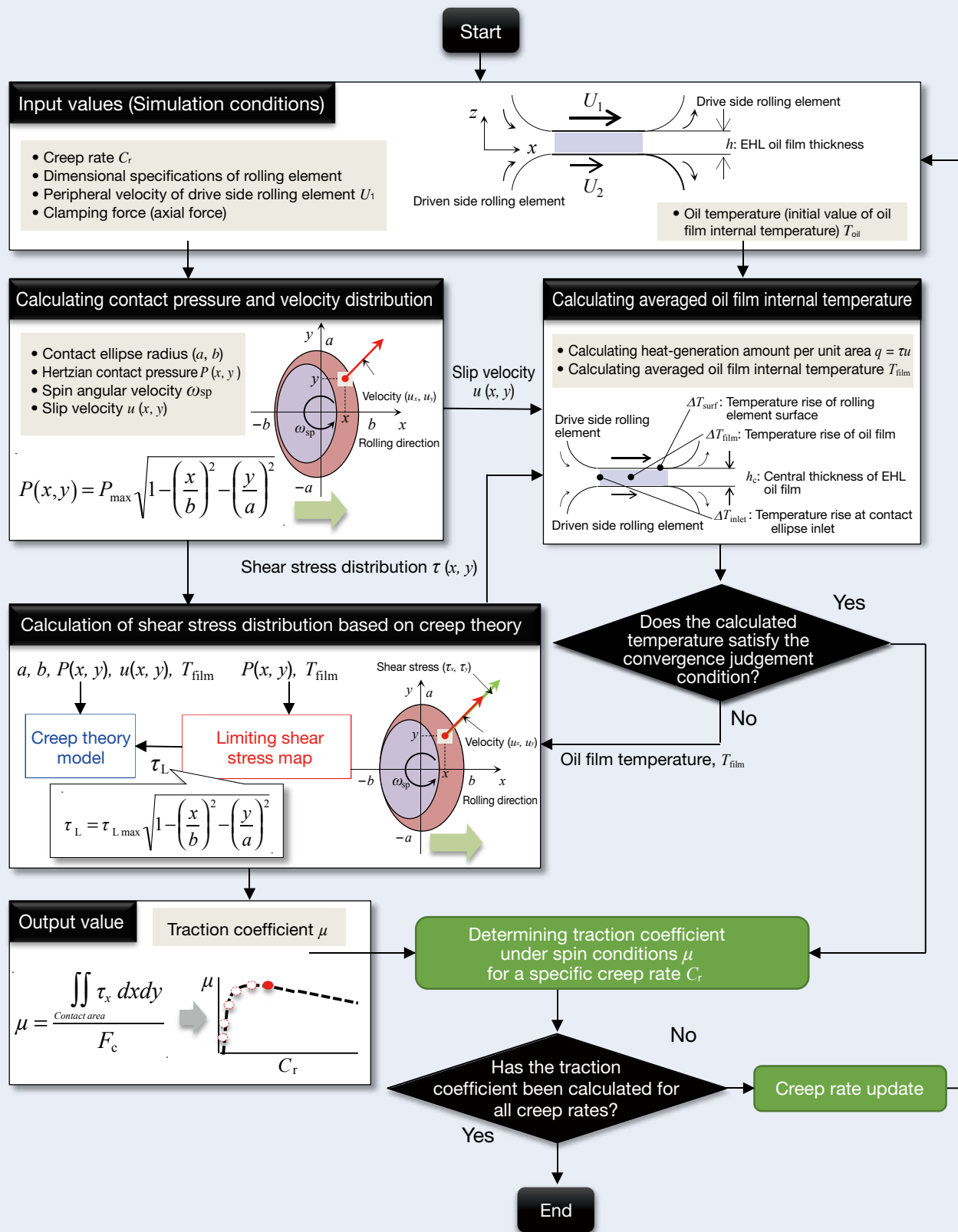


Fig. 9 Method for estimating traction curves using a data map of limiting shear stress

4.1. Proposed traction curve estimation method

The outline of the calculation procedure of the traction curve by the proposed method is shown in Figure 9. The basic calculation procedures are the same as those of the conventional method described in the preceding section, but the way of determining the limiting shear stress is different.

For the calculation of limiting shear stress by the proposed method, values referenced from the data map (limiting shear stress map) are utilized. This limiting shear stress map is created from the contact pressure, the maximum value $\tau_{L,max}$ of the limiting shear stress under the pure rolling condition, and the estimated value of the oil film average temperature calculated using the maximum shear stress. The limiting shear stress map prepared from the test with high-power two-roller traction tester results

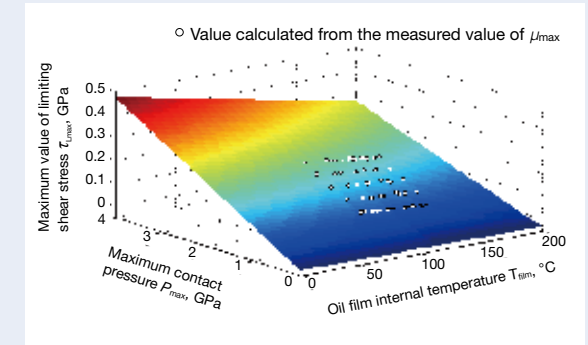
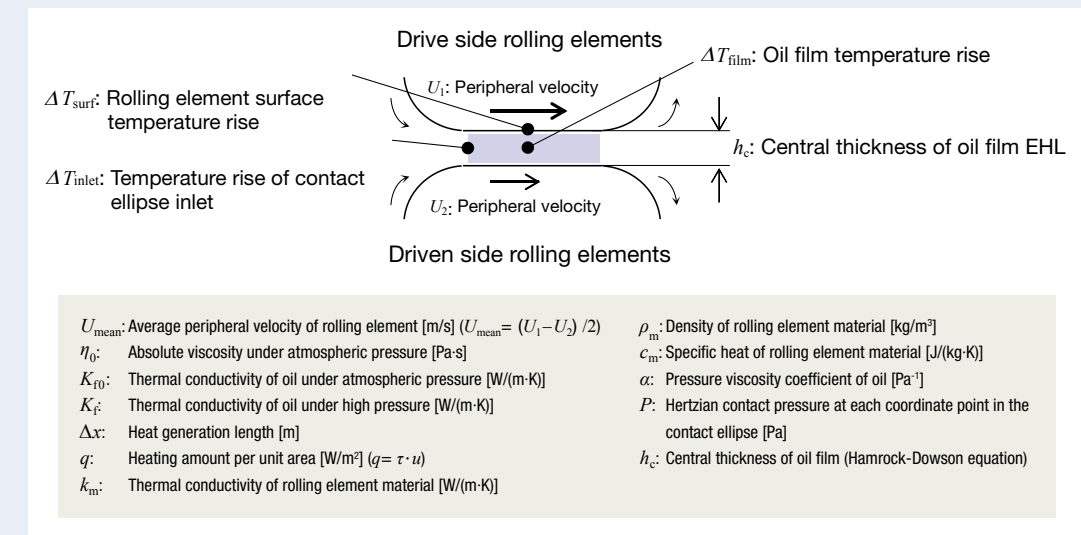


Fig. 10 Data map of limiting shear stress



Definition	Equation
Oil film temperature rise	$T_{film} = T_{oil} + \Delta T_{inlet} + \Delta T_{surf} + \Delta T_{film}$
The average temperature rise amount at contact ellipse inlet	$\Delta T_{inlet} = \frac{U_{mean} \eta_0}{5K_{f0}}$
The average temperature rise of rolling element surface	$\Delta T_{surf} = \sqrt{\frac{\Delta x}{2\pi k_m \rho_m c_m U_{mean}}} \cdot q$
Oil temperature rise amount relative to rolling element surface temperature	$\Delta T_{film} = \begin{cases} \frac{h_c}{8K_f} \cdot q & (\alpha \cdot P \leq 25) \\ \frac{h_c}{4K_f} \cdot q & (\alpha \cdot P > 25) \end{cases}$

Fig. 11 Mathematical model for estimating oil-film temperature

is shown in Figure 10.

The maximum value τ_{Lmax} of the limiting shear stress is obtained as the product $\tau_{Lmax} = \mu_{max} P_{max}$ of the maximum contact pressure P_{max} and the maximum traction coefficient. When estimating the traction curve, τ_{Lmax} referred to from the limiting shear stress map is substituted into the formula shown in Figure 9 to give the limiting shear stress distribution inside the contact ellipse.

As shown in Figure 11, the oil film average temperature T_{film} is assumed to be a total of the supply oil temperature T_{oil} , the average temperature rise amount ΔT_{inlet} at the contact ellipse inlet, the average temperature rise amount ΔT_{surf} of the rolling element surface, and the oil film temperature rise amount ΔT_{film} relative to the rolling body surface temperature ($T_{film} = T_{oil} + \Delta T_{inlet} + \Delta T_{surf} + \Delta T_{film}$). ΔT_{surf} is obtained such that a value at each point inside the contact ellipse is calculated and the resulting values are averaged. ΔT_{film} is also obtained in the same way.

When creating the limiting shear stress map, as to the calorific value q ($q = \tau u$) per unit area required for calculating ΔT_{surf} and ΔT_{film} , it is calculated using the

peripheral velocity difference ΔU between the rolling elements, along with the shear stress ($\tau = \mu_{max} P_{mean}$) obtained from the average contact pressure P_{mean} ($P_{mean} = 2/3 P_{max}$) according to Hertzian contact theory and the measured maximum traction coefficient μ_{max} . On the other hand, when estimating the traction curve with reference to the created map, q on each coordinate point is obtained from the shear stress distribution on the contact ellipse and the slip velocity distribution, and these are used for calculating the oil film temperature.

It is to be noted that the oil film temperature and shear stress distribution change depending on each other and therefore both are obtained by iterative calculation. In order to obtain the iterative calculation, start with applying the supply oil temperature as the initial value of the oil film temperature and continue calculations until the change in the calculation result of the oil film temperature converges within the threshold or until the number of repetitions in the calculation number reaches the upper limit.

4.2. Proposed traction curve estimation result

The traction curve was estimated by the proposed method and compared with the actual measurement result. The results are shown in Figure 12 and Figure 13, which show the results when the maximum contact pressure is 2.0 GPa and 3.0 GPa, respectively. Also, in each figure, the results at different peripheral velocities and oil temperatures are shown together.

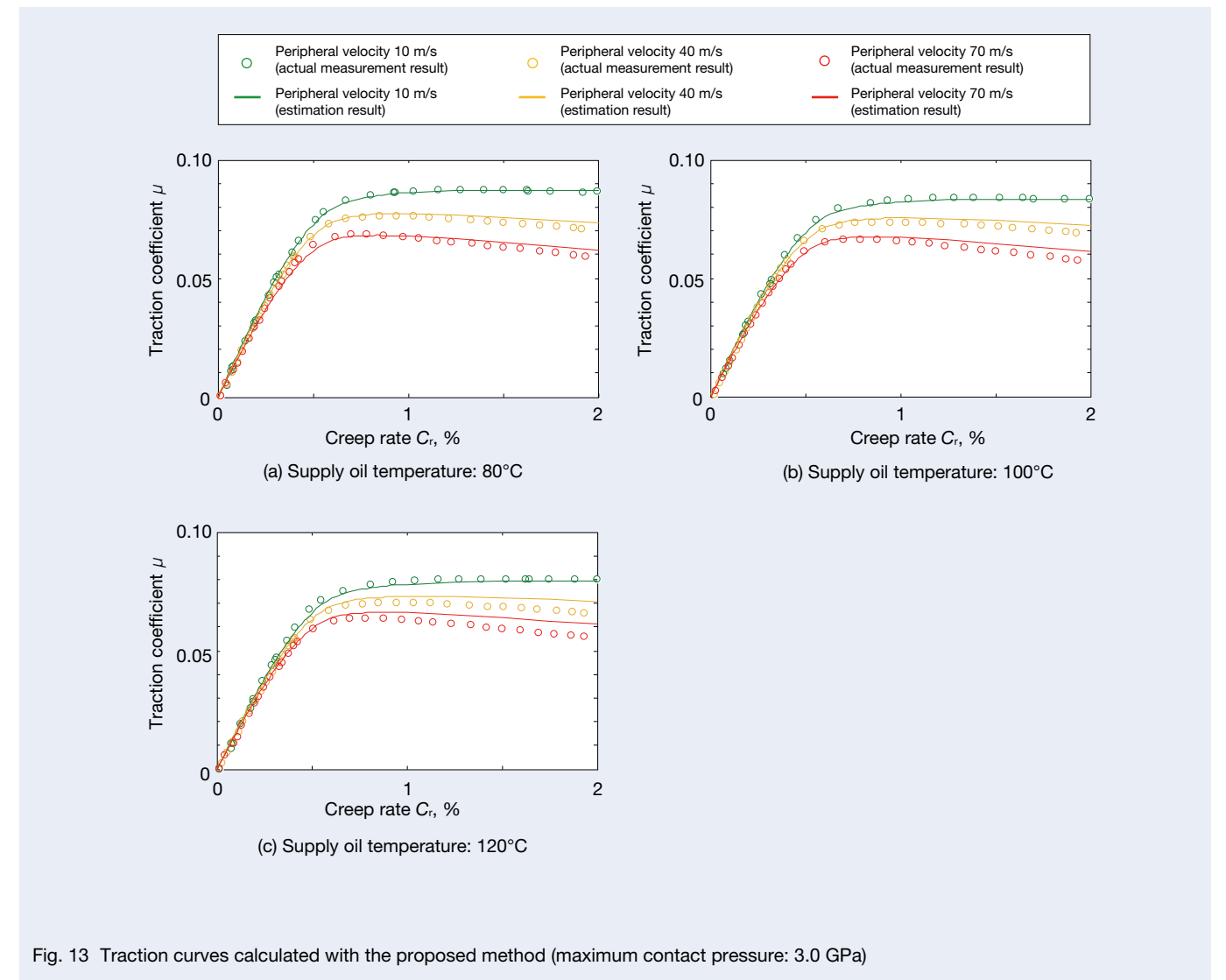
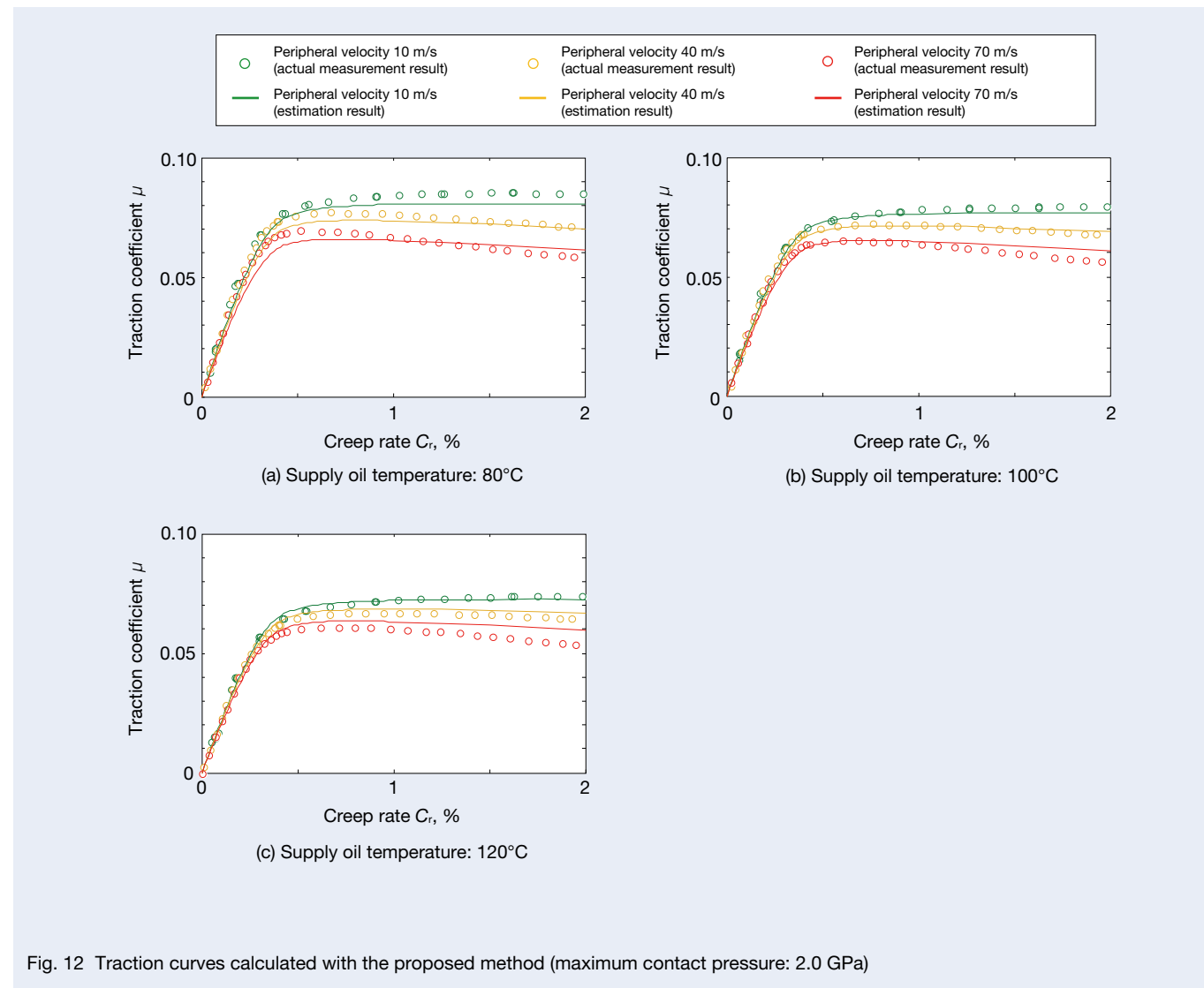
When comparing the estimation result and the actual measurement result in each condition, they are nearly identical in the rising portion, the maximum value, and the negative gradient portion of the curve.

From the above results, according to the proposed method, even if the traction curve actual measurement result (the regression curve of the traction curve negative gradient part) under the pure rolling condition is unknown, the amount of decrease of the limiting shear stress due to the temperature increase can be estimated, which means that it can be said that the traction curve under the spin motion condition can be calculated using it.

5. Conclusion

This paper proposes the traction curve estimation method as an applied version of the conventional method based on creep theory in order to contribute to the guarantee of function and improvement of the performance of the traction drive device, together with an evaluation of the validity of the proposed method. The results are as shown below.

- According to the proposed method, the traction curve is obtained while estimating the amount of decrease of the limiting shear stress accompanying the temperature rise, and therefore the actual measurement result (the regression curve of the traction curve negative gradient part) used in the calculation by the conventional method is unnecessary.
- The traction curve calculated using the proposed method is in good agreement with that measured by the high-power two-roller traction tester, thereby confirming that the proposed method is applicable under practical operating conditions.



References

- 1) L. D. Wedeven, G. G. Wedeven, S. H. Kratz, T. E. King, J. L. Linden, F. Caracciolo and D. G. McWatt, "USCAR traction test methodology for traction-CVT fluids," SAE Technical Paper, 2002-01-2820 (2002) 1-31.
- 2) L. D. Wedeven, T. E. King, J. L. Linden, F. Caracciolo and D. G. McWatt, "WAMhs Traction Machine and Test Methodology for USCAR," Proc. 13th International Colloquium Tribology, Esslingen, (2002) 1873-1887.
- 3) T. Makino and T. Kawase, "Effects of Spin on Traction Characteristics," Journal of Japanese Society of Tribologists, 44-1 (1999) 53-60.
- 4) R. Kawabata and M. Muraki, "Traction Perpendicular to Rolling Direction Based on Spin and Side-slip," Transactions of the JSME Ser. C, 71-708 (2005) 2643-2660.
- 5) H. Achiha, S. Natsumeda, Y. Nakamura, and I. Fujishiro, "Traction characteristics under high contact pressure, high rolling speed and high temperature," Proc. International Tribology Conference Yokohama 1996, 1, (1996) 139-144.
- 6) M. Muraki and Y. Kimura, "Influence of Temperature Rise on Shear Behaviour of an EHL Oil Film," Transactions of the JSME Ser. C, 56-828 (1990) 2226-2234.
- 7) H. Hata, T. Gouda and M. Koishi, "Traction Performance of Traction Fluid under the Severe Conditions," Proc. International Tribology Conference Nagasaki 2000, 1, (2000) 603-607.
- 8) K. Hata, S. Aoyama and T. Miyaji, "Various Performance and Characteristics of Traction Oil," Idemitsu Tribo Review, 28 (2005) 1-21.
- 9) K. Kato, T. Iwasaki, M. Kato and K. Inoue, "Evaluation of Limiting Shear Stress of Lubricants by Roller Test," Transactions of the JSME Ser. C, 58-546 (1992) 558-564.
- 10) H. Itagaki, M. Kita and H. Hashiguchi, "Development of a High-Power Two-Roller Traction Tester and Traction Curve Measurement," NSK Technical Journal, 689 (2017) 27-35.
- 11) H. Itagaki, H. Hashiguchi, M. Kita, and H. Nishii, "Development of a High-Power Two-Roller Traction Tester and Measurement of the Traction Curve," Tribology Online, 11-6 (2016) 661-674.
- 12) T. Makino and T. Kawase, "A Calculation of Traction Properties Based on a Non-Linear Viscoelastic Model (Part 1) -Measurement of Traction and Curve Fitting-," Journal of Japanese Society of Tribologists, 43-5 (1998) 421-428.
- 13) H. Tanaka, "Toroidal-type CVT," (2000) 13-24, CORONA PUBLISHING CO., LTD.
- 14) T. Mawatari, A. Nakajima and H. Matsumoto, "Shear Stress Analysis of EHL Oil Films Based on Thermal EHL Theory -Effect of Inlet Oil Temperature-," Tribology Online, 3-5 (2008) 268-273.
- 15) M. Tomita, M. Tabuchi and T. Sano, "Examination of the Maximum Traction Coefficient Prediction Method (First Report)," Proc. 2015 JSAE Congress (Spring), 35-11 (2011) 1-4.
- 16) M. Tomita, T. Sano and M. Inoue, "Examination of the Maximum Traction Coefficient Prediction Method (Second Report)," Proc. 2015 JSAE Congress (Autumn), 119-12 (2012) 5-8.
- 17) T. Sano, M. Tomita, M. Inoue, Y. Takeuchi and M. Yorinaga, "Study of the Prediction Method for Maximum Traction Coefficient," SAE International Journal of Passenger Cars - Mechanical Systems -, 6-2 (2013) 868-877.
- 18) Y. Nakamura and M. Funahashi, "Oil Solidified High-Pressure Traction Curve Estimation with Spin by Elastic Contact Mechanics," Journal of Japanese Society of Tribologists, 72-717 (2006) 1663-1669.
- 19) K. Baek, K. Kyogoku and T. Nakahara, "Transient Traction Characteristics between Rail and Wheel under Low Velocity and Low Slip Ratio: Variation of Traction Coefficient by Environmental Conditions," Transactions of the JSME Ser. C, 73-726 (2007) 611-618.



Hirofumi Itagaki

Improving the Efficiency of Derivative Development through Systematic Restructuring

Masaya Oba
Steering R&D Center

Abstract

In order to continue business in a diversifying and complicated market environment, it is necessary to refine design in stages from a systematic viewpoint and build a method of derivative development based on core assets. In this article, we will introduce our efforts in working toward this goal.

By defining the development process and creating products accordingly, we can verify the validity of the process and work on improvements from this point forward. After this, we will establish core assets, define the derivative development process, and shift these ideals into practice for verification.

1. Preface

In today's product development under the conditions of diversified and complicated requirements and short delivery time of the market introduction progress, the environment in which derivative development is placed is becoming increasingly challenging. Our automotive parts business is no exception, and the influence on quality and cost involved in an increase in product variations is at a level that cannot be ignored. Therefore, in order to cope with this situation in the future, the target is to develop standard deliverables as the base of all products for all layers of the hierarchical system development, thereby enabling the realization of product line development that uses them for establishing efficient derivative development. In developing the aforementioned standard deliverables (equivalent to core assets), various methods are implemented, including Universal Specification Describing Manner (USDMM)¹⁾ and Process Flow Diagram (PFD)²⁾.

This paper will describe points devised and actualized in implementing these methods and also future prospects.

2. Objectives

2.1 Target products and business environment

The product discussed in this paper is Electric Power Steering (EPS) for automobiles. Along with the widespread adoption of electrically-operated vehicles and the demand for fuel economy, power steering is also shifting from the conventional hydraulic type to the electric type and, therefore, the majority of recent passenger vehicles use EPS. This technology is essential for autonomous driving, and the market size for EPS is expected to expand further.

Our company has entered this market as an independent system supplier and has delivered products to multiple vehicle manufacturers in and outside of Japan

as well as for multiple vehicle types. In other words, the current business situation is in developing products simultaneously with many variations for a market that continues to expand.

2.2 Issues to be resolved

In regard to continuing this business, a serious concern remains with the increasing development costs.

EPS is now required not only to perform turning of the vehicle but also to be a system that is responsible for being part of the complicated cooperative operation of the whole vehicle. For example, functions such as automatic parking assistance and lane keeping support, which cooperate with instructions from the vehicle instead of direct steering operations by the driver, have already been commercialized. Another requirement is to bolster security countermeasures along with network connections such as vehicle-to-vehicle/road-to-vehicle interaction for autonomous driving in the near future. Thus, the requirements for EPS development are expected to become increasingly diversified and complicated in the years ahead.

Due to these issues, the development cost continues to rise. Looking at the number of personnel involved in software development for a certain period and the change in outsourcing expenses that cover manpower shortages, it was confirmed that an increase in rightward rising has occurred (Figure 1).

The diversification and complexity of requirements are considered external factors regarding the cost increase. As for other internal factors, our system development style may also be influential.

In order to develop multiple products concurrently, derivative development based on existing products is being conducted. Developing unique products for each vehicle manufacturer, even each vehicle model, is becoming increasingly common, and there is some indication that variation will continue to increase in line with business expansion. Nevertheless, there are no signs of convergence

so far, and continuing with the same development style may result in concerns that variations will diverge and lead to failure at the development site (Figure 2).

2.3 Target image

In order to respond to the aforementioned problems, instead of responding to each market requirement in an individually different on-demand manner, it is necessary to change to a style that creates products by developing differences from the customer requirements through

forming core assets with a clear reuse strategy. In other words, the goal is to break out of the derivative style of individually different specification for each product and construct a system that allows for providing a derived product line type based on core assets (Figure 3).

Here, the object to be treated as the core asset is the EPS system as a whole, and the system development is regarded as a set of constituent elements in a hierarchical structure detailed in Figure 4, and in which core assets are built.

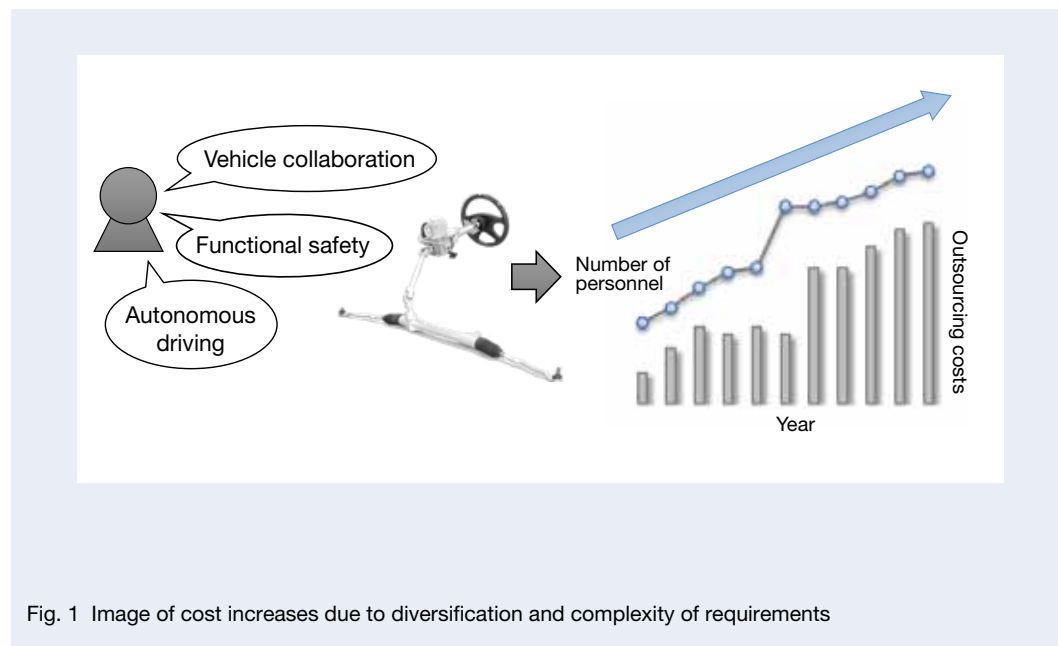


Fig. 1 Image of cost increases due to diversification and complexity of requirements

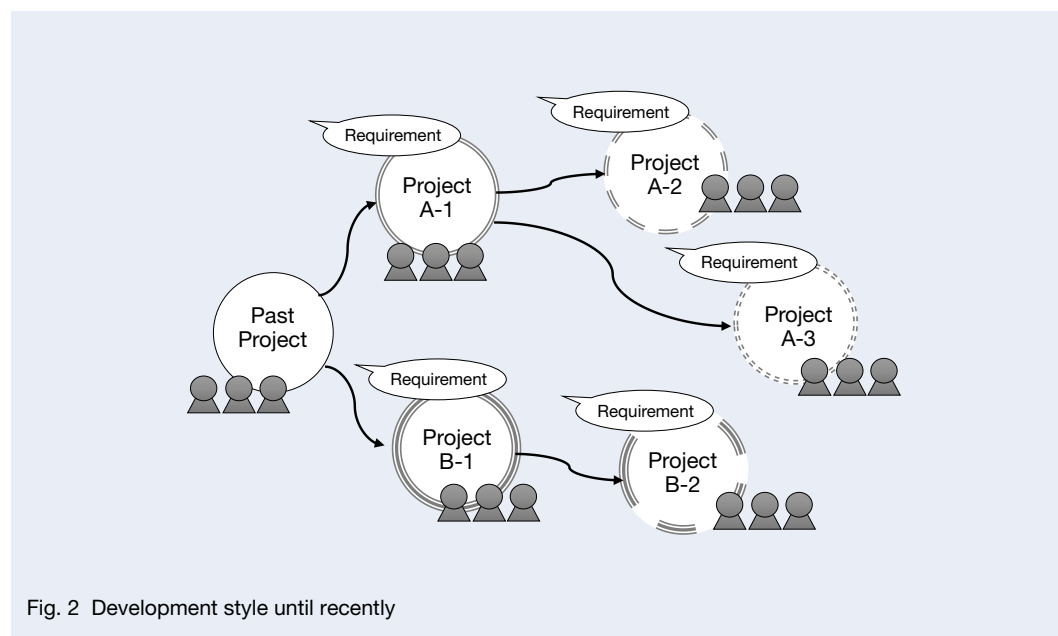


Fig. 2 Development style until recently

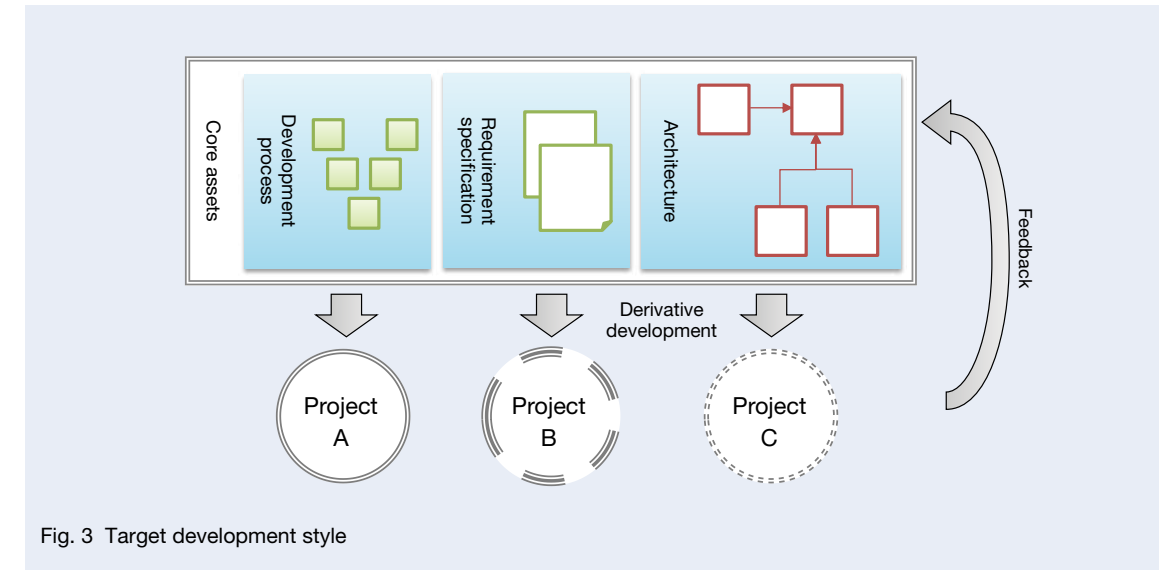


Fig. 3 Target development style

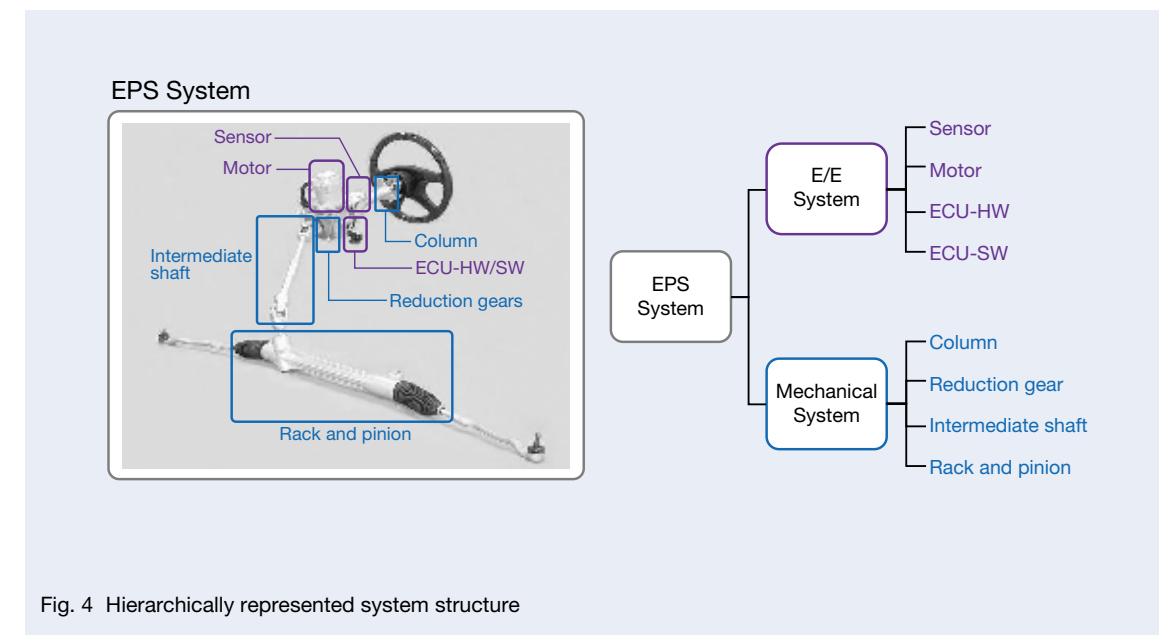


Fig. 4 Hierarchically represented system structure

3. Policy

3.1 Issues

In developing the product line type derivative development system, the issues to be resolved were extracted from the current development deliverables and development process. The main issues are described below.

Issue 1: Clarification of requirements

In the existing development deliverables for the development of a product, there is the product specification to be created for each component of the product. Using software as an example, what is required

to be implemented as software function specification is stated. In addition, there is also a customer requirement to be received from the vehicle manufacturers.

However, there was a lack of clarification of descriptions connecting customer requirements to software function specifications, or software requirements of what is required for software. Therefore, even when confirming the existing materials and source codes, there was a point where the reason for requesting certain functions was unclear. That is, explaining which requirement resulted in the design/implementation was difficult.

As the system becomes more advanced, the number of deliverables decreases. For example, regarding hardware and software, which the engineer(s) directly designed

and implemented, the concerned specifications exist. The deliverables of the hierarchy that is one level unclear therefrom; that is, the hierarchy of the E/E (electric/electronic) system and even the highest and most unclear level EPS system are not the final manufacturing objects and therefore the lack of deliverables and the dilution of contents are seen occasionally.

Issue 2: Determination and expression of common/unique subjects

In developing products for multiple automotive manufacturers, existing deliverables are independently created for each product. For this reason, those that are common among the products, or those unique to a specific vehicle manufacturer, have not been summarized. It is believed that forming effective core assets can be attained by understanding that the former can be considered commonly reusable and the latter as unique variability. This must be examined, as well as methods for considering

how to express and manage them.

Issues 1 and 2 are both related to the composition of the requirement specifications, the state of which is shown in Figure 5.

Issue 3: Construction of the hierarchical development process

As mentioned in 1, as the system becomes more advanced, there is the tendency for the number of deliverables to decrease. This is due to the fact that deliverables are not constructed because the process of hierarchical system development is not clarified.

In order to reliably develop various requirements given to the system, a development process must be constructed through gradual system refinement for distributing the requirements, ranging from the highest hierarchy level unclear EPS system layer to the specific layer of creating an actual item.

Issue 4: Construction of a development process

In the targeted product line type development style, while developing products based on core assets, feedback regarding the new commonality found among them is to be made into a core asset. This development process should also be constructed.

Issues 3 and 4 are both related to the construction of the development system, the state of which is shown in Figure 6.

3.2 Methodology

As methodologies to cope with the issues of the “Component of requirement specification sheet” and the “Construction development process” described in item 3.1, USDM for the former and PFD for the latter were adopted. The reasons are described below.

- (1) Component of requirement specification: USDM
USDM is description manners of requirement specification. It was determined that its features are suitable for resolving issues 1 and 2 (Table 1).
- (2) Construction of the PFD development process
PFD is a technique for designing processes. The process is positioned as input and output of one or more deliverables, and these chains are represented in terms of flow diagrams. Also, preparing a process description and deliverable definition in correspondence with the respective drawings makes possible a clear definition of the process and the deliverable.

This technique was deemed useful due to the fact that dealing with issues 3 and 4 is required in order to clarify the development process, which until recently did not exist.

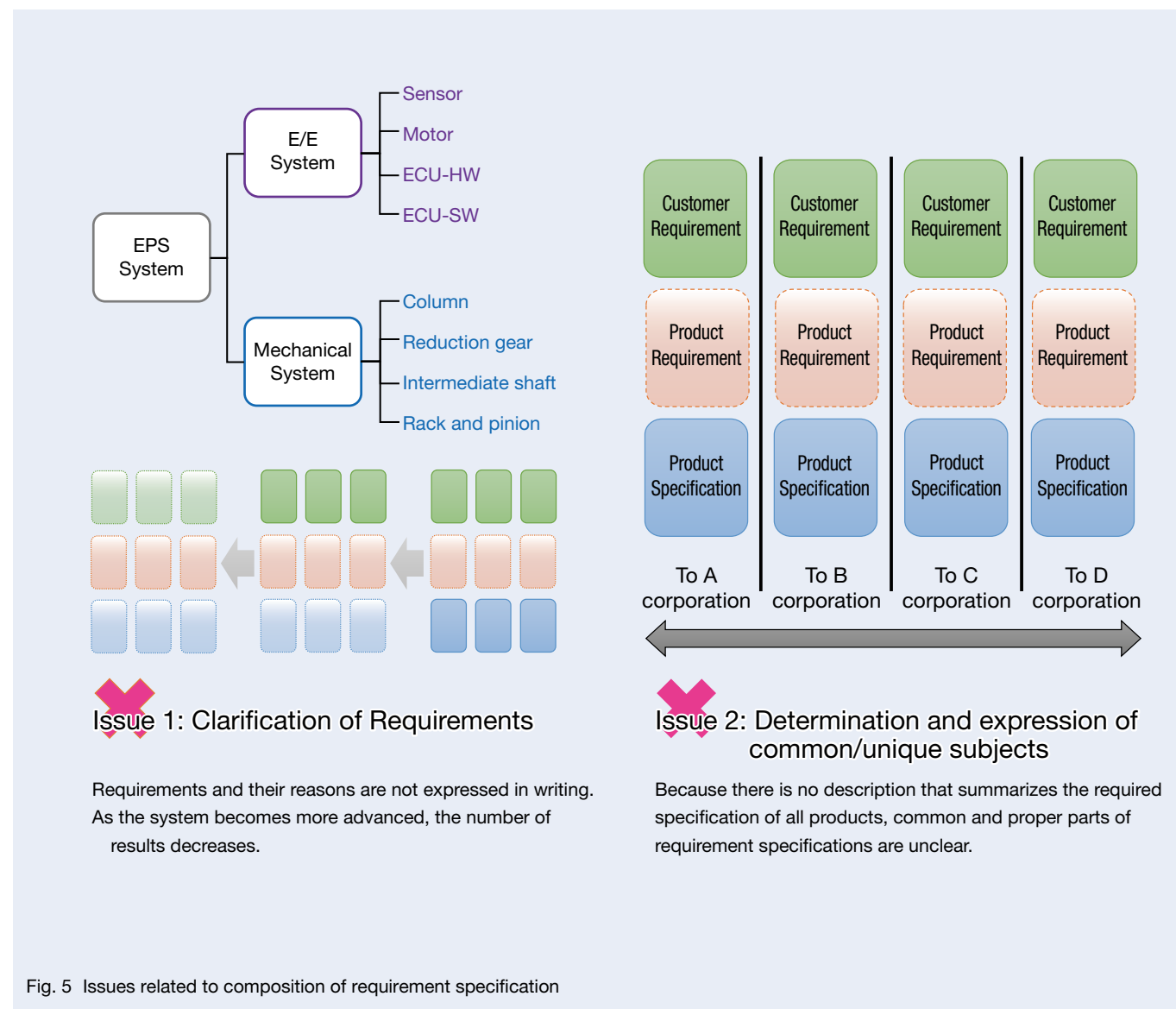


Fig. 5 Issues related to composition of requirement specification

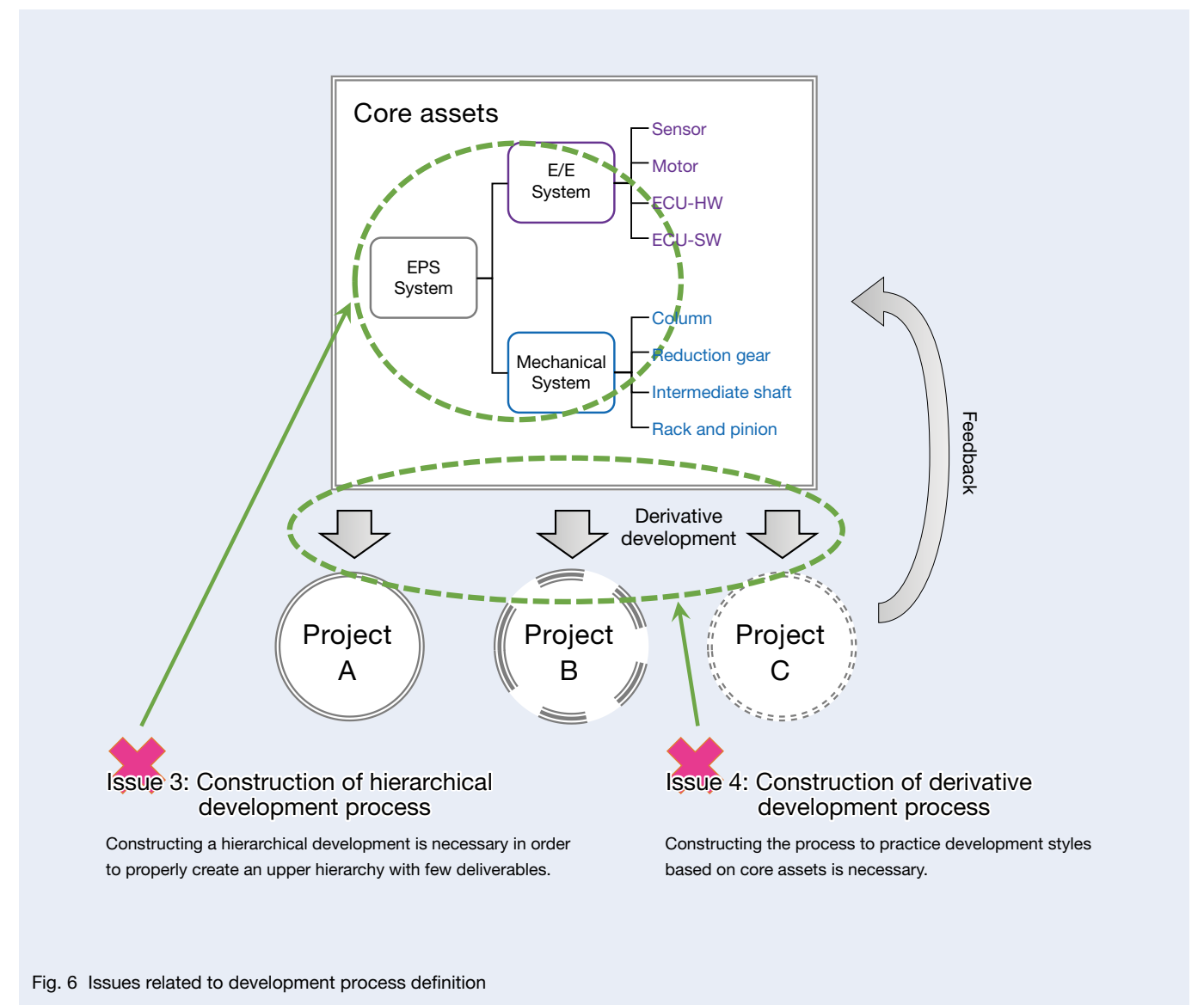


Fig. 6 Issues related to development process definition

Table 1 Features of USDM and reasons for adoption

Features	Reason for Adoption of Issues
Clearly distinguish between the requirements and specifications and summarize the distinctions in a hierarchical structure	Issue 1: Clarification of Requirements It is necessary to clarify not only the specification but also the requirements behind it so that the point that makes these distinctions is set as a premise that is beneficial for summary. Because clarifying the required specification of each hierarchy of the EPS System is desired, it is beneficial to summarize the required specification in the form of having a featured hierarchical structure.
Describe "Reason" and "Explanation" along with the requirements	Issue 1: Clarification of Requirements To clarify the requirements, clearly stating the reason in the background is beneficial for understanding the contents of the request (why you want to do it), identifying commonality (is what you want to do the same?), and deriving appropriate specifications (whether this method is really suitable).
Description in Excel-based table format	Issue 2: Determination and Expression of Common/Unique Subjects Excel is a widely used tool and has a high degree of freedom for adding rows and columns. USDM also points this out as an advantage, and as an example of its application, the implementation of the Traceability Matrix ¹⁾ can be seen. Moreover, it is beneficial as a means to identify and share common and unique subjects.

4. Tackled Contents: Requirement Specification Prepared Using USDM

4.1: Clarification of requirements

Issue 1: Clarification of requirements involving two problems include requirements that have not been clarified for the specification and the number of existing products is low at the upper layer. In order to resolve these issues, a two-way approach with USDM will be used.

The bottom-up approach is adopted for coping with the requirements that have not been clarified for the specification. More specifically, the part of tacit knowledge that has not been clarified by deriving the requirements that are required for the specification in the opposite direction from the specification description of the existing deliverable will be clarified. It is to be noted that this approach covers the development hierarchy in which deliverables whose specifications are already described (e.g., software function specifications) exist.

In dealing with the lower number of existing products at the upper layer, the top-down approach is adopted. A clarification was made in a descending manner through discussing and organizing again the requirements necessary for the EPS system: preparing the PS system requirement specifications → E/E System requirement specifications → software requirement specifications.

Each approach is described in detail below.

4.1.1 Summarizing the current state using the bottom-up approach

In this approach, for example, based on the existing software function specifications, the requirement specifications are summarized according to the following procedure (Figure 7).

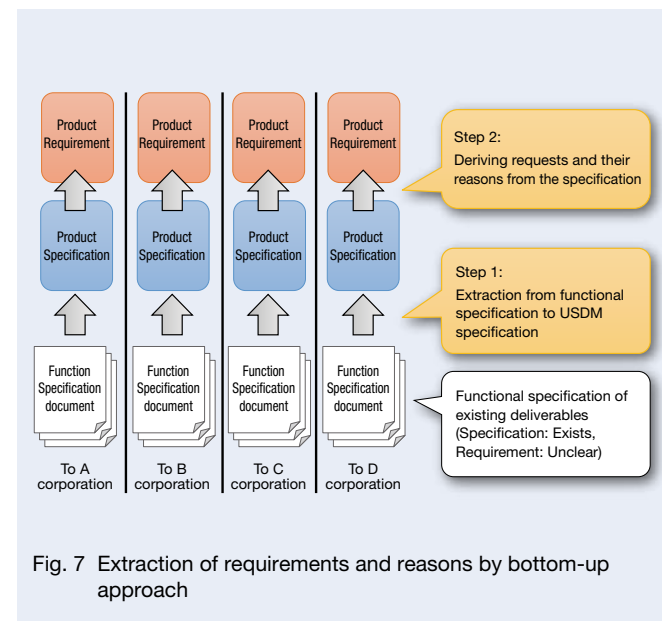


Fig. 7 Extraction of requirements and reasons by bottom-up approach

Successful derivation of requirements, reasons, and specifications in this procedure will be filled out as items in the USDM format, which makes it possible to summarize not only the realization mechanism (specifications) but also the background requirements together with the reasons (Figure 8).

However, not all will become obvious in the summary process. There is also a case in which the background (reasons) of the requirements remains unknown despite the extraction of the requirements from the specifications. In such a case, the "reason" column of USDM remains unfilled. However, even in this case, it is possible to clarify what is unclear (Figure 9).

With this approach, the following effects were obtained.

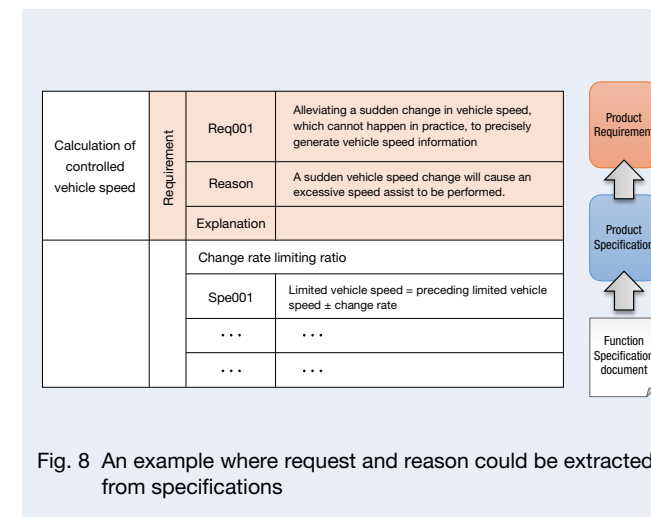


Fig. 8 An example where request and reason could be extracted from specifications

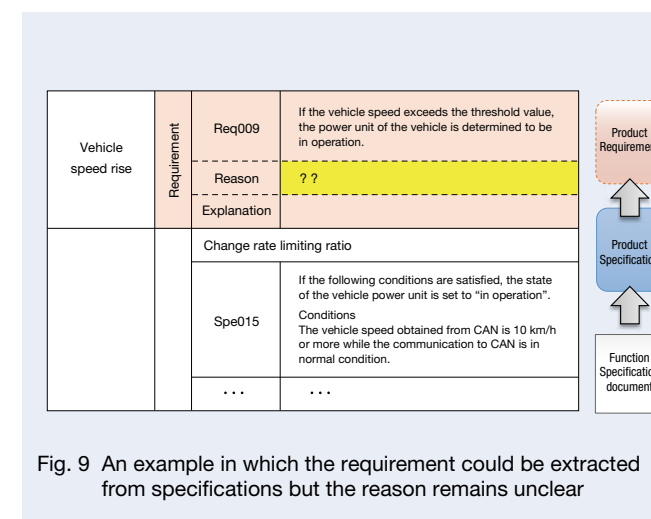


Fig. 9 An example in which the requirement could be extracted from specifications but the reason remains unclear

- The fact that requirements and reasons could be extracted made it possible to summarize the content that was previously regarded as tacit knowledge as formal intelligence.
- Even if extraction failed, it was possible to gather appropriate information and hold discussions by narrowing down unclear details.

4.1.2 Summary using the top-down approach

This approach refines the requirement specifications gradually. For example, the EPS system can be set as the top layer and the E/E System and Mechanical System can be set as subcategories, followed by lower layers.

At that time, since the requirement specification of the upper hierarchy has been unclear so far, it is necessary to decide the policy concerning the granularity description.

When assuming that the number of hierarchies of USDM is composed of three hierarchies (1st requirement → 2nd requirement → specification), the description of specification of USDM in a development hierarchy is that work to be done in the development of the next lower hierarchy is distributed (that is, the hierarchy of the EPS system is responsible for distributing work to the Mechanical E/E System). In each development hierarchy, an architecture based on the requirement specification of the concerned hierarchy is constructed and components thereof are identified. By detailing the description of the requirement specification so that the specification of USDM can be assigned to the constituent element, it is possible to distribute with the granularity of the required specification and the architecture maintained (Figure 10).

Moreover, extracting the requirements required for the topmost EPS system as the starting point, without duplication, clarifies the scope that the lower layer has to develop, which leads to optimal solutions for the whole system without concerning the optimal solution of each component. Ensuring this so-called coverage of requirements cannot be achieved with the bottom-up approach (Figure 11).

- With this approach, the following effects were obtained.
- It was possible to clarify the requirement specifications of the upper hierarchy that were previously unclear.
 - It was possible to clarify the correspondence relationship between the granularity description and the architecture.
 - Comprehensive extraction of requirements made it possible to examine the optimal solution for the whole system.

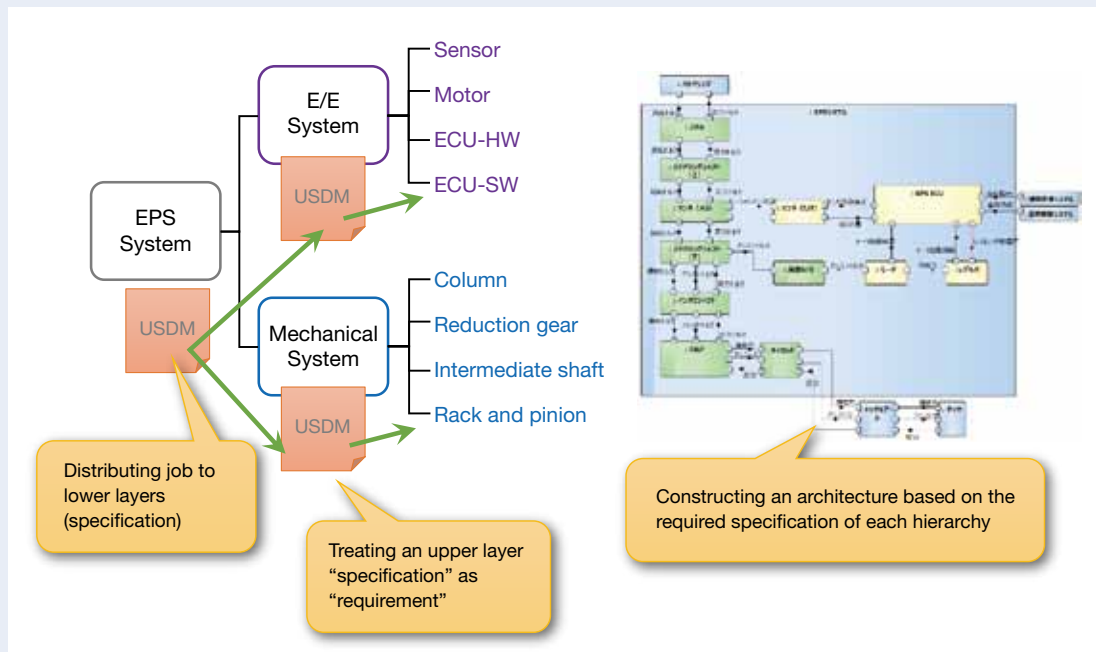


Fig. 10 Distribution of step-wise requirements in a top-down approach

4.2 Determination and expression of common/unique subjects

In issue 2: common/unique judgment and expression, based on the result of the bottom-up approach of the preceding section 4.1, resolving the issue will be made by summarizing the requirement specifications in accordance with the following procedure (Figure 12).

Here, in Step 1, it was possible to arrange them side by side using USDM, but the issue of how to perform common/unique expressions found in Step 2 has arisen.

As for how to deal with this issue, expanding the description of USDM was considered (Figure 13). The ● marked columns on the right side are the horizontal arrangement of each product performed in Step 1 and show a corresponding relationship between description of the requirement specification summarized by the bottom-up approach and product. At a glance, it is possible to find the variability of whether it is common among all products or whether it is unique to a certain product.

With this approach, the following effects were obtained.

- Construction could be established wherein the common and unique were found and the method of expressing the resulting contents by expanding USDM was established.
- As a result, it was possible to summarize useful information for examining the scope to be covered as core assets.

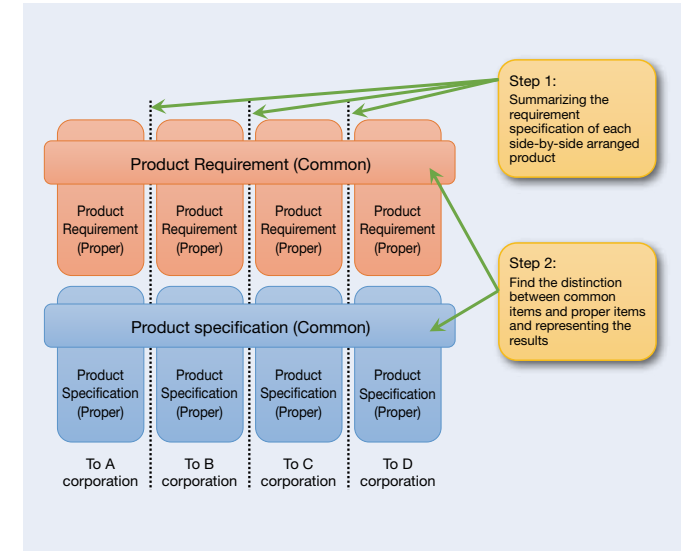


Fig. 12 Definition of common or unique distinctions

The entire range that the system implements

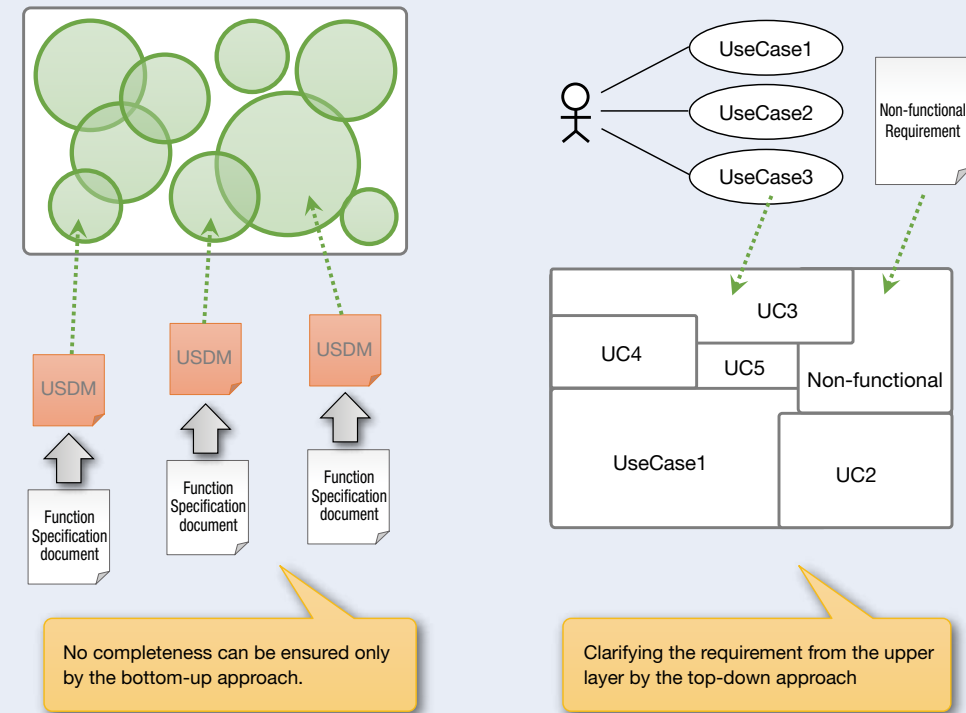


Fig. 11 Ensuring requirements are covered

			Step1 Side-by-side arrangement of products				
			Step2 Expression of variability				
			A	B	C	D	
CAN information acquisition	Requirement	Req010	Information acquisition from the power unit ECU using CAN communication	●	●		●
	Reason		Information is provided from the vehicle by CAN communication.	Expression of variability			
	Explanation		For details of the information, see xxxx.				
	Variation 1		Alternative 1	●			
	Spe065	Acquiring CAN message A	Mandatory	●			
	Variation 2		Alternative 2		●		
	Spe066	Acquiring CAN message B	Mandatory		●		
	Spe067	In case of unreceivable condition...	Optional		●		
	Variation 3		Alternative 3				●
	Spe068	Acquiring CAN message D	Mandatory			●	
	Spe069	In case of unreceivable condition...	Mandatory			●	

Fig. 13 Example representation of variability using USDM

5. Approached Contents: Construction of Development Process Using PFD

5.1 Construction of the hierarchical development process

Regarding issue 3: Construction of the hierarchical development process, an attempt was made by clarifying the implementation procedure as a process when performing the top-down approach in item 4.1.2.

When summarizing requirement specifications as USDM using the top-down approach, as described above, it is necessary to find an architecture in which the correspondence relationship of the requirement specification is clarified in each hierarchy.

Assuming that a series of development processes in a specific layer is to construct input deliverables to the development process of the lower layer, it is possible to express the process of the overall system development in

an overview at the outline level. In PFD, processes can be hierarchically represented by double circle notation, so the development process of the lower layer is refined using the hierarchical representation (Figure 14).

In this way, visualizing the development process with PFD provided the following effects.

- It was possible to lead to active discussions about the business operation, on such topics as: if this deliverable is expressed so far, the lower layer is not a problem; this process is to be divided because the deliverable is complicated; and the function safety response is done here, and these discussions easily generate ideas by chain representation.
 - Easier recognition of inconsistent information and resources became easy.
- It is easy to discuss topics related to the constraints, such as it is necessary for human resources with such knowledge to carry out this process; and the response of this process in half a year is no problem.

- Communication with the concerned persons became easier.
- Represent processes and deliverables in flow format makes it easy to have discussions with the concerned persons such as senior managers who do not have prior knowledge.

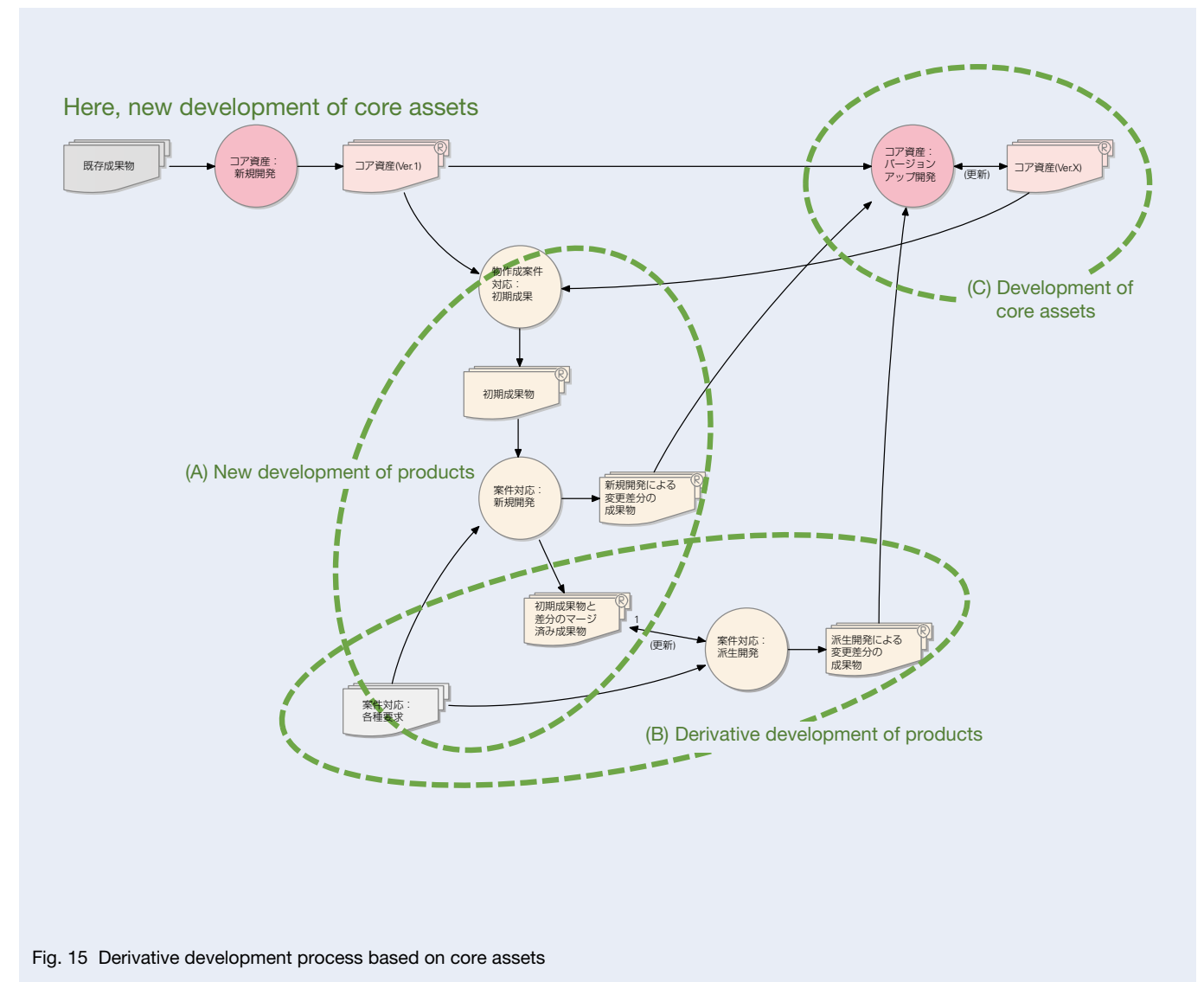
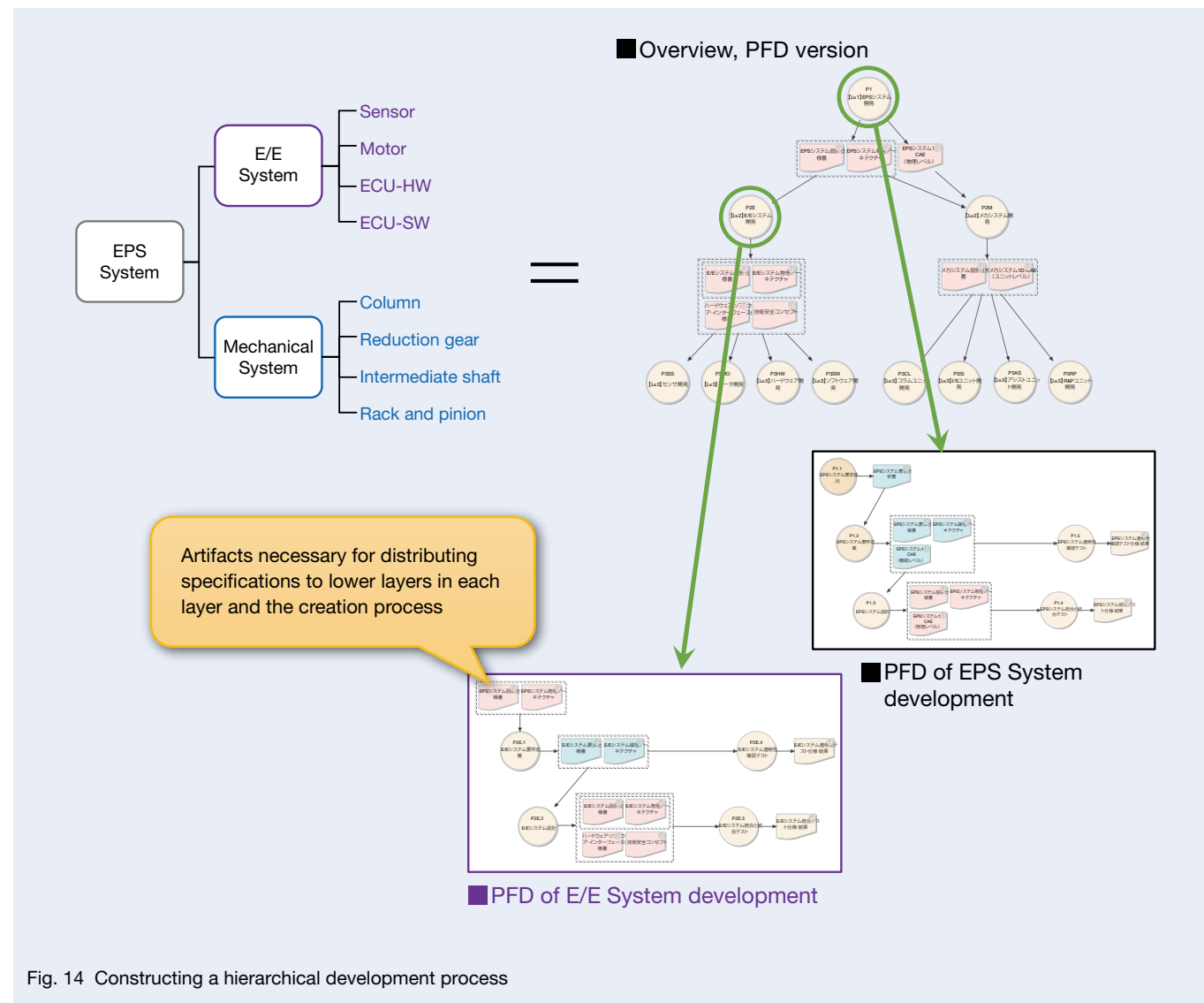
5.2 Construction of the development process based on core assets

In the activity of 5.1 above, the process of creating a new deliverable is summarized. As the activities after building core assets, anticipated developments include, for example, (A) new product development, (B) product derivative development, and (C) core asset update. Figure 15 shows the result of examining the entire process with the addition of new core assets.

Visualization of the development process using core assets clarified the following.

- (A) New development process of products
Doing derivative development for products based on core assets
- (B) Derivative development product
Doing derivative development based on the newly developed deliverable according to (A)
- (C) Update of core assets
Applying the information compared in (A) and (B) to core assets; that is, based on current core assets, making upgrades by derivative development.

All the aforementioned three patterns can be regarded as some derivative development, making it possible to establish visualizations thereof. Therefore, it is possible to believe that XDDP (eXtreme Derivative Development Process)²⁾ etc., which is a process for derivative development, can be applied to each pattern.



6. Future Plans

This paper has described that in order to continue the business in a diversified and complicated market environment, breaking free from the conventional development style is necessary, as is refining the development step by step from the viewpoint of the entire system. This paper also has described establishing core assets, setting a goal for change to a product line type development based on the core assets, and efforts to achieve that goal.

The subsequent activities are to verify the validity of the development process for the brush-up by defining a hierarchical development process and constructing deliverables according to it. The work to be proceeded is conversion of specifications and architectures into core assets by the bottom-up approach centered on software development.

The scheduled plan for making a full-scale transition to the target ideals is to be achieved by such that joining these two large flows to build deliverables based on a series of system development processes, a subsequent derivative development based on the core assets is implemented in a trial manner based on the process definition, and the process is verified and brushed up.

References

- 1) Y. Shimizu, "Technology that Specifies Requirements and Technology to Express," (2010), Gijutsu-Hyohron Co., Ltd.
- 2) Y. Shimizu, "Technology for Improving Process to Make "Derived Development" Succeed," (2007), Gijutsu-Hyohron Co., Ltd.
- 3) Y. Shimizu, "Writing PFD (Process Flow Diagram): Third Edition," (2009), System Creates Inc., <http://soft-koha-hp.la.coocan.jp/process/PFDform3.pdf>.



Masaya Oba

Weight Reduction of Column-Type EPS through Gearbox Thinning

Takefumi Kichikawa, Tetsuya Koike, and Takayuki Ishii
Steering R&D Center

Abstract

NSK develops and produces electric power steering (EPS) systems that improve the fuel economy of automobiles and reduce their environmental impact. In recent years, calls for environmental conservation have intensified globally, making the reduction of CO₂ emissions through improved automobile fuel economy more important than ever.

Lowering weight, improving efficiency, and increasing output are some example methods for improving fuel efficiency through EPS systems. For this new development, we focused on reducing EPS weight through gearbox thinning. We reduced the weight of the gearbox housing by 20% while satisfying required performance through a casting quality prediction method and a FEM analysis of the optimum design method.

1. Introduction

In the 1980s, NSK began to develop electric power steering (EPS) systems. EPS systems, which are energy saving compared to the conventional mainstream hydraulic power steering systems, are environmentally-friendly products because they do not use hydraulic oil. In 1989, NSK mass-produced the pinion-type EPS systems for light vehicles for the first time in the world. And in 1990, NSK also started production of column-type EPS systems for light vehicles. Since then, NSK has developed compact, high power, high performance EPS systems and expanded the types of vehicles in which its EPS systems can be installed. At present, its EPS systems are also applicable to state-of-art models such as hybrid vehicles and electric vehicles.

In recent years, movements to further suppress CO₂

emissions have been increasing in order to strengthen global environmental conservation throughout the world. Especially in Europe, the strengthening of the emission regulations such as Euro 6 has begun. Under such circumstances, the role of EPS systems for automobiles has become increasingly important.

NSK has developed "the World's Lightest Electric Power Steering," which aims at enhancing environmental performance. It achieves a compact, lightweight form that contributes to fuel efficiency, and weight reduction resulting in becoming 13% lighter than the current product was achieved in January 2016 (according to our survey in FY2015)¹⁾. (Figure 1)

This paper reports on "Weight reduction of column-type EPS through gearbox thinning," which is one of the aforementioned development efforts, especially aluminum casting quality.

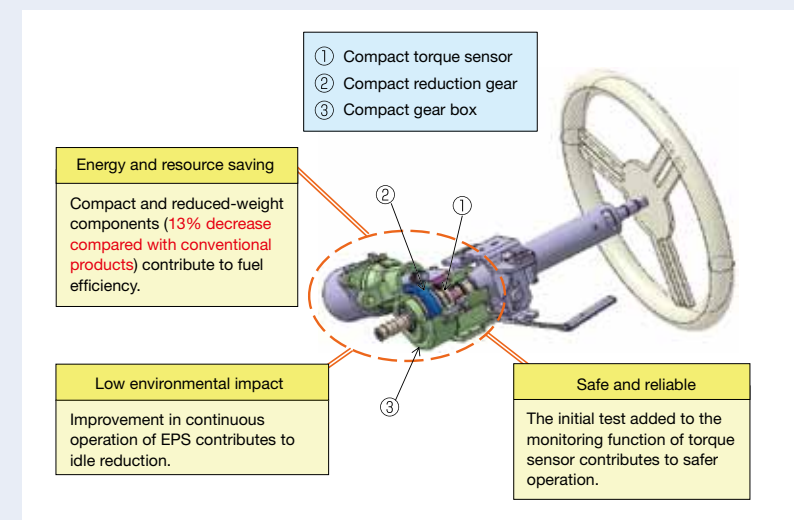


Fig. 1 The world's lightest column-type EPS system equipped with a tilt mechanism

2. Weight Reduction by Realizing Aluminum Gearbox Thinning

Among NSK's column-type EPS systems, the gearbox housing occupies the largest percentage of weight (Figure 2). Therefore, this development led to the decision to reduce weight by focusing on the gearbox housing.

As a means of weight reduction, the possible measures such as substitution with low specific gravity material (magnesium, resin, etc.) or thinning of the walls of the product are considered. Simply, if considering the weight reduction rate, material replacement is most effective. However, resins and the like are much lower in strength and rigidity than aluminum as a material and therefore it is difficult to satisfy the performance of the reduction gear unit with a simple substitution. For this reason, it is necessary to conduct an optimum structural design of the whole unit including other parts.

On the other hand, weight reduction by thinning the aluminum-walls deals with this by optimally designing the gear box alone with making full use of the previous design knowledge, making it possible to achieve this development in a short period of time when compared with

material change. However, since the degree of dependence on material strength becomes high from the perspective of design, it is necessary to pay attention to the casting quality more than ever.

Among the quality factors that affect the material strength, the porosity is the factor that has a particular effect. Figure 3 shows the benchmark results of the porosity content rate (proportion of the porosity amount to the product) of the column-type EPS gearbox that is on the market. From this result, the NSK products tend to have larger variations in the porosity content rate than those of the other companies and a slightly larger upper limit. It is assumed that the NSK product had a thick wall because of its design to have strength and rigidity, which generates shrinkage porosity as one form of porosity.

Although the porosity content rate shown in Figure 3 is not at a level that is problematic in terms of strength, it is thought that the shrinkage porosity can be reduced by designing in consideration of the casting process. Therefore, in this development, the weight reduction by thinning walls together with improving the casting quality concurrently are achieved.

Part		Weight (%)
 Upper Column	Housing	9%
	Shaft Hollow	9%
	Tilt BRKT	13%
	Tilt Lever	2%
	Inner Column	7%
 Colum-type EPS	Other	10%
	Gear Box	19%
	Worm Wheel	5%
 Reduction Gear	T-sensor Shaft	7%
	W/W Shaft	6%
	Worm	9%
	Sensor, Other	5%

100% ⇒ Without ECU & MOTOR

Fig. 2 Column-type EPS weight ratio by part

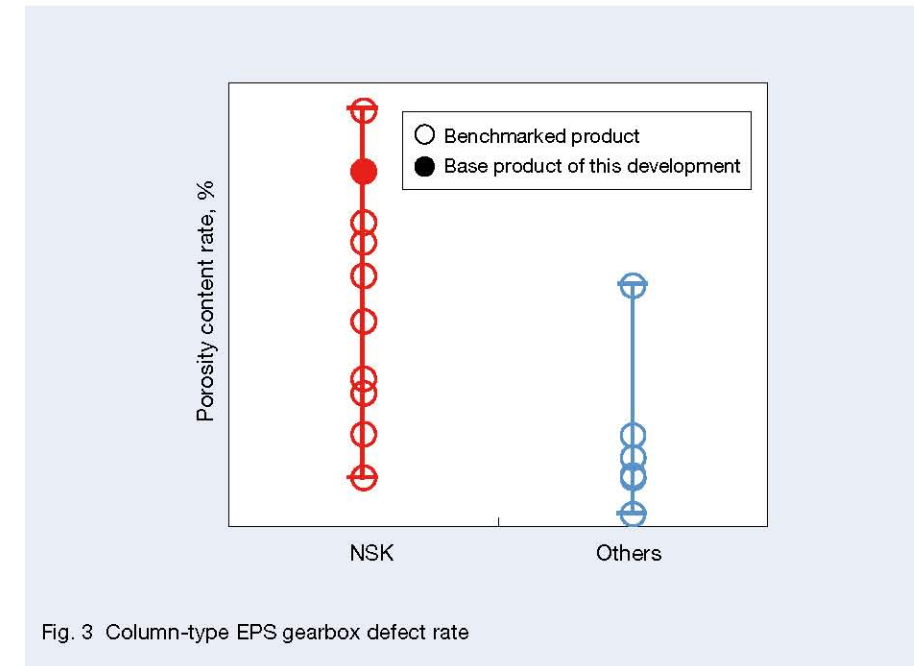


Fig. 3 Column-type EPS gearbox defect rate

3. Design Considerations Involved in Thinning

In thinning the aluminum die casting product, there are items to pay attention to from the perspectives of product performance and manufacturing (casting). Details of each point of note are shown below.

3.1 Decline in structural properties due to decrease in cross-sectional area

As the cross-sectional area decreases due to thinning, the structural properties (strength, rigidity) decrease, possibly making it impossible to satisfy the performance required for the gearbox.

3.2 Quality degradation due to deterioration of molten metal flow

The runner narrows due to thinning, and the molten metal tends to be cooled during filling. As a result, the flow property of molten metal may be deteriorated. The deterioration of the flow property of the molten metal provides causes of defective flow of molten metal that include, for example, flow line, cold shut, unfilled state, and gas entrainment state, and the quality tends to deteriorate. These defects are caused by an increase in solid fraction due to a drop in the temperature of the molten metal during filling as well as a back pressure due to compression of air in the cavity, and the like.

As measures against these defects, the following are considered.

1. Completing the filling before the molten metal begins to solidify.
2. Exhausting the air in the cavity as much as possible.

For 1, the possible solution is conducting a design of a casting scheme whose filling time is less than the allowable filling time calculated from the generally proposed casting investigation formula and setting a suitable injection speed²⁾. For 2, the possible solutions include, for example, a casting system plan to stably replace the air and molten metal in the mold and setting an appropriate injection speed switching position.

3.3 Quality degradation due to the occurrence of shrinkage porosity

Shrinkage porosity is a problem that can occur relatively easily. Although improvement can be expected if the whole product can be thinned evenly, from the viewpoint of securing the strength and rigidity of the product, an appropriate wall thickness is set for each part, so that a difference in thickness tends to occur. Therefore, the thin portion solidifies first, and the molten metal to the thick portion cannot be supplied sufficiently, possibly resulting in the formation of a shrinkage. As a countermeasure against this, in addition to optimizing the casting conditions, it is conceivable to reduce the difference in wall thickness (to avoid a sudden change from a thick portion to a thin portion), or the like.

4. Factor Estimation of Porosity Generation (Conventional Product)

Before conducting a thin-walled shape design, estimation regarding the condition and cause of porosity in the conventional product was performed.

Figure 4 shows the analysis results of the porosity condition inside the conventional gearbox. This analysis uses an X-ray CT three-dimensional measuring device and three-dimensional image processing software. The gray part of the CT image is the aluminum die casting part, and the part shown in blue is the porosity. From this result, it was possible to confirm the location of the porosity. However, since it is difficult to judge what causes the porosity, a factor analysis was carried out using a cast simulation.

The porosity distribution predicted by the casting simulation is shown in Figure 5. The orange portion in the figure is a site with a high probability of occurrence of porosity. The result, which has almost the same tendency as the CT analysis result, is valid as a method for predicting the casting quality. However, this prediction result is insufficient as a factor analysis because both shrinkage porosity and gas porosity are output. Therefore, a simulation was made wherein the gas entrainment distribution at the completion of filling, and it was compared with the porosity distribution to isolate the cause of the blow cast. Figure 6 shows the gas entrainment distribution state. The warmer the color, the greater the amount of gas entrainment.

From both prediction results, it is estimated that the shrinkage porosity occupies a large proportion in the left side of the distribution in Figure 5, and the gas porosity occupies a large proportion in the right.

It is thought that the cause of the above-mentioned shrinkage porosity is due to uneven wall thickness as a result of the shape of the product, and the cause of the gas porosity is that this position is close to the final filled part and gases entrained in the filling process gather.

From these results, the following points were considered in thin-walled shape design: a shape suppressing porosity, a casting system plan design of suppressing the gas entrainment during filling process, and new casting conditions.



Fig. 5 Casting simulation of porosity distribution (conventional product)



Fig. 4 X-ray CT of porosity distribution (conventional product)

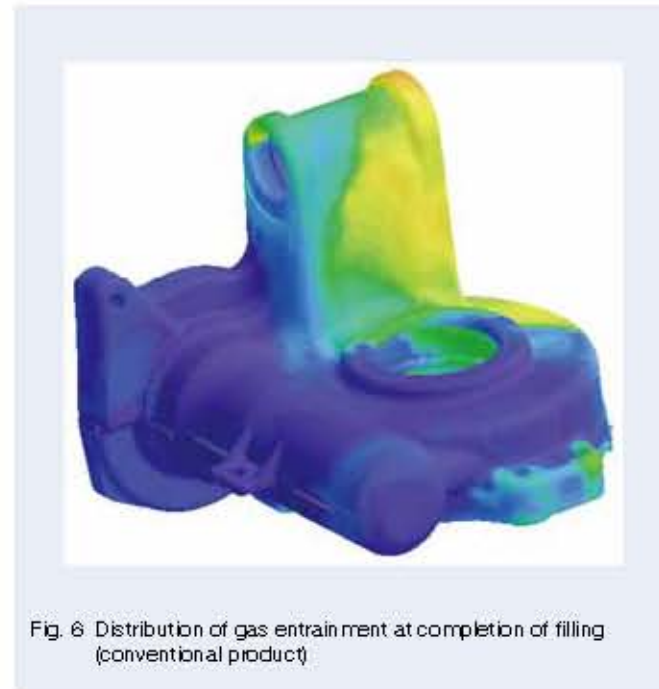


Fig. 6 Distribution of gas entrainment at completion of filling (conventional product)

5. Examination of Thin-walled Shape

In order to confirm the effect of weight reduction by thinning, design and casting examination of thinning was conducted based on NSK's conventional product. Hereinafter, the thin-walled product is called a developed product.

5.1 Optimum shape design

It is impossible to satisfy the performance required for the gearbox by merely thinning the conventional product. As countermeasures therefor, the addition of ribs, increase of some wall thickness, etc. are available. However, as mentioned in the preceding section, unless the proper design is made, these will lead to the generation of a shrinkage porosity. Therefore, in this developed product, the rib design was conducted in which rapid change in a cross-sectional area is suppressed and the flow of molten metal is taken into consideration.

In this report, the details of the optimum shape design are skipped, but as to collision loads (column bending direction input, impact input), EPS operation etc., a shape causing the stress to disperse is examined using FEM. As a result, the housing shape is optimized for the establishment thereof. An example of the FEM analysis result is shown in Figure 7. Based on these results, a shape was determined that is 20% lighter than the conventional product.

5.2 Casting quality prediction

As a procedure for predicting the casting quality, firstly, it was judged from the casting investigation formula that filling for forming the above-determined shape can be completed before the start of solidification. At this time, calculation of the casting condition, which makes it

difficult to cause air turbulence, was made.

However, it is difficult to judge to what extent the gas actually remains in the cavity, or whether a molten metal flow defect such as a flow line, cold shut, or the like occurs, only by the casting investigation formula. In addition, although consideration is given to the shrinkage porosity in shape design, its effect is unconfirmed. Therefore, utilizing casting simulation software, the porosity distribution (the influence of the shrinkage porosity and gas porosity), and the molten metal flow defect were predicted.

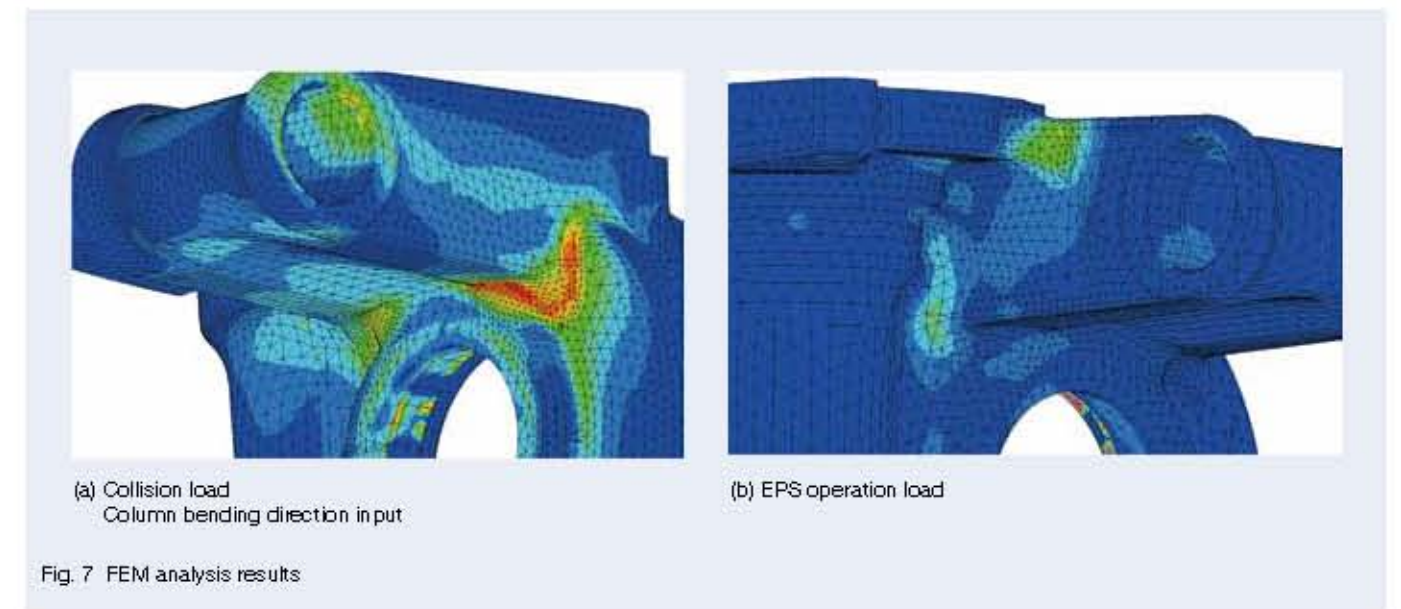
5.2.1 Simulating porosity distribution

First of all, methods and casting conditions that can suppress gas entrainment as much as possible were examined.

The set plans include Plan A and Plan B. Plan A is used for simultaneously filling the molten metal into the product from each gate, which is the most basic idea regarding casting. Plan B is used with a sub runner devised so as to shorten the filling time as much as possible. The following is an indication of the merits and demerits of each plan.

Since Plan A is designed so that molten metal is poured through each gate at the same time, turbulence is unlikely to occur. However, due to the restrictions on the gate arrangement being large and the resulting difficulty in securing the gate cross-sectional, it is difficult to shorten the filling time. Although Plan B can shorten the filling time, there is a possibility that turbulence may occur because there is a filling time difference for each gate.

Gas entrainment prediction was made for the above plans. The results are shown in Figure 8. The warmer the color, the greater the amount of gas entrainment. From this figure, it was confirmed that the filling delay of Plan B with the sub runner occurred compared to the gas



(a) Collision load
Column bending direction input

(b) EPS operation load

Fig. 7 FEM analysis results

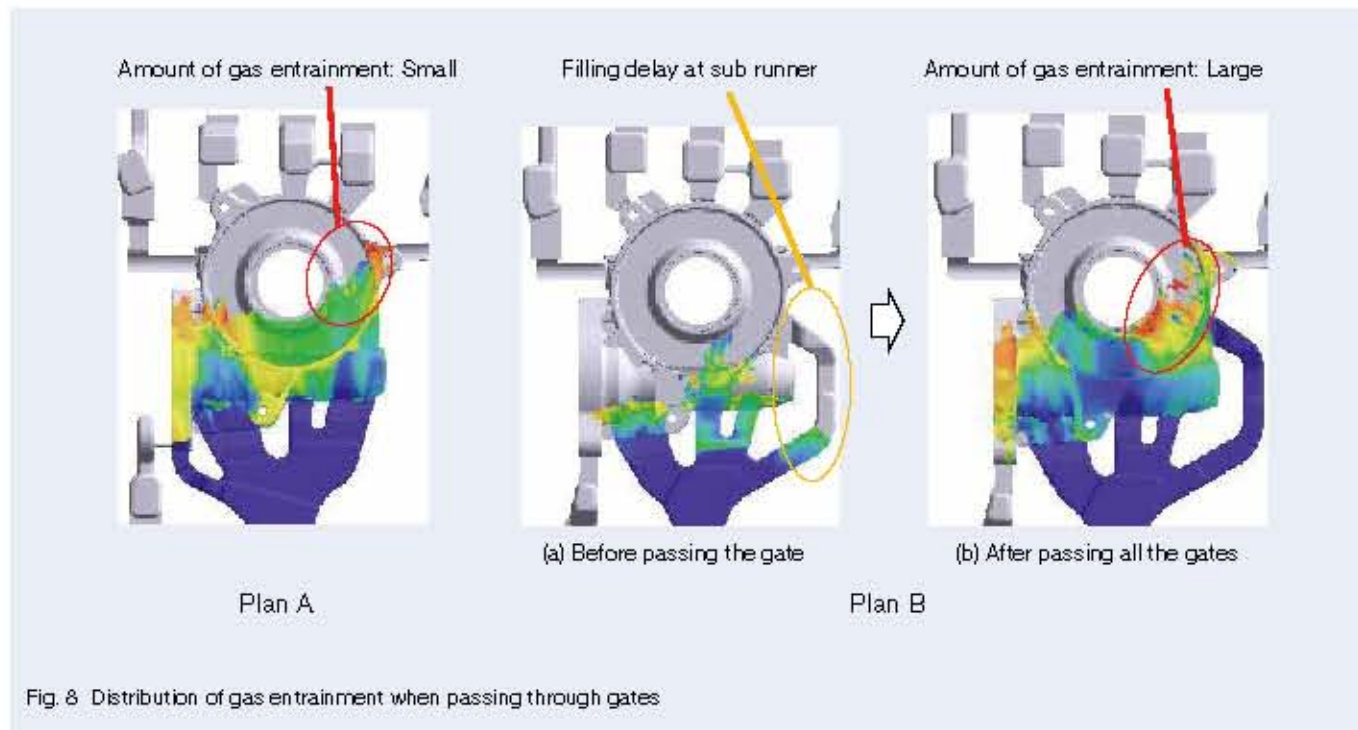


Fig. 8 Distribution of gas entrapment when passing through gates

entrapment distribution of Plan A with the simultaneous filling, and when filling the product, turbulence occurred and the gas was easily entrained. Therefore, this development employed the plan that can conduct the simultaneous filling.

In order to improve the quality, it is important to suppress the gas entrapment at the start of filling and

to reduce the gas remaining in the product as much as possible. Thus, the gas entrapment state at the completion of filling is simulated to investigate the optimum injection speed and adjustment of the gate arrangement. The gas entrapment amount was judged based on the conventional product.

Figure 9 shows the gas entrapment simulation results.

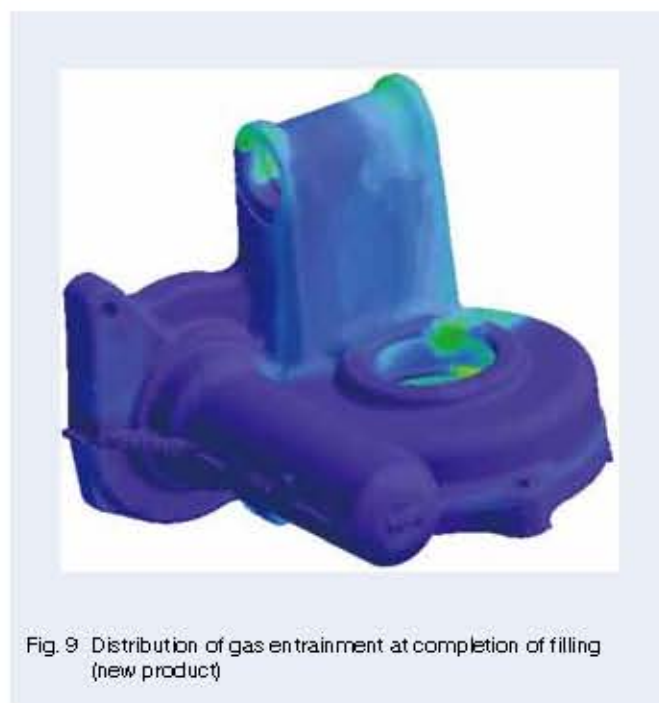


Fig. 9 Distribution of gas entrapment at completion of filling (new product)



Fig. 10 Casting simulation of porosity distribution (new product)

From the comparison with the same simulation result of the conventional product (Figure 6), it is possible to understand that the amount of entrained gas is smaller in the developed product than that in the conventional product, and the range is also reduced in distribution.

Figure 10 shows the simulation results of the porosity distribution under the above-mentioned plans and the casting condition. From the comparison with the same simulation result of the conventional product (Figure 5), it is possible to understand that the amount of entrained gas is smaller in the developed product than that in the conventional product, and the range is also reduced in distribution.

In addition, since the porosity at the part where the influence of the shrinkage is large is also decreasing, it is possible to understand that the method of suppressing the shape investigation was also effective.

In this way, employing not only the plan and the casting condition, which took into consideration the gas entrapment, but also conducting the optimal shape design made it possible to predict that the developed product has the quality equal to or higher than that of the conventional product.

5.2.2 Simulating the molten metal flow defect

The occurrence of a molten metal flow defect such as a cold shut, flow line, or the like is caused by the existence of a temperature state below the solid phase temperature or a temperature state close to the solid phase temperature in the product at the completion of filling. Even in the conventional product (base product of this development) shown in Figure 3, no signs such as flow line, cold shut, or the like have been confirmed.



Fig. 11 Temperature distribution at completion of filling

However, in this development, since there is a possibility that molten metal flow defects may occur due to thinning, measures are taken by adjusting the plan and casting conditions. The effect of these efforts was judged by simulating the temperature at the completion of filling. As a judgment method, the product temperature at the completion of filling was assumed to be the solidification temperature of aluminum die-cast ADC 12 not less than 582°C²⁹. Figure 11 shows the temperature simulation result at the completion of filling. The warmer the color, the higher the temperature, and the solidification temperature 582°C or lower, as the lower limit value, is displayed in blue. From the simulation results, it can be confirmed that the inside temperature of the product is higher than the solidification temperature at the completion of filling. As a result, it was judged that no defects such as a cold shut, flow line, or the like occurred.

6. Results and Discussion

6.1. Results and discussion of casting quality analysis

In accordance with the plan and casting conditions investigated in the preceding section, analysis of the porosity condition in the prototype gearbox was carried out. Figure 12 shows the X-ray CT analysis of porosity distribution. In addition, the relative comparison results with the conventional product of the porosity content rate and the maximum porosity size obtained from the analysis are shown in Figure 13.

From the results of the CT image and the porosity content rate, it was confirmed that in the developed



Fig. 12 X-ray CT of porosity distribution (new product)

product, the porosity content decreased by 84% and the maximum porosity size decreased by 88% compared with the conventional product. In addition, the porosity content ratio of this developed product is very low compared with the NSK products so far, and it is considered that the quality had also remarkably improved.

It has been confirmed that casting quality higher than conventional products can be realized by utilizing casting simulation, which proved that this developed product is capable in terms of quality even if it is thinned.

6.2 Performance verification result

Performance verification of the developed product was carried out according to the in-house standards. Although detailed contents of the verification method and the verification results are omitted, as shown in Table 1, the developed product satisfied the in-house standards in terms of both strength and rigidity according to its optimum design.

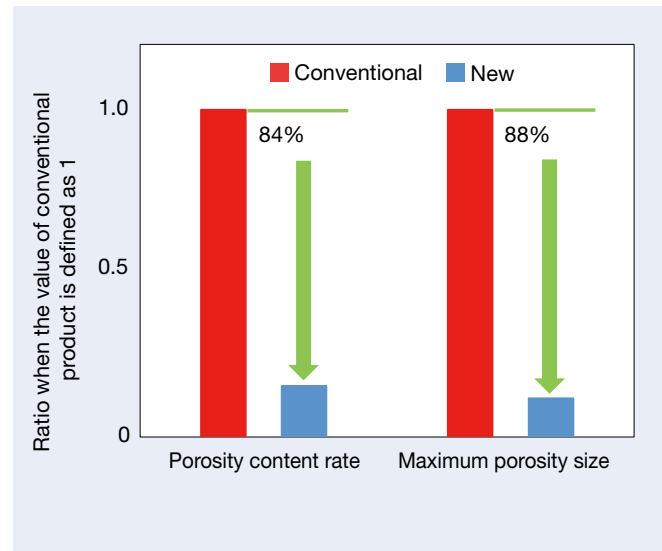


Fig. 13 Relative comparison of porosity content rate and maximum porosity size

Table 1 Performance verification results

Performance verification item		Result
Impact strength	Impact strength test	○
	Column bending test	○
Durability strength	Torque operation durability strength	○
	Column bending durability test	○
Steering wheel support rigidity	Column bending rigidity	○
Bearing support rigidity	Meshing rigidity	○

7. Conclusion

It was possible to achieve the production development in which the resulting product satisfies the performance while achieving a weight saving of 20% compared with the conventional product, and the casting quality is made higher than before. From now on, the planned activities will be conducted, which include applying the manner obtained in this development to other aluminum die cast parts (column housing, rack housing), and continuing to attain weight reduction of the EPS as a whole.

References

- 1) "The World's Lightest Electric Power Steering System," NSK Technical Journal, 689 (2017) 76-77.
- 2) N. Nishi, "Casting Defect Improvement Method in Die Casting," Proc. 2016 Nouryoku-Kaihatsu Seminar Z0221, (2016) IV, Japan Organization for Employment of the Elderly, Persons with Disabilities and Job Seekers.
- 3) N. Nishi, "Explanation by Illustration for Basic Technology of Die-Cast," (2015) 19, THE NIKKAN KOGYO SHIMBUN, LTD.



Takefumi Kichikawa



Tetsuya Koike



Takayuki Ishii

Recent Technical Trends in Hub Unit Bearings

Takashi Sakaguchi

Automotive Powertrain Bearing Technology Center

Abstract

In recent years, environmental regulations regarding CO₂ emissions and fuel consumption have spread across the world, leading to increased requests for low friction in bearings and weight reduction in particular. Challengingly, hub unit bearings require reliability that does not fail even in harsh environments. In terms of reliability design, the application of water-resistant grease and high-reliability seals reduces market risk in emerging countries where operating conditions are more severe. A 29% reduction in friction has been achieved by incorporating highly functional grease and devising an enhanced seal design.

In addition, transitional responsiveness has become increasingly necessary for handling stability in recent years. Finding correlations in not only bench tests but also actual vehicle tests will be required in future efforts.

1. Introduction

In recent years, reducing CO₂ emissions and improving fuel consumption have become major issues for the automobile industry regarding environmental problems such as air pollution and global warming. In order to deal with these issues, environmental regulations are being strengthened in each country. In response thereto, NSK is now engaging in an effort to reduce the friction and weight of hub unit bearings.

Incidentally, as a standard specification for the next-generation eco vehicle, EVs (electric vehicles) have been rapidly spreading in recent years. The EV is designed to be powered by an electric motor and therefore the cruising distance is considered a current problem. Regarding improving the cruising distance, it is important to consider how to increase energy efficiency, and as a measure of dealing with this, there are regenerative brakes. These brakes, which have a structure using an electric motor as a generator at the time of deceleration, are a

method to convert the rotational energy of the tires into electric energy and reuse the generated electric energy. Conventionally, friction of the hub unit bearing during acceleration or low-speed running has been noted as energy loss. However, as a factor influencing deceleration, the friction of the hub unit bearing has been regarded as more important since the invention of regenerative braking.

On the other hand, the degree of contribution to the hub unit bearing is increasing with respect to steering stability as the rigidity of the vehicle body is increased. In recent years, the responsiveness, maneuverability, and rigidity felt when the steering wheel is turned, along with the transient responsiveness assumed by automatic driving control, are emphasized as performance that can be steered in response to the driver's intention. For hub unit bearings, it is necessary to respond to advanced requirements such as consideration of high rigidity and transient rigidity.

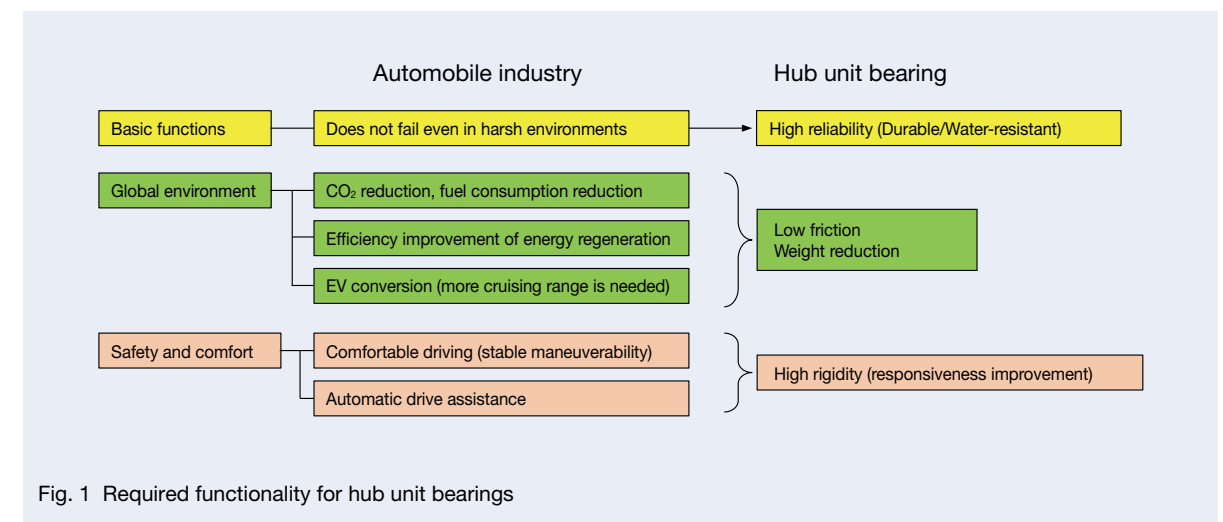


Fig. 1 Required functionality for hub unit bearings

The production volume of automobiles continues to grow globally, especially in markets in emerging nations where demand is expanding markedly. Hub unit bearings are to be used in emerging nations where infrastructure maintenance is insufficient and there are many unpaved roads, and is performed in harsh environments, making it therefore necessary for the hub unit bearings to have a high-reliability design that is robust against muddy water environments.

Figure 1 shows the required functionality for hub unit bearings. This paper will describe recent efforts for achieving high reliability, low friction, light weight, and high rigidity (improvement of responsiveness), which constitute elemental technologies.

2. Efforts for Achieving High-reliability Design

2.1 Functions of the hub unit bearing

As shown in Figure 2, the hub unit bearing supports the

rotation of the wheels (tires, wheels) of the automobile. It is a bearing that supports the vehicle body and is required to have high reliability because its breakage may also cause an accident.

In the markets of emerging nations, as noted in the preceding section, there are many abnormal noise problems caused by the usage environment. Although the cause of failure tends to vary depending on the area, the flaking due to water invasion into inside the bearing occurs more frequently in Russia and Southeast Asian nations compared to the other regions.

Figure 3 shows the situation of the seal lip of bearings from the Russian market, and there are many cases of large amounts of mud clogging the seal lips. In winter, the snow melting agent used on frozen roads mixes with the mud and enters between the seal lips and causes water intrusion inside the bearing due to the gap created by the clog. Meanwhile, in the Chinese market, there are few malfunctions due to water intrusion but many problems caused by impression due to impact load.

There are two main methods of countermeasures for the defective phenomenon peculiar to these markets of

emerging nations. For areas with many defects due to impression as in the Chinese market, selection of bearing capacity to improve durability under excessive input load is most important. For markets such as Russia and Southeast Asian nations, where there are many defects caused by water intrusion, improvement of the seal suppresses muddy water intrusion, and even if it is still insufficient, technology to make a small amount of water intrusion harmless by improving the water resistance of the grease itself is introduced into the markets. The design techniques of these greases and seals will be explained in the next section.

2.2 Application of high-reliability seal

Figure 4 shows the design concept of a high-reliability seal. This seal consists of the sub-lip or labyrinth lip provided at the side where muddy water enters or farther from the lip sliding portion to maintain a favorable lip sliding environment for better sealing performance. Regarding the outer seal, a labyrinth lip with an extended plate on the rotating wheel prevents the mud that

interferes with the movement of the lip from entering and keeps the sliding environment inside structure in good condition. Regarding the inner seal, the sealing performance is improved by reducing the size of the space where the muddy water gathers, which prevents the mud from sticking.

In order to improve the sealing performance, it is general practice to increase the number of lips or increase the contact surface pressure between the lip and sliding surfaces. However, this practice results in an increase in seal friction, which is against the recent specifications of low friction, and therefore employing this practice becomes difficult. Therefore, for high-reliability seals, optimizing lip surface pressure distribution by FEM analysis to adjust the total reaction force of all lips reduces the increase in friction caused by the labyrinth structure as much as possible. Both the outer seal and the inner seal have already been introduced into the market, and the market effect is recognized particularly in emerging nations.

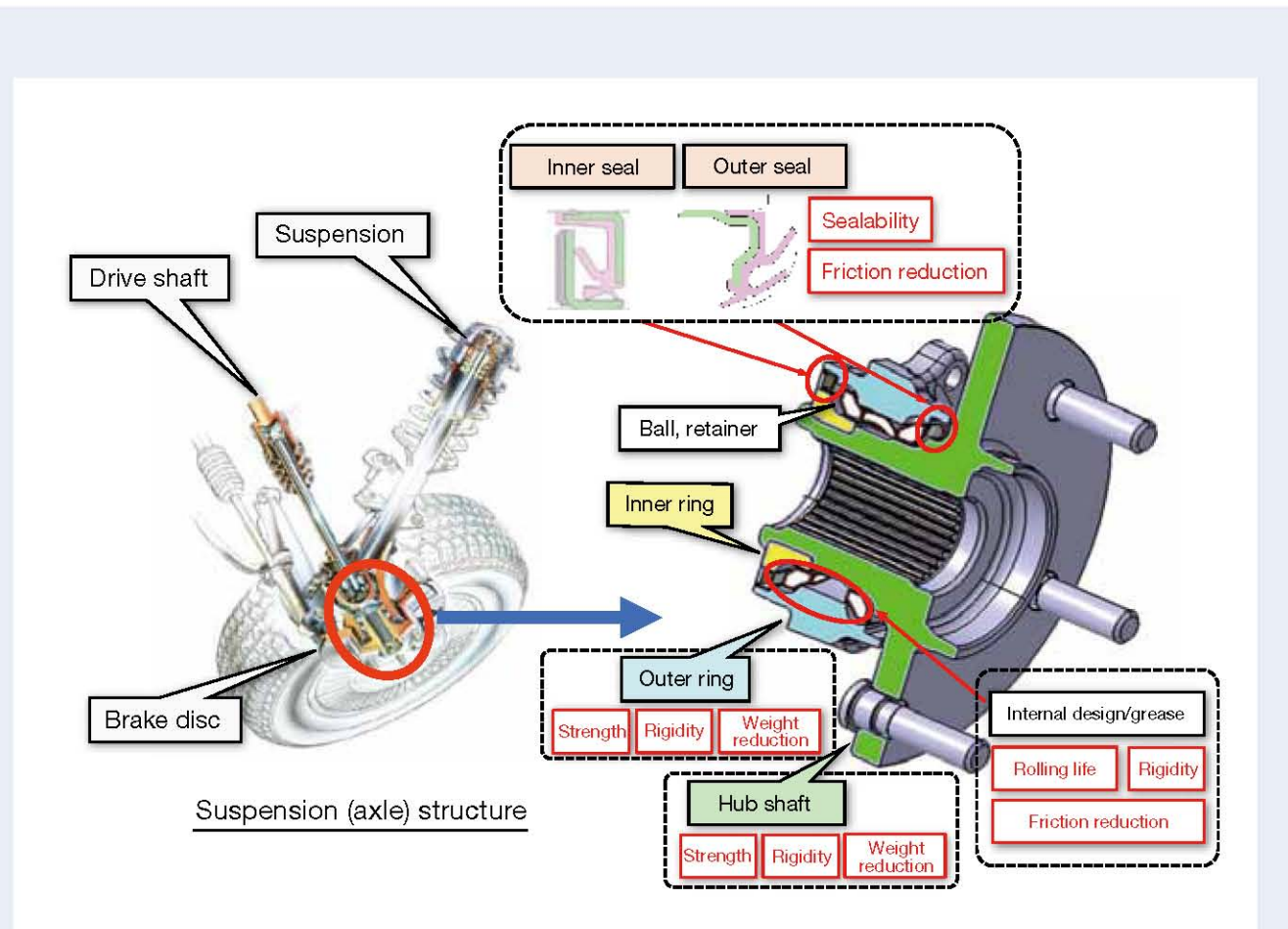


Fig. 2 Components and functional requirements

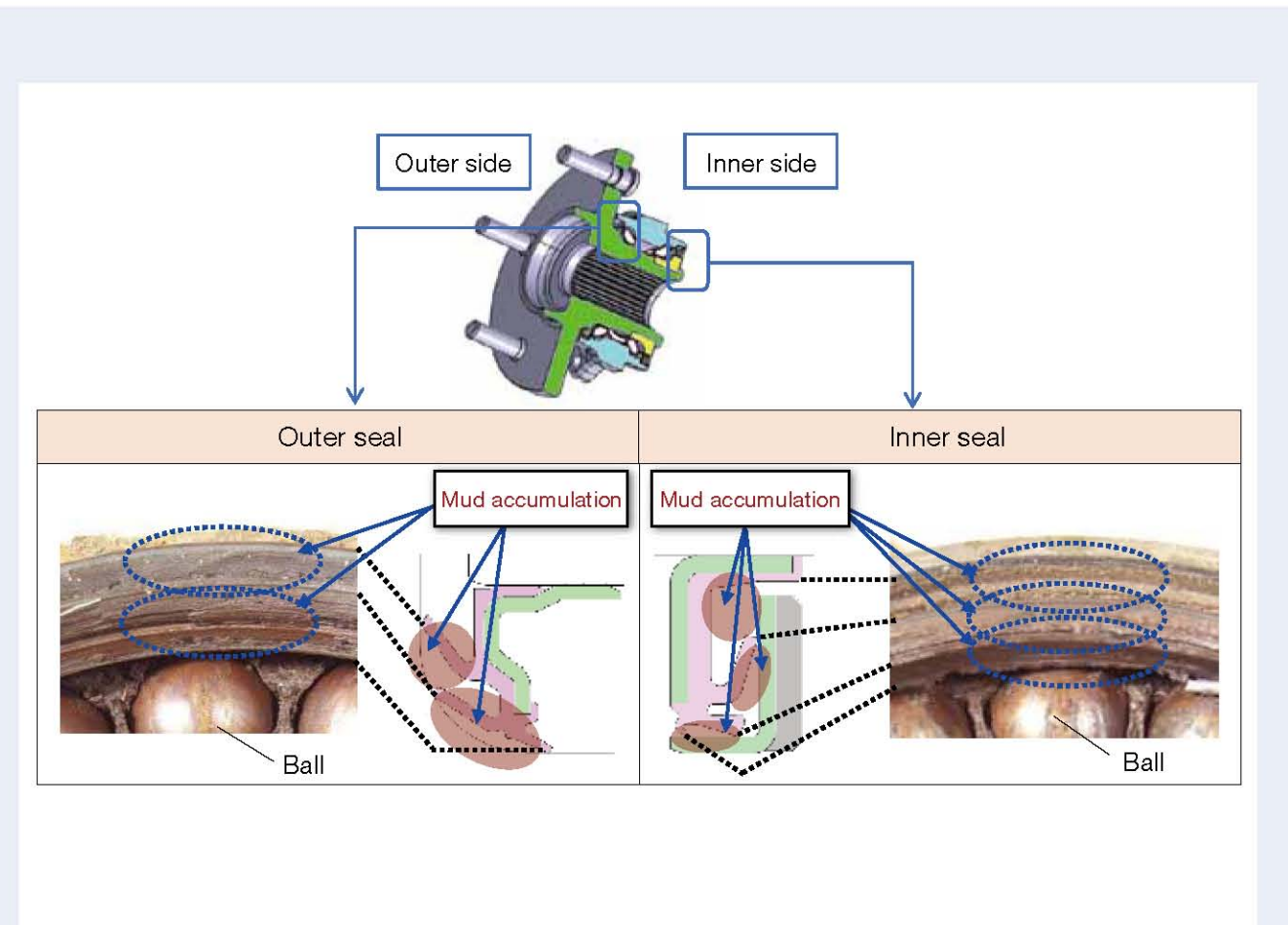


Fig. 3 Clogged mud between seals (Russian market)²⁾

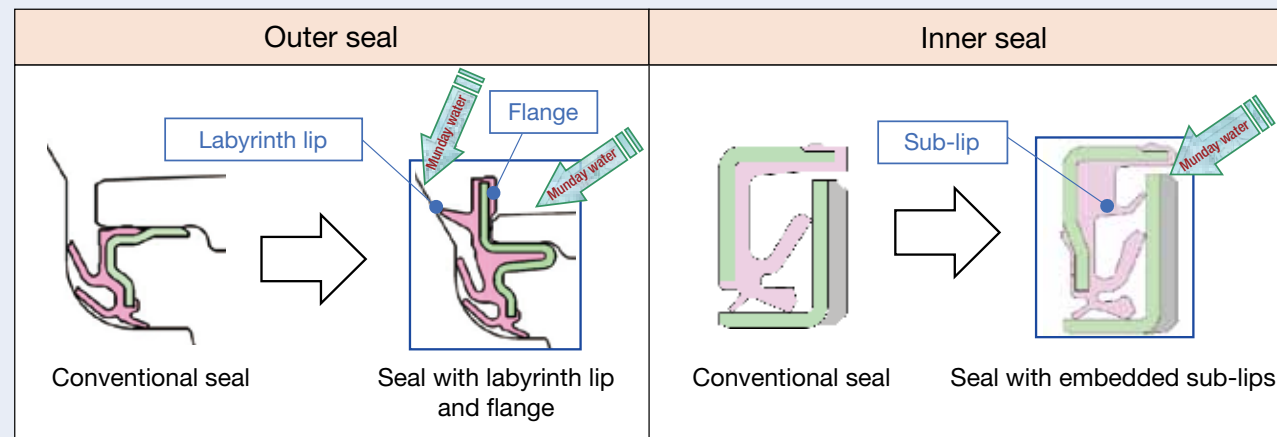


Fig. 4 Concept of a high-reliability seal²⁾

2.3 Improvement of water resistance by grease

Although the effect of improving the water resistance by the high-reliability seal is recognized, completely eliminating water intrusion remains difficult and therefore a trace amount of water may enter the bearing. When water is mixed in the grease in the bearing, as shown in Figure 5, the water is dispersed as fine particles in the grease. When water enters the contact surface together with the grease, it is difficult for the grease to form lubrication film, and the raceway surface and ball come into metallic contact, resulting in abrasion and micro cracks and then flaking.

Therefore, waterproof grease, which has been introduced to the market, was developed as a technology that can make a slight amount of water intrusion harmless.

As shown in Figure 6, the effect of developed grease is mainly composed of two actions. One is to adjust the type and amount of additives so that water is separated into grease as large grains, making it less accessible to the contact surface. The other is to form an oxide film thicker than the conventional grease on the raceway surface by contriving the compounding technique of additives so that contact between water and metal can be suppressed.

In fact, as shown in Figure 6, the effect of improving the flaking life of waterproof grease has been confirmed in the accelerated test under water contamination using a hub unit bearing.

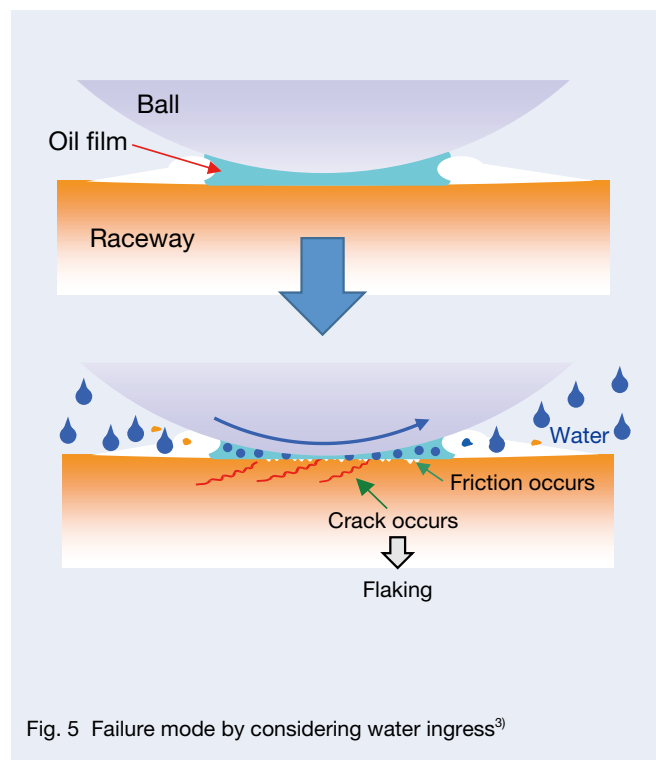


Fig. 5 Failure mode by considering water ingress³⁾

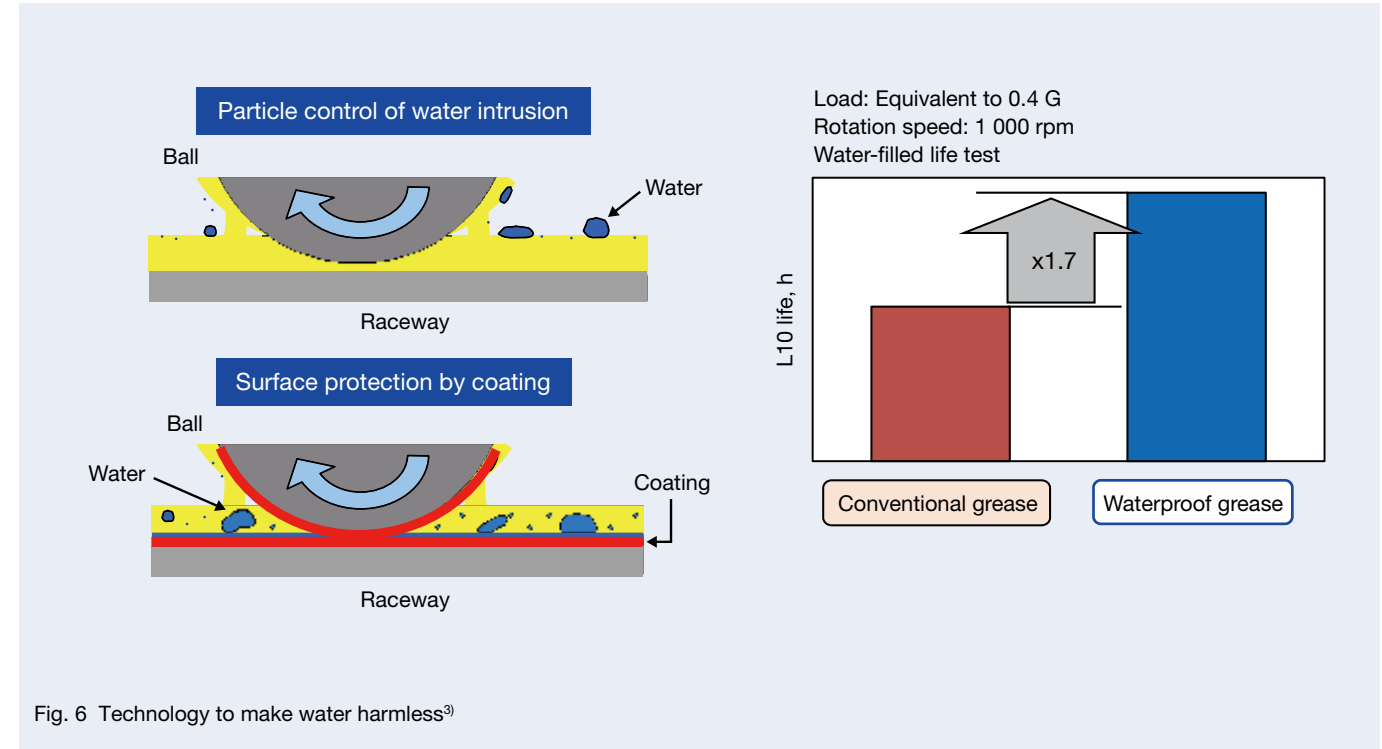


Fig. 6 Technology to make water harmless³⁾

3 Low-friction Technology

3.1 Low-friction technology in hub unit bearings

Figure 7 summarizes the recent efforts for low-friction technology in hub unit bearings. The friction of the hub unit bearing can be considered to be divided into two elements, the interior of the bearing and the seal. The friction inside the bearing varies depending on the preload and conditions of use, and the friction of the seal varies depending on the number and design of the lips, but the contribution of both friction inside the bearing and friction of the seal are approximately 50% each.

In order to reduce the friction inside the bearing, it is effective to optimize the internal design, reduce the base oil kinematic viscosity of the grease, and decrease the frictional resistance. At NSK, the friction of conventional hub unit bearings was reduced by 10% by optimizing internal specifications such as ball diameter, raceway groove radius, preload, and so on. Another method of reducing the base oil kinematic viscosity of the grease is combining the two methods above. The internal friction of conventional hub unit bearings can be reduced by 25%. Details will be explained in Section 3.2.

Regarding low-friction technology of the seal, it is effective to reduce reaction force and sliding surface friction by optimizing the lip shape. Regarding

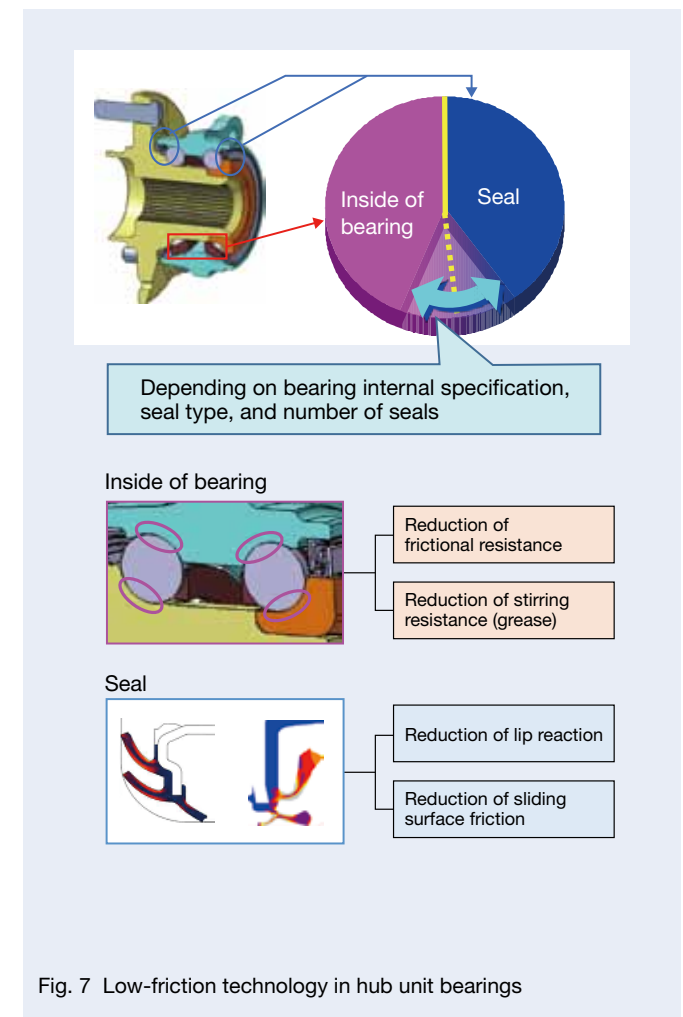


Fig. 7 Low-friction technology in hub unit bearings

optimization of the lip shape, FEM has optimized it so that compatibility between low friction of the seal and high muddy water durability can be verified at the design stage. By optimizing the lip shape, it is possible to reduce the friction of conventional hub unit bearings by about 20%. As for the reduction of sliding surface friction, it is possible to reduce the friction of the seal by 31% by combining the two methods above. Details will be explained in Section 3.3.

As shown in Figure 8, application of the low-friction item of the inside of the bearing and the seal makes it possible to anticipate a 29% reduction in friction of the hub unit bearing.

3.2 Reduction of internal friction of the bearing

In general, the internal friction of rolling bearings can be expressed by the sum of frictional resistance and stirring resistance (Figure 9). Frictional resistance is the friction caused by base oil shearing at the contact surface between the ball and the raceway surface and generally increases as the input load to the bearing increases. On the other hand, stirring resistance is the friction caused by viscous

resistance generated when the ball pushes aside the grease and generally increases as the rotation speed of the bearing increases. Since hub unit bearings are used under heavy load and in a low speed environment, their frictional resistance is greater than their stirring resistance.

In order to reduce the frictional resistance, it is effective to reduce the friction coefficient of the grease, that is, the base oil kinematic viscosity. However, since the base oil kinematic viscosity drops remarkably in the high temperature region, there is a concern of poor lubrication. Therefore, as shown in Figure 10, NSK developed a low-friction and reliable grease even in high temperature and high load range by employing a base oil with less viscosity change due to temperature change. As shown in Figure 5, this high performance grease has the water resistance effect similar to water-resistant grease by adjusting the formulation and types of additives.

Since the change in viscosity of grease due to temperature is small, not only high temperature characteristics but also fretting characteristics at low temperature can be expected, as in the case of friction.

This grease has already promoted market development mainly in Europe.

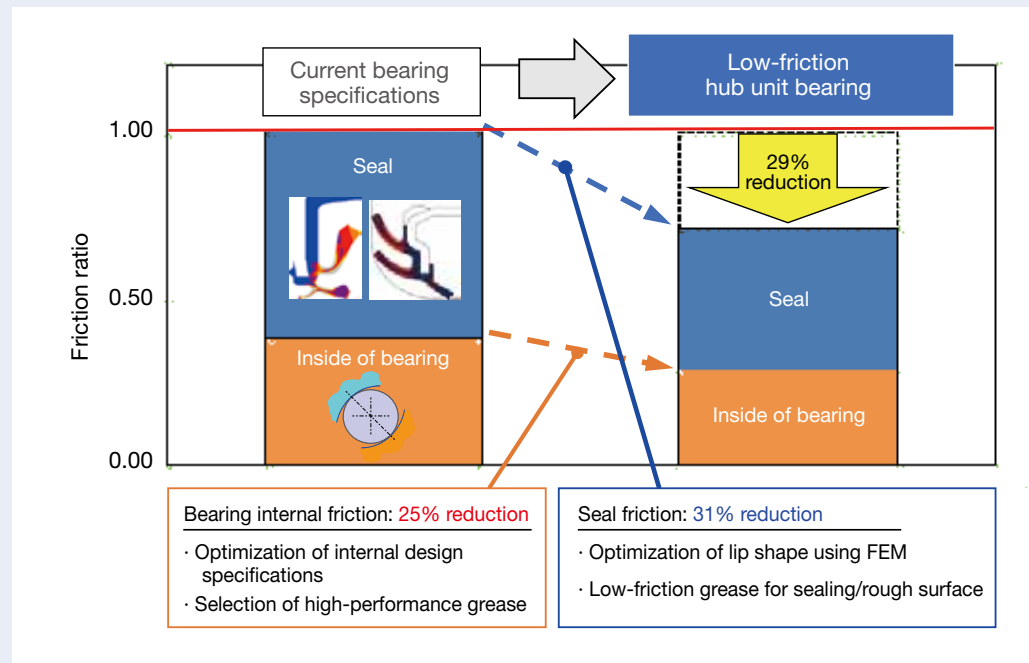


Fig. 8 Effect of individual friction reduction items

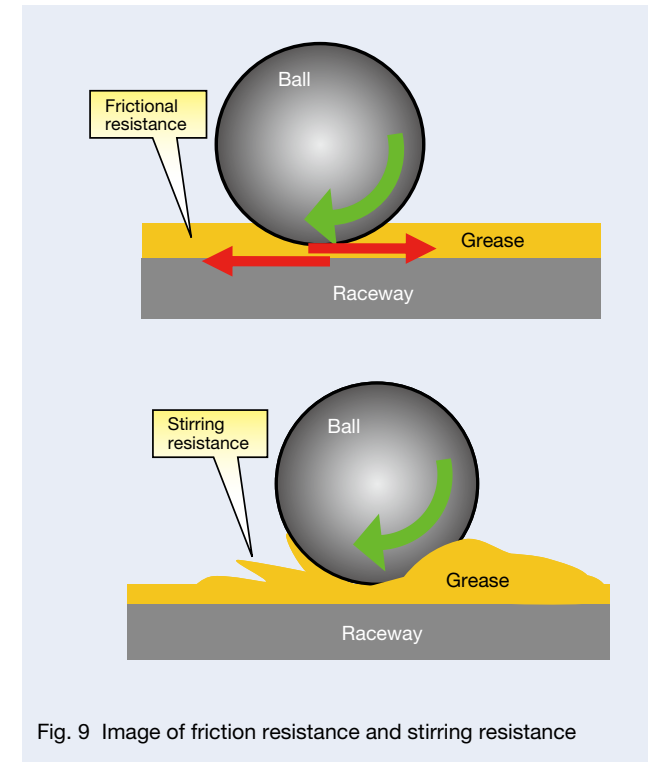


Fig. 9 Image of friction resistance and stirring resistance

3.3 Reduction of seal friction

In most conventional cases, the same grease used for the raceway surface inside the bearing is applied to the seal. However, in recent years, it has become possible to reduce friction at seals also by applying grease dedicated to the seal with less viscosity change due to temperature, as explained in Section 3.2. Since viscosity change by temperature is small, the friction reduction effect due to grease characteristics can be expected not only for dynamic torque at room temperature but also for seal starting torque at low temperature.

In recent years, as a technique for reducing the lip friction coefficient, shown in Figure 11, a technology has also been developed for reducing friction by increasing the surface roughness of the seal lip/slinger and reducing the contact area. However, since the airtightness of the lip is a contradictory event, balancing between friction and airtightness should be considered when designing the lip.

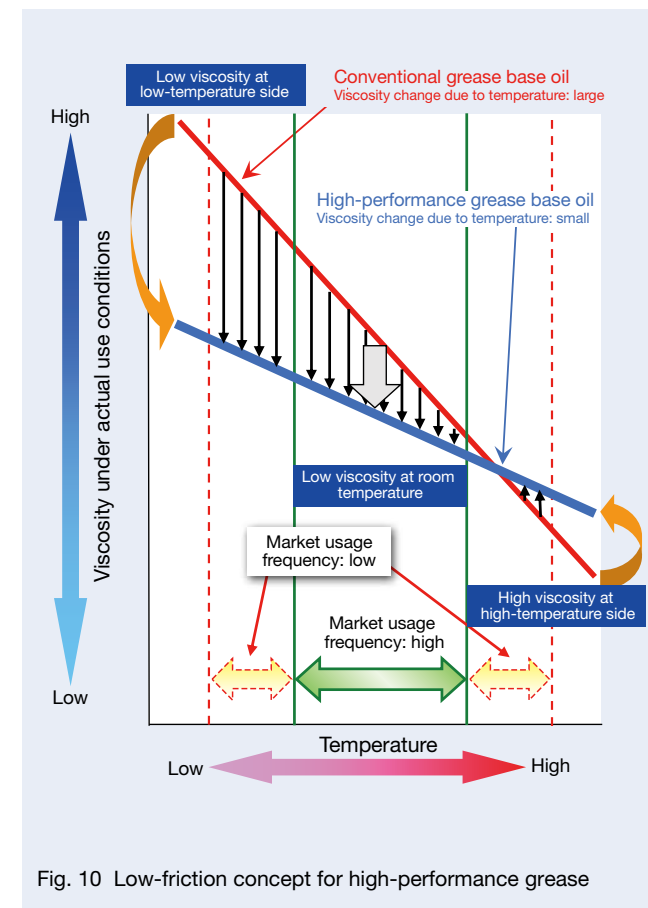


Fig. 10 Low-friction concept for high-performance grease

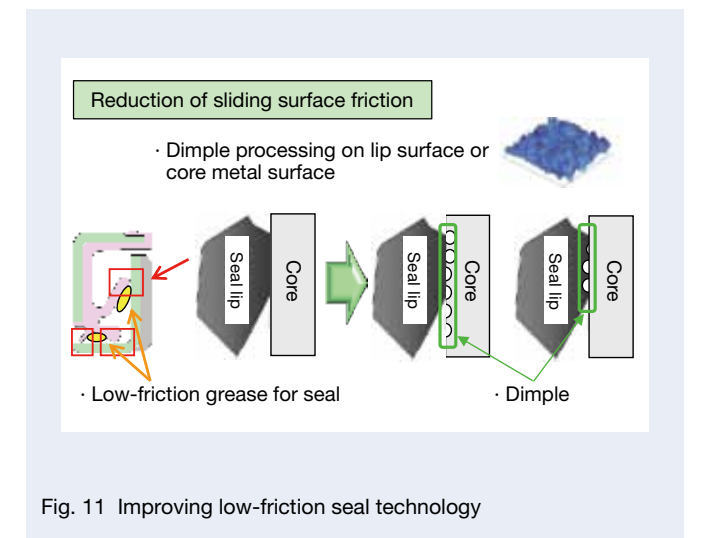


Fig. 11 Improving low-friction seal technology

4. Weight Reduction

The weight reduction effect of the outer ring and the hub shaft, shown in Figure 2, is particularly large. Figure 12 shows the strength analysis model with the wheel of the hub shaft. In order to reduce the weight of the bearing, it is necessary to take into consideration the strength of the actual parts such as wheels and brake discs as well as bearings. When it comes to the strength analysis of the hub shaft with peripheral parts, a simulation closer to actual vehicle operation becomes possible since the rigidity and contact condition of the wheels and brakes are also considered.

Regarding the outer race, roundness deformation of the bearing raceway surface when connected to a knuckle or beam axle is necessary. Since large roundness deformation of the outer ring raceway significantly shortens the rolling life, an advanced outer ring analysis considering the peripheral parts is also needed.

As mentioned above, in recent years, further weight reduction is required for not only the bearings alone but also peripheral parts, in order to further improve the accuracy of unit analysis, and NSK proposes a weight reduction design considering the peripheral structure.

5. High-rigidity (Improved Responsiveness)

Lastly, NSK's efforts on high rigidity (improved responsiveness) will be reported. Regarding steering stability (rigidity), conventionally, bearings have focused on the static rigidity in the high-load region mainly for the purpose of stability in cornering. However, in recent years, the demand level for steering stability, and straightness at the time of lane change, has been raised and, in particular,

transient responsiveness is required for hub unit bearings. It is conceivable that such demand is due to the increased contribution degree of hub unit bearings, which is related to the recent increase in vehicle body rigidity and improvement in suspension, and the request for high stability in future technologies such as automatic driving control.

In response to this demand and in order to determine primary factors for vehicle responsiveness, NSK has been conducting research and development while applying the knowledge it has gained through on-board/actual vehicle evaluation. In order to deal with transient responsiveness, accumulation of the above technical capability is indispensable.

6. Conclusion

This paper described NSK's latest technology based on recent trends of automobile society. It is anticipated that the demand on the global environment, such as improvement of CO₂ emissions and fuel economy, will accelerate rapidly from now on. In response to such market needs, hub unit bearings have responded to a number of demands such as low friction, weight reduction, high rigidity, and more. Meanwhile, for markets where demand is expanding markedly, such as in emerging markets, a reliable design that does not fail under harsh environments, which is the essence of hub unit bearings, continues to be required. Although reliability design and low-friction technology/weight reduction, etc. are basically contradictory performance requirements, we will continue to develop compatible specifications flexibly for each region and all needs in the future.

References

- 1) H. Ishikawa, "Technical Trends and Tribology of Hub Unit Bearing," *Journal of Japanese Society of Tribologists*, 54-9 (2009) 580-585.
- 2) T. Chiba, "Technical Trend of Hub Unit Bearing and Introduction of High Reliability Seal," *THE TRIBOLOGY*, 350 (2016) 17-19.
- 3) K. Yamaguchi, "Hub Unit Bearing Specification for Emerging Markets," *Proc. The 23rd lecture meeting of Tribology-Kenkyukai* (2012).



Takashi Sakaguchi

Low-Friction Technology for Tapered Roller Bearings

Yuujiro Saikawa

Automotive Powertrain Bearing Technology Center

Abstract

Recently, strengthened global regulations and a growing environmental consciousness have increased requests for the reduction of CO₂ emissions and improvement of fuel consumption.

In the case of transmissions for instance, reducing weight, increasing compactness, and decreasing friction loss are ongoing goals. In addition, there is a need to reduce friction in rolling bearings used in transmissions.

Generally, ball bearings or tapered roller bearings (TRBs) are used for rolling bearings that support the transmission shaft. Thus, the important issue is to find a way to reduce the friction of tapered roller bearings, which tend to have a lot of friction compared to ball bearings.

NSK has reduced friction loss by 70% compared with conventional bearings. In this article, we introduce the evolution of low-friction technology for TRBs through six generations.

1. Introduction

In recent years, due to the strengthening of global environmental regulations and rising environmental awareness, reduction of CO₂ emissions and improvement of fuel economy are strongly required for automobiles.

In addition to the reduction in size and weight of the transmission, lowering the viscosity of transmission oil for the purpose of reducing loss, etc. is progressing and the rolling bearings used in transmissions are requested to reduce friction¹⁻³⁾.

Ball bearings and tapered roller bearings are generally used for rolling bearings that support the shaft of transmissions, but the reduction of friction of tapered roller bearings, which have greater friction than ball bearings, has become an important issue.

In this report, an introduction will be made as to the evolution of low-friction technology for tapered roller bearings developed by NSK.

2. Friction of Tapered Roller Bearings

Regarding tapered roller bearings, Aihara reported the theory of frictional resistance⁴⁾, and in line with the theory NSK has been striving to reduce the friction. According to Aihara's report, friction factors of tapered roller bearings are classified into the following (1) to (4), as shown in Figures 1 and 2.

- (1) Rolling friction between inner and outer ring raceway surfaces and roller rolling surface: T_R
 - (2) Sliding friction between inner ring rib and roller end face: T_S
 - (3) Sliding friction between roller and cage: very low
 - (4) Stirring resistance of lubricating oil
- Among them, the two items of (1) Rolling friction

between inner/outer ring raceway surfaces and roller rolling surface: T_R and (2) Sliding friction between inner ring rib and roller end face: T_S occupy most of the friction factor of the tapered roller bearing. For this reason, conventionally, low friction of tapered roller bearings has been realized with the primary purpose of reducing these two frictions. On the other hand, in order to achieve further lowering the friction in the coming years, NSK is also introducing the developed product focusing on (4) the stirring resistance of the lubricating oil to the market.

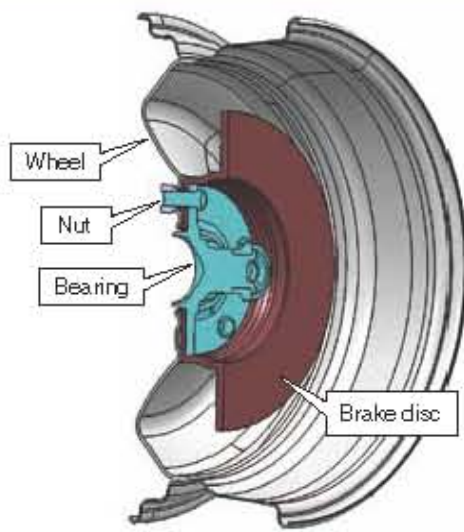


Fig. 12 Example strength analysis model of hub shaft with wheel

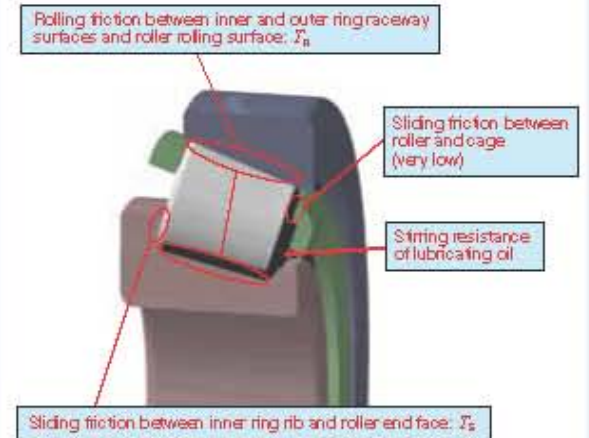


Fig. 1 Friction factors in TRBs

3 Evolution of Low-friction Technology

In order to realize low-friction technology for tapered roller bearings, NSK has made improvements from various viewpoints and has developed low-friction tapered roller bearings step by step from the first generation of such bearings in the 1980s to the sixth generation. The features of each generation are explained below.

3.1 The first generation

The sliding friction between inner ring rib and roller end face T_S can be calculated theoretically by the following Equation (1)⁵⁾.

$$T_S = e \cdot \mu_0 \cdot \cos\beta \cdot F_a \cdot f(A, t, \sigma) \quad (1)$$

- e : Contact position between roller end face and rib
- μ_0 : Coefficient of friction between roller end face and rib
- β : 1/2 of the tapered roller angle
- F_a : Axial load
- A : Oil film parameter
- t : Temperature
- σ : Roughness

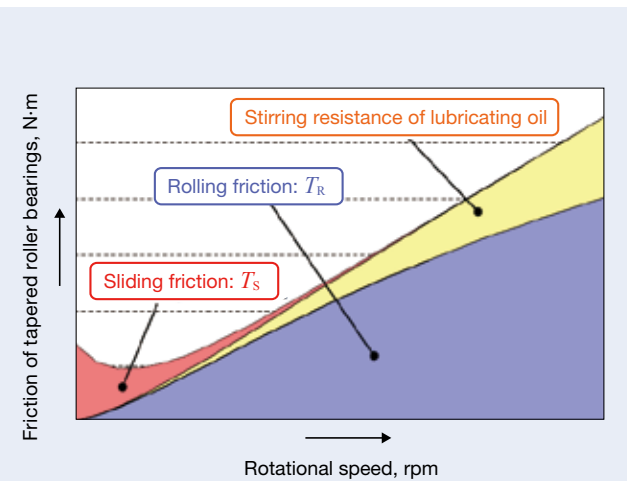


Fig. 2 Relationship between rolling friction T_R and sliding friction T_S

In the first generation, sliding friction between inner ring rib and roller end face: T_S is reduced by optimization of the contact position between roller end face and rib e (Figure 3) and the improvement of face roughness σ of the inner ring large-rib and roller end face.

Thereby, an approximately 20% reduction of friction was realized in the full rotation range compared with the standard specification (Figure 4).

3.2 The second generation

It is possible to find T_R rolling friction between inner and outer ring raceway surfaces and roller rolling surface from the following Equation (2)⁵⁾.

$$T_R = \frac{Z}{D_a} (R_e M_i + R_i M_e) \quad (2)$$

- Z : the number of rollers
- D_a : Diameter of roller
- R_e : Radius of outer ring raceway (Figure 5)
- R_i : Radius of inner ring raceway (Figure 5)
- M_e : Outer ring rolling resistance
- M_i : Inner ring rolling resistance

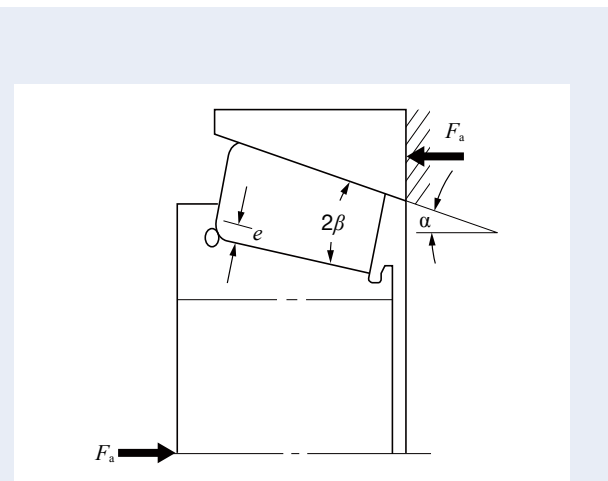


Fig. 3 Contact position e of cone back face rib and roller end face

In the second generation, the rolling friction T_R between the rolling contact surface and the inner/outer ring raceway surface was reduced by optimum design of bearing internal specifications.

From Equation (2), when designing the bearing internal specifications such as the contact angle α , the number of rollers Z , the roller length L_{WE} , the roller diameter D_a and the like with an emphasis on low friction, the other required functions for the bearing, such as life and rigidity, will be lowered (Table 1). Therefore, paying attention to the fact that tapered roller bearings are usually used in pairs, by optimizing the dimensions of the two bearings and the balance of the internal specifications, as shown in Figure 6, it became possible to achieve low friction technology while ensuring lifetime and rigidity. In addition to the features of the first generation, optimizing the bearing dimensions and internal specification with two bearings in combination made it possible to achieve a friction reduction of approximately 10% for the first generation (Figures 4 and 7)⁶⁾.

3.3 The third generation

By utilizing NSK's originally developed long-life materials and heat treatment technology (TF series)⁷⁾, reducing the size of bearings became possible. Also, a friction reduction was achieved for the second generation by reducing the size of bearings.

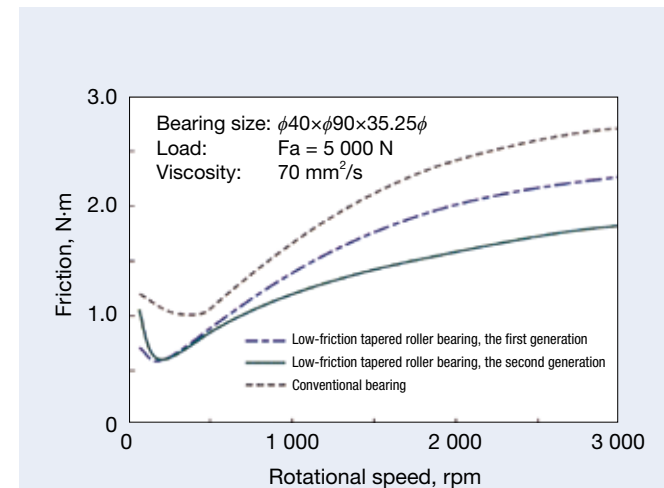


Fig. 4 Comparison of friction between a conventional bearing and low-friction bearings

Table 1 Relationship between specifications and performance

Performance	Bearing specification			
	Contact angle	Number of rollers	Roller length	Diameter of roller
Low friction	High	Few	Short	Large-diameter
Low surface pressure	Low	Many	Long	Large-diameter
Long-life	High	Many	Long	Large-diameter
Rigidity	Low	Many	Long	Large-diameter

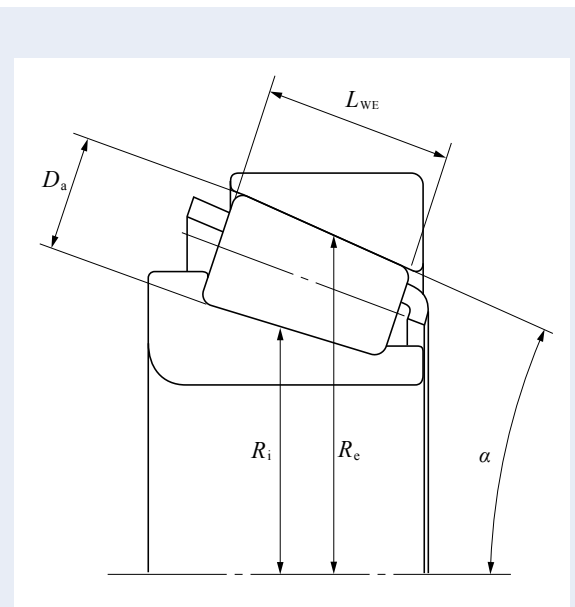


Fig. 5 Outer ring raceway radius R_e and inner ring raceway radius R_i

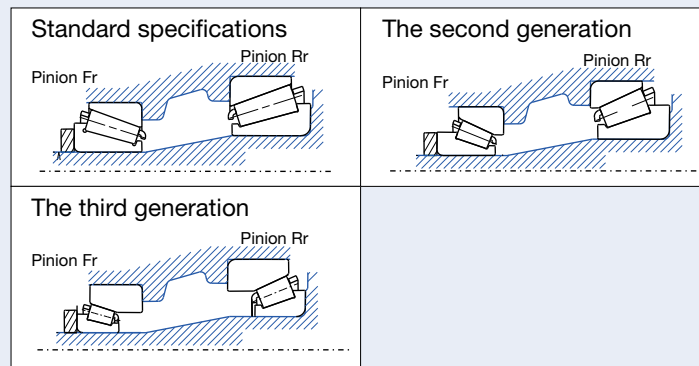


Fig. 6 Image of second generation and third generation bearings

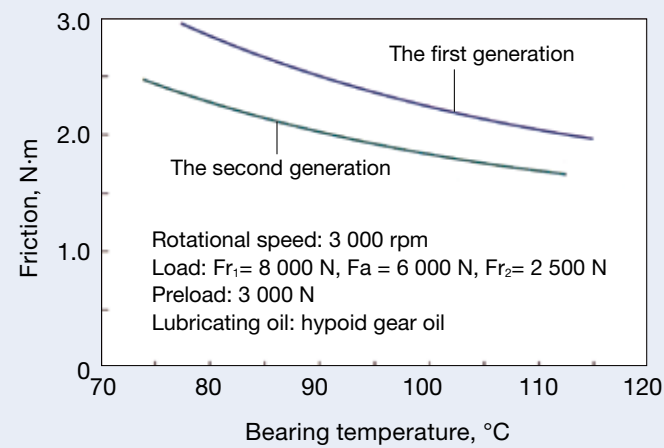


Fig. 7 Friction comparison of first generation and second generation paired bearings

3.4 The fourth generation

In order to achieve even lower friction for the third generation, if the reduction of the number of rollers, the reduction of the roller length, and the miniaturization are carried out, as shown in Figure 8, a phenomenon, known as edge loading, occurs in which the contact surface pressure increases locally.

As a countermeasure against this, it is possible to suppress the occurrence of edge loading by setting the inner and outer ring raceway surfaces to a barrel-shaped special crowning shape, as shown in Figure 9.

In the fourth generation, not only by suppressing edge loading, but also by optimizing the contact surface pressure distribution and reviewing internal specifications at the same time, an equal or longer lifetime was secured and rigidity with respect to conventional specifications in terms of life and support rigidity was supported, enabling

low friction⁸⁾.

Figure 10 shows the life evaluation results of the third generation and the fourth generation in a comparative manner. Both the regular load condition and the heavy load condition have a longer lifetime in the fourth generation than in the third generation. Figure 11 shows the rigidity of the third generation and that of the fourth generation in a comparative manner. Regarding the rigidity, the fourth generation is superior to the third generation. Furthermore, as shown in Figures 12 and 13, an approximately 20% reduction in weight and approximately 30% reduction in friction were achieved relative to those of the third generation.

As described above, in order to make the tapered roller bearing highly functional, it is a very effective technique to optimize the crowning shape.

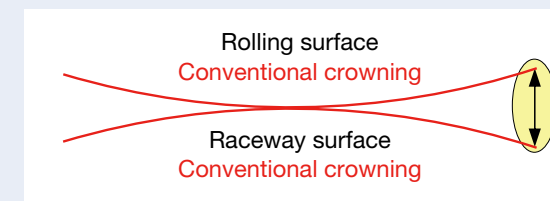
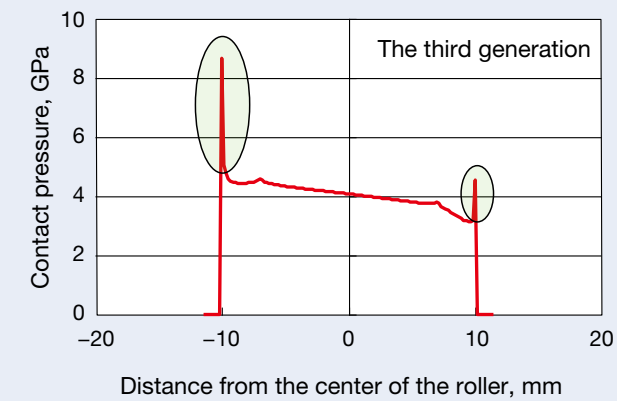


Fig. 8 Contact pressure between roller and ring raceway, and image of 3rd generation crowning

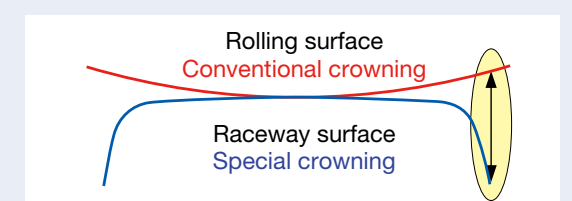
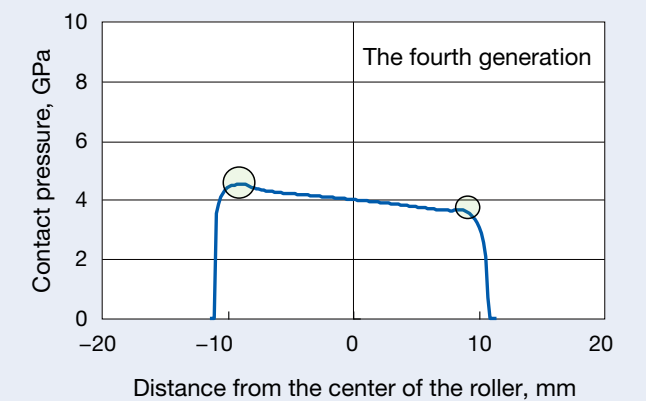


Fig. 9 Contact pressure between roller and ring raceway, and image of 4th generation crowning

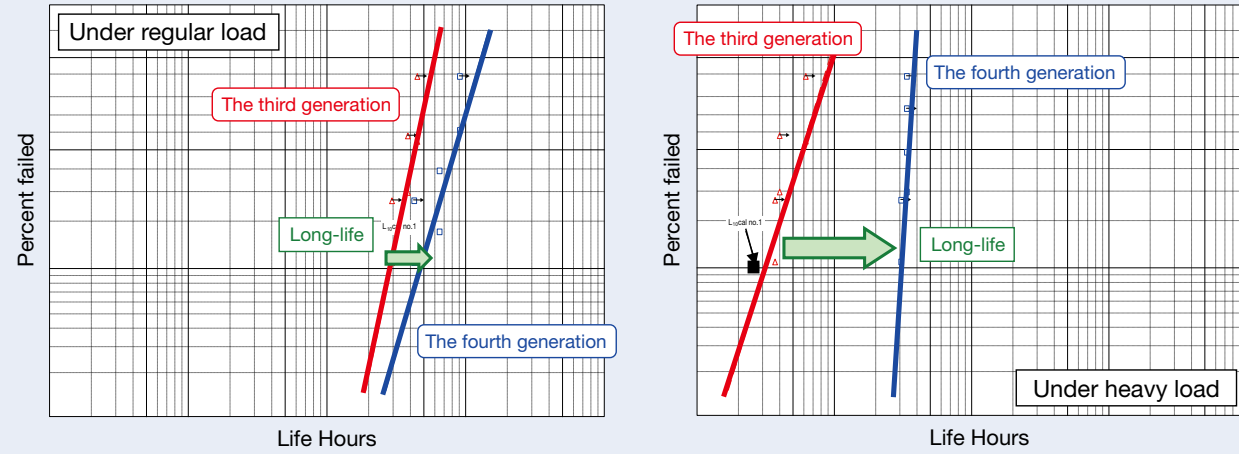


Fig. 10 Bearing endurance test results (3rd and 4th generations)

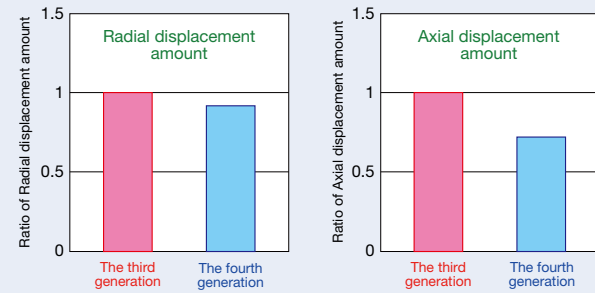


Fig. 11 Bearing rigidity (3rd and 4th generations)

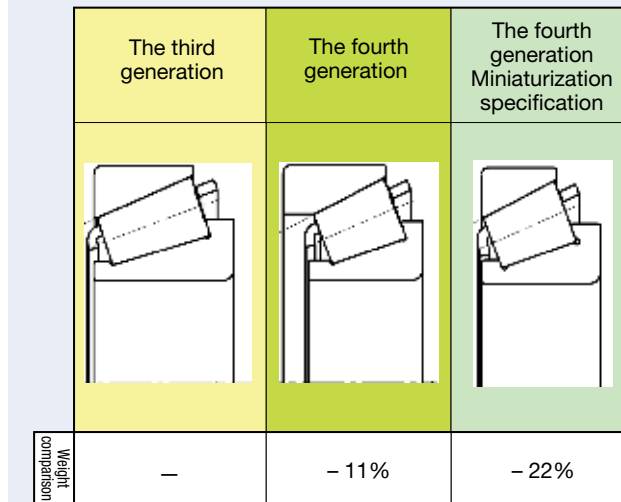


Fig. 12 Weight comparison (3rd and 4th generations)

3.5 The fifth generation

The first generation to the fourth generation have achieved stepwise friction reduction by reducing the mechanical losses due to sliding friction T_s and rolling friction T_R , and by reducing the size by long-life technology.

In order to further reduce friction, attention was paid to the stirring resistance of the lubricating oil, which is the third largest friction generation factor, after T_s and T_R . A tapered roller bearing with a plastic cage capable of reducing this stirring resistance was developed and applied to the fifth generation.

In order to reduce the stirring resistance, it is important to control the amount of lubricating oil flowing into the bearing, and the shape of the plastic cage was determined based on the oil flow analysis result. Figure 14 shows two features of the developed plastic cage. The first

feature is to reduce the oil inflow area on the small end side by narrowing the space between the cage and the inner ring small rib, and the second feature is to fill the internal space with the cage. As a result, it becomes possible to supply the required minimum amount of oil between the rolling elements and the raceway ring, and an approximately 20% reduction in friction was achieved in the high-speed rotation region only by applying the plastic cage (Figure 15)⁹⁾. It is to be noted that since the shape of this cage is complicated, injection molding using a plastic material is adopted for manufacturing, thereby increasing the degree of design freedom.

In recent years, the use of low viscosity lubricating oil has been increasing for the purpose of improving the efficiency of transmissions, but the use of a plastic cage further reduces the amount of oil supplied to the interior of the bearing, which makes it difficult to secure the necessary minimum amount of oil film. In such a case, seizure of the tapered roller bearing may occur on the sliding surface of the roller end face and the inner ring large-rib portion. Therefore, the oil pool shown in Figure 14 was provided in the cage to improve the lubricity of the end face of the roller and the large-rib portion of the inner ring. As a result, it became possible to retain the lubricating oil on the end face of the roller, and the seizure resistance of the roller end face and the large-rib portion was improved with respect to the conventional bearing using the iron-made cage (Figure 16).

In the fifth generation tapered roller bearing, by utilizing the high moldability of the plastic cage, sufficient lubricating oil was secured in the necessary portion, and it was possible to supply only the minimum required amount of lubricating oil that is required in other places. This resulted in achieving seizure resistance and improving the low-friction technology.

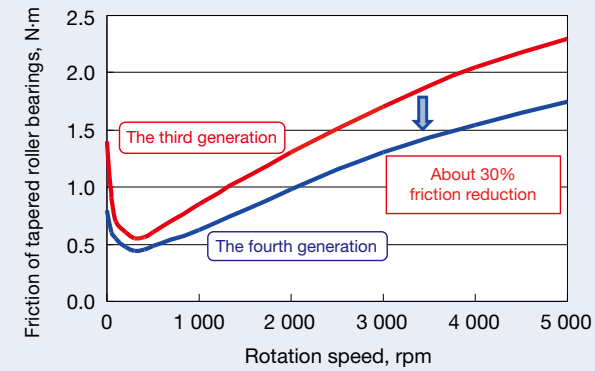


Fig. 13 Bearing friction measurements (3rd and 4th generations)

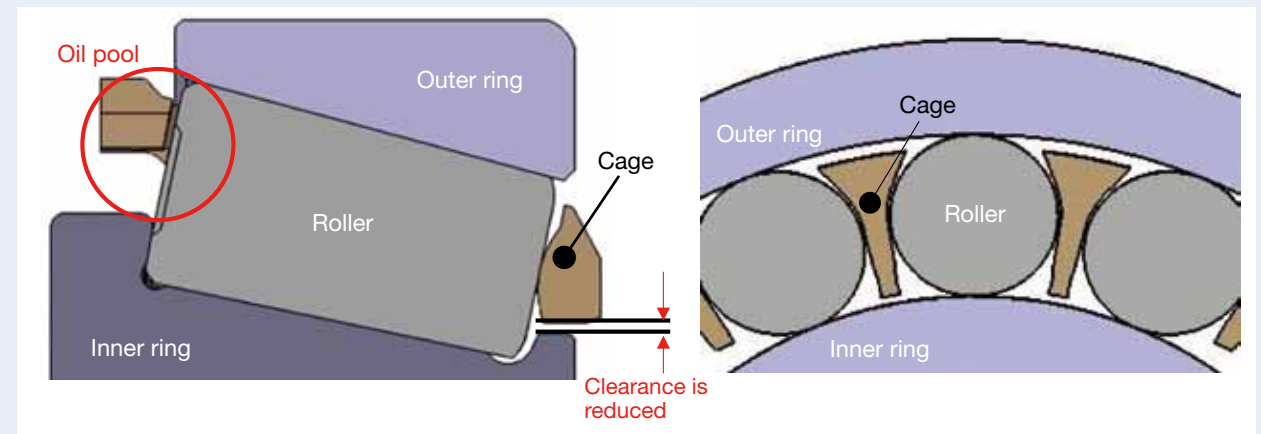


Fig. 14 Cross section of a TRB with a plastic cage

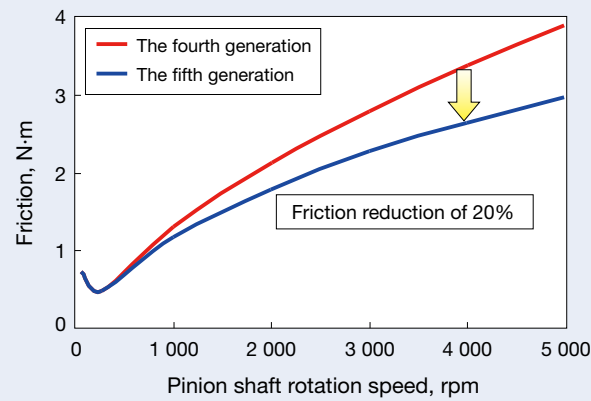


Fig. 15 Friction measurements (4th and 5th generations)

3.6 The sixth generation

Tapered roller bearings are generally used on the high-torque output side (counter shaft or differential shaft) of transmissions. Since the power produced by an engine undergoes speed reduction within the transmission, the rotation speed of the output shaft is lower than that of the input shaft. When the tapered roller bearing rotates at low speed, the sliding friction between inner ring rib and roller end face: T_s shown in Figure 1 and Figure 2 greatly affects overall friction in the bearing. As mentioned before, in the first generation, sliding friction between inner ring rib and roller end face: T_s is reduced by optimization of the contact position between roller end face and rib and the improvement of roughness of the inner ring large-rib and roller end face.

In the sixth generation, in which further reduction of the sliding friction T_s is targeted, by further improving the roughness of the inner ring large-rib and roller end face, a maximum of a 60% reduction in friction in the low speed range and a maximum of a 20% reduction in friction in the entire rotation speed range were achieved (Figure 17). Compared to the 1980s when the development of the first generation was conducted, the processing technology has been improved, which makes it possible to further improve the roughness of the inner ring large-rib and the roller end face.

As this developed product is able to reduce the friction in the low speed range without having to change bearing size, the number of rollers, and shapes of rolling contact surface and raceway surface, it can be expected to apply to various transmissions. In addition, when low viscosity oil is used, experimental results show that a low-friction effect is obtained even in the high speed region, and it is a technology suitable for low viscosity lubrication environments expected to increase in the future use.

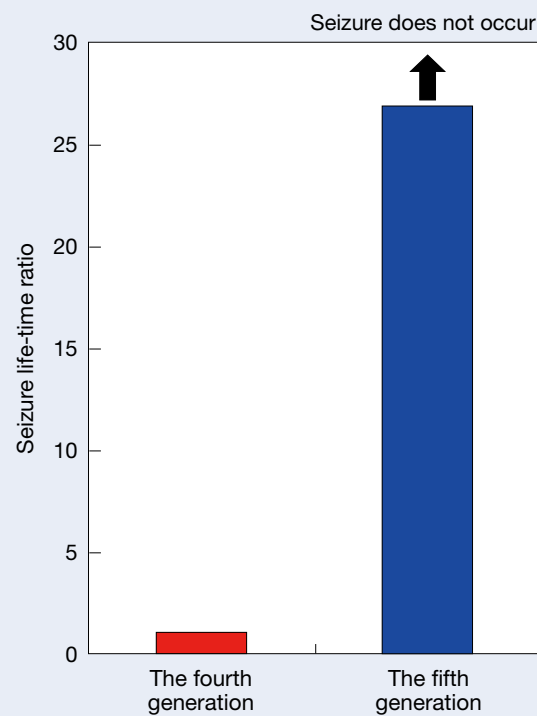


Fig. 16 TRB seizure life (4th and 5th generations)

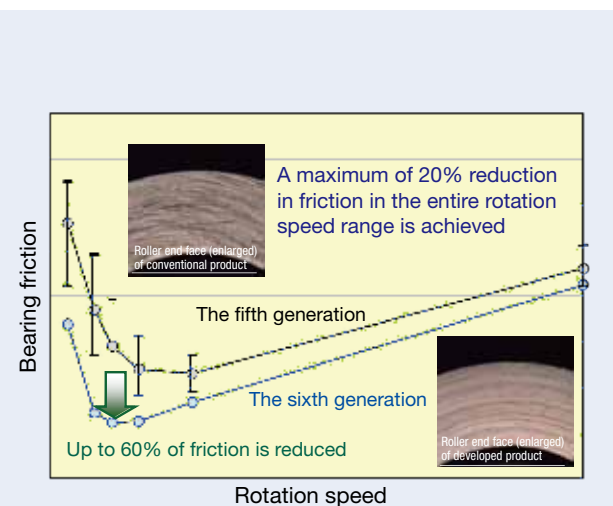


Fig. 17 Friction measurements (5th and 6th generations)

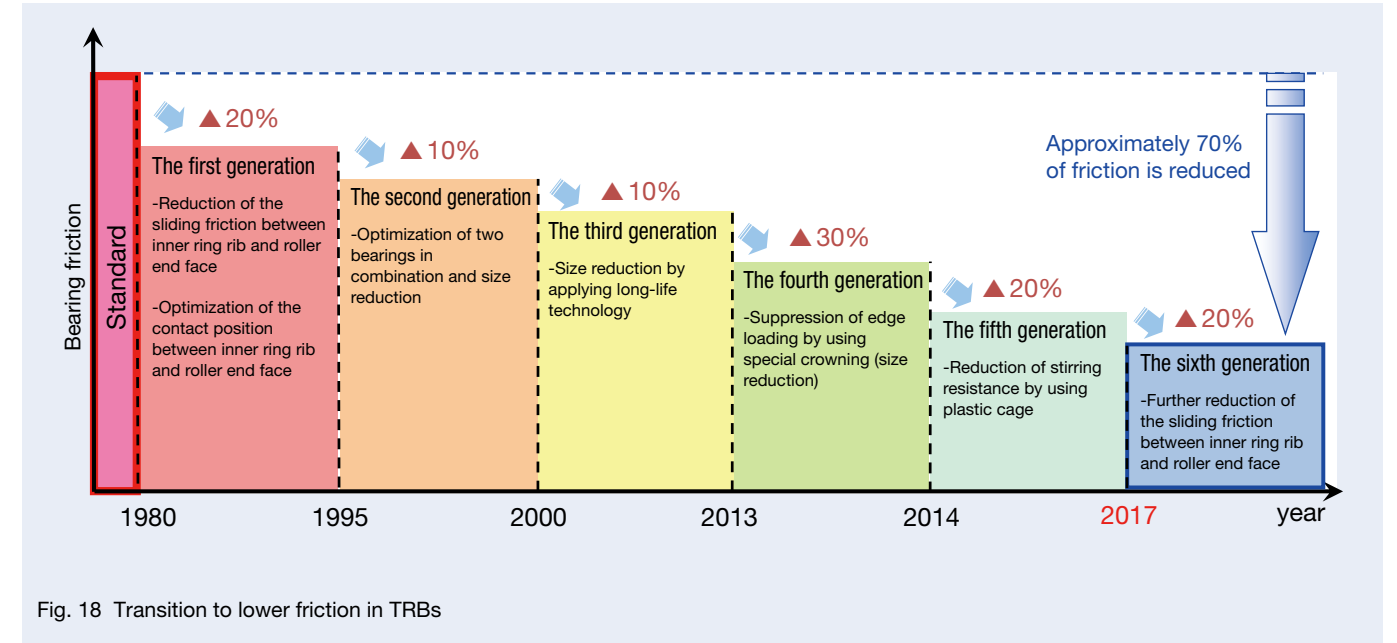


Fig. 18 Transition to lower friction in TRBs

4. Conclusion

This report has introduced the evolution of low-friction technology for tapered roller bearings developed by NSK.

Originally, when reducing friction, other functions such as life and rigidity were also lowered, but the reduction of friction while maintaining durability has been achieved by optimization of internal specifications, utilization of materials and heat treatment technology, improvement of crowning, and controlling the flow of lubricating, as are seen in the first to sixth generations. For tapered roller bearings that are applied to the development results of all of the first to sixth generations, it is possible to reduce the friction by up to 70% of the standard specification (Figure 18).

Looking forward, we will continuously contribute to improving fuel economy of automobiles by using NSK's four core technologies (tribology, material technology, analytical technology, and mechatronics technology) to promote the development of new products that meet market needs.

References

- 1) Y. Hayashi and K. Ikezawa, "The Latest Technology of Drivetrain Bearing contributing to Better Fuel Economy," *Journal of Society of Automotive Engineers of Japan*, 64-11 (2010) 65-70.
- 2) T. Ootsubo and S. Kadokawa, "Trends and New Technologies of Automatic Transmission Bearings," *NSK Technical Journal*, 677 (2004) 46-53.
- 3) T. Asami and T. Saito, "High Efficiency Tapered Roller Bearings," *Proc. 2013 JSAE Congress (Spring)*, 73-13 (2013) 7-10.
- 4) S. Aihara, "Friction of Roller Bearings and EHL Viscous Rolling Resistance," *NSK Technical Journal*, 649 (1988) 1-5.
- 5) "Technical Report," NSK Ltd. CAT. No. 728h (2013) 168-171.
- 6) "Low Frictional Torque Tapered Roller Bearing," *NSK Technical Journal*, 672 (2001) 76-77.
- 7) Y. Murakami, N. Mitamura and K. Furumura, "Long Life Super TF & Hi-TF Bearings under Severe Lubrication Conditions," *NSK Technical Journal*, 652 (1992) 9-16.
- 8) H. Takata, S. Suzuki and E. Maeda, "Experimental Study of Fatigue Life of Profiled Roller Bearings," *NSK Technical Journal*, 653 (1992) 1-7.
- 9) T. Saito, H. Maejima and T. Hiramoto, "Development of New-Generation Low-Frictional-Torque Tapered Roller Bearings," *NSK Technical Journal*, 685 (2012) 8-13.



Yuujiro Saikawa

CFD Analysis of Tapered Roller Bearings and Ball Bearings for Reducing Agitation Torque

Yingyi Wen, Dr. Shinji Miyata, NSK Ltd., Fujisawa, Japan

Abstract

There is a growing need to reduce torque losses in bearings that are used in automotive power transmissions for improving fuel economy. Agitation Torque associated with oil lubricant are one important factor of torque losses under sufficient lubricating conditions. To reduce agitation torque, the internal design of rolling bearings has been optimized through the use of conventional experiments, verification, and product development. Aiming for greater efficiency and quicker development, a calculation program for predicting the amount of agitation torque and the tendency of lubricant oil flow passing through various parts of tapered roller bearings and ball bearings was developed using computational fluid dynamics (CFD) analysis. Torque losses and quantities in ordinary sized bearings, such as those that are found in automotive differentials and transmissions, were measured with test machines under sufficient lubricating conditions. Calculated values using CFD analysis were quantitatively in good agreement with measured results in the experimental range. Thus, the authors conclude that CFD analysis is capable of simulating tendencies of varying agitation torque and distribution of oil. Finally, using this analysis method, the influence of bearing cage design on oil flow and agitation torque can be reliably investigated, resulting in further development of low-torque tapered roller bearings and ball bearings. Oil flows in these bearings are controlled and optimized by specially shaped plastic cages. Thus, agitations torque is reduced significantly in comparison with conventional products.

1. Introduction

As a response to the issues of global warming and energy conservation, automobile manufacturers are improving the fuel economy of vehicles for the purpose of saving finite resources of fossil fuels and reducing CO₂ emissions. Highly efficient power trains are being pursued by weight savings and loss reduction of each component. Thus, there is a growing need to reduce torque losses in bearings that support power transmissions gears in automotive transmissions and differentials^[1].

To reduce torque losses, bearing manufactures have been focusing on rolling and sliding friction losses. The shape and roughness of raceway surfaces and sliding contact surfaces were optimized using kinematic performance analysis of bearings^{[2][3][4]}. However, losses that are caused by agitation torque were seldom taken into consideration. While great reductions in rolling and sliding torque are achieved, agitation torque becomes an important factor of the total torque losses in bearings, especially under sufficient lubricating conditions. For example, in differentials, where a large amount of high viscosity oil is used as lubricant, the agitation torque of tapered roller bearings accounts for up to 26 % of the total torque^[5]. To reduce torque losses of bearings, it is necessary to cut agitation torque as well.

Matsuyama et al^{[6][7]} experimentally examined the influence of oil flow on torque, and developed a low-torque tapered roller bearing by cutting oil flow passing between the inner ring and the cage. However, the potential adverse effect of less oil supply to the contact surfaces on the ribs of inner ring was not discussed. Nevertheless, so

far, efforts on reducing agitation torque were taken most by means of conventional experimental trials. To improve the efficiency of development of low-torque bearings, CFD analysis can be considered a good solution.

In this Paper, a predicting method of the agitation torque and the oil distribution tendency in tapered roller bearings and ball bearings was developed using CFD analysis. With this analysis method, the influence of bearing cage design on oil flow and agitation torque was investigated, resulting in further development of low-torque tapered roller bearings and ball bearings.

2. CFD Analysis of Tapered Roller Bearings

2.1 CFD analysis technique

Generally, the single-phase flow model and the assumption of uniform flow of constant velocity are preferred in CFD calculations of agitation torque. In reality, oil and air are stirred by rolling elements and form free surface flows within the bearing. In order to precisely simulate this flow and analyse the tendency of such flow in detail, a gas-liquid two-phase flow model was adopted, and the volume-of-fluid (VOF) method was used. The VOF method is a numerical technique for tracking and locating the free surface. In this case, it is expected to be able to capture the shape of the air-oil interface with high accuracy. Based on a general-purpose CFD tool, a program for calculating agitation torque and oil quantity distribution was developed and incorporated into the analysis software. In the program, the expression for computing flow-induced resistance (i.e. agitation torque) on wall cell faces is as follows:

$$\vec{T} = \vec{R}_b \times (\vec{F}_t + \vec{F}_n) = \vec{R}_b \times \left(\tau_\omega \frac{\vec{v}_{par}}{|v_{par}|} + p\vec{m}_b \right) A_b \quad (1)$$

Where \vec{T} is the agitation torque vector, \vec{R}_b is the radius vector from the rotational axis to the centre of a wall cell, \vec{F}_t is shear force, \vec{F}_n is pressure force, τ_ω is shearing stress, \vec{v}_{par} is the velocity vector component parallel to the wall at the centre of a near-wall cell, p is pressure, \vec{m}_b is the outward-pointing unit vector normal to the wall, and A_b is the wall cell face area. Only the circumferential component of flow-induced force is considered in the calculation. The agitation torque of bearings equals to the sum total of the torque on wall cell faces.

In this paper, CFD analyses of the oil flow inside bearings are conducted using this program

2.2 Experimental validation

Generally in CFD analysis, the mesh size, calculation model, and parameters greatly affect the accuracy of the results. Therefore, verification experiments are required when developing a new analysis method. In this paper, the torque losses of tapered roller bearings for automotive differentials were measured using a torque testing machine (see Figure 1) under sufficient lubricating conditions. Then the measured results were compared to calculated values for verification. The bearings used in the experiment have the same characteristics (which are shown in Table 1) except for the shape of the cages. The three different cage shapes are presented in Figure 2, and the test conditions are shown in Table 2. Figure 3 shows the comparison of torque between calculation and experiment. The rolling torque of the bearings is calculated using an original program of kinetic friction

analysis^[8]. The calculation equation used in this program took EHL rolling resistance into consideration and was carefully examined for nearly two hundred tapered roller bearings^[8]. The comparison result indicates that analysis results are consistent with measured values qualitatively. Thus, we concluded that the agitation torque of tapered roller bearings can be predicted with practical accuracy using the newly developed analysis method.

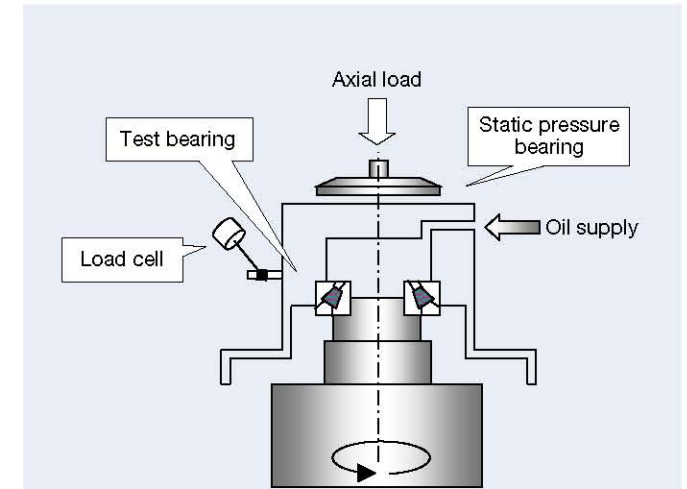


Fig. 1 Torque testing machine for tapered roller bearing

Table 1 Characteristics of the bearings

Inner diameter (mm)	45
Outer diameter (mm)	95.25
Width (mm)	35
Contact angle (°)	22.5
Aver. roller diameter (mm)	12.2



Fig. 2: Cage shapes used in the experiment

Table 2: Test Conditions

Rotation speed (min ⁻¹)	2 000
Oil temperature (°C)	60
Oil viscosity (mm ² /s@40°C)	68
Oiling quantity (L/min)	0.5

2.3 Development of low-torque tapered roller bearing

Compared to ball bearings of equal size, tapered roller bearings have a large load capacity and the advantage of high rigidity. They are widely used to support rotational motion in vehicles. However, they also have the disadvantage of high friction torque and a great deal of heat generation. To avoid the negative influence of heat generation on the contact surfaces, it is essential to ensure the supply of oil while reducing agitation torque of tapered roller bearings.

2.3.1 Investigations of cage design for reducing agitation torque

According to equation (1), reducing agitation torque means to reduce shearing stress and Pressure from oil, and the surface area in contact with oil. Therefore, from the perspective of CFD analysis, it is considered effective to cut down the amount of oil for reducing agitation torque. On the other hand, the results of analysis shows that tapered roller bearing works as a pump when rotated

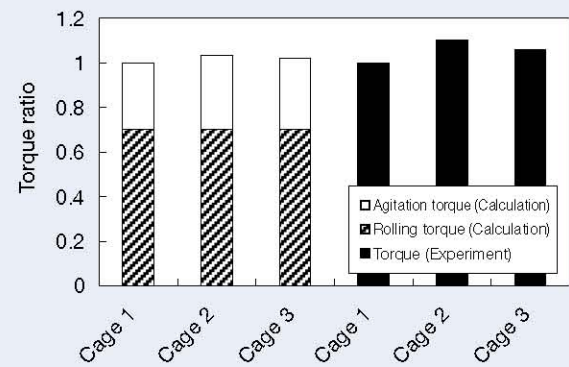


Fig. 3 Comparison of torque of tapered roller bearings

due to centrifugal force. Consequently, oil flow runs through the bearing from the small rib to the large rib of the inner ring. In addition, negative pressure is generated when rollers are rotating inside a tapered roller bearing, and a force that draws in oil occurs. Based on these concepts, new shapes of cages were devised, as shown in Figure 4.

Table 3 Calculation Conditions

Rotation speed (min ⁻¹)	2 000
Oil temperature (°C)	60
Oil viscosity (mm ² /s@40°C)	68
Oiling quantity	Steady oil-level height

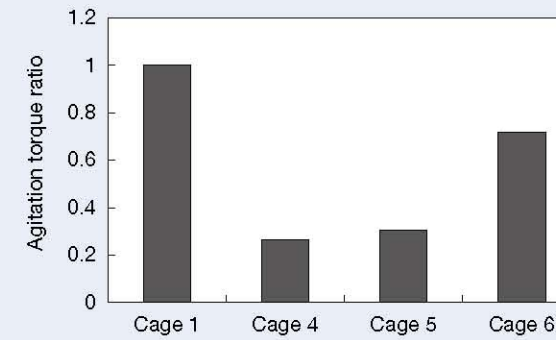


Fig. 5 Comparison of agitation torque of tapered roller bearings with different cages

The effects of these cages were examined by CFD analysis. Table 3 shows the calculation conditions. The results of agitation torque are shown in Figure 5. Designs of cages 4, 5, 6 were proven to be effective in torque reduction. Cage 4 narrows the inlet of oil near the small rib, and cage 5 form labyrinths around the inlet of oil, both of which prevent oil from flowing into the bearings (see Figure 6). As a result, agitation torque drops significantly. The design of cage 6 reduces the space inside the bearing, hence restricts the inflow of oil that is drawn by the negative pressure mentioned above (see Figure 7).

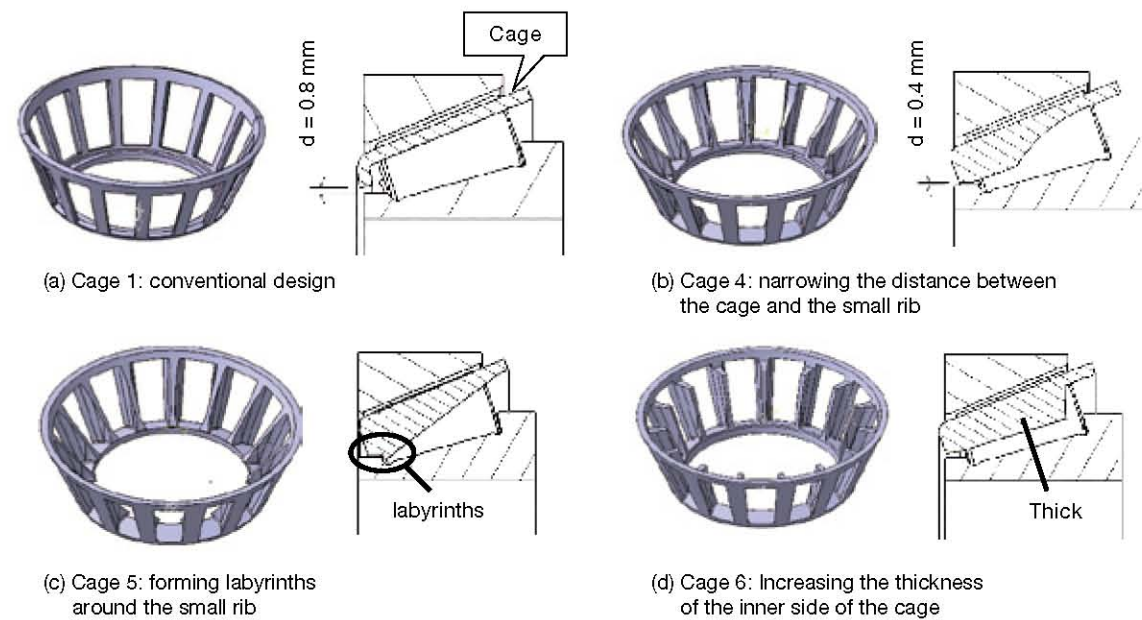


Fig. 4 Cage shapes for reducing agitation torque

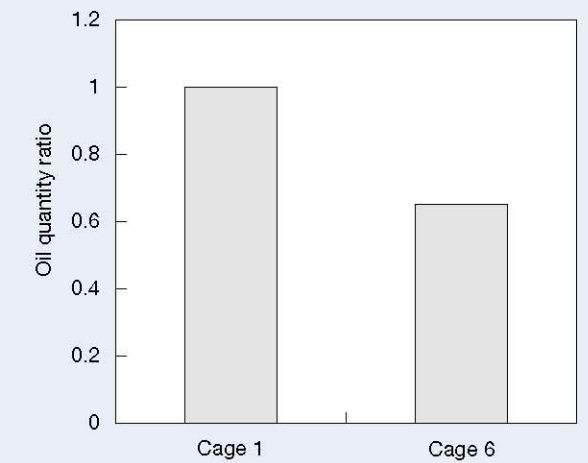


Fig.7 Comparison of oil quantity running through the whole bearing

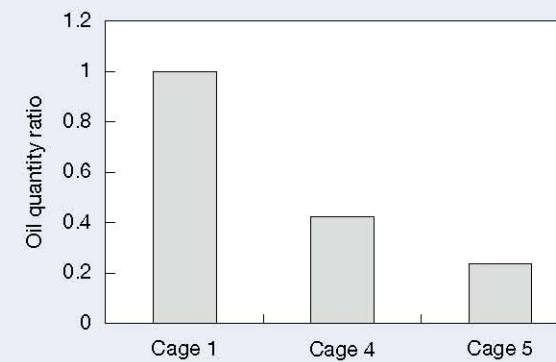


Fig. 6 Comparison of oil quantity running through the whole bearing

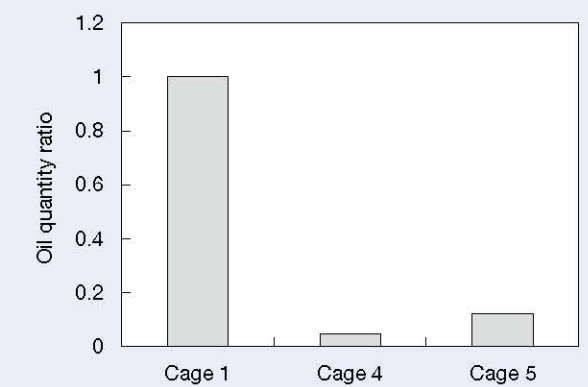


Fig. 8 Comparison of oil quantity running through the inner ring side of the bearing

Conversely, as shown in Figure 8, simply narrow the inlet of oil around the small rib of the inner ring will significantly reduce the oil flow running through the inner ring side of the bearing (i.e. oil flow running between the cage and the inner ring; see Figure 9). This may cause a great drop of the amount of oil around the sliding contact surfaces on the large rib of the inner ring. In the case of insufficient oil supply for the contact part of the large rib, the heat generated by sliding friction becomes excessive, which may result in heat-seizure^[9].

To avoid heat-seizure, cage shapes that may help

maintain oil supply around the large rib were examined using CFD analysis. According to the calculation results, three kinds of cage designs are effective: A. to narrow the distance between the cage and the outer ring by increasing the thickness of the outer side of the cage (as shown in Figure 10 (b)); B. to widen the inlet of oil by enlarging the distance between the cage and the small rib of the inner ring, and C. to widen or straighten the outlet of oil (e.g. shortening the cage, as shown in Figure 10 (c)). As shown in Figure 11 (a), the design of A makes it difficult for oil to enter the outer side of the bearing and therefore

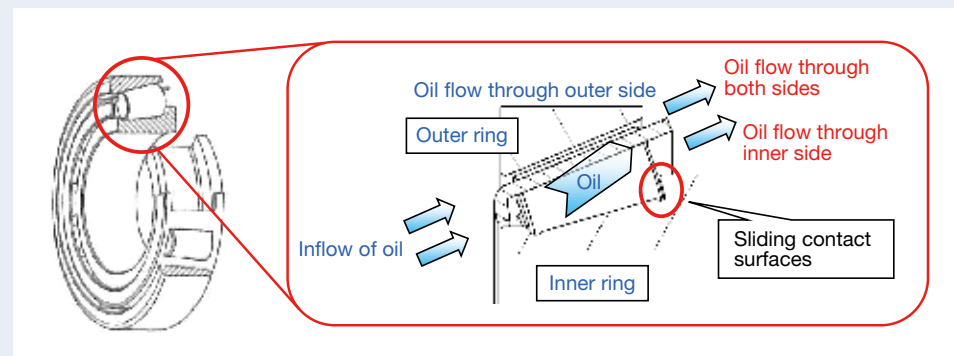


Fig. 9 Definition of oil flow running through the inner/outer ring sides of the bearing

has the effect of inducing oil to the inner side. Design C widens the outlet of oil, thereby increases the amount of oil flowing out from the bearing. As a result, the quantity of oil running through the whole bearing is increased, while the amount of oil running through the inner ring side of the bearing remains the same, as shown in Figure 11 (a). Moreover, the decrease of surface area of the cage in contact with oil leads to a reduction in agitation torque (shown in Figure 11 (b)).

For the purpose of reducing agitation torque while ensuring proper lubrication for the large rib of the inner

ring, a low-torque tapered roller bearing is developed. From the results of the investigation mentioned above, the cage designs of cage 6, cage 7 and cage 8 were chosen and applied to the low-torque bearing. Figure 12 represents the shape of the newly developed bearing. More specifically, in the new bearing, a) the distance between the cage and the outer ring is much narrower than that of the conventional bearing shown in Figure 10 (a), (b) cage bars are thickened in the radial direction and (c) shortened in the axial direction, and thereby forms an oil path for guiding oil to the large rib of the inner ring.

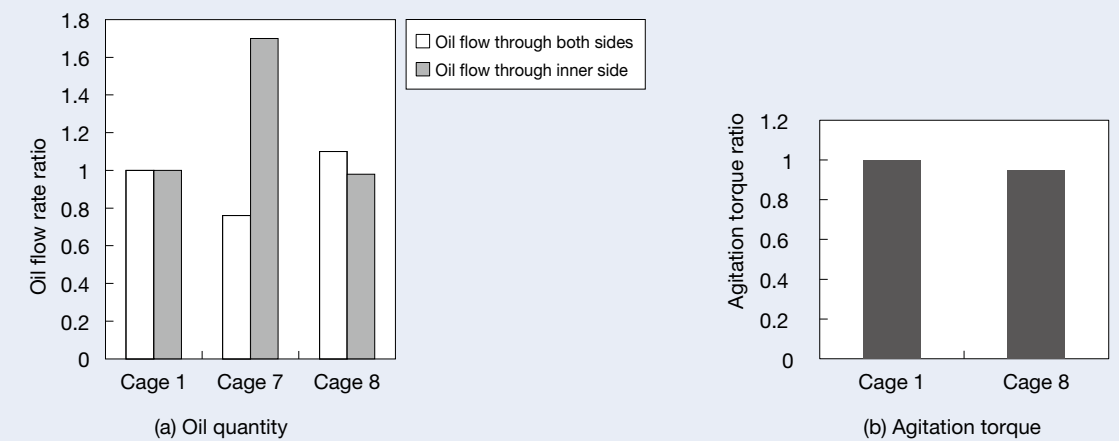


Fig. 11 Comparison of oil quantity and agitation torque

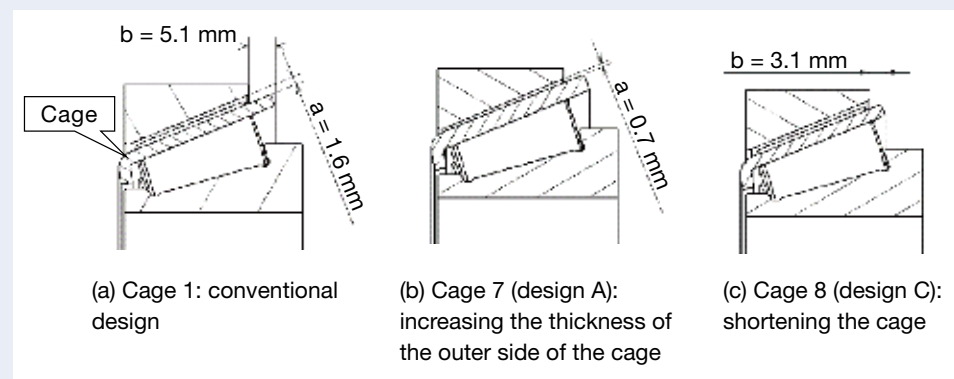


Fig. 10 Cage shapes for maintaining oil quantity

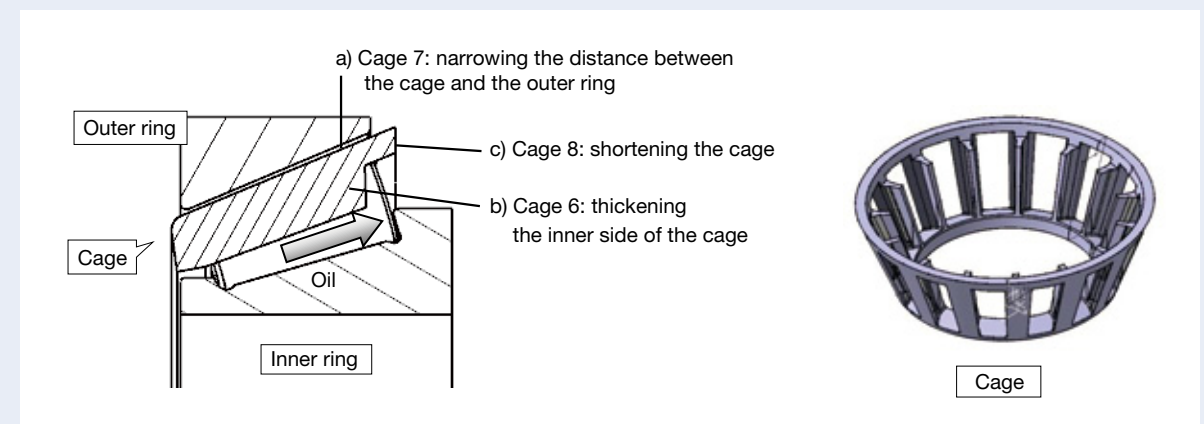


Fig. 12 Newly developed low-torque bearing

2.3.2. Verification of the effect of the low-torque tapered roller bearing

The effect of the low-torque roller bearing is examined using CFD analysis. Then the Torque losses and the amounts of oil running through the inner/outer ring sides of the bearing were measured on the torque testing machine shown in Figure 1. The trial piece of the cage in the newly developed bearing is made of plastic.

Figure 13 shows the comparison of measured values and calculation results of torque between a conventional bearing (the same as the bearing shown in Figure 4 (a)) and the low-torque tapered roller bearing. The two bearings have the same characteristics (which are shown in Table 1) except for the cages. Under the same test conditions as shown in Table 3, the torque of the newly developed bearing is 10 % lower than that of the conventional one. Based on the analysis result, it can be presumed that the low-torque bearing reduces agitation torque by about 50 %. As shown in Figure 14, in the newly developed bearing, although the quantities of oil running through the outer ring side and the whole bearing are less than those of the conventional one, the amount of oil running between the cage and the inner ring does not drop significantly. This means that the low-torque bearing supplies an equivalent amount of oil to the large rib of the inner ring as the conventional one does, while reducing excess oil in the bearing and halving the agitation torque, which is confirmed by CFD analysis and experiment.

3. CFD Analysis of Ball Bearings

Compared to tapered roller bearings, the torque losses of ball bearings are small. Therefore, they are increasingly used to support motors and power transmission gears in hybrid cars [10]. Yet greater reduction of torque is required for bearings used in hybrid cars. However, to date, it has been considered difficult to further reduce torque losses in ball bearings. In this Paper, a low-torque ball bearing for hybrid vehicles is developed using CFD analysis. It is proven that this ball bearing can cut agitation torque and thereby reduces the total torque loss significantly in comparison with conventional products.

3.1 Examination of CFD analysis method

To examine the CFD analysis method for ball bearings, the torque losses of two ball bearings used in hybrid cars were calculated using the program mentioned above. Then the calculated results were compared to measured values for verification. The measured values of agitation torque were calculated using the method shown in Figure 15. When oiling quantity is close enough to zero, the measured value of running torque of the bearing may be considered the same as the sum of rolling and sliding friction torque. Thus, when oiling quantity is not zero, the value of running torque minus the sum of rolling and sliding friction torque equals the value of agitation torque.

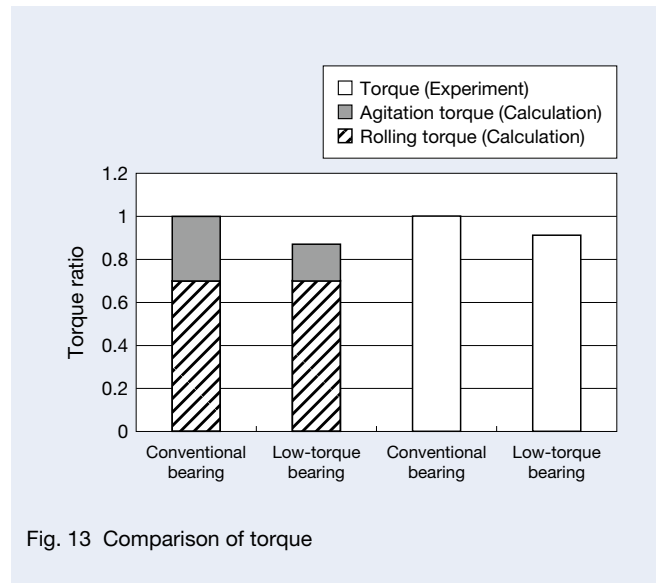


Fig. 13 Comparison of torque

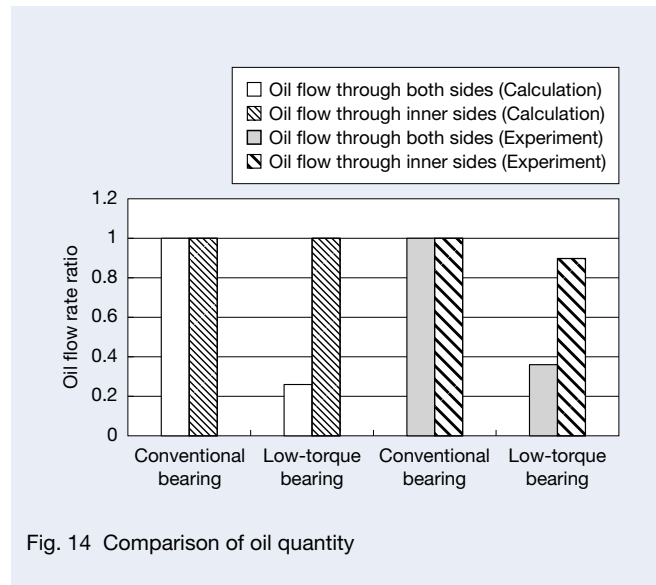


Fig. 14 Comparison of oil quantity

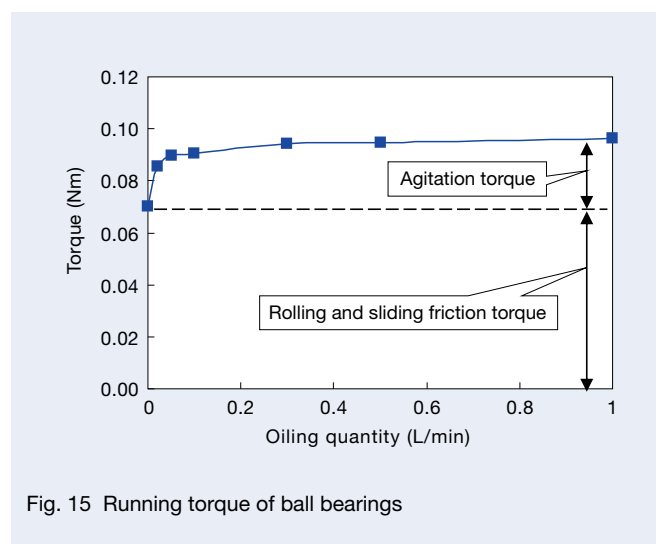


Fig. 15 Running torque of ball bearings

The two bearings used in the examination are presented in Figure 16. Test conditions are shown in Table 4. The testing machine used in the experiment is shown in Figure 17. Figure 18 shows the comparison of agitation torque between CFD analysis and experiment. Calculated values are qualitatively in good agreement with measured results. Thus, it seems reasonable that the CFD analysis method can predict the agitation torque of ball bearing qualitatively with practical accuracy.

Table 4 Test Conditions

Rotation speed (min ⁻¹)	3 000
Oil temperature (°C)	50
Oil viscosity (mm ² /s@40°C)	23.6
Oiling quantity (L/min)	1

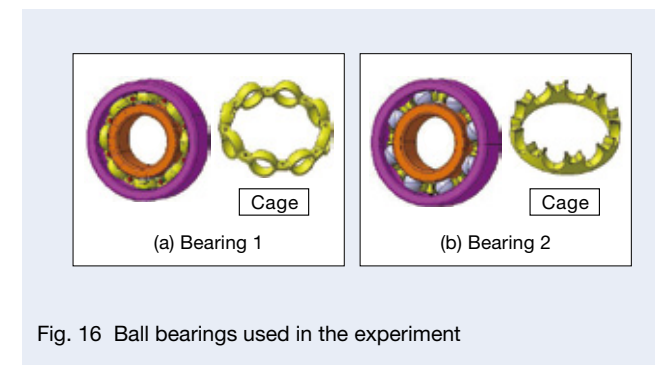


Fig. 16 Ball bearings used in the experiment

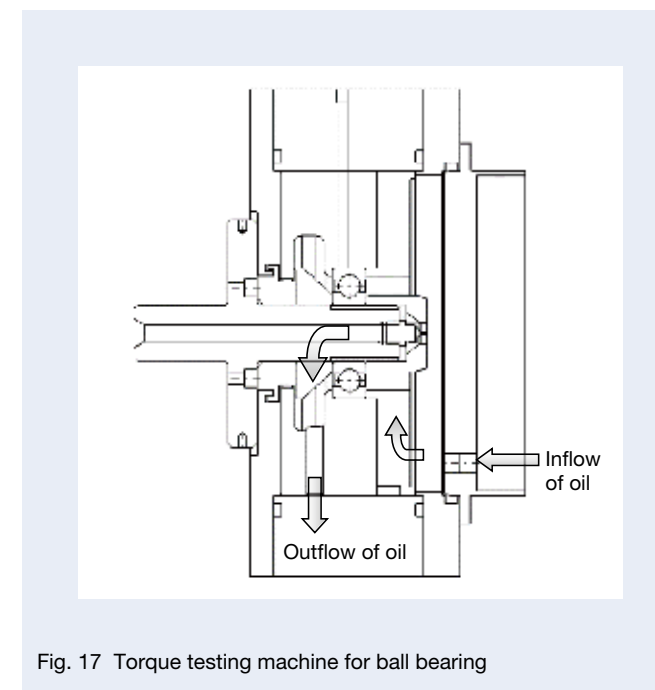


Fig. 17 Torque testing machine for ball bearing

3.2 Development of low-torque ball bearing

In general, the typical cages used in ball bearings can be divided into iron pressed cages and snap plastic cages, as shown in Figure 19. In the torque measurement mentioned in 3.1, an iron pressed cage was used in bearing 1, and a snap plastic cage was used in bearing 2 (see Figure 16). The bearings have the same characteristics except for the cages. According to the results of analysis and experiment mentioned above, the agitation torque caused by snap plastic cages is lower than the torque caused by iron ones. So, we focused on plastic cages and attempted to optimize the cage shape to further reduce agitation torque. From the perspective of oil flow analysis, it is considered effective to flatten the uneven shape of the cage in the direction of rotation. Based on this idea, flat parts (see Figure 20) are added to the concave between the ball packets, as shown in Figure 21. This approach is also applied to the rib side (see Figure 21) of the cage (where usually holes are set in consideration of formability) in order to lower agitation torque thoroughly.

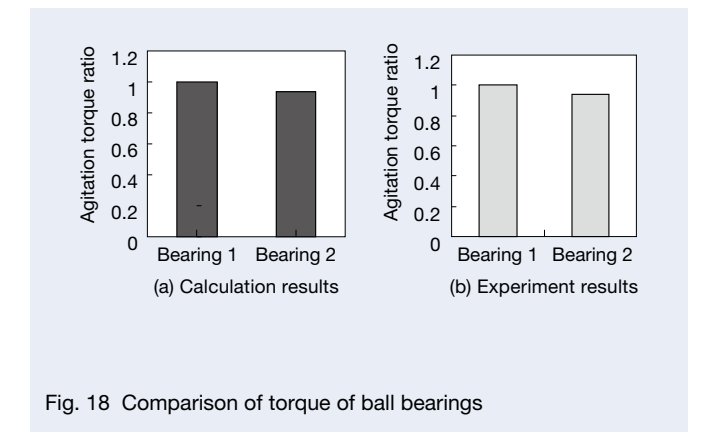


Fig. 18 Comparison of torque of ball bearings

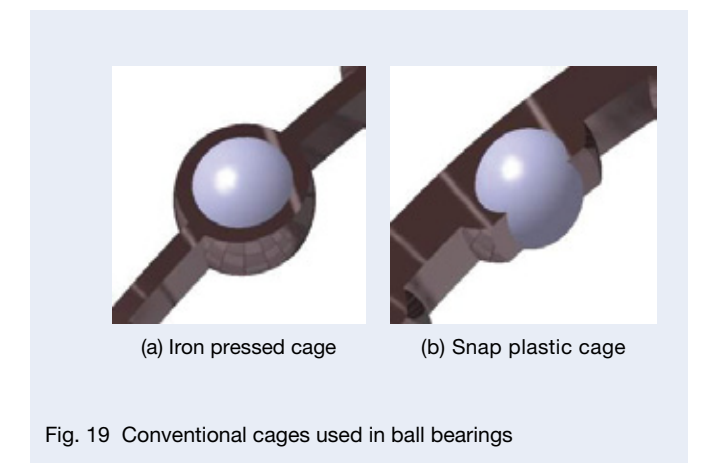


Fig. 19 Conventional cages used in ball bearings

It is reasonable to consider that enlarging the proportion of the flat parts may bring greater reduction of agitation torque. To further improve the cage shape, the influence of the shape of the flat parts was examined using CFD analysis and measurement. The width of the flat parts is increased by reducing the number of balls. Figure 22 shows the results. Agitation torque drops further when reducing the number of balls (thereby increasing the proportion of the flat parts).

Calculation and measurement results shown in Figure 23 indicate that the low-torque ball bearing using the newly developed cage (with 6 balls) reduces both agitation torque and the total torque losses significantly in comparison with conventional bearings. Figure 24 shows the calculation results of flow-induced force on the cage surfaces. The force is a composition of pressure force and shear force. The newly developed cages receive smaller force than the conventional ones, which means the new cage shape is effective in torque reduction. CFD analysis shows that the low-torque ball bearing with the newly developed cage allows oil to smoothly pass through the inside of the bearing and thereby reduces agitation torque.

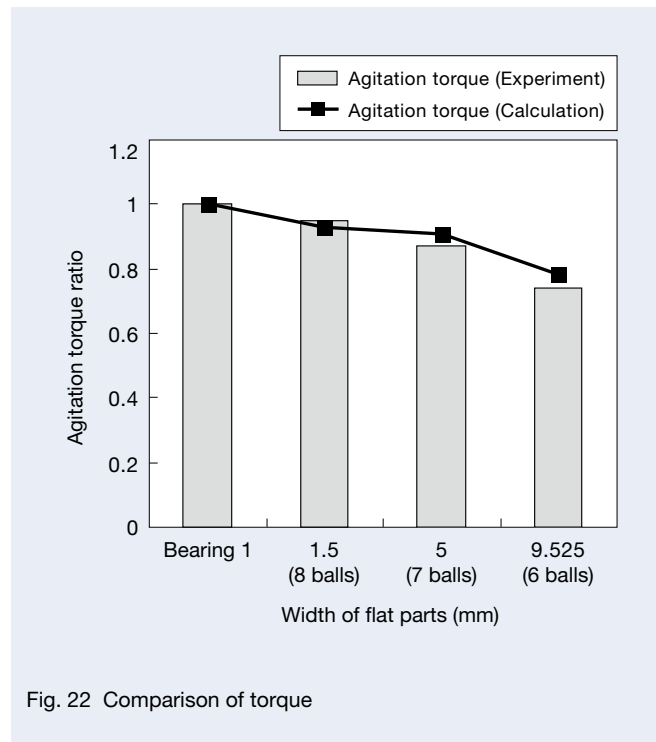


Fig. 22 Comparison of torque

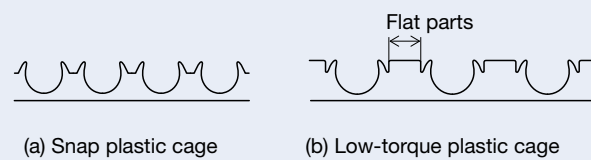


Fig. 20 Flat parts on cage

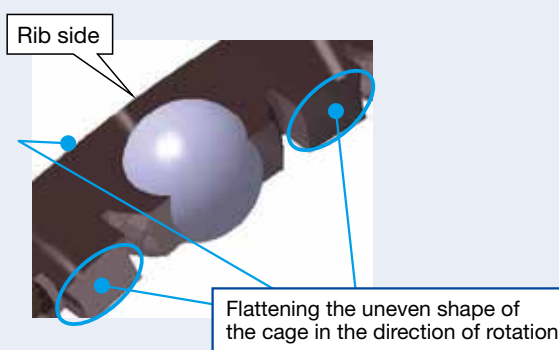
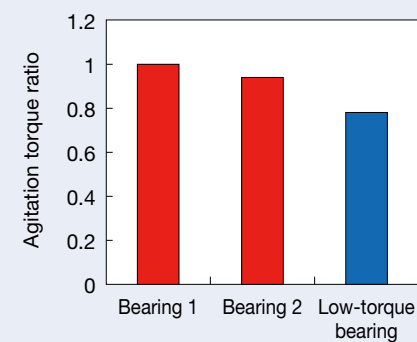
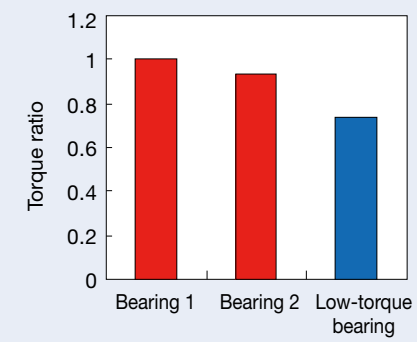


Fig. 21 Image of the newly developed low-torque cage shape



a) Calculation results



b) Experiment results

Fig. 23 Comparison of torque

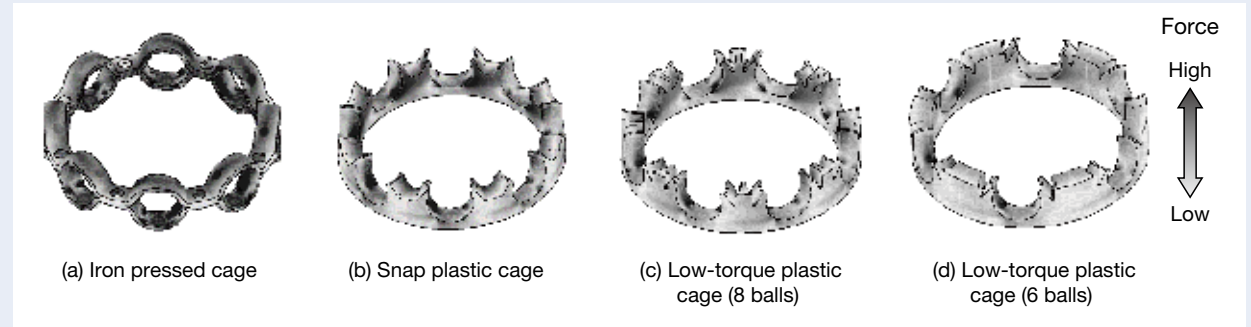


Fig. 24 Flow-induced force on cage surfaces

4. Conclusion

A prediction method of the agitation torque and the tendency of oil flow in tapered roller bearings and ball bearings are developed using CFD analysis. The method was verified by experiments. Using this technique, the influence of bearing cage design on oil flow and agitation torque was investigated and examined, which leads to development of low-torque tapered roller bearings and ball bearings. Oil flows in these bearings are controlled and optimized by specially shaped plastic cages. As a result, agitation torque is significantly reduced in comparison with conventional products.

Acknowledgments

The authors gratefully acknowledges their colleague, Mr. Tsuchida, for his kind assistance in measuring the torque of the ball bearings in this article.

References

- Hayashi, Y. and Ikezawa, K.: The Latest Technology of Drivetrain Bearing Contributing to Better Fuel Economy. *Journal of JSAE* (in Japanese), 64(11), 2010, pp. 65–70
- Aramaki, H.: Low Frictional Torque Technology of Rolling Bearings. *NSK Motion & Control*, 17, 2005, pp. 25–31
- Aramaki, H.: Rolling Bearing Analysis Program Package “BRAIN”. *NSK Motion & Control*, 3, 1997, pp. 15–24
- Natsumeda, S.: Computer Simulation Technique for Predicting Performance of Rolling Bearings. *NSK Technical Journal* (in Japanese), 673, 2002, pp. 31–35
- Saito, T.: Development of New-Generation Low-Frictional-Torque Tapered Roller Bearings. *NSK Technical Journal* (in Japanese), 685, 2012, pp. 8–13
- Matsuyama, H. et al: Development of Super-Low Friction Torque Technology for Tapered Roller Bearings, *Koyo Engineering Journal* (in Japanese), 167, 2005, pp. 24–30
- Chiba, H., Matsuyama, H. and Toda, K.: Effect of Lubricating

- Oil Flow Behavior on Friction Torque of Tapered Roller Bearing. *Koyo Engineering Journal* (in Japanese), 168, 2005, pp. 25–30
- Aihara, S.: A New Running Torque Formula for Tapered Roller Bearings Under Axial Load. *ASME Journal of Tribology*, 109, 1987, pp. 471–478
- Harris, A. T. and Kotzalas, N. M.: *Advanced Concepts of Bearing Technology*. “Rolling Bearing Analysis” series Fifth Edition. U.S.: CRC Press 2007
- Tsuchida, Y.: Development of Ultra Low-Torque Ball Bearings for Hybrid Vehicles. *NSK Technical Journal* (in Japanese), 685, 2012, pp. 14–20



Yingyi Wen



Shinji Miyata

Enhanced Performance of Rolling Bearings by Improving the Resistance of Rolling Elements to Surface Degradation

Hiroki Komata,¹ Yasuhiro Iwanaga,¹ Tohru Ueda,¹ and Koji Ueda¹

Reference

Komata, Hiroki, Iwanaga, Yasuhiro, Ueda, Tohru, Ueda, Koji, and Mitamura, Nobuaki, "Enhanced Performance of Rolling Bearings by Improving the Resistance of Rolling Elements to Surface Degradation," Bearing Steel Technologies: 10th Volume, Advances in Steel Technologies for Rolling Bearings, STP 1580, John M. Beswick, Ed., pp. 272–290, doi:10.1520/STP158020140085, ASTM International, West Conshohocken, PA 2015.²

Abstract

Bearing flaking often initiates from the surface of the raceway under poor lubrication conditions. The life of a bearing with this type of surface originated flaking is usually much shorter than the calculated life. As global environmental issues continue to grow, the requirement to reduce the size and weight of machines to improve fuel consumption for given applications increases. Such a requirement makes the conditions for the rolling bearings used in these machines more severe, which increases the likelihood and accelerates surface originated flaking. Therefore, it is very important to develop bearings with increased resistance to surface originated flaking. The mechanism of surface originated flaking, however, is not fully understood. From previous studies of co-authors, it was obvious that fatigue crack initiation and propagation were strongly related to the direction of the tangential force acting on a raceway surface. It was also evident that the bearing life decreased as the tangential force increased due to an increase in the surface roughness of the rolling elements. These results indicated that bearing life can be extended by improving the resistance of the rolling elements to surface degradation. Based on the finding described above, a new material for rolling elements with a high surface hardness produced by nitride precipitates was developed. It was demonstrated that 6206 bearings with these rolling elements had a superior life when tested in lubricant contaminated with debris. Downsizing of a rolling element bearing can be achieved by using this newly developed material for rolling elements.

Keywords

Rolling bearing, flaking, surface tangential force, surface roughness

Introduction

Flaking due to rolling contact fatigue (RCF) is a common type of bearing failure and is generally classified into two types: subsurface originated and surface originated^[1]. Subsurface originated flaking usually occurs under ideal lubrication conditions and initiates from a non-metallic inclusion present in the material. In recent years, the occurrence of subsurface originated flaking has decreased due to improvements in bearing steel cleanliness.

By contrast, surface originated flaking occurs under poor lubrication conditions such as when there is insufficient oil film thickness or contaminated lubrication. Dents

caused by debris or surface micro-peelings are formed on a raceway, which causes early flaking. In some cases, the surface originated flaking life is actually less than the life calculated by Lundberg–Palmgren's theory.

Today, there is a requirement to reduce the size and weight of machine components, including rolling bearings, to improve fuel consumption for given applications. This results in more severe operating conditions for rolling bearings used in these applications. Rolling bearings used in automotive transmissions and differential gears are subjected to wear debris that accelerates the surface originated flaking and hampers the further development of a more compact bearing. Therefore, clarifying the

mechanism of surface originated flaking is desired to develop a longer-life bearing under poor lubrication condition.

A significant amount of research, especially for the surface originated flaking caused by dents (dent initiated flaking), has been conducted. The research has included a study of the mechanism of dent formation^[2–4], calculating the stress at a dent edge^[5–7], and development of extended dent initiated flaking life^[1, 8–11].

Chiu and Liu^[7] clarified that the stress concentration at a dent edge determines flaking life. They suggested that the larger the r/c value, where r is the radius of a dent shoulder and c is half the value of a dent width, the smaller the stress concentration at a dent edge. Furumura et al.^[1, 8] applied the theory of Chiu and Liu^[7] and focused on the use of retained austenite as a means to maximize the r/c value and to reduce stress concentration. In order to achieve a higher r/c for a dent formed on a raceway, Furumura et al.^[1, 8] increased the amount of retained austenite in a raceway surface. Thus, they were able to develop a long-life bearing that restricted dent initiated flaking.

According to the Chiu and Liu^[7] theoretical model, stress concentrations of the leading edge and the trailing edge of a dent in rolling direction are equal. This means the rate of flaking that occurs at both edges must be the same. However, the Chiu and Liu^[7] model cannot explain why in actual service the dent initiated flaking tends to occur on the trailing edge in the rolling direction more often than the leading edge. From the many studies being carried out to identify the reason for this, two possible factors have emerged. One is that the rolling direction is involved^[12, 13]. Biboulet et al.^[13] pointed out that the local

contact pressure at the trailing edge of a dent was slightly larger than the leading edge in pure rolling condition from EHL analysis.

The other is that the direction of the tangential force (sliding direction) is involved^[14–19]. Morales-Espejel et al.^[19] conducted an EHL analysis that took sliding into consideration and determined that the sliding direction was related to the position of a dent edge where excessive pressure was generated. However, it has not been clarified experimentally which of these factors is more dominant.

The co-authors, therefore, conducted ball-on-rod RCF tests using specimens with artificial dents to clarify the cause of flaking that occurs on the trailing edge of a dent in the rolling direction, as reported in previous papers^[20, 21]. The results from the tests and reports by other researchers^[14–19] confirmed that where a crack initiates was strongly related to the direction of the surface tangential force. Furthermore, it was clarified that the tangential force also played a role in the flaking that initiated from surface peelings created under conditions of insufficient oil film thickness^[21]. These results indicate that to extend flaking life, it is important to reduce the surface tangential force acting on the raceway. Surface roughness of two contacting surfaces is known to be one of the factors influencing the surface tangential force^[22, 23]. It will be shown in this paper that the surface roughness of a rolling element (ball) affects the surface originated flaking life. Moreover, a method for extending the surface originated flaking life of a ball bearing by means of reducing the degradation in the surface roughness of a ball, which occurs under poor lubrication conditions, will be proposed.

Manuscript received July 14, 2014; accepted for publication October 13, 2014; published online November 7, 2014.

¹NSK LTD., Basic Technology Research Center, Fujisawa-shi, 251-8501, Japan.

²ASTM 10th International Symposium on Advances in Steel Technologies for Rolling Bearings, on May 6–7, 2014 in Toronto, Ontario, Canada.

Copyright V C 2014 by ASTM International, 100 Barr Harbor Drive, PO Box C700, West Conshohocken, PA 19428-2959.

The Effect of Tangential Force on Surface Originated Flaking

In order to clarify the phenomenon and determine what is the main factor affecting surface originated flaking, co-authors conducted ball-on-rod RCF tests using rod specimens that had artificial dents on their surface^[20]. Figure 1 shows a schematic of the ball-on-rod RCF test rig, which is composed of two outer rings with a tapered bore, a 12.6mm diameter rod specimen, and three 27/32 in. diameter balls. The rod specimens were made in through-hardened and tempered SAE 52100 bearing steel. The surface roughness of the rod specimens was less than 0.10 μmRa . Test conditions consisted of a maximum contact pressure (P_{max}) between the rod specimen and balls of 4.8GPa, a rod rotating speed of 8000 min^{-1} , and ISO-VG68 oilbath lubrication.

Figure 2 shows the slip speed distribution in a contact surface between a rod specimen and ball. The slip direction around the center of the contact area is opposite to the slip direction at the sides due to differential slip. Therefore, some of the specimens had artificial dents located in the center of the contact area and some with dents at the side of the contact area, as shown in Fig. 2. The artificial dents in the specimens were created using a Rockwell C indenter.

Figure 3(a) shows flaking initiated from a dent located in the center of the contact area, where the rod specimen acts as a driven component and the direction of the surface tangential force acting on the rod specimen is in the same direction as the rolling direction. Figure 3(b) shows a crack initiated from a dent located on the side of contact area, where the rod specimen acts as a driving component and the direction of the surface tangential force is in the opposite direction to the rolling direction. It was observed that flaking occurred at the trailing edge of a dent and a crack initiated at the leading edge of a dent as shown in Fig. 3(a) and Fig. 3(b), respectively. These results indicate that the position of crack initiation at the

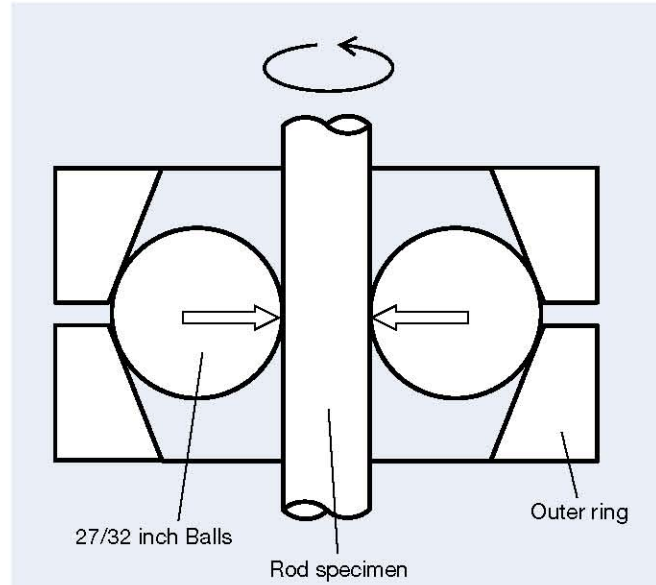


FIG. 1 Schematic of the ball-on-rod RCF test rig.

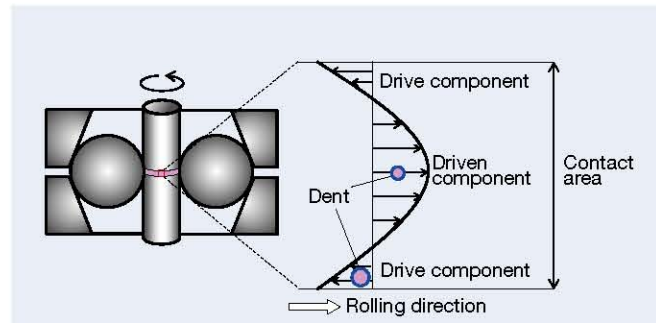
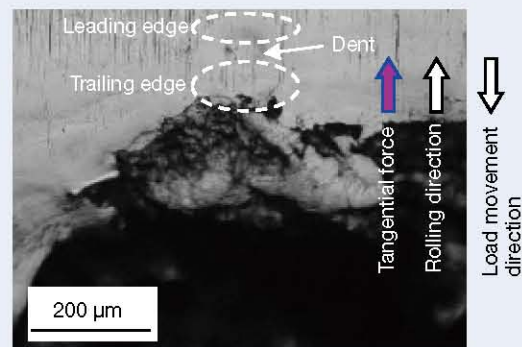
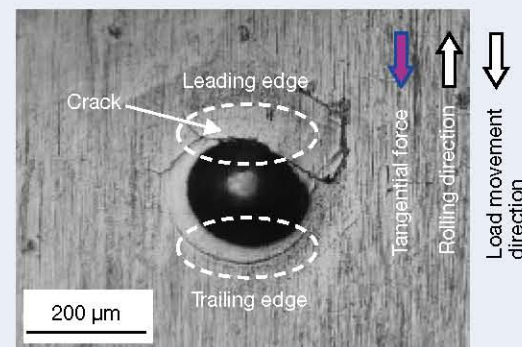


FIG. 2 The slip speed distribution in contacting surfaces between a rod specimen and ball.



(a) A dent located at center of contact area.



(b) A dent located at side of contact area.

FIG. 3 The flaking and crack initiated from a dent edge in ball-on-rod RCF test.

dent edge is strongly related to the direction of the surface tangential force and not the rolling direction.

The co-authors also conducted ball-on-rod RCF tests using balls with a rougher surface in order to clarify the factors affecting surface micro-cracks (peelings), which cause another type of the surface originated flaking (peeling initiated flaking)^[21]. Peeling in a rod specimen is greatly accelerated by using balls with a rougher surface. The test conditions were the same as described above, except the P_{max} was 6.0GPa. The surface roughness of the balls was 0.18 μmRa .

Figure 4 shows the surface appearance of a rod specimen after a 1h test. Peeling was observed around the center and side areas subjected to a higher slip speed and a high surface tangential force. Figure 5 shows optical micrographs of cross sections A-A', B-B', and C-C' shown in Fig. 4. The direction of the tangential force in section A-A' is the same as in section C-C' and the direction of the surface crack propagation is also the same in these two sections. In contrast, the direction of the surface crack propagation in section B-B', which is subjected to an opposite surface tangential force, is opposite to the direction of crack propagation in sections A-A' and C-C'. These results show that the surface tangential force

influences surface cracks causing the peeling initiated flaking, not only the dent initiated flaking. The surface tangential force plays a significant role in both types of the surface originated flaking.

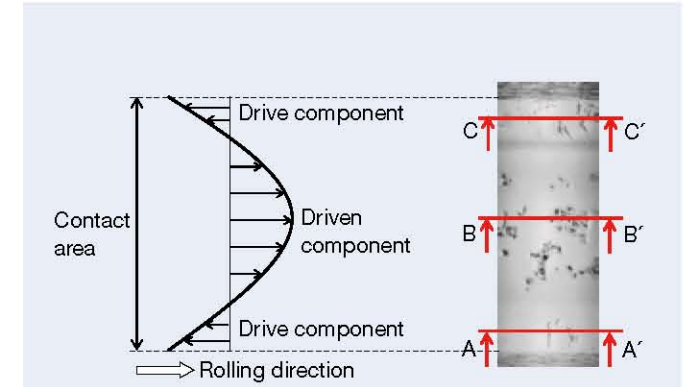


FIG. 4 Surface appearance of a rod specimen after 1h test.

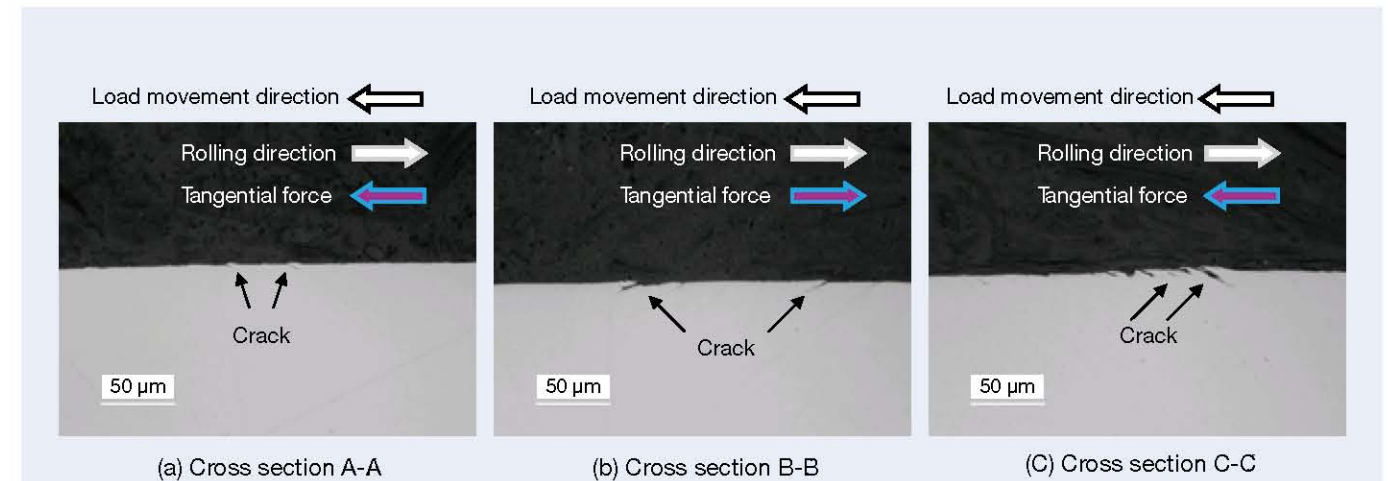


FIG. 5 Optical micrographs of cross section A-A', B-B', and C-C'.

Influence of Surface Roughness on the Tangential Force

The surface roughness of two contacting surfaces is known to be one of the factors affecting the tangential force [22, 23]. In order to clarify the influence of surface roughness on tangential force in the surface originated flaking of actual rolling bearings, life testing was conducted using 6206 deep groove ball bearings with a 30mm bore diameter and a 62mm o.d. The 6206 bearings were made-up from sets of inner rings and balls with different combinations of surface roughness in order to investigate the influence of surface roughness of an each part separately. Details of the bearing sets, i.e., the different combinations of inner ring raceway and ball surface roughness, are shown in Table 1. The surface roughness of all of the outer ring raceways was the same, $0.03\mu\text{m}R_a$. The variation in the surface roughness of the inner ring raceways and balls was produced by changing the grinding conditions. The rings and balls of the test bearings were all made in through-hardened and tempered SAE 52100 bearing steel.

TABLE 1 Surface roughness combinations of balls and inner rings.

Bearing Set	Surface Roughness ($\mu\text{m}R_a$)		Lubricant Film Parameter λ	Number of Tested Bearings
	Ball	Inner Ring Raceway		
A1	0.006	0.05	2.39	5 per set
A2	0.111	0.19	0.65	
A3		0.31	0.39	
B1	0.111	0.05	0.99	10 per set
B2		0.19	0.56	
B3		0.31	0.37	
C1	0.209	0.05	0.56	10 per set
C2		0.19	0.43	
C3		0.31	0.32	

A schematic of the life test rig is shown in Fig. 6. The test rig used a cantilever system to apply a radial load directly to the test bearing. The life tests were conducted using nine bearing sets in total, as shown in Table 1, and under clean lubrication conditions, a radial load of 13.8kN, a rotating speed of 3900min^{-1} , a temperature of outer ring of 80°C and ISO-VG68 forced-circulation oil lubrication with 10 and 1 μm filtering. The number of tested bearings per set is also shown in Table 1.

Figure 7 shows the results of the life tests in the form of a Weibull plot. Acceleration of vibration were measured during life testing, and the time to reach double level of initial vibration was regarded as failure life. The flaking in inner raceways occurred in all failure bearings, and all of the flaking initiated from peeling on the raceway surface, except when the ball surface roughness was $0.006\mu\text{m}R_a$, as shown in Fig. 8. Figure 7(a), 7(b), and 7(c) show a comparison of the failure life achieved for each inner raceway surface roughness with varying ball surface roughness. All of the plots in Fig. 7 show the flaking lives of the inner rings and the arrows denote run-out. The results clearly show that the flaking life of the inner ring reduced significantly as the surface roughness of the balls was increased.

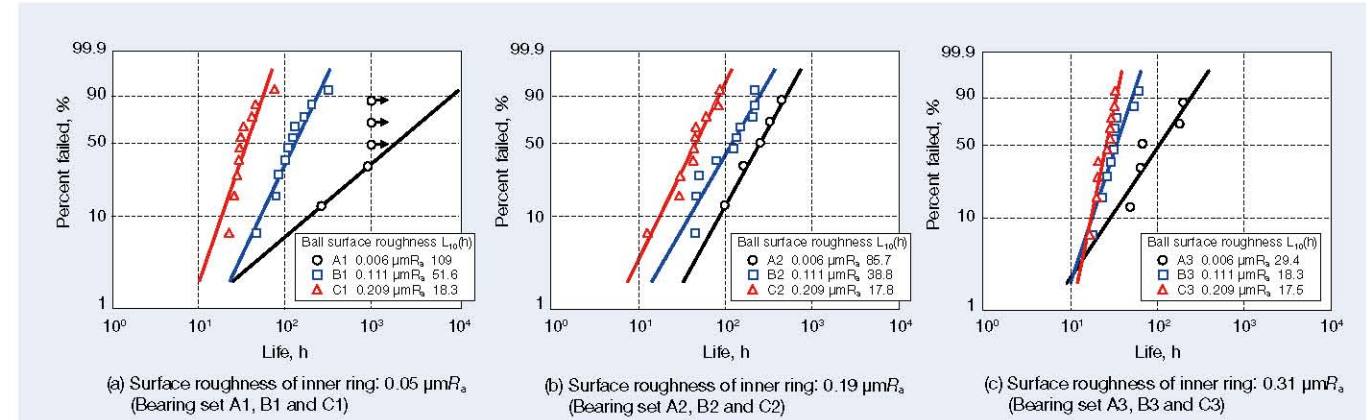
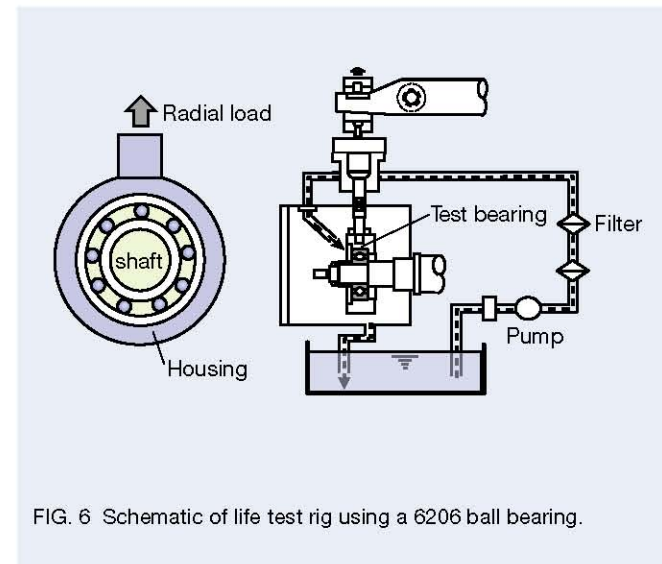


FIG. 7 Weibull plots of the life test results using 6206 ball bearings with various surface roughness.

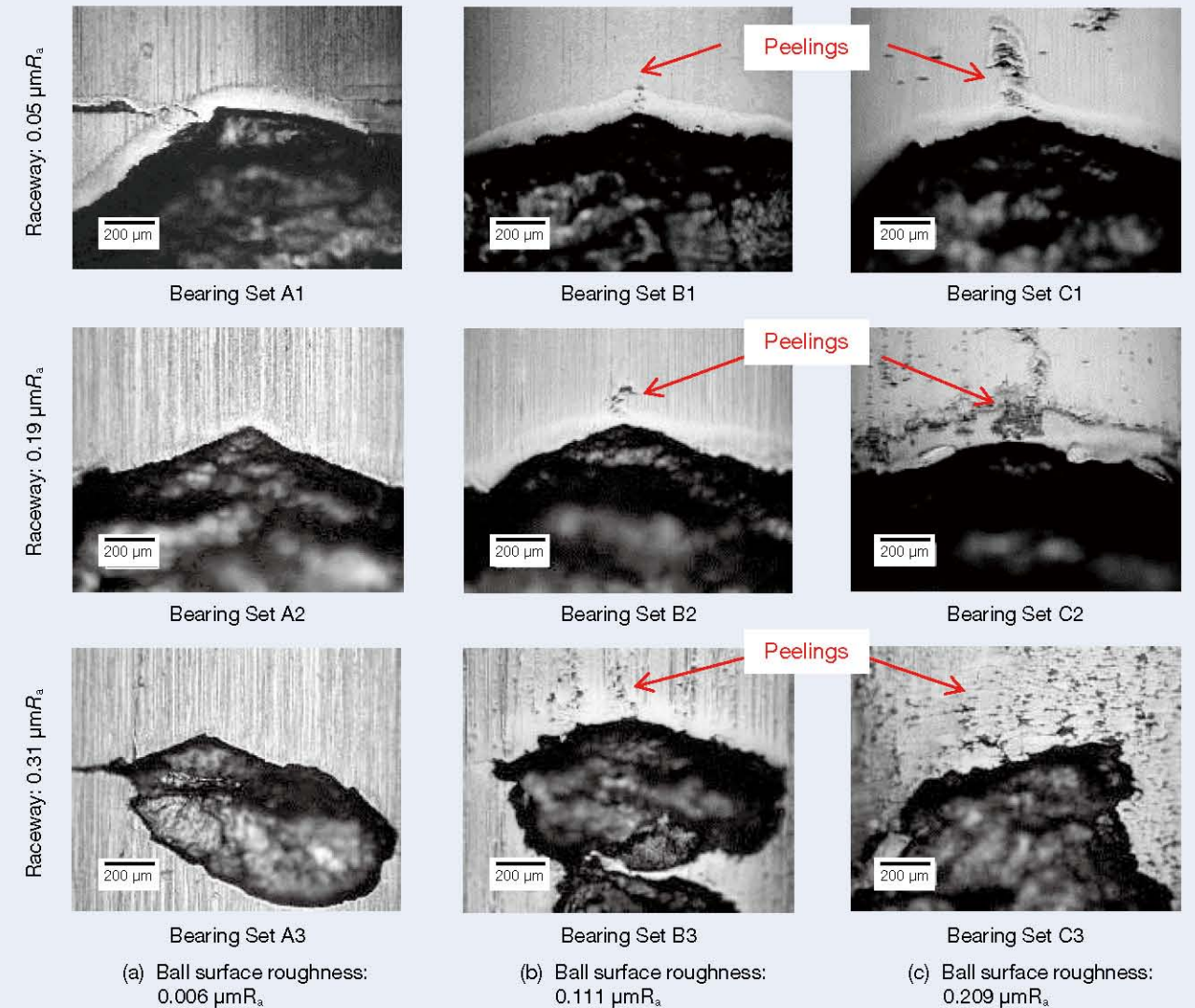


FIG. 8 Appearances of flaking occurring in inner rings.

Figure 9(a) shows the relationship between the surface roughness of inner ring raceway and the flaking life (L_{10}) for each ball surface roughness. The flaking life tends to increase as the surface roughness of both the inner raceway and balls decreases. However, in the case of the balls with the highest initial surface roughness ($0.209 \mu m R_a$), the flaking life did not change significantly when the surface roughness of the inner ring raceway was increased. These results indicate that increasing the surface roughness of the balls accelerates the peeling initiated flaking of the raceway to a greater extent than the surface roughness of the raceway itself.

It is generally known that the greater the surface roughness of two contacting surfaces, the greater the tangential force^[22]. The co-authors also clarified experimentally that there is a clear correlation between the direction of the surface tangential force and where in a crack initiates relative to the dent, or the direction of the surface crack propagation, as in the case of ball-on-rod RCF tests as described above. It was proved that the tangential force acting on a contacting surface affects the surface originated flaking life. On the basis of previously published papers^[14–22], these life test results revealed that the surface originated flaking life was reduced by the increase in the tangential force acting on the raceway surface due to the degradation in the surface roughness of the balls.

It is, on the other hand, well-known that RCF life correlates with the lubricant film parameter Λ ($\Lambda = h_{\min}/\sigma$; where h_{\min} is the minimum lubricant film thickness and σ is the composite surface roughness of two

contacting surfaces) under clean lubrication conditions without debris^[24–26]. Skurka^[24] and Takata and Aihara^[26] have reported that the lower the Λ value, the shorter the RCF life in a region where the Λ value is three or less.

The life tests in this study had Λ values of three or less depending on the surface roughness combination of the inner ring raceway and balls as shown in Table 1. It is difficult to separate the influence of Λ from the surface roughness on the increase in the surface tangential force because metal-to-metal contact increases with an increase in the tangential force in lower Λ conditions. Takemura et al.^[27] pointed out that the larger the composite surface roughness of two contacting surfaces, the shorter the flaking life, even though the Λ value is the same. However, Takemura et al. did not consider the effect of surface roughness of each contacting part separately.

The flaking life L_{10} data was, therefore, plotted against Λ for each ball surface roughness as shown in Fig. 9(b), which showed that the flaking life tended to increase as Λ increased. However, the flaking life became shorter as the ball surface roughness increased, even when the Λ value was the same (the flaking life of a bearing composed of rough balls and smoother raceways is shorter than one composed of smooth balls and rough, even when the Λ value was the same). These results indicate that an acceleration of the surface tangential force acting on a raceway due to an increase in the surface roughness of the balls has a greater influence on the surface originated flaking life than a reduction in the Λ value.

A New Approach for Enhancing Performances of Rolling Bearings

Previous researches and developments for extending the surface originated flaking life of a bearing have focused on improving material strength or reducing stress concentrations in the area where flaking occurs^[1, 8–11]. The test results shown in this paper, however, indicate that the surface originated flaking is strongly related to the surface roughness of the balls, which are the counterpart to the inner and outer rings. The ball surface roughness will degrade due to dent formation or wear under poor lubrication conditions such as insufficient oil film thickness or contaminated lubrication. The degradation in ball surface roughness gives rise to the tangential force acting on the raceway surface, which reduces the surface originated flaking life.

These considerations lead to a new approach for extending the service life of rolling bearings operating under poor lubrication condition, such as developing a method for improving the resistance of the counterpart against surface degradation and thereby reduce the surface tangential force.

The surface originated flaking tends to occur on the surface of a driven component, as reported in the previous paper^[20]. In a ball bearing, a raceway is the driven part at the center of the contacting area with a high Hertzian contact pressure. It is important to improve the resistance to surface degradation of the counterpart contacting with a part that is susceptible to surface originated flaking to extend the life. Therefore, improving the resistance to surface feature degradation of a ball would be an effective solution to extend the service life of a ball bearing operated under poor lubrication conditions.

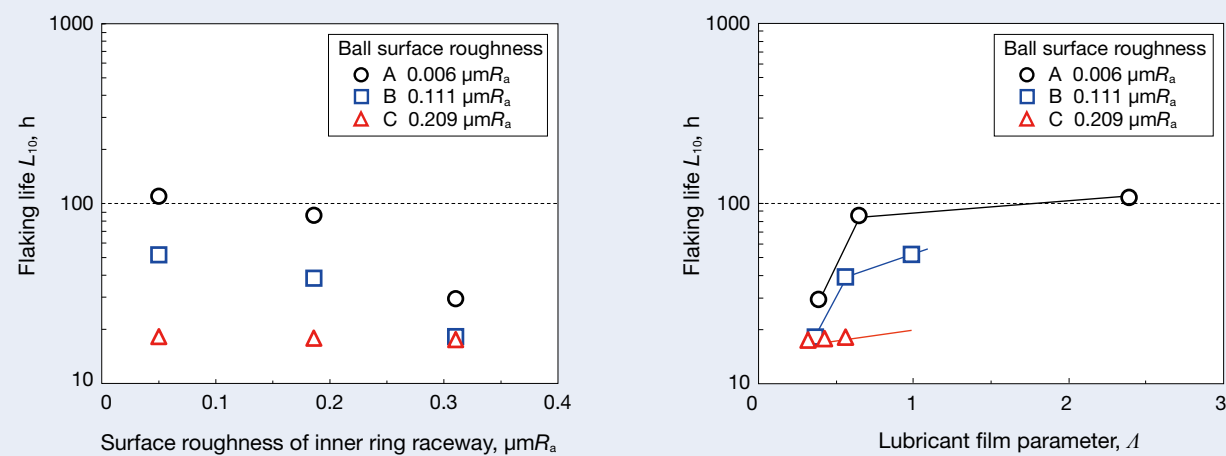
The Method for Improving Resistance to Surface Degradation of Balls

The hardness of a material is one of the most important factors affecting resistance to surface degradation. Naturally, the harder the material is, the higher the wear and dent resistance. The hardness of martensite, which is the main phase of a through-hardened bearing steel, is roughly determined by the solute carbon content, and hardly affected by alloying elements. There is little scope to increase the material hardness by increasing the hardness of the martensite because the carbon content of a bearing steel is already high.

Producing finely dispersed precipitates within the martensite can increase the hardness of a material. Typically in bearing steels, globular cementite is precipitated throughout the material. If the amount of cementite is significantly increased, for instance by carburizing, then it may precipitate at the grain boundaries to form a grain boundary network, which may sometimes become a fracture origin. This can be avoided by using alloying elements such as molybdenum (Mo), vanadium (V), tungsten (W), or titanium (Ti), which form carbides that precipitate independently of the cementite. These alloying elements are, however, very expensive.

An inexpensive alloying element such as silicon (Si) can be used, although it is less effective in forming carbides. Silicon is used in various structural steels, and forms a very hard nitride during the nitriding or carbonitriding process. Moreover, silicon does not concentrate in the cementite and is mostly soluble in the matrix. Therefore, where cementite is finely dispersed, silicon is a suitable element for promoting additional finely dispersed precipitates separate to the cementite in high carbon martensite steel such as bearing steels. Consequently, a nitrided or carbonitrided material containing high quantities of silicon for precipitating silicon nitride improves resistance to surface degradation.

Therefore, finely dispersed silicon nitrides within a ball surface were produced by carbonitriding the steel containing high quantities of silicon. The steel used for



(a) Relationship between surface roughness of inner ring raceway and flaking life (L_{10}) for each ball surface roughness.

(b) Relationship between lubricant film parameter Λ and flaking life (L_{10}) for each ball surface roughness.

FIG. 9 Life test results using 6206 ball bearings with various surface roughness.

TABLE 2 Surface hardness and morphology of balls.

	Nitride precipitated ball	SAE52100 ball
Surface hardness	892 HV	801 HV
Micrograph of surface		

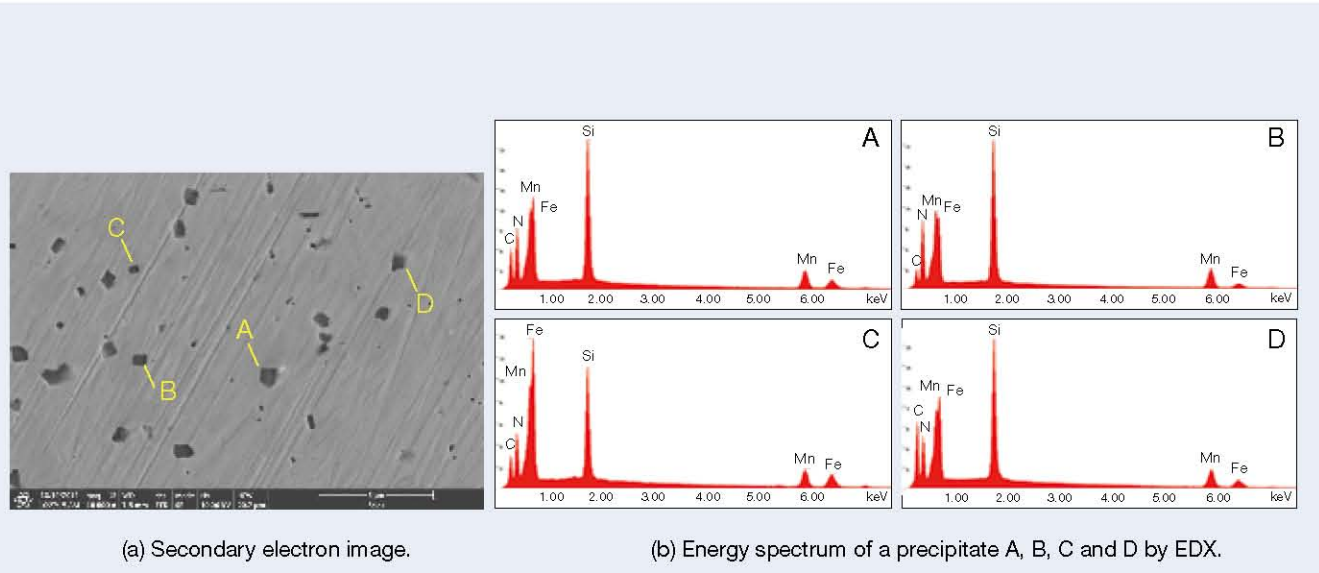


FIG. 10 SEM micrograph of nitride precipitated ball surface and EDX analysis of precipitates.

a ball contains about 0.3 to 0.4 mass % higher silicon than SAE 52100. Other chemical compositions are almost the same as SAE 52100. Table 2 shows the hardness and optical micrographs of ball surfaces obtained for a through-hardened and tempered SAE 52100 bearing steel and a carbonitrided steel containing higher quantities of silicon (herein-after called nitride precipitated ball).

The nitride precipitated ball surface contains fine precipitates (black spots) that are not present in the surface of the SAE 52100 ball. Several sizes and shapes of precipitates, observed in SEM micrograph shown in Fig. 10(a), were analyzed by an energy dispersive X-ray (EDX) analyzer built into a FE-SEM. As shown in Fig. 10(b), these precipitates consisted of silicon, nitrogen (N), and manganese (Mn), which is an alloying element in the steel. The fine precipitates are considered to be Si-Mn nitrides. The surface hardness of the nitride precipitated ball was harder than that of SAE 52100 ball by approximately 90 HV due to the high hardness of Si-Mn nitrides.

Improved Durability of Nitride Precipitated Balls Against Surface Degradation

In order to confirm the effect of the increase in hardness due to nitride precipitates on the resistance to surface degradation, the bearing rotation tests using 51305 thrust ball bearings with three balls were conducted under insufficient oil thickness (low λ) condition. Tests were conducted using the nitride precipitated balls and SAE 52100 balls. The rings of the thrust ball bearings

were made in through-hardened and tempered SAE 52100 bearing steel. A schematic of the thrust type test rig used for this evaluation is shown in Fig. 11. The test conditions consisted of an axial load of 6.2kN (P_{max} of 2.5GPa), a rotating speed of 1000min⁻¹, ISO-VG10 oil bath lubrication, an oil temperature of 60°C. The oil film thickness parameter λ value was 0.3.

Tests were interrupted at regular intervals to check for a change in the surface morphology of the balls. Figure 12(a) shows optical micrographs of SAE 52100 and a nitride precipitated ball surfaces after 100h on test. It was found that the surface damage sustained by the

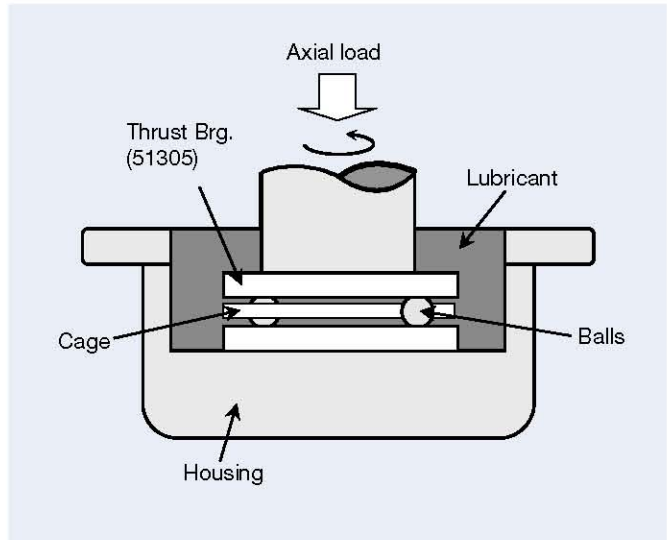


FIG. 11 Schematic of the thrust type test rig.

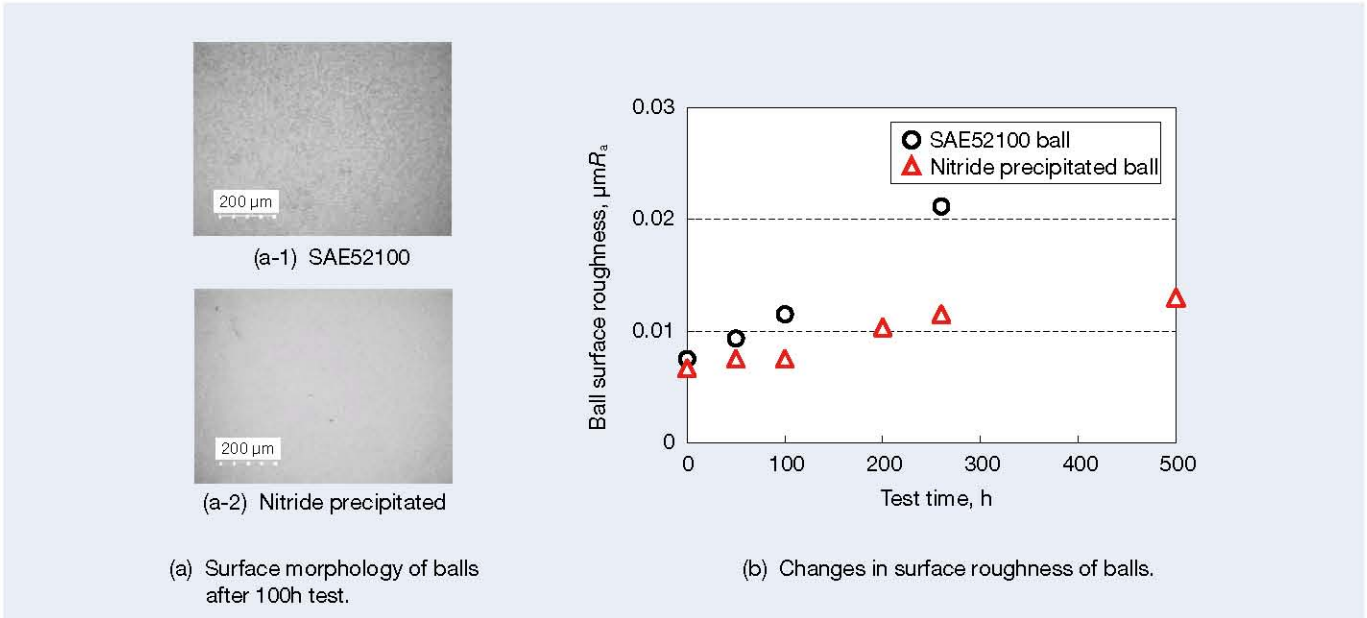


FIG. 12 Changes in surface feature of balls with test time.

nitride precipitated ball was much less than the damage sustained by the SAE 52100 ball. Fig. 12(b) shows the changes in surface roughness of each kind of balls with increasing test time. The nitride precipitated ball has greater resistance to surface roughness degradation than the SAE 52100 ball under insufficient oil film thickness conditions.

The dent resistance of the nitride precipitated ball was also evaluated using the same test rig shown in Fig. 11. The test bearings were the same as those used for the previous test carried out under low λ conditions describe above. Contamination with a uniform size of 100 µm, as shown in Fig. 13(a), was placed on the raceway before test and then the bearing was rotated for 20 revolutions with an axial load of 1.7kN (P_{max} of 2.0GPa) to form dents on the surface of the balls. The contamination used for this test had a hardness of 750 HV, and was obtained for martensitic stainless steel.

Examples of the dents formed on a ball surface are also shown in Fig. 13(b). The depth of the dents in the surface of the balls was measure and the depth distribution of the dents obtained for the nitride precipitated balls and SAE 52100 balls was compared, as shown in Fig. 14. From the comparison, it can clearly be seen that the dents in the nitride precipitated balls were shallower the dents in the SAE 52100 balls.

The results from the two kinds of test carried out show that increasing the ball hardness by finely dispersed nitride precipitates improves the durability of the ball surface against degradation caused by dents and wear under poor lubrication conditions.

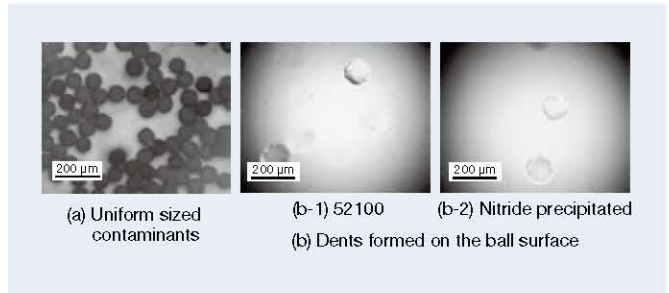


FIG. 13 Uniform sized contaminants and dents formed on the ball surface.

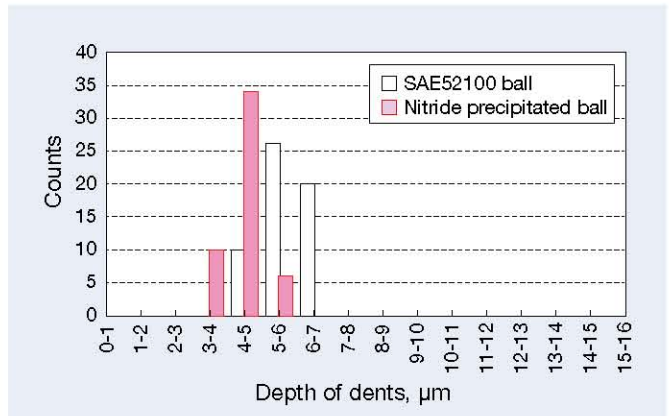


FIG. 14 Depth distributions of dents formed on the ball surface.

Enhanced Flaking Life of Rolling Bearings Installed the Improved Balls

Life tests using 6206 deep groove ball bearings with balls containing finely dispersed nitride precipitates in their surface (nitride precipitated balls) were conducted to demonstrate the above assumption, which is that improving the resistance of a ball to surface degradation would extend the service life of a ball bearing under poor lubrication conditions.

Bearing rings were made in through-hardened and tempered SAE 52100 bearing steel. The tests were conducted using two bearing sets as shown in Table 3, under contaminated lubrication conditions, a radial load of 6.2kN, a rotating speed of 3000min⁻¹, a temperature of outer ring of 80°C and ISO-VG68 oil-bath lubrication. The rig used for the life tests was basically the same design as illustrated in Fig. 6, except for the lubrication system. The debris used for contamination was made of cementite, had a hardness of 870 HV and a particle size ranging from 74 to 147µm. The amount of debris used was 0.05 g per 1.2 l of lubricating oil. The criteria for judgment whether or not the failure occurs in test bearings is the same as describe above.

The life test results are shown in Fig. 15. For the two sets of bearings tested, the only flaking that occurred initiated from a dent on the raceway. The dent initiated flaking life of the bearing set E, composed of the nitride precipitated balls and SAE 52100 rings, was nearly twice as long as that of bearing set D, composed of SAE 52100 balls and rings.

The life testing of bearing sets D and E was interrupted for 1h to check for dents formed on the surface of the balls. This was to verify that an increase in life was achieved by improving the resistance of the balls to surface degradation. Figure 16 shows a comparison in surface morphology of a nitride precipitated ball and a SAE 52100 ball after 1h of testing. It can clearly be seen that the number of dents formed in the surface of the nitride precipitated ball is significantly less than the number of dents formed in the surface of the SAE 52100 ball. Figure 16, together with the results from previous studies, confirms that an extension in life was achieved through the use of the nitride precipitated balls, which improved resistance to surface degradation and reduced the surface tangential force acting on the edges of the raceway dents.

Bearing materials developed in the past to extend bearing life involved the use of expensive alloying additions and sometimes complicated heat treatment processes. The impact on the environment from manufacturing such bearings and their recycling efficiency has been less than favorable. Consequently, such bearings sometimes fail to meet the current environmental demands. The most notable point discussed in this study is that fully functional bearings can be manufactured only by making changes to the material used for the balls, which is just one of the components of a rolling bearing.

Furthermore, this technology is versatile, and can be used to develop more compact, lightweight bearings without decreasing productivity.

TABLE 3 Bearing sets used for the 6206 life test.

	Bearing D	Bearing E
Bearing ring	SAE52100	SAE52100
Ball	SAE52100	Nitride precipitated
Number of tested bearings	14	9
Symbol in Fig. 15	○	●

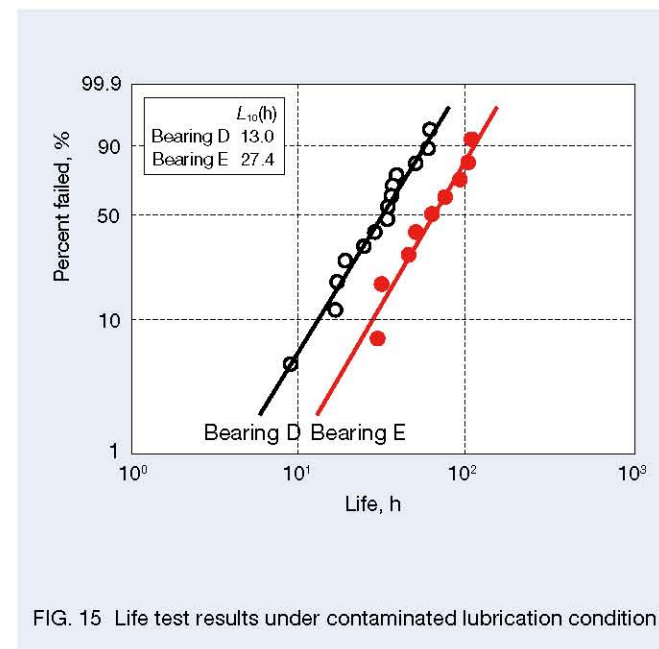


FIG. 15 Life test results under contaminated lubrication condition.

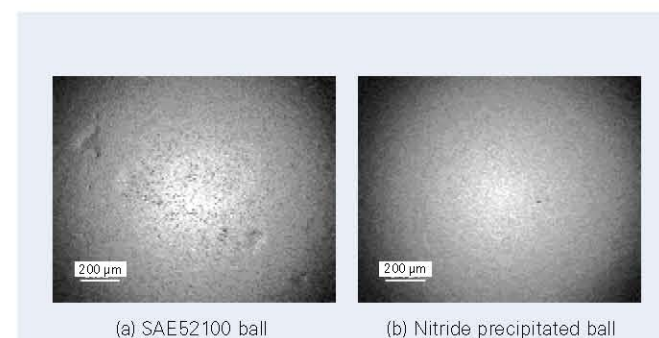


FIG. 16 Surface morphology of balls after one hour life test.

Conclusion

The influence of tangential force on surface originated flaking was investigated in this study. The effect of the surface roughness of a ball on surface tangential force is also discussed. In addition, it was confirmed that a change in the ball material for the purposes of reducing surface degradation, which occurs during bearing operation, was effective for extending the flaking life of a ball bearing. A change in a ball material was also shown to minimize the surface tangential force acting on a bearing raceway. Conclusions are as follows:

- Previous ball-on-rod RCF test results showed that in the case of dent initiated flaking, the position of the crack initiation at the edge of a dent was determined by the direction of the surface tangential force. The direction of the surface crack propagation in the case of peeling was also strongly related to the direction of the surface tangential force. Thus, surface tangential force plays a significant role in surface originated flaking.
- An increase in the surface roughness of the balls accelerated peeling initiated flaking, which is a type of surface originated flaking. The higher the surface roughness of the ball, the shorter the peeling initiated flaking life of the raceway, even though the surface roughness of the raceway and furthermore the lubricant film parameter K are the same.
- In comparison to a bearing with balls made in standard SAE 52100 bearing steel, a bearing with balls made in a steel with fine silicon and manganese nitride precipitates had twice the dent initiated flaking life when tested under contaminated lubricant conditions. Thus, authors believe that the improved ball with finely dispersed silicon and manganese nitride precipitates in the surface can extend bearing life by providing greater resistance to surface degradation and an increase in surface roughness, thereby, reducing the surface tangential force acting on the raceway.

Acknowledgments

The writers would like to thank Dr. Andrew Dodd of NSK EUROPE for checking this paper.

References

- 1) Furumura, K., Murakami, Y., and Abe, T., "The Development of Bearing Steels for LongLife Rolling Bearings Under Clean Lubrication and Contaminated Lubrication," Proceedings of the 4th International Symposium on Bearing Steels, Creative Use of Bearing Steels, ASTM STP 1195, ASTM International, Philadelphia, PA, 1993, pp. 199–210.
- 2) Sayles, R. S. and Ioannides, E., "Debris Damage in Rolling Bearings and its Effects on Fatigue Life," Trans. ASME F, Vol. 110, No. 1, 1988, pp. 26–31.
- 3) Dwyer-Joyce, R. S., Hamer, J. C., Sayles, R. S., and Ioannides, E., "Lubricant Screening for Debris Effects to Improve Fatigue and Wear Life," Proceedings of the 18th Leeds–Lyon Symposium on Tribology, Elsevier, Amsterdam, 1992, pp. 57–63.
- 4) Ville, F. and Ne'lias, D., "An Experimental Study on the Concentration and Shape of Dents Caused by Spherical Metallic Particles in EHL Contacts," Tribol. Trans., Vol. 42, No. 1, 1999, pp. 231–240.
- 5) Webster, M. N., Ioannides, E., and Sayles, R. S., "The Effect of Topographical Defects on the Contact Stress and Fatigue Life in Rolling Element Bearings," Proceedings of the 12th Leeds–Lyon Symposium on Tribology, Butterworths, Lyon, France, 1985, pp. 207–221.
- 6) Ai, X. and Nixon, H. P., "Fatigue Life Reduction of Roller Bearings Due to Debris Denting: Part I—Theoretical Modeling," Tribol. Trans., Vol. 43, No. 2, 2000, pp. 197–204.
- 7) Chiu, Y. P. and Liu, J. Y., "An Analytical Study of the Stress Concentration Around a Furrow-Shaped Surface Defect in Rolling Contact," Trans. ASME F, Vol. 92, 1970, pp. 258–263.
- 8) Murakami, Y., Matumoto, Y., and Furumura, K., "Long-Life TF Bearings Under Debris Contaminated Lubrication," NSK Tech. J., Vol. 650, 1989, pp. 1–11.
- 9) Toda, K., Mikami, T., and Johns, T. M., "Development of Long Life Bearing in Contaminated Lubrication," SAE Technical Paper 921721, SAE, Warrendale, PA, 1992.
- 10) Toda, K., Mikami, T., and Hoshino, T., "Effect of Ridge Around Dent and Retained Austenite on Rolling Fatigue Life," J. Jpn. Inst. Metals, Vol. 58, 1994, pp. 1473–1478.
- 11) Maeda, K., Nakashima, H., and Kashimura, H., "Development of Long-Life TAB and ETA Bearings and Their Automotive Applications," NTN Tech. Rev., Vol. 65, 1996, pp. 17–22.
- 12) Lubrecht, A. A., Venner, C. H. L. S., Jacobson, B., and Ioannides, E., "Surface Damage— Comparison of Theoretical and Experimental Endurance Lives of Rolling Bearings," Proceedings of the Japan International Tribology Conference, Nagoya, Japan, Oct 29–Nov 1, 1990, pp. 185–190.
- 13) Biboulet, N., Lubrecht, A. A., and Houpert, L., "Contact Pressure in Indented Elastohydrodynamic Lubrication Contacts," IMechE Part J, Vol. 222, No. 3, 2008, pp. 415–421.
- 14) Ne'lias, D. and Ville, F., "Detrimental Effects of Debris Dents on Rolling Contact Fatigue," Trans. ASME F, Vol. 122, No. 1, 2000, pp. 55–64.
- 15) Ai, X. and Cheng, H. S., "The Influence of Moving Dent on Point EHL Contacts," Tribol. Trans., Vol. 37, No. 2, 1994, pp. 323–335.

- 16) Ai, X. and Lee, S. C., "Effect of Slide-to-Roll Ratio on Interior Stresses Around a Dent in EHL Contacts," *Tribol. Trans.*, Vol. 39, No. 4, 1996, pp. 881-889.
- 17) Xu, G., Sadeghi, F., and Hoeprich, M. R., "Dent Initiated Spall Formation in EHL Rolling/Sliding Contact," *Trans. ASME F*, Vol. 120, No. 3, 1998, pp. 453-462.
- 18) Shimizu, K., Hirota, T., Nagata, H., Ishihara, T., and Imajou, Y., "Effects of Indentation on Bearing Surface Fatigue Based on an X-Ray Analysis of Residual Stress," *Fujikoshi Eng. Rev.*, Vol. 49, No. 2, 1993, pp. 29-48.
- 19) Morales-Espejel, G. E., and Gabelli, A., "The Behavior of Indentation Marks in Rolling-Sliding Elastohydrodynamically Lubricated Contacts," *Tribol. Trans.*, Vol. 54, No. 4, 2011, pp. 589-606.
- 20) Ueda, T. and Mitamura, N., "Mechanism of Dent Initiated Flaking and Bearing Life Enhancement Technology Under Contaminated Lubrication Condition. Part 1: Effect of Tangential Force on Dent Initiated Flaking," *Tribol. Int.*, Vol. 41, No. 11, 2008, pp. 965-974.
- 21) Hashimoto, S., Ueda, K., Ueda, T., and Mitamura, N., "Effect of Tangential Force on Surface Originated Flaking of Rolling Bearing," *Proceedings of the International Tribology Conference, Hiroshima, Japan, Oct 30-Nov 3, 2011.*
- 22) Soda, N. and Yamamoto, T., "The Role of Surface Traction for the Pitting on Gear Teeth," *J. JSLE*, Vol. 20 1975, pp. 268-278.
- 23) Ueda, T. and Mitamura, N., "Mechanism of Dent Initiated Flaking and Bearing Life Enhancement Technology Under Contaminated Lubrication Condition. Part II: Effect of Rolling Element Surface Roughness on Flaking Resulting From Dents, and Life Enhancement Technology of Rolling Bearings Under Contaminated Lubrication Condition," *Tribol. Int.*, Vol. 42, Nos. 11-12, 2009, pp. 1832-1837.
- 24) Skurka, J. C., "Elastohydrodynamic Lubrication of Roller Bearings," *Trans. ASME F*, Vol. 92, 1970, pp. 281-291.
- 25) Tallian, T. E., "On Competing Failure Modes in Rolling Contact," *ASLE Trans.*, Vol. 10, No. 4, 1967, pp. 418-439.
- 26) Takata, H. and Aihara, S., "Effect of Oil Film Thickness Upon Rolling Fatigue Life," *NSK Bear. J.*, Vol. 636, 1977, pp. 11-16.
- 27) Takemura, H., Mitamura, N., and Murakami, Y., "Rolling Bearing Fatigue in Low Lambda Regions," *Proceedings of the ISATA, 31th ISATA, Aachen, Germany, Oct 31-Nov 4, 1994,* pp. 71-78.



Hiroki Komata



Yasuhiro Iwanaga



Tohru Ueda



Koji Ueda

Relationship between Supplied Oil Flow Rates and Oil Film Thicknesses under Starved Elastohydrodynamic Lubrication

Taisuke Maruyama* and Tsuyoshi Saitoh

NSK Ltd., 1-5-50 Kugenumashinmei, Fujisawa-shi, Kanagawa 251-8501, Japan;

E-Mail: saitou-ts@nsk.com

*Author to whom correspondence should be addressed; E-Mail: maruyama-ta@nsk.com;

Tel.: +81-466-21-3224; Fax: +81-466-27-9766.

Academic Editors: Romeo P. Glovnea and Michel Fillon

Received: 12 December 2014 / Accepted: 8 April 2015 / Published: 28 April 2015

Abstract

Many studies have already considered starved lubrication. However, there have been no reports on the oil film thicknesses under steady starved EHL (elastohydrodynamic lubrication), where the ultra-low volume of oil supplied per unit time is uniform. The present study examined the relationship between the supplied oil flow rate and oil film thickness under steady starved lubrication. A ball-on-disk testing machine was used in experiments to measure the oil film thickness by means of optical interferometry. A microsyringe pump was used to accurately control the supplied oil flow rate. The supplied oil flow rate was kept constant, and the minimum oil film thickness was measured for 1 h after the start of the tests to determine the relationship between the supplied oil flow rate and oil film thickness.

Keywords: starvation; EHL; oil film thickness; oil quantity; point contacts

1. Introduction

Rolling bearings are used in load support^[1] and power transmission of various machines. The supplied oil flow rate is an important parameter that affects the bearing life and friction torque. In order to keep the bearing life long, the supplied oil flow rate must be high enough to form an oil film thicker than the surface roughness of raceway. However, an excessive supplied oil flow rate increases the bearing torque. Therefore, bearings should ideally be lubricated at the minimum supplied oil flow rate. Moreover, minimizing the amount of waste oil can also contribute to solving several problems, such as churning heating effect and ensuing emissions, side leakage out of contact, spillage, cost, conservation of environment, and so on.

Many studies have examined the oil film thickness under starved EHL (elastohydrodynamic lubrication). Wedeven *et al.*^[2] studied the effects of the lubricating oil distribution at EHL inlet areas on the oil film thickness. Based on the fact that no hydrodynamic pressure was generated in contact areas when EHL inlet areas were starved, they found that the horseshoe shapes peculiar to EHL disappeared and that oil film thickness distributions similar to those in the case of Hertzian contact were formed. Furthermore, they theoretically determined the minimum meniscus lengths at EHL inlet areas to prevent starved lubrication. Liu *et al.*^[3], Parinam *et al.*^[4] and Wang *et al.*^[5] proposed an equation that represents the

degree of starvation at EHL contact. They stated that the oil film thickness under starved lubrication can be estimated from the thickness of liquid film existing at EHL inlet areas. Moreover, Mohammadpour *et al.*^[6] indicated inlet and outlet boundary condition using entrainment flow with partial counter-flow in pure rolling EHL point contacts. Wolveridge *et al.*^[7], Yang *et al.*^[8] and Mihailidis *et al.*^[9] calculated the starved oil film thickness in the case of line contacts. Chevalier *et al.*^[10] pointed out that predicting the reduction in the oil film thickness is difficult in the case of completely starved lubrication where no meniscus lengths exist. They proposed an approach where the reduction in oil film thickness is predicted from the volume of the supplied oil existing on surfaces. Guangteng *et al.*^[11] and Cann^[12] performed experiments using optical interferometry to examine the relationship between the rolling speed and oil film thickness and found that starved lubrication occurred when the speed was increased above a certain value. Cann *et al.*^[13,14] also investigated the transition of oil film and considered situations where the oil film thickness decreased with time. Svoboda *et al.*^[15] described the transition between fully flooded and starved lubrication in EHL point contacts with surface texturing. Damiens *et al.*^[16] and Yin *et al.*^[17] studied the starved EHL condition in the case of ellipsoidal contacts. They compared the above case with a case involving point contacts. Gershuni *et al.*^[18] conducted ball-on-disk tests

and observed the grease replenishment. Wang *et al.*^[19] measured and analyzed the oil film thickness under pure rolling reciprocating motions. They found that using the EHL theory based on starved lubrication produced results very close to the experimental values.

However, there have been no reports on the oil film thickness under steady starved lubrication when the ultra-low volume of oil supplied per unit time is uniform. In other words, no basic data exist for cases where the supplied oil flow rate is controlled in the manner of oil-air lubrication. Actually, Chiu^[20] had already estimated the meniscus distance from the contact center as a function of the supplied oil flow rate. Nevertheless, they indicated that there was no significant dependence of meniscus distance on oil flow rate within their limits examined (from 5 to 100 drops per minute). Thus, the present study investigated the relationship between the supplied oil flow rate and oil film thickness under steady starved lubrication where the supplied oil flow rate was kept constant. Moreover, these experiments were conducted under the ultra-low oil flow rate (less than $1.67 \times 10^{-1} \text{ mm}^3/\text{s}$) to reveal the influence of oil flow rate on oil film thickness. This paper reports the results.

2. Experimental Methods

Figure 1 shows the schematic of the point contact EHL testing machine (ball-on-disk type) used in this research. With this device, light was emitted from a white light source to the Hertzian contact area, and the interference fringe was subjected to a spectrometer. The results were photographed with a high-speed video camera. Table 1 presents the specifications of the high-speed video camera. The oil film thickness was calculated from the wavelengths of resulting spectroscopic images.

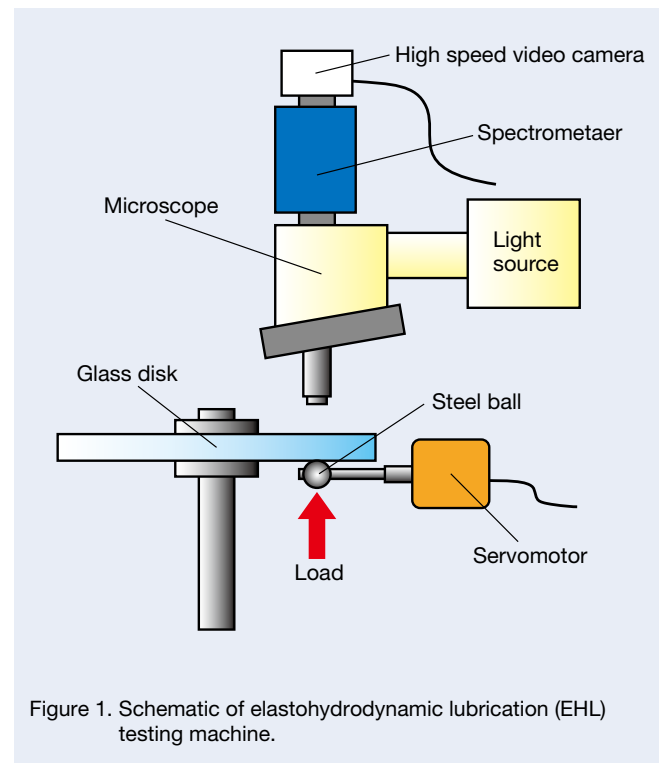


Figure 1. Schematic of elasto-hydrodynamic lubrication (EHL) testing machine.

Table 1. Camera specifications.

Image pickup device	CMOS
Number of pixels	512 × 512 pixels
Frame rate	500 frames/s

Figure 2 shows an enlarged view of the test portion. A semi-reflective Cr layer was attached to one side of the glass disk specimen. A SiO₂ spacer layer was placed on this Cr layer. The thickness of the spacer layer was approximately 800 nm. A ball specimen was pressed against the lower side of this disk specimen. The oil film thickness was measured by the spacer layer method^[21].

A microsyringe pump was used to supply a trace amount of lubricating oil to the contact area. The minimum oil flow rate provided by the microsyringe pump was $1.67 \times 10^{-3} \text{ mm}^3/\text{s}$. The oil filler port of this microsyringe pump was pressed against the disk, as shown in Figure 2, and oil was supplied to the contact area based on the centrifugal force generated by the rotation of the disk. In this manner, a sufficient amount of lubricating oil was already applied to the disk specimen before the start of the test—that is, the test was started under fully flooded lubrication. In order to keep the centrifugal force acting on the lubricating oil constant, the position where the ball specimen was to be pressed against the disk specimen was fixed at a location 40 mm away from the center of the disk specimen. Table 2 gives the specifications of the ball test and glass disk specimens, and Table 3 presents the test conditions.

Figure 3 shows a view of the interference fringe in the contact area. In this study, the oil film profiles were observed along the Y-axis ($X = 0$), which was perpendicular to the rolling direction. In this paper, the disk rotation center side is referred to as the “inside”, and the outer side of the disk is referred to as the “outside”.

Table 2. Specimens.

	Ball specimen	Disk specimen
Diameter	25.4 mm	100 mm
Material	SUJ2	BK7 (Glass)
Young's modulus	210 GPa	73.1 GPa
Poisson's ratio	0.3	0.23
Surface roughness	8.1 nmRa	2.3 nmRa

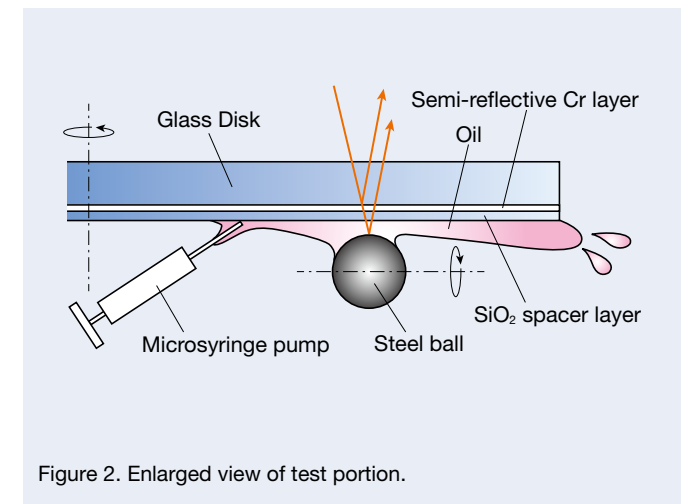


Figure 2. Enlarged view of test portion.

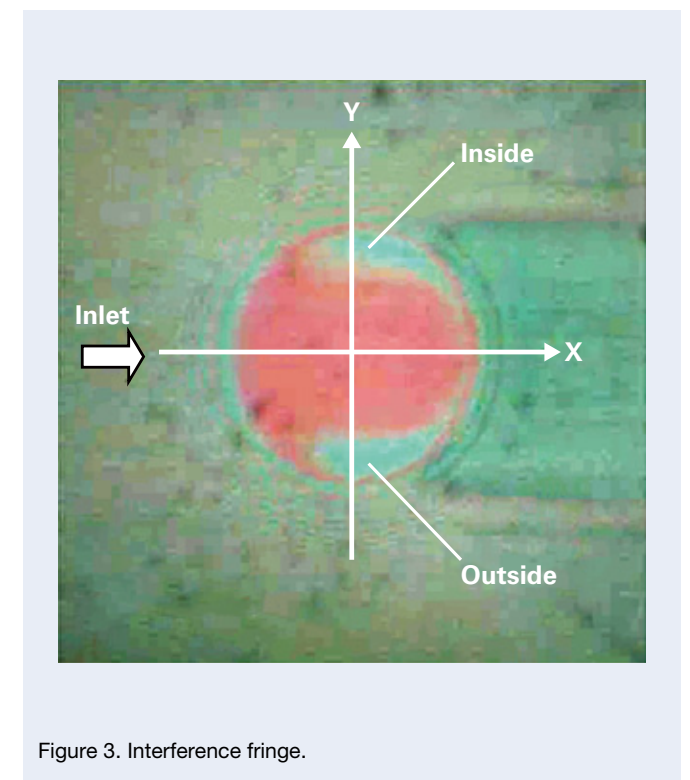


Figure 3. Interference fringe.

3. Experimental Results

3.1 Preparatory Experiments

First, the transition of oil film thickness without oil resupply was measured to find the experimental conditions of starved lubrication in this study. A test was carried out where a sufficient amount of lubricating oil was first applied to the disk specimen, and the results confirmed the starved lubrication process. Figure 4 shows the transition of the interference fringe when the rolling speed was 1.8 m/s. The interference fringe was confirmed to be symmetrical about the X-axis. The interference fringe lost symmetry 1 h after the start of the test. The thin oil film portion called the horseshoe-shaped zone was only left on the 'inside'. The starved area (oil/air meniscus) of the EHL inlet region, which was small as shown by the left chart of Figure 4, became very large, as shown by the right chart. Thus, the starved area extended to the contact area.

Table 3. Test conditions.

Temperature	25 °C
Oil	Poly-alpha-olefin oil (PAO)
Kinematic viscosity	19 mm ² /s at 40 °C
Load	29.7 N
Maximum contact pressure	0.49 GPa
Radius of Hertzian contact	170 μm
Contact radius	40 mm
Rolling speed	0.6 m/s to 1.8 m/s
Slide-to-roll ratio	0%
Supplied oil flow rate	0 mm ³ /s to 1.67 × 10 ⁻¹ mm ³ /s

Figure 5 shows the transition of the oil film profile. Immediately after the start of the test, the oil film profile was laterally symmetric, and the oil film became thinner only on the "outside" over time. The centrifugal force generated in the rotating disk acted from the "inside" to the "outside". The oil film only became thinner on the "outside" because the lubricating oil became starved owing to the effect of the centrifugal force. Wedeven *et al.*, observed similar interference fringes in their test results [2]. The oil film thickness on the "inside" did not change because the lubricating oil applied to the rotation center side was replenished under the effect of the centrifugal force.

Figures 6 and 7 show the measurement results when the rolling speed was reduced to 1.2 m/s. Figure 6 shows that the starved area 1 h after the start of the test was smaller than that shown in Figure 4. Also, Figure 7 shows that the position where the oil film became thinner was not located at the edge of the "outside" but shifted a little to the inside of the contact area. The amount of reduction in the oil film

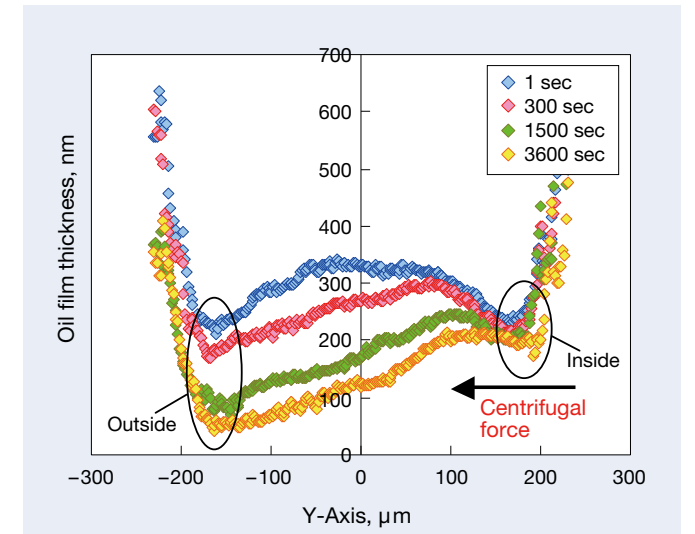


Figure 5. Transition of oil film profile: Y-axis. Rolling speed = 1.8 m/s.

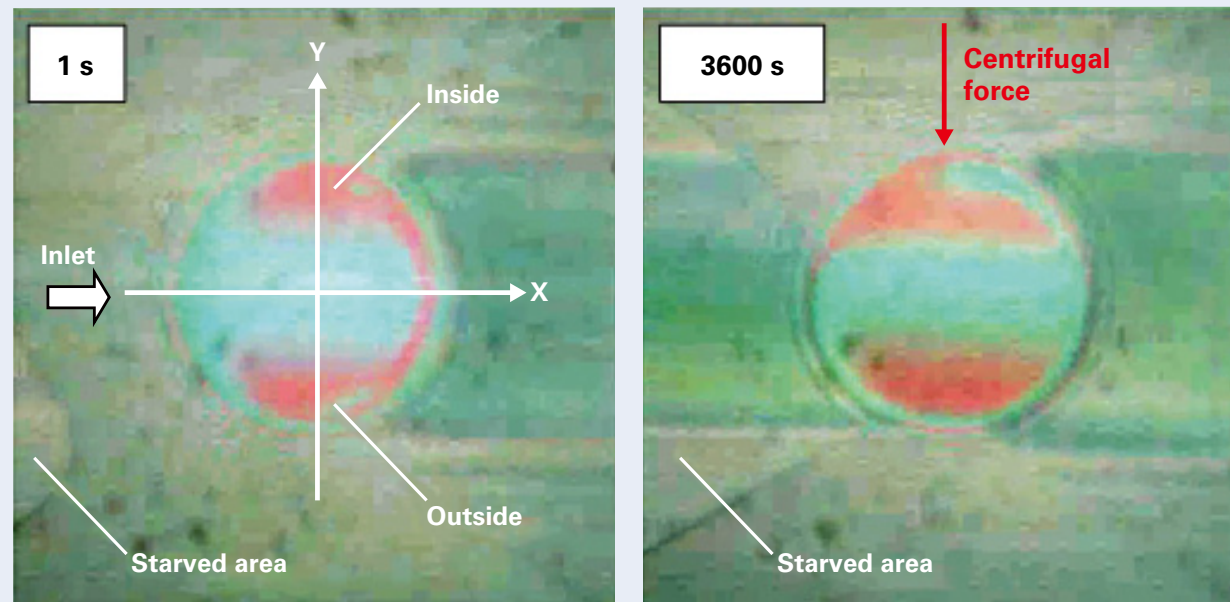


Figure 4. Transition of interference fringe: (left) 1 s later, (right) 3600 s later. Rolling speed = 1.8 m/s.

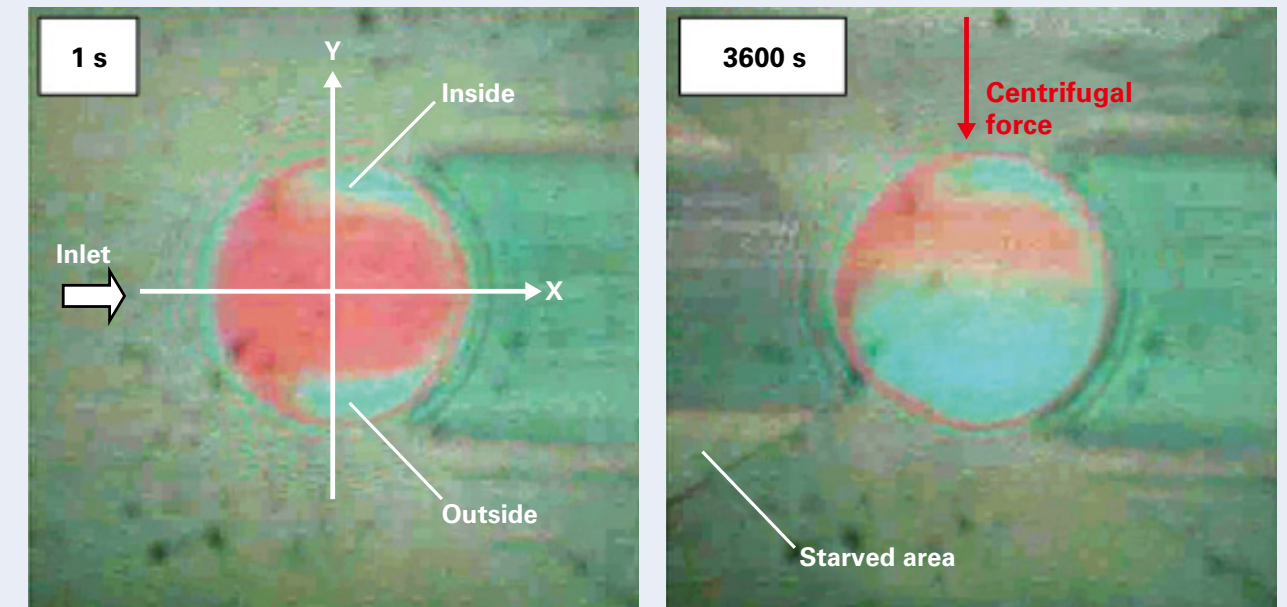


Figure 6. Transition of interference fringe: (left) 1 s later, (right) 3600 s later. Rolling speed = 1.2 m/s.

thickness also decreased. These results were caused by the fact that the centrifugal force was reduced by the decrease in the rolling speed. Because the centrifugal force dropped, the racetrack was replenished with lubricating oil from the wettability effect of the oil.

Figures 8 and 9 shows the measurement results when the rolling speed was reduced to 0.6 m/s. As shown in Figure 8, even 1 h after the start of the test, the starved area located at the EHL inlet region did not extend to the EHL contact area. Figure 9 shows that the oil film profile 1 h after the start of the test underwent almost no change compared to the corresponding profile immediately after the start. That is, the results confirmed that a lower speed produced a smaller centrifugal force acting on the lubricating oil, which lessened the tendency for starved lubrication.

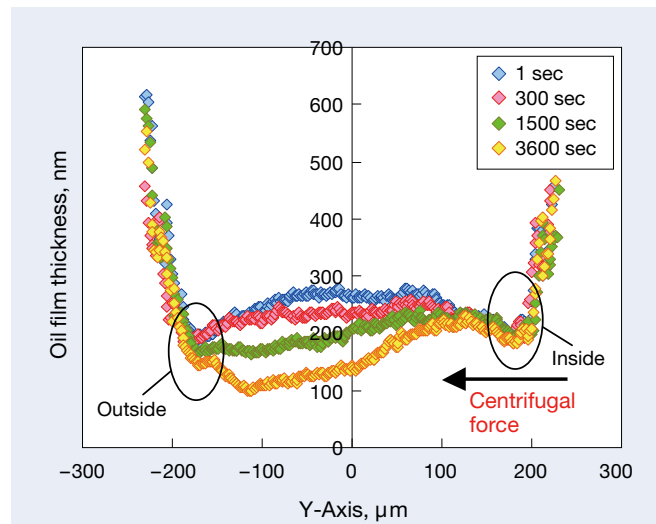


Figure 7. Transition of oil film profile: Y-axis. Rolling speed = 1.2 m/s.

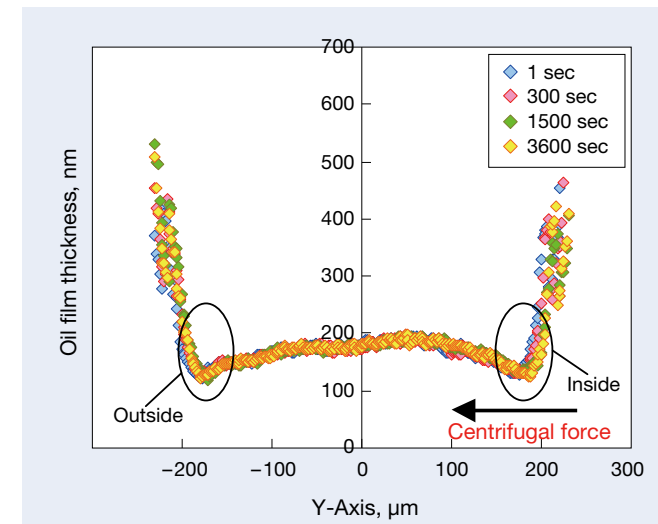


Figure 9. Transition of oil film profile: Y-axis. Rolling speed = 0.6 m/s.

Figure 10 shows the relationship between the rolling speed and minimum oil film thickness (minimum values on Y-axis). The oil film thickness immediately after the start of the test increased with the rolling speed. This result is approximately the same as that from the Hamrock-Dowson equation^[22]. However, when the rolling speed was 1.2 m/s or more, higher speeds meant reduced oil film thicknesses 1 h after the start of the test. These results agree with those of Guangteng *et al.*^[11], Cann *et al.*^[12] and Chiu^[20]. Based on the above results, the rolling speed to reproduce starved lubrication was taken to be 1.8 m/s in this study.

Figure 11 shows the chronological changes in the minimum oil film thickness. Although no change occurred when the rolling speed was low, the oil film thickness decreased with time when the rolling speed was high. When the rolling speed was 1.8 m/s, the oil film thickness was almost constant at approximately 50 nm from 2700 s or more after the start of the test. Consequently, in this study, lubrication was considered to be in a steady starved lubrication 1 h after the start of the test.

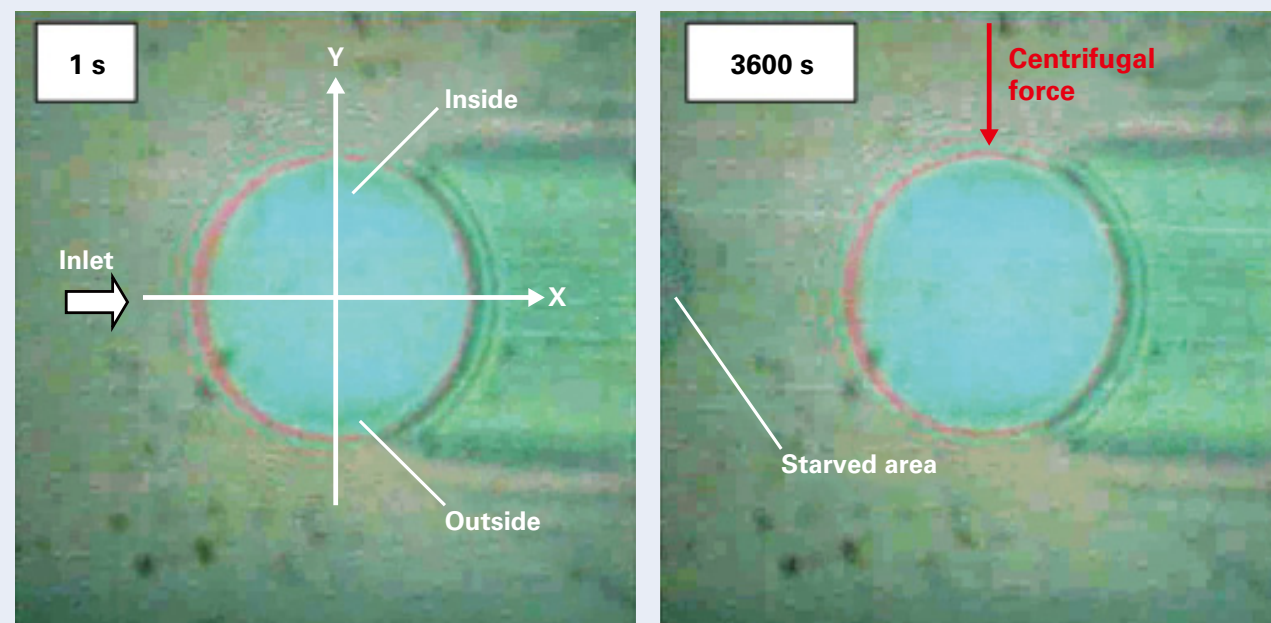


Figure 8. Transition of interference fringe: (left) 1 s later, (right) 3600 s later. Rolling speed = 0.6 m/s.

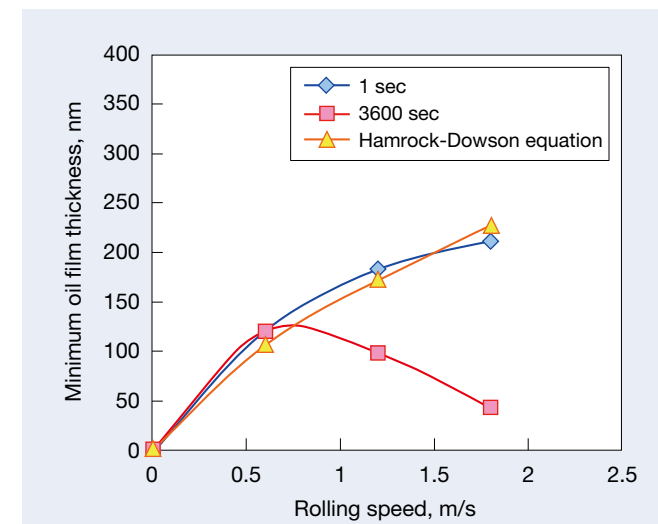


Figure 10. Relationship between rolling speed and minimum oil film thickness.

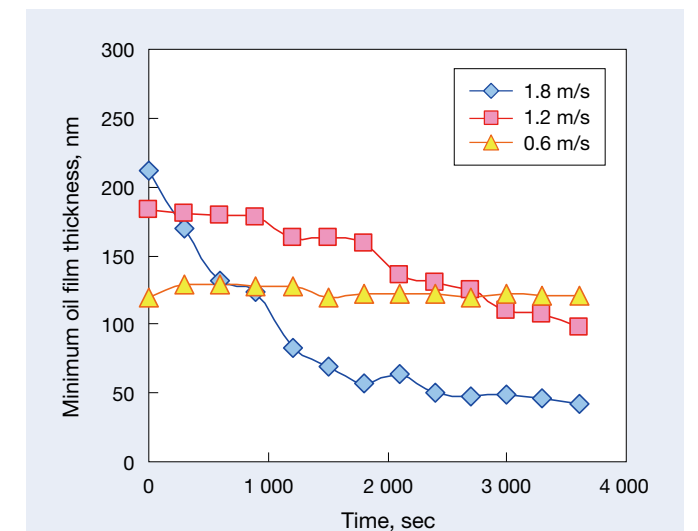


Figure 11. Transition of minimum oil film thickness.

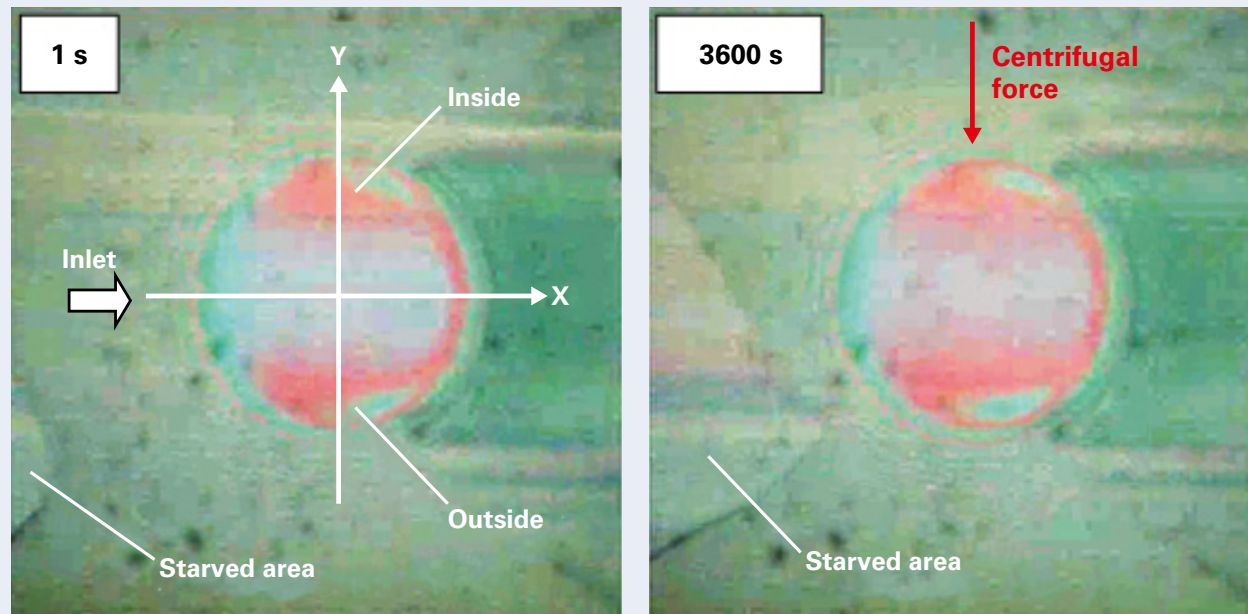


Figure 12. Transition of interference fringe: (left) 1 s later, (right) 3600 s later. Supplied oil flow rate = $1.67 \times 10^{-1} \text{ mm}^3/\text{s}$.

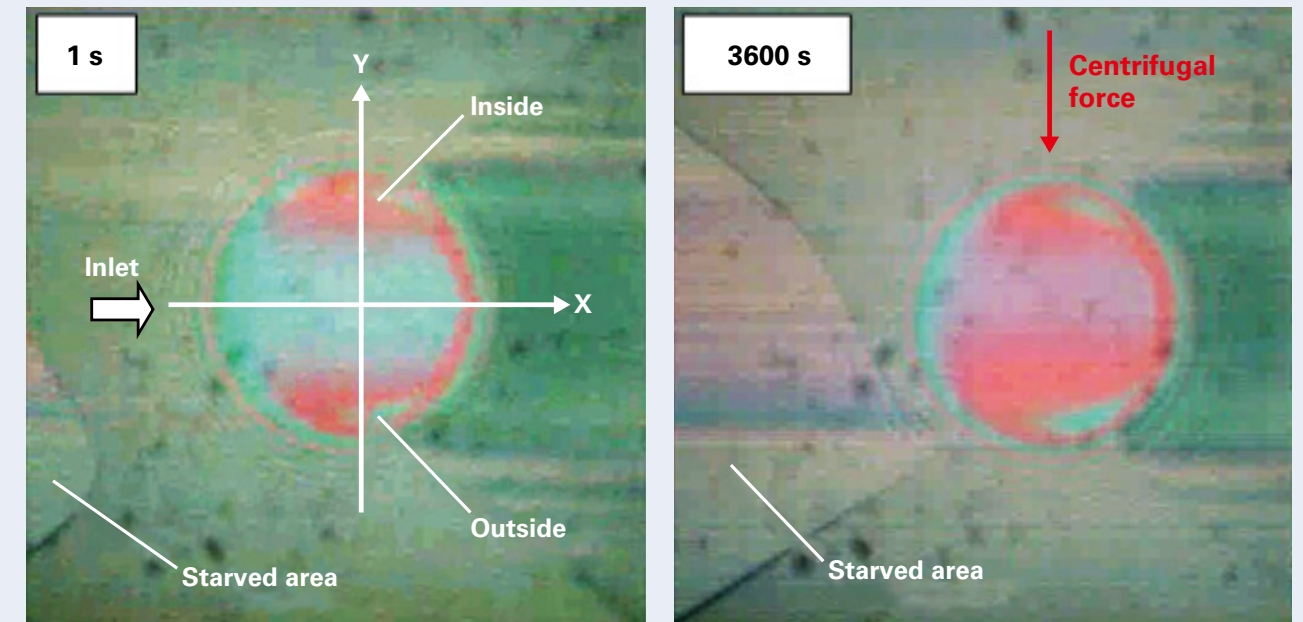


Figure 14. Transition of interference fringe: (left) 1 s later, (right) 3600 s later. Supplied oil flow rate = $1.67 \times 10^{-2} \text{ mm}^3/\text{s}$.

3.2 Relationship between Supplied Oil Flow Rates and Oil Film Thicknesses

The oil film thickness was then measured for different supplied oil flow rates, which were changed from $1.67 \times 10^{-3} \text{ mm}^3/\text{s}$ to $1.67 \times 10^{-1} \text{ mm}^3/\text{s}$. The results of these measurements are given below.

First, the oil film thickness was measured when the supplied oil flow rate was set to $1.67 \times 10^{-1} \text{ mm}^3/\text{s}$. Figures 12 and 13 shows the results of these measurements. Figure 12 shows that, 1 h after the start of the test, the starved area at the EHL inlet region was larger than that immediately after the start of the test. However, it did not extend to the EHL area, and the interference fringe formed a horseshoe shape that was almost symmetrical about the X-axis. According to the oil film profile shown in Figure 13, the oil film thickness did not decrease at all. Therefore, when the rolling speed is 1.8 m/s, sufficient lubrication can be achieved by setting the supplied oil flow rate to $1.67 \times 10^{-1} \text{ mm}^3/\text{s}$.

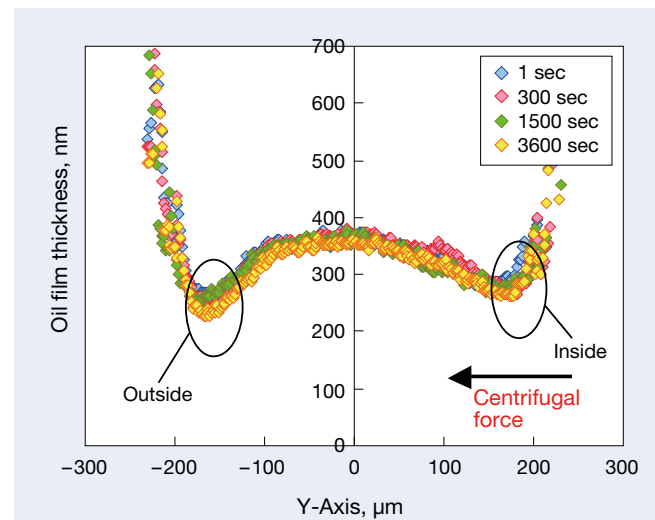


Figure 13. Transition of oil film profile: Y-axis. Supplied oil flow rate = $1.67 \times 10^{-1} \text{ mm}^3/\text{s}$.

Figures 14 and 15 show the oil film measurements when the supplied oil flow rate was set to $1.67 \times 10^{-2} \text{ mm}^3/\text{s}$. The starved area shown in Figure 14 was larger than that shown in Figure 12 but did not extend to the EHL contact area. According to Figure 15, the oil film on the “outside” was a little thinner in the profile 300 s after the start of the test. Therefore, the lubrication was considered to be in a state of starved lubrication when the supplied oil flow rate was $1.67 \times 10^{-2} \text{ mm}^3/\text{s}$. Furthermore, the oil film thickness was constant 300 s after the start of the test.

Figures 16 and 17 show the oil film measurements when the supplied oil flow rate was set to $1.67 \times 10^{-3} \text{ mm}^3/\text{s}$. Figure 16 shows that that the starved area at the EHL inlet region was even larger than that in Figure 14 and extended to the EHL contact area. Figure 17 shows that the oil thickness decreased with time and that the amount of reduction was larger on the “outside”.

Figure 18 shows the transition of the minimum oil film thickness when the supplied oil flow rate was changed. A higher supplied oil flow rate decreased the time for the oil film thickness to become constant. In addition, a lower supplied oil flow rate produced a thinner oil film thickness.

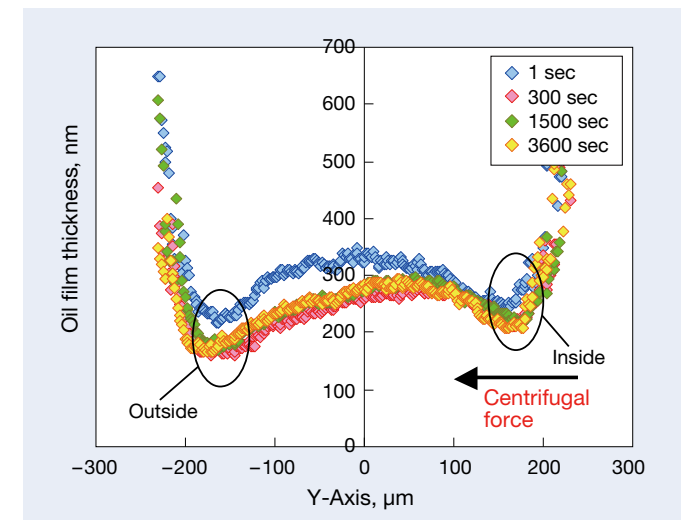


Figure 15. Transition of oil film profile: Y-axis. Supplied oil flow rate = $1.67 \times 10^{-2} \text{ mm}^3/\text{s}$.

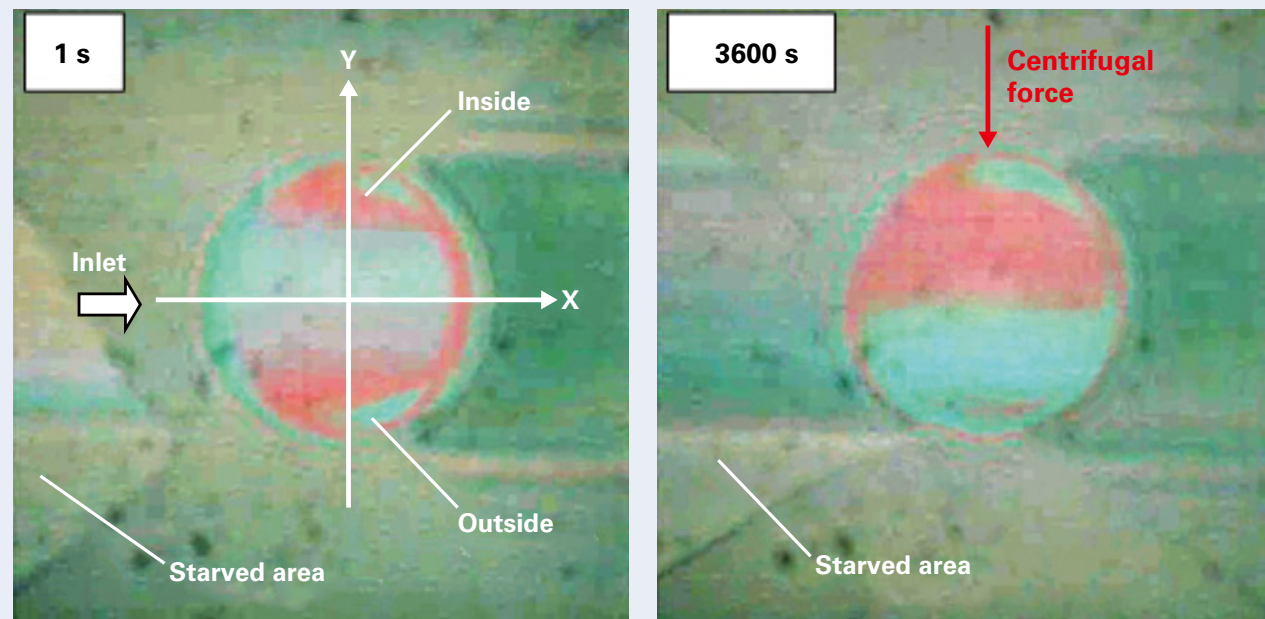


Figure 16. Transition of interference fringe: (left) 1 s later, (right) 3600 s later. Supplied oil flow rate = $1.67 \times 10^{-3} \text{ mm}^3/\text{s}$.

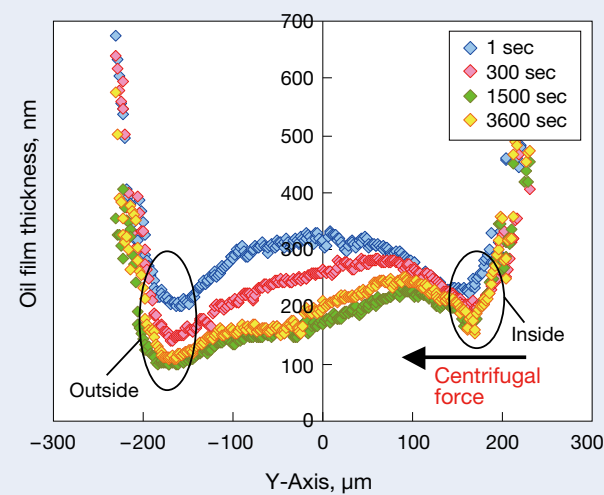


Figure 17. Transition of oil film profile: Y-axis. Supplied oil flow rate = $1.67 \times 10^{-3} \text{ mm}^3/\text{s}$.

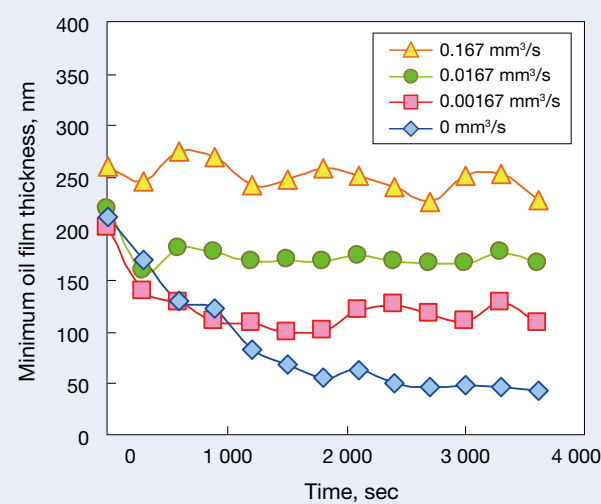


Figure 18. Transition of minimum oil film thickness.

4. Discussion

Figure 19 shows the relationship between the supplied oil flow rate Q and minimum oil film thickness h_{\min} 1 h after the start of the test. The values resulting from the Hamrock-Dowson equation and the measured oil film thickness without oil resupply ($Q = 0 \text{ mm}^3/\text{s}$) are shown together. When the supplied oil flow rate was approximately $10^{-1} \text{ mm}^3/\text{s}$ or more, oil films formed to approximately the same thicknesses as those from the Hamrock-Dowson equation. Therefore, fully flooded lubrication was achieved in this domain. When the supplied oil flow rate was reduced to approximately $10^{-2} \text{ mm}^3/\text{s}$ or less, the oil thickness gradually became thinner. Consequently, the starved lubrication was assumed to occur in this domain. When the supplied oil flow rate was reduced to $1.67 \times 10^{-3} \text{ mm}^3/\text{s}$, the oil film thickness was twice or more the corresponding thickness achieved without oil resupply. In consequence, even a very low lubricant flow rate was confirmed to contribute to lubrication.

Rauscher et al., theoretically determined the relationship between the supplied oil flow rate Q and thickness h_{∞} of liquid on a rotating disk [23]. If the radius coordinate r on a disk specimen satisfies equation (1), then the liquid film thickness h_{∞} is sufficiently small compared to r .

$$r \gg \left(\frac{9Q^2}{4\pi^2\nu\omega} \right)^{1/4} \quad (1)$$

where ν is the kinematic viscosity of lubricating oil and ω is the angular velocity of the disk specimen. Therefore, they considered the following approximation to hold.

$$\frac{\partial h_{\infty}}{\partial r} \approx 0 \quad (2)$$

In this study, the value of Q was so low that Equation (1) was sufficiently satisfied. Based on the Navier-Stokes equations, they approximated the liquid film thickness h_{∞} by Equation (3).

$$h_{\infty} = \left(\frac{3Q\nu}{2\pi\omega^2r^2} \right)^{1/3} \quad (3)$$

On the other hand, Wedeven et al. [1] experimentally estimated the distance x_b from the inlet lubricant boundary to the center of the Hertzian contact by Equation (4).

$$x_b = a + \left(\frac{h_b/h_c - 1}{1.21} \right)^{2/3} \frac{(Rh_c)^{2/3}}{a^{1/3}} \quad (4)$$

where a is the Hertzian radius, h_b is the liquid film thickness at lubricant boundary, h_c is the central oil film thickness and R is the radius of ball specimen. According to Equations (3) and (4), the inlet distance x_b can be calculated if the liquid film thickness h_{∞} on the disk specimen is regarded as the liquid film thickness h_b at lubricant boundary.

Furthermore, Hamrock et al. [24] calculated the minimum oil film thickness $h_{\min,S}$ under starved lubrication by Equation (5).

$$h_{\min,S} = h_{\min,F} \left(\frac{\frac{x_b}{a} - 1}{3.34 \left(\left(\frac{R}{a} \right)^2 \frac{h_{\min,F}}{R} \right)^{0.58}} \right)^{0.25} \quad (5)$$

where $h_{\min,F}$ is the minimum oil film thickness under fully flooded lubrication. From those equations, the minimum oil film thickness $h_{\min,S}$ under starved lubrication can be calculated by the supplied oil flow rate Q . Figure 19 also shows the minimum oil film thickness as a function of the supplied oil flow rate for the calculated results by Equation (5), comparing with the experimental results. It can be seen that the calculated results disagree with the results of experiments. This is because h_{∞} was assumed to be h_b . In fact, the lubricating oil was supplied into a racetrack under a centrifugal force. However, Figure 19 indicates that h_b was much thinner than h_{∞} due to the racetracks, generated behind EHL contact areas.

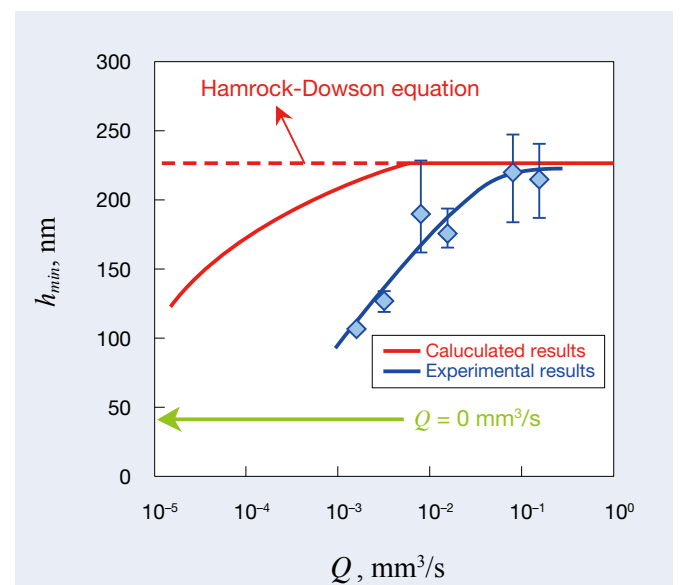


Figure 19. Relationship between supplied oil flow rate and minimum oil film thickness (3600 s later).

5. Conclusions

In this research, the ultra-low volume of oil supplied per unit time was assumed to be constant, and the relationship between the supplied oil flow rate and oil film thickness under steady starved lubrication was investigated. The obtained results are presented below:

1. An oil film measurement method using a microsyringe pump was developed to reproduce starved lubrication by means of an EHL testing machine.
2. Based on the Hamrock-Dowson equation, with fully flooded lubrication, the oil film thickness increases with the rolling speed; with starved lubrication, the oil film thickness decreases because the lubricating oil is affected by centrifugal forces.
3. The oil film thickness on the “outside” of an EHL contact area becomes lower than that on the “inside”. This is also caused by the fact that the lubricating oil is affected by centrifugal forces.
4. The relationship between the supplied oil flow rate and oil film thickness was determined. In this relationship, if the supplied oil flow rate is set to approximately 10^{-2} mm³/s or less, the minimum oil film thickness decreases with the decrease of the supplied oil flow rate.
5. The minimum oil film thickness $h_{min,S}$ under starved lubrication was calculated by the supplied oil flow rate Q . However, the calculated results didn't agree with the experimental results, which meant that h_s was much thinner than h_w because the racetracks were generated behind EHL contact areas.

In practice, it is considered that bearings are almost always used in the starved lubrication, irrespective of the supplied meniscus distance due to the racetrack generation. For instance, eccentric loads of roller bearings [1] may affect the outlet conditions even when the fully flooded lubrication is assumed. On the other hand, it was indicated that the surface tension could replenish the lubricant in the racetrack and prevent the starved lubrication [20]. Therefore, it is significantly important to consider the influence of outlet conditions on starved lubrication, as pointed by Mohammadpour et al. [6]. It is hoped that the results of this study will contribute to a better understanding of starved lubrication, and to the development of bearings.

Author Contributions

Taisuke Maruyama performed the experiments, analyzed the data, and wrote the paper. Tsuyoshi Saitoh supervised this work.

Conflicts of Interest

The authors declare no conflict of interest.

References

- 1) Johns, P.M.; Gohar, R. Roller bearings under radial and eccentric loads. *Tribol. Int.* 1981, 14, 131–136.
- 2) Wedeven, L.D.; Evans, D.; Cameron, A. Optical analysis of ball bearing starvation. *ASME Trans. J. Lubricat. Technol.* 1971, 93, 349–363.
- 3) Lui, J.; Wen, S. Fully flooded starved and parched lubrication at a point contact system. *Wear* 1992, 159, 135–140.
- 4) Parinam, A.; Karan, R. Analysis of starved EHL line contacts for lubricants with linear pressure viscosity dependence. *Int. J. Adv. Technol.* 2014, 5, 11–27.
- 5) Wang, W.Z.; Li, S.; Shen, D.; Zhang, S.; Hu, Y.Z. A mixed lubrication model with consideration of starvation and interasperity cavitations. *Proc. Inst. Mech. Eng. J J. Eng. Tribol.* 2012, 226, 1023–1038.
- 6) Mohammadpour, M.; Johns-Rahnejat, P.M.; Rahnejat, H.; Gohar, R. Boundary conditions for elastohydrodynamics of circular point contacts. *Tribol. Lett.* 2014, 53, 107–118.
- 7) Wolveridge, P.E.; Baglin, K.P.; Archard, J.F. The starved lubrication of cylinders in line contact. *Proc. Inst. Mech. Engrs.* 1970–1971, 185, 1159–1169.
- 8) Yang, P.; Wang, J.; Kaneta, M. Thermal and non-Newtonian numerical analyses for starved EHL line contacts. *J. Tribol.* 2006, 128, 282–290.
- 9) Mihailidis, A.; Agouridas, K.; Panagiotidis, K. Non-Newtonian starved thermal-elastohydrodynamic lubrication of finite line contacts. *Tribol. Trans.* 2013, 56, 88–100.
- 10) Chevalier, F.; Lubrecht, A.A.; Cann, P.M.E.; Colin, F.; Dalmaz, G. Film thickness in starved EHL point contacts. *ASME J. Tribol.* 1998, 120, 126–133.
- 11) Guangteng, G.; Cann, P.M.; Spikes, H.A. A study of parched lubrication. *Wear* 1992, 153, 91–105.
- 12) Cann, P.M. The transition between fully flooded and starved regimes in EHL. *Tribol. Int.* 2004, 37, 859–864.
- 13) Cann, P.M.E.; Chevalier, F.; Lubrecht, A.A. Track depletion and Replenishment in a grease lubricated point contact: A quantitative analysis. *Tribol. Series* 1997, 32, 405–413.
- 14) Cann, P.M. Starved grease lubrication of rolling contacts. *Tribol. Trans.* 1999, 42, 867–873.
- 15) Svoboda, P.; Košťál, D.; Popelka, M.; Krupka, I. The experimental study of transition between fully flooded and starved regime in EHL contact. *Eng. Mech.* 2013, 20, 13–25.
- 16) Damiens, B.; Venner, C.H.; Cann, P.M.E.; Lubrecht, A.A. Starved lubrication of elliptical EHD contacts. *ASME J. Tribol.* 2004, 126, 105–111.
- 17) Yin, C.; Yang, P.; Tan, H.; Wang, J. Thermal elastohydrodynamic lubrication of starved elliptical contacts. *Tribol. Int.* 2009, 42, 964–974.
- 18) Gershuni, L.; Larson, M.G.; Lugt, P.M. Lubricant replenishment in rolling bearing contacts. *Tribol. Trans.* 2008, 51, 643–651.
- 19) Wang, J.; Hashimoto, T.; Nishikawa, H.; Kaneta, M. Pure rolling elastohydrodynamic lubrication of short stroke reciprocating motion. *Tribol. Int.* 2005, 38, 1013–1021.
- 20) Chiu, Y.P. An analysis and prediction of lubricant film starvation in rolling contact systems. *Tribol. Trans.* 1974, 17, 22–35.
- 21) Johnston, G.J.; Wayte, R.; Spikes, H.A. The measurement and study of very thin lubricant films in concentrated contacts. *Tribol. Trans.* 1991, 34, 187–194.
- 22) Hamrock, B.J.; Dowson, D. Isothermal elastohydrodynamic lubrication of point contacts: Part III—fully flooded results. *ASME Trans. J. Lubricat. Technol.* 1977, 99, 264–275.
- 23) Rauscher, J.W.; Kelly, R.E.; Cole, J.D. An asymptotic solution for the laminar flow of a thin film on a rotating disk. *Trans. ASME J. Appl. Mech.* 1973, 40, 43–47.
- 24) Hamrock, B.J.; Dowson, D. Isothermal elastohydrodynamic lubrication of point contacts: Part IV—starvation results. *ASME Trans. J. Lubricat. Technol.* 1977, 99, 15–23.

© 2015 by the authors; licensee MDPI, Basel, Switzerland. This article is an open access article distributed under the terms and conditions of the Creative Commons Attribution license (<http://creativecommons.org/licenses/by/4.0/>).

BELTOP8 High-Reliability and Low-Friction Ball Bearings for CVTs

The belt CVT is a mainstream automotive transmission in markets such as Japan and China, as this transmission features both excellent fuel consumption and smooth running. The belt CVT, which transmits engine power through use of a belt and pulley, is capable of changing speed continuously in a stepless manner. The requirements of a rolling bearing that supports the pulley include the ability to perform belt-drive power transmission under heavy load and without breakage, high rigidity that sufficiently prevents the belt from tilting or loading irregularly, and durability that prevents the housing from wearing.

Meanwhile, with the aim of improving the fuel economy of automobiles, demand is growing for smaller/lighter and more efficient transmissions, and rolling bearings used in transmissions are also required to be compact/lightweight and with low friction.

In view of such circumstances, NSK announced in 2011 high-reliability, low-friction ball bearings that contribute to improving the reliability and efficiency of CVTs. Now, a newly developed BELTOP8 (Photo 1) is introduced below, to which two new functions were added that contribute to the need for compactness and light weight.



Photo 1 BELTOP8

1. Configuration, Structure, and Specifications

As shown in Figure 1, BELTOP8 has the following eight features in configuration.

1. Longer life by special heat treatment (UR, HTF) of inner and outer rings
2. Longer life and improved seizure resistance by special heat treatment (UR, EQTF) of balls
3. Longer life, lower friction, and lighter weight due to plastic cage
4. Sophisticated functions by setting appropriate internal specifications
5. Compact and lightweight bearings (narrow offset groove)
6. Creep prevention by introducing a creep-less outer ring (high rigid outer ring)
7. Prevention of housing wear by addition of solid lubricant coating*
8. Suppression of riding-up flaw by rounding the grooved shoulder edge*

*New function

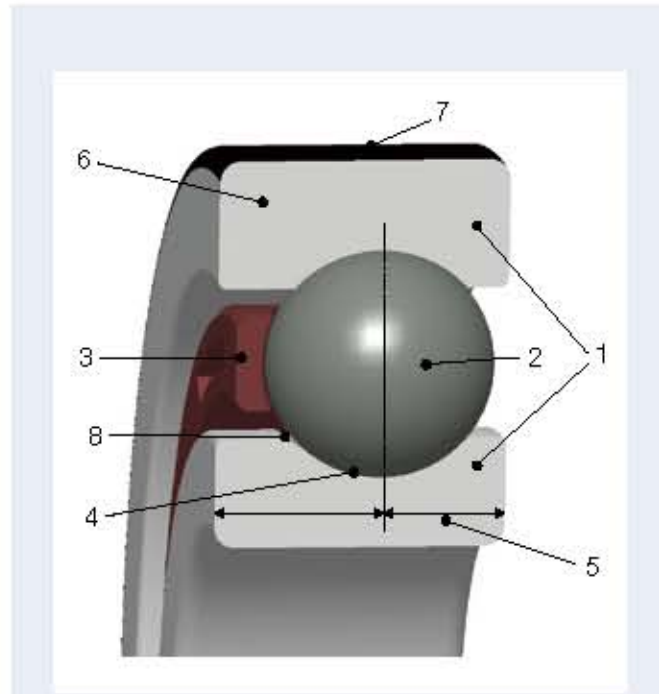


Fig. 1 Characteristics of the 8 points of configuration in BELTOP8

2. Features

- High reliability (Figure 2)

It is possible to establish longer life by optimizing internal specifications and employing UR/HTF in races. In addition, by applying EQTF to the ball and employing a plastic cage instead of the conventional cage, it is possible to suppress deterioration of the surface roughness of the ball during operation of the bearing, which provides a longer life.

Moreover, through utilizing the creep prevention technique by the increase of rigidity of the outer ring and the addition of a solid lubricant coating, it is possible to suppress the vibration increase in CVTs caused by housing wear.

- Torque lowering (Figure 3 and Figure 4)

The plastic cage allows for reduced stirring resistance of the lubricating oil by bearing rotation, resulting in lower friction.

- Size and weight reduction

Size and weight reduction was achieved by optimizing the internal specifications, the applied long-life technologies (UR, HTF, and EQTF), and the suppression of scratch due to climbing resulting from the application of the offset groove and groove shoulder rounding.

3. Applications

The long life, low torque, improved creep resistance, small size, and lightweight technologies used in this product are not limited to the belt CVT but can be applied to various types of transmissions including automatic transmission and the transmission for EV/HEV.

4. Summary

BELTOP8 consists of items developed based on NSK's basic technology, experience, and achievements. It is a rolling bearing that contributes to the high reliability, low torque, size reduction, and weight reduction of a belt CVT used under harsh environments and is currently used in many belt CVTs.

NSK will continue to actively develop and propose products for the needs of the rapidly changing automobile market.

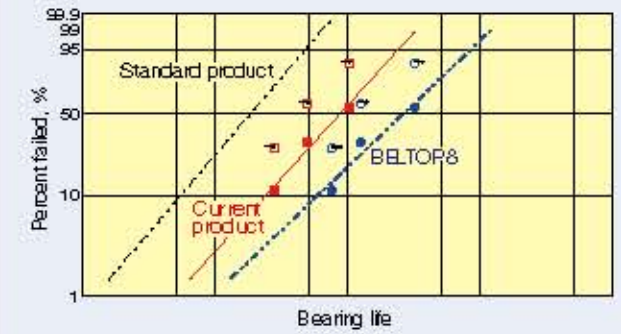


Fig. 2 Fatigue test results

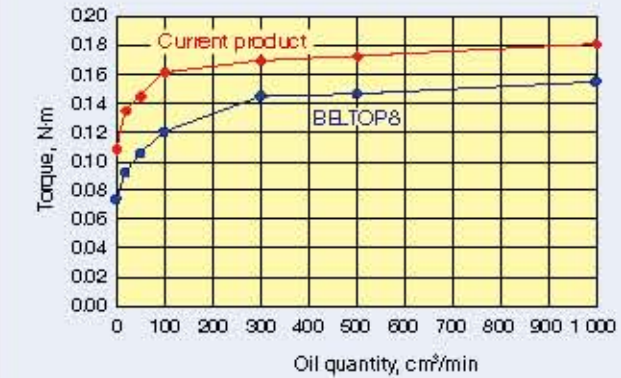


Fig. 3 Relationship between dynamic frictional torque and oil quantity

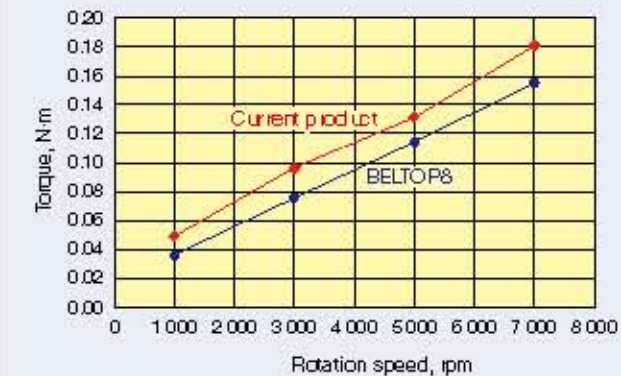


Fig. 4 Relationship between dynamic frictional torque and speed of rotation

Super-Long-Life Needle Rollers for Automobile Transmissions

In recent years, the strengthening of fuel efficiency regulations has resulted in demand for improvement of the fuel economy of automobiles globally. In automobile automatic transmissions, the viscosity of lubricating oil is being lowered and the amount of oil is being reduced in order to improve fuel economy. Therefore, needle bearings used in automatic transmissions are being lubricated less and the operating environments are becoming increasingly severe. Under such circumstances, prevention of early damage of the needle bearing and prevention of abrasion or the like occurring in a mating part in contact with the roller have become key concerns.

NSK has developed a super-long-life needle roller that prevents damage such as needle bearing damage or abrasion generated in a mating part under a diluted lubrication environment and introduces it below.

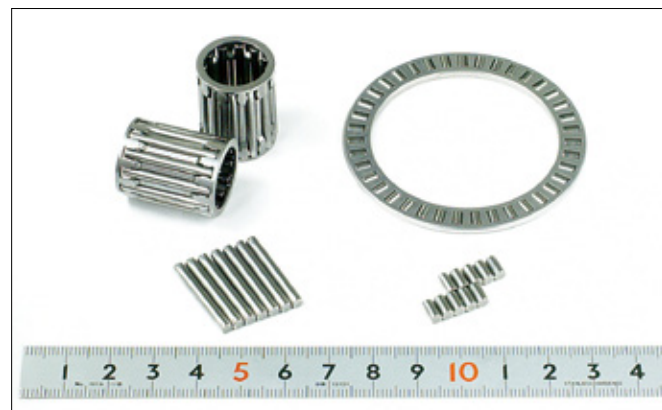


Photo 1 Super-long-life needle roller (planetary needle roller bearing, thrust needle roller bearing)

1. Configuration, Structure, and Specifications

Among NSK's needle rollers, the quenched and tempered standard rollers for two kinds of bearing steels, as well as the long-life quenched, tempered, and carbonitrided needle rollers, are widely used.

However, under the recent severe lubrication environments, there is an increasing number of instances in which damage to the needle roller itself or damage to a mating part due to metal contact occurs even in long-life needle rollers.

Consequently, NSK has developed a product that improves the lubrication film between two contact surfaces of the long-life needle roller by applying a special hardening process to the outermost surface as well as forming an oil sump through dimpling of the surface layer. (Figure 1)

2. Features (Figure 2)

(1) Improved lifetime durability

(Application examples with thrust needle roller bearings)

Increasing the hardness of the surface layer of the needle roller improved the durability of the roller itself under a diluted lubrication environment by more than two times, when compared to the long-life needle roller.

(2) Prevention of damage of the mating part

(Application examples with planetary needle roller bearings)

Recesses on the surface of the needle rollers act as oil reservoirs and improve the oil film even under diluted lubrication environments. This results in the prevention of surface damage such as abrasion to the mating parts.

Table 1 NSK needle roller lineup

Roller Specification		Heat treatment	Hardness of the surface	Dimple on the surface	
1	Conventional roller	Standard Specification	quenching-tempering	Normal	None
2	Special heat treatment (NSK long-life roller)	carbonitriding and quenching-tempering	Normal	None	None
3	Developed product (NSK super-long-life roller)	carbonitriding and quenching-tempering	Super hard	Available	Available

3. Applications

This technology is most suitable for applications involving thrust needle bearings and needle bearings for planetary gears used in automatic transmissions. These products are able to meet aggressive durability specifications from low viscosity lubricating oils and low oil volume environments and thus contribute to improving the fuel economy of automobiles.

4. Summary

NSK will propose the optimal needle roller bearing technology (standard specification, long-life, and super-long-life) based on each application and its operating environment.

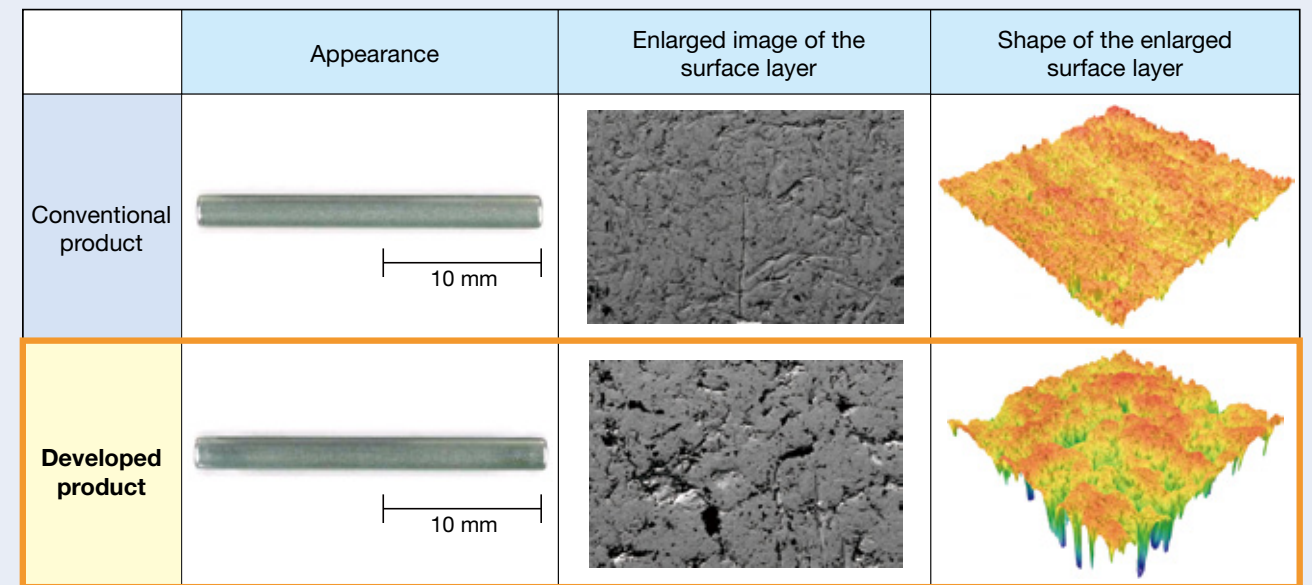


Fig. 1 Needle roller surface properties developed by special processing

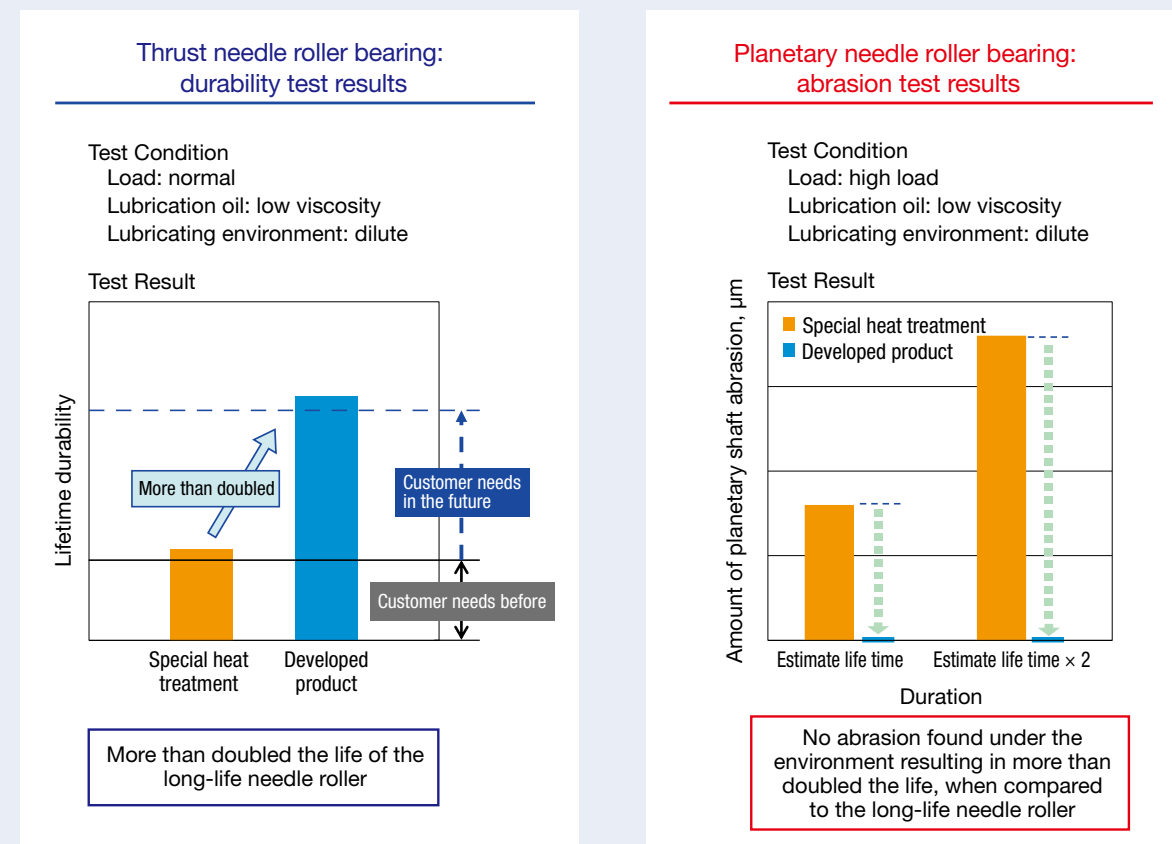


Fig. 2 Effect of developed product

Plastic Pin Internal Contractile Steering Column

Among the three major functions of a vehicle, turning, moving, and stopping, the steering column allows turning.

In addition, the steering column not only supports the air bag in the event of an accident but also has a function to shrink. Therefore, the steering column is required to have stable breakaway loads and shrink loads when absorbing an impact.

Now, NSK has developed a steering column with a breakaway structure using a new mechanism for stabilizing the breakaway load at the time of collision. This steering column will be introduced below.

1. Configuration, Structure, and Specifications

Photograph 1 shows a steering column equipped with a breakaway structure that uses the new mechanism. Photograph 2 shows the breakaway part, which is the main component of the breakaway structure.

The aluminum bracket is fixed onto the column pipe with plastic pins. The aluminum bracket is connected to the tilt bracket via multi-plates and is fixed when the lever is locked. When the lever is released, it is possible to change the vertical and axial positions of the steering wheel without any restriction.

The structure is configured in such a way that when an impact load is delivered from the steering wheel, with the aluminum bracket fixed, the plastic pin is sheared between the column pipe and the aluminum bracket, and then the steering column pipe shrinks (Figure 1).

2. Features (Table 1)

(1) Improving stability of breakaway load

During the separation of the tilt bracket in the conventional mechanism, since the breakaway portion is attached onto the interface panel, the breakaway load varies depending on the accuracy of the mating surface. However, a breakaway mechanism using plastic pins in the column pipe reduces variation of the moving load, thereby improving the stability of the breakaway load.

With the conventional mechanism, the steering column falls after shrink, which may cause injury to the occupant, making it necessary to design a separate part in order to prevent the steering column from falling. With the new mechanism, the tilt bracket does not break away, because the steering column is held by the tilt bracket, which prevents the steering column from falling.



Photo 1 Steering column with the newly developed product



Photo 2 New breakaway mechanism portion

(2) Improving layout flexibility

Shrinking only the column pipe portion minimizes the space for shrinkage, thereby improving the layout flexibility.

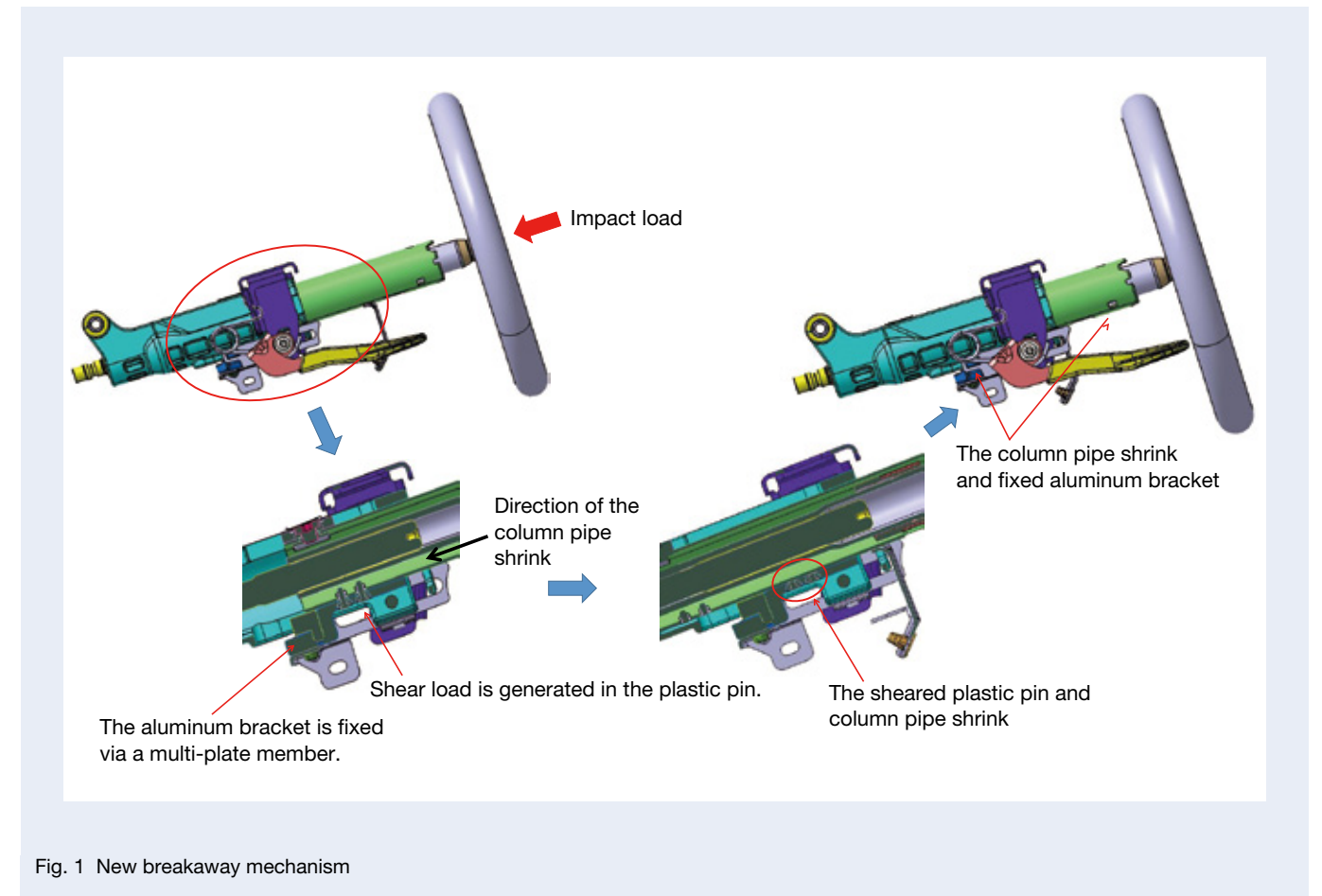


Fig. 1 New breakaway mechanism

Table 1 Comparison between a conventional column mechanism and the new breakaway mechanism

Item	Conventional column mechanism (tilt bracket breakaway)	New breakaway mechanism (Plastic pin type internal shrinkage column)
Stability after breakaway load	○	◎
Fall prevention after breakaway	△	◎
Layout flexibility	△	◎

3. Summary

Mass production of the plastic pin type internal shrinking column that has been introduced is scheduled to start.

We remain committed to developing this product in an effort to further contribute to increased automobile safety.

Worldwide Sales Offices

P: Phone F: Fax ☆: Head Office

NSK LTD.-HEADQUARTERS, TOKYO, JAPAN

Nissel Bldg., 1-6-3 Ohsaki, Shinagawa-ku, Tokyo 141-8560, Japan
INDUSTRIAL MACHINERY BUSINESS DIVISION-HEADQUARTERS
 P: +81-3-3779-7227 F: +81-3-3779-7644
AUTOMOTIVE BUSINESS DIVISION-HEADQUARTERS
 P: +81-3-3779-7189 F: +81-3-3779-7917

●Africa

South Africa:

NSK SOUTH AFRICA (PTY) LTD.

SANDTON 25 Galaxy Avenue, Linbro Business Park, Sandton 2148, South Africa
 P: +27-11-458-3600 F: +27-11-458-3608

●Asia and Oceania

Australia:

NSK AUSTRALIA PTY. LTD.

MELBOURNE ☆ 100 Logis Boulevard, Dandenong South, Victoria, 3175, Australia
 P: +61-3-9765-4400 F: +61-3-9765-4466

SYDNEY Suite A315, 20 Lexington Drive, Bella Vista, New South Wales, 2153, Australia
 P: +61-2-9839-2300 F: +61-2-8824-5794

BRISBANE 1/68 Selhurst Street, Coopers Plains, Queensland 4108, Australia
 P: +61-7-3347-2600 F: +61-7-3345-5376

PERTH Unit 1, 71 Tacoma Circuit, Cannling Vale, Western Australia 6155, Australia
 P: +61-8-9256-5000 F: +61-8-9256-1044

New Zealand:

NSK NEW ZEALAND LTD.

AUCKLAND 3 Te Apunga Place, Mt. Wellington, Auckland 1060, New Zealand
 P: +64-9-276-4982 F: +64-9-276-4082

China:

NSK (SHANGHAI) TRADING CO., LTD.

JIANGSU No.8 NSK Rd., Huaqiao Economic Development Zone, Kunshan, Jiangsu, China (215332)
 P: +86-512-5796-3000 F: +86-512-5796-3300

NSK (CHINA) INVESTMENT CO., LTD.

JIANGSU ☆ No.8 NSK Rd., Huaqiao Economic Development Zone, Kunshan, Jiangsu, China (215332)
 P: +86-512-5796-3000 F: +86-512-5796-3300

BEIJING Room 1906, Beijing Fortune Bldg., No.5 Dong San Huan Bei Lu, Chao Yang District, Beijing, China (100004)
 P: +86-10-6590-8161 F: +86-10-6590-8168

TIAN JIN Unit 4604, 46/F., Metropolitan Tower, 183 Nanjing Road, Heping District, Tianjin, China (300051)
 P: +86-22-8319-5030 F: +86-22-8319-5033

CHANGCHUN Room 902-03, Changchun Hongwell International Plaza, No.3299 Renmin Street, Changchun, Jilin, China (130061)
 P: +86-431-8898-8882 F: +86-431-8898-8670

SHENYANG Room 1101, China Resources Building, No.286 Qingnian Street, Heping District, Shenyang Liaoning, China (110004)
 P: +86-24-2334-2888 F: +86-24-2334-2058

DALIAN Room 1805 Xiwang Tower, No.136 Zhongshan Road, Zhongshan District, Dalian, Liaoning, China (116001)
 P: +86-411-8800-8168 F: +86-411-8800-8180

NANJING Room A1 22F, Golden Eagle International Plaza, No.89 Hanzhong Road, Nanjing, Jiangsu, China (210029)
 P: +86-25-8472-6671 F: +86-25-8472-6687

FUZHOU Room 1801-1811, B1#1A Class Office Building, Wanda Plaza, No.8 Anjiang Road, Fuzhou, China (350009)
 P: +86-591-8380-1030 F: +86-591-8380-1225

WUHAN Room 1512, No.198 Yuncui Road, Office Building, Oceanwide City Square, Jianghan District, Wuhan, China (400039)
 P: +86-27-8556-9630 F: +86-27-8556-9615

QINGDAO Room 802, Fargory International Plaza, No.26 Xianggang Zhong Road, Shinan District, Qingdao, Shandong, China (266071)
 P: +86-532-5568-3877 F: +86-532-5568-3876

GUANGZHOU Room 1011-16, Yuexiu Financial Tower, No.28 Zhujiang Road East, Zhujiang New Town, Guangzhou, Guangdong, China (510627)
 P: +86-20-3817-7800 F: +86-20-3786-4501

CHANGSHA Room 1048, 10/F, Zhongtian Plaza, No.788 Wuyi Road, Changsha, Hunan, China (410006)
 P: +86-731-8571-3100 F: +86-731-8571-3255

LUOYANG Room 1108, Fangda Hotel, 6 XiYuan Road, LuoYang HeNan, China (471003)
 P: +86-379-6068-8188 F: +86-379-6068-8190

XI'AN Room 1007, B Changan Metropolis Center 88 Nanguanzheng Street, Xi'an, Shanxi, China (710068)
 P: +86-29-8765-1896 F: +86-29-8765-1895

CHONGQING Room 612, Commercial Apartment, Sofitel Hotel, No.288, Keyuan Rd.4, Jiulongpo District, Chongqing, China (400039)
 P: +86-23-6806-5310 F: +86-23-6806-5292

CHENGDU Room 1117, Lipu Tower, No.82 North Kehua Road, Chengdu, Sichuan, China (610041)
 P: +86-28-8528-3680 F: +86-28-8528-3690

NSK CHINA SALES CO., LTD.

JIANGSU No.8 NSK Rd., Huaqiao Economic Development Zone, Kunshan, Jiangsu, China (215332)
 P: +86-512-5796-3000 F: +86-512-5796-3300

NSK HONG KONG LTD.

HONG KONG ☆ Suite 705, 7th Floor, South Tower, World Finance Centre, Harbour City, T.S.T., Kowloon, Hong Kong, China
 P: +862-2739-9933 F: +862-2739-9323

SHENZHEN Room 624-626, 6/F, Kerry Center, Renminnan Road, Shenzhen, Guangdong, China
 P: +86-755-25904886 F: +86-755-25904883

Taiwan:

TAIWAN NSK PRECISION CO., LTD.

TAIPEI ☆ 11F., No.87, Song Jiang Rd., Jhongshan District, Taipei City 104, Taiwan
 P: +886-2-2509-3305 F: +886-2-2509-1393

TAICHUNG 3F. -2, No. 540, Sec. 3, Taiwan Blvd., Xitun Dist., Taichung City 407, Taiwan
 P: +886-4-2708-3393 F: +886-4-2708-3395

TAINAN 5F. No.8, Daye 1st Rd., Southern Taiwan Science Park, Tainan City 741, Taiwan
 P: +886-6-505-5861 F: +886-6-505-5061

TAIWAN NSK TECHNOLOGY CO., LTD.

TAIPEI ☆ 11F., No.87, Song Jiang Rd., Jhongshan District, Taipei City 104, Taiwan
 P: +886-2-2509-3305 F: +886-2-2509-1393

TAICHUNG 10F-3, No.925, Sec.4, Taiwan Blvd., Xitun Dist., Taichung City 407, Taiwan
 P: +886-4-2358-2945 F: +886-4-2358-7682

TAINAN 5F. No.8, Daye 1st Rd., Southern Taiwan Science Park, Tainan City 741, Taiwan
 P: +886-6-505-5861 F: +886-6-505-5061

India:

NSK INDIA SALES CO.PVT.LTD.

CHENNAI ☆ TVH Beliciana Towers, 2nd Floor, Block I No.71/1, MRC Nagar Main Road, MRC Nagar, Chennai-600 028, Tamil Nadu, India
 P: +91-44-2847-9600 F: +91-44-2847-9601

DELHI Unit No-202, 2nd Floor, Block-A, Iris Tech Park, Sector-48, Sohna Road, Gurgaon-122018, Haryana, India
 P: +91-124-4838000 F: +91-124-4104-532

MUMBAI 321, 'A' Wing, Ahura Centre, 82, Mahakali Caves Road, Andheri (East), Mumbai -400 093, India
 P: +91-22-2838-7787 F: +91-22-2838-5191

Indonesia:

PT. NSK INDONESIA

JAKARTA Summitmas II, 8th Floor, Jl. Jend Sudirman Kav. 61-62, Jakarta 12190, Indonesia
 P: +62-21-252-3458 F: +62-21-252-3223

Korea:

NSK KOREA CO., LTD.

SEOUL Posco Center (West Wing) 9F, Westem-wing, 440, Teheran-ro, Gangnam-gu, Seoul, 135-777, Korea
 P: +82-2-3287-0300 F: +82-2-3287-0345

Malaysia:

NSK BEARINGS (MALAYSIA) SDN. BHD.

SHAH ALAM ☆ No. 2, Jalan Pernaju, U1/15, Seksyen U1, Hicom Glenmarie Industrial Park, 40150 Shah Alam, Selangor, Malaysia
 P: +60-3-7803-8859 F: +60-3-7806-5882

IPoh No.24, Jalan Kikik, Taman Inderawasih, 13600 Pral, Penang, Malaysia
 P: +60-4-3902275 F: +60-4-3991830

JOHOR BAHRU 88 Jalan Ros Merah 2/17, Taman Johor Jaya, 81100 Johor Bahru, Johor, Malaysia
 P: +60-7-3546290 F: +60-7-3546291

IPOH No.10&10A, Jalan Industri Paloh, Kawasan Perindustrian Ringan Paloh, 30200 Ipoh, Perak Darul Ridzuan, Malaysia.
 P: +60-5-2555000 F: +60-5-2553373

Philippines:

NSK REPRESENTATIVE OFFICE

MANILA 8th Floor The Salcedo Towers 169 H.V. dela Costa St., Salcedo Village Makati City, Philippines 1227
 P: +63-2-893-9543 F: +63-2-893-9173

Singapore:

NSK INTERNATIONAL (SINGAPORE) PTE LTD.

SINGAPORE 238A, Thomson Road, #24-01/05, Novena Square Tower A, Singapore 307684
 P: +65-6496-8000 F: +65-6250-5845

NSK SINGAPORE (PRIVATE) LTD.

SINGAPORE 238A, Thomson Road, #24-01/05, Novena Square Tower A, Singapore 307684
 P: +65-6496-8000 F: +65-6250-5845

Thailand:

NSK BEARINGS (THAILAND) CO.,LTD.

BANGKOK 26 Sol Onnuch 55/1 Pravet Subdistrict, Pravet District, Bangkok 10250, Thailand
 P: +66-2320-2555 F: +66-2320-2826

Vietnam:

NSK VIETNAM CO., LTD.

HANOI Techno Center, Room 204-205, Thang Long Industrial Park, Dong Anh District, Hanoi, Vietnam
 P: +84-24-3955-0159 F: +84-24-3955-0158

NSK REPRESENTATIVE OFFICE

HO CHI MINH CITY Suite 307, Metropolitan Building, 235 Dong Khoi Street, District 1, HCMC, Vietnam
 P: +84-28-3822-7907 F: +84-28-3822-7910

Worldwide Sales Offices

P: Phone F: Fax ☆: Head Office

●Europe

United Kingdom:

NSK EUROPE LTD. (EUROPEAN HEADQUARTERS)

MAIDENHEAD Belmont Place, Belmont Road, Maidenhead, Berkshire SL6 6TB, U.K.
 P: +44-1628-509-800 F: +44-1628-509-808

NSK UK LTD.

NEWARK Northern Road, Newark, Nottinghamshire NG24 2JF, U.K.
 P: +44-1638-805-123 F: +44-1638-805-000

France:

NSK FRANCE S.A.S.

PARIS Quartier de l'Europe, 2 Rue Georges Guynemer, 78283 Guyancourt, France
 P: +33-1-30-57-39-39 F: +33-1-30-57-00-01

Germany:

NSK DEUTSCHLAND GMBH

DUSSELDORF ☆ Harkortstrasse 15, D-40880 Ratingen, Germany
 P: +49-2102-4810 F: +49-2102-4812-290

STUTTGART Liebknechtstrasse 33, D-70565 Stuttgart-Vaihingen, Germany
 P: +49-711-79082-0 F: +49-711-79082-289

WOLFSBURG Tischlerstrasse 3, D-38440 Wolfsburg, Germany
 P: +49-5361-27647-10 F: +49-5361-27647-70

Italy:

NSK ITALIA S.P.A.

MILANO Via Garibaldi 215, Garbagnate Milanese (Milano) 20024, Italy
 P: +39-299-5191 F: +39-299-025778

Netherlands:

NSK EUROPEAN DISTRIBUTION CENTRE B.V.

TILBURG De Kroonstraat 38, 5048 AP Tilburg, Netherlands
 P: +31-13-4647647 F: +31-13-4647648

Poland:

NSK REPRESENTATIVE OFFICE

WARSAW Ul. Migdalowa 4/73, 02-786, Warsaw, Poland
 P: +48-22-645-1525 F: +48-22-645-1529

Russia:

NSK POLSKA SP. Z O.O.

SAINT-PETERSBURG Office I 703, Bldg 29, 18th Line of Vasilievskiy Ostrov, Saint-Petersburg, Russia, 199178
 P: +7-812-332-5071 F: +7-812-332-5072

Spain:

NSK SPAIN S.A.

BARCELONA C/Tarragona, 161 Cuerpo Bajo, 2a Planta, 08014, Barcelona, Spain
 P: +34-93-289-2763 F: +34-93-433-5776

Turkey:

NSK RULMANLARI ORTA DOGU TIC. LTD. STI.

ISTANBUL 18 Mayis Mah. Ataturk Cad., Ulya Engin Is Merkezi No: 88 Kat. 6, P.K. : 34738, Kozyatagi-Istanbul, Turkey
 P: +90-216-477-7111 F: +90-216-477-7174

United Arab Emirates:

NSK BEARINGS GULF TRADING CO.

DUBAI JAFZA View 19, Floor 24 Office LB192402/3, PO Box 282163, Downtown Jebel Ali, Dubai, UAE
 P: +971-4-804-8207 F: +971-4-884-7227

●North and South America

United States of America:

NSK AMERICAS, INC. (AMERICAN HEADQUARTERS)

ANN ARBOR 4200 Goss Road, Ann Arbor, Michigan 48105, U.S.A.
 P: +1-734-913-7500 F: +1-734-913-7511

NSK CORPORATION

ANN ARBOR 4200 Goss Road, Ann Arbor, Michigan 48105, U.S.A.
 P: +1-734-913-7500 F: +1-734-913-7511

NSK PRECISION AMERICA, INC.

FRANKLIN ☆ 3450 Bearing Drive, Franklin, Indiana 46131, U.S.A.
 P: +1-317-738-5000 F: +1-317-738-5050

SAN JOSE 780 Montague Expressway, Suite 505, San Jose, California, 95131, U.S.A.
 P: +1-408-944-9400 F: +1-408-944-9405

NSK LATIN AMERICA, INC.

MIAMI 3470 NW 82nd Avenue Suite 625, Miami FL 33122, U.S.A.
 P: +1-305-477-0605 F: +1-305-477-0377

Canada:

NSK CANADA INC.

TORONTO ☆ 5685 McAdam Road, Mississauga, Ontario, Canada L4Z 1N4
 P: +1-905-890-0740 F: +1-800-800-2788

MONTREAL 2150-32E Avenue Lachine, Quebec, Canada H8T 3H7
 P: +1-514-633-1220 F: +1-800-800-2788

VANCOUVER 3353 Wayburne Drive, Burnaby, British Columbia, Canada V5G 4L4
 P: +1-877-994-6675 F: +1-800-800-2788

Argentina:

NSK ARGENTINA SRL

BUENOS AIRES Garcia del Rio 2477 Piso 7 Oficina "A" (1429) Buenos Aires-Argentina
 P: +54-11-4704-5100 F: +54-11-4704-0033

<As of February 2018>

For the latest information, please refer to the NSK website.

www.nsk.com

NSK Ltd. has a basic policy not to export any products or technology designated as controlled items by export-related laws. When exporting the products in this brochure, the laws of the exporting country must be observed. Specifications are subject to change without notice and without any obligation on the part of the manufacturer. Every care has been taken to ensure the accuracy of the data contained in this brochure, but no liability can be accepted for any loss or damage suffered through errors or omissions. We will gratefully acknowledge any additions or corrections.

Motion & Control

No. 29 June 2018

Published by NSK Ltd.

